Mechanics of Nonlocal Dissipative Solids: Gradient Plasticity and Phase Field Modeling of Ductile Fracture

Fadi Aldakheel

$$\{\dot{\boldsymbol{\varphi}}, \dot{\alpha}, \dot{d}, \dot{\boldsymbol{\varepsilon}}^p\} = \mathrm{Arg}\{ \inf_{\dot{\boldsymbol{\varphi}}, \dot{\alpha}, \dot{d}, \dot{\boldsymbol{\varepsilon}}^p} \Pi(\dot{\boldsymbol{\varphi}}, \dot{\alpha}, \dot{d}, \dot{\boldsymbol{\varepsilon}}^p)\}$$

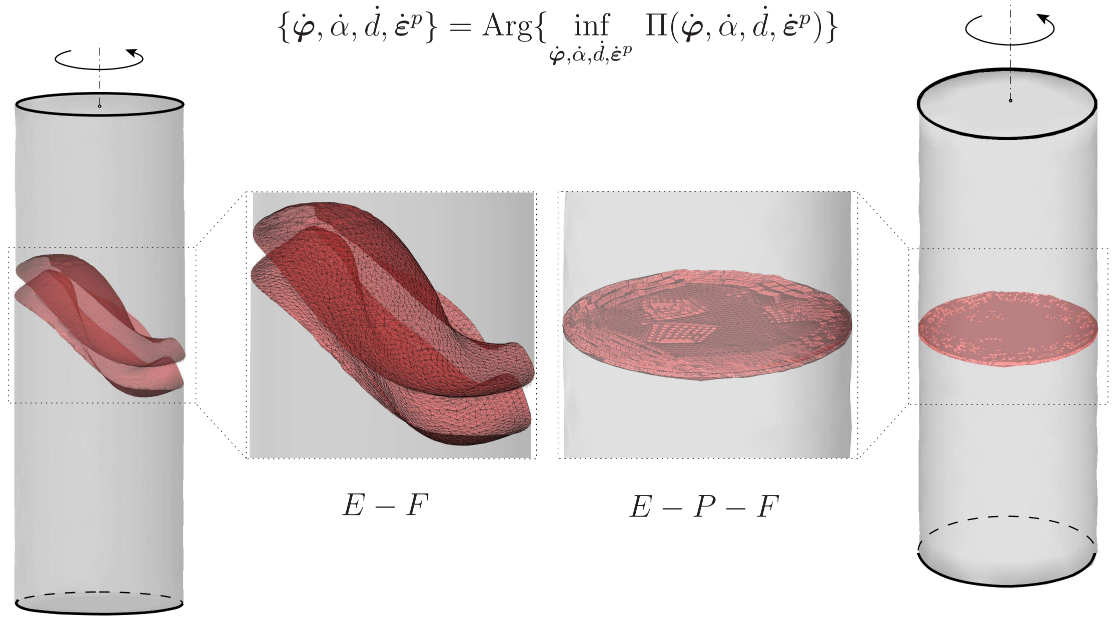

$$\dot{d} = \tfrac{1}{\eta_f} \Big\langle \, (1-d)\, \zeta [\, \tfrac{\widehat{w}_0^{ep}}{w_c} - 1 \,] - [\, d - l_f^2 \Delta d \,] \, \Big\rangle$$

Bericht Nr.: I-34 (2016)
Institut für Mechanik (Bauwesen), Lehrstuhl I
Professor Dr.-Ing. habil. C. Miehe
Stuttgart 2016

Mechanics of Nonlocal Dissipative Solids: Gradient Plasticity and Phase Field Modeling of Ductile Fracture

Von der Fakultät Bau- und Umweltingenieurwissenschaften
der Universität Stuttgart zur Erlangung der Würde
eines Doktor-Ingenieurs (Dr.-Ing.)
genehmigte Abhandlung

von

Fadi Aldakheel

aus Deirazzor - Syrien

Hauptberichter: Prof. Dr.-Ing. Christian Miehe
Mitberichter: Prof. Dr.-Ing. Jörn Mosler

Tag der mündlichen Prüfung: 25. Mai 2016

Institut für Mechanik (Bauwesen) der Universität Stuttgart

2016

Herausgeber:

Prof. Dr.-Ing. habil. C. Miehe

Organisation und Verwaltung:

Institut für Mechanik (Bauwesen)
Lehrstuhl I
Universität Stuttgart
Pfaffenwaldring 7
70569 Stuttgart
Tel.: +49 (0)711 685-66378
Fax: +49 (0)711 685-66347

© Fadi Aldakheel
Institut für Mechanik (Bauwesen)
Lehrstuhl I
Universität Stuttgart
Pfaffenwaldring 7
70569 Stuttgart
Tel.: +49 (0)711 685-66380
Fax: +49 (0)711 685-66347

Alle Rechte, insbesondere das der Übersetzung in fremde Sprachen, vorbehalten. Ohne Genehmigung des Autors ist es nicht gestattet, dieses Heft ganz oder teilweise auf fotomechanischem Wege (Fotokopie, Mikrokopie) zu vervielfältigen.

ISBN 978-3-937859-22-4 (D 93 Stuttgart)

Acknowledgements

This dissertation is the outcome of four and a half challenging and exciting years of my research work carried out between 2011 and 2016, during my employment as research associate at the Institute of Applied Mechanics (Civil Engineering) at the University of Stuttgart. I own my gratitude to all those who helped in making this thesis possible, as well as those who supported me in my life.

First of all, I would like to express my deep gratitude to my supervisor, Professor Christian Miehe, for giving me the opportunity to do my doctoral study under his guidance and for his support in academic and personal matters and for the fruitful discussions that contributed decisively to the achievement of this work. My sincere thanks are extended to Professor Jörn Mosler, for his interest in my work, his comments and for his acceptance to become the co-examiner for my doctoral thesis.

Next, I want to thank all my colleagues from both chairs of the Institute of Applied Mechanics for the pleasant working conditions, the excellent social atmosphere and their friendship. In particular, I would like to thank Steffen Mauthe, Stephan Teichtmeister and Daniel Kienle for discussions and the help in many scientific questions. Additionally, I would like to convey my gratitude to my current and former colleagues Ashish Sridhar, Gautam Ethiraj, Hüsnü Dal, Marc-Andre Keip, Daniel Vallicotti, Lukas Böger, Aref Nateghi and Nadine Steinecke for all kind of collaborations, discussions and laughter-filled company at the institute and conferences. I am very grateful to Swaroop Nagaraja and Nishant Prajapati who provided me with significant support to my dissertation through their master theses. The supervision of these works was a true pleasure. I would also like to gratefully acknowledge the financial support of this work through the international master program COMMAS position at the University of Stuttgart while being the COMMAS Course Director at the same time.

To my friends, Yousef Heider, Wassim Moussa and Fayez Mansour, I would like to extend my gratitude for the nice memories we had in Stuttgart. A special thanks goes to my best teacher and friend Ing. Husein Weis, for all his support since i was child till now.

With all my heart, I thank my parents, Refat Aldakheel and Fathia Almtoali for their everlasting love, patience, encouragement and for supporting me to become the person that I am today. I would like to convey my heartfelt thanks to my beloved wife Gehan Aldakheel and our future child for all the support and understanding during the last year.

Finally, I am truly grateful to my brother, Shadi Aldakheel and his wonderful family. My lovely brother, I did not see you and your sweet kids: Fadi, Sulaf and Celina since three years due to the difficult situation in Syria, but you are all in my heart and mind.

Stuttgart, May 2016 Fadi Aldakheel

Abstract

The underlying work is concerned with the development of physically-motivated constitutive models for the description of size effects within the context of inelastic deformations. A key aspect of this thesis is to develop a theoretical and computational framework for gradient-extended dissipative solids. It incorporates spatial gradients of selected micro-structural fields that account for length scale effects and describe the evolving dissipative mechanisms. In contrast to classical theories of local continuum mechanics, where the internal variables are determined by ordinary differential equations (ODEs), these global micro-structural (order parameter) fields are governed by partial differential equations (PDEs) and boundary conditions reflecting the continuity of these variables. The proposed framework for gradient-extended dissipative solids is first used to address the development of phenomenological theories of strain gradient plasticity. The corresponding model guarantees from the computational side a mesh-objective response in the post-critical ranges of softening materials. In this regard, a mixed variational principle for the evolution problem of gradient plasticity undergoing small and large strains is developed. A novel finite element formulation of the coupled problem incorporating a long-range hardening/softening parameter and its dual driving force is also proposed. A second employment of the introduced framework is related to the thermo-mechanical coupling in gradient plasticity theory within small strain deformations. Two global solution procedures for the thermo-mechanically coupled problem are introduced, namely the product formula algorithm and the coupled-simultaneous solution algorithm. For this purpose, a family of mixed finite element formulations is derived to account for the coupled thermo-mechanical boundary-value problem. A further application of the proposed framework deals with the phase-field modeling of ductile fracture undergoing large strains. To this end, a novel variational-based framework for the phase-field modeling of ductile fracture in gradient-extended elastic-plastic solids is proposed. Herein, two independent length scales, that regularize both the plastic response as well as the crack discontinuities, are introduced. This ensures that the failure zone of ductile fracture takes place inside the plastic zone, and guarantees from the computational perspective mesh objectivity in the post-critical range. The performance of these models is tested on a broad range of homogeneous and heterogeneous representative numerical simulations.

Zusammenfassung

Die vorliegende Arbeit befasst sich mit der Entwicklung physikalisch fundierter, konstitutiver Modelle zur Beschreibung von Größeneffekten unter inelastischen Deformationen. Die Erarbeitung einer theoretisch wie algorithmisch instruktiven Abhandlung zur Modellierung gradienten-erweitereter, dissipativer Festkörper stellt einen zentralen Aspekt dieser Arbeit dar. Ausgewählte Felder zur Charakterisierung von Miktrostukturen werden mitsamt zugehöriger räumlicher Gradienten berücksichtigt, um dissipative und Längenskalen-Effekte in ihrer zeitlichen Evolution zu erfassen. Diese globalen Mikrostruktur-Felder (Ordnungsparameter) werden im Gegensatz zu klassischen Theorien der lokalen Kontinuumsmechanik, innerhalb derer interne Variablen durch die Lösung gewöhnlicher Differentialgleichungen bestimmt werden, durch partielle Differentialgleichungen und assoziierte Randbedingungen beschrieben. Die vorgestellte Theorie für gradienten-erweiterte, dissipative Körper wird zunächst verwendet, um phänomenologische, verzerrungs-induzierte Plastizitätstheorien zu entwickeln. Für den postkritischen Bereich einer Entfestigung garantiert das zugehörige Modell Objektivität hinsichtlich beliebiger Vernetzung im Rahmen einer algorithmischen Umsetzung. Hierzu wird ein gemischtes Variationsprinzip für die Evolutionsgleichungen der Gradientenplastizität unter kleinen und großen Deformationen vorgestellt. Zur numerischen Approximation des gekoppelten Problems wird eine innovative Finite Elemente Formulierung verwendet, welche Ver- und Entfestigungsparameter sowie die assoziierte thermodynamische Kraftgröße inkorporiert. Eine zweite Anwendung der vorgestellten Formulierung stellt die thermo-mechanische Wechselwirkung bei Gradientenplastizität unter kleinen Deformationen dar. Zwei globale Lösungsverfahren werden für das gekoppelte Problem vorgestellt: ein auf Operator-Splits basierender und ein gekoppelt-simultaner Algorithmus. Erneut wird hierzu eine Familie gemischter Elementformulierungen hergeleitet, um die präzise Approximation von thermo-mechanisch gekoppelten Prozessen sicher zu stellen. Eine letzte Anwendung findet die Varationsstruktur in der Phasenfeldmodellierung von duktilen Bruchvorgängen unter großen Deformationen. Für diese Beschreibung duktilen Versagens mittels Phasenfeldern wird eine innovative variationelle Formulierung für gradienten-erweiterte, elastisch-plastische Festkörper vorgestellt. Zwei unabhängige Längenskalen zur Regularisierung von plastischer Materialantwort und Bruch-Diskontinuität werden für diesen Zweck eingeführt. Diese Felder stellen sicher, dass duktiles Materialversagen in Zonen der plastischen Deformation auftritt und dass bei der algorithmischen Umsetzung Netz-Objektivität im postkritischen Bereich gewahrt bleibt. Validität und Performanz dieser Modelle werden anhand eines breiten Spektrums homogener wie heterogener numerischer Simulationen repräsentativ untersucht.

Contents

1. Introduction **1**
  1.1. Motivation and state of the art 1
    1.1.1. Phenomenological theories of isotropic gradient plasticity 2
    1.1.2. Phase field formulation of ductile fracture 5
  1.2. Outline of the thesis 6

2. Fundamentals of Continuum Mechanics **9**
  2.1. Basic kinematics of finite deformation 9
    2.1.1. Motion of a material body 9
    2.1.2. Material deformation gradient 10
    2.1.3. Metric tensors and strain measures 11
  2.2. Definition of stress tensors and heat flux 11
    2.2.1. Stress tensors 12
    2.2.2. Heat flux 13
  2.3. Physical balance principles 13
    2.3.1. Global equations 13
    2.3.2. Local equations 14
  2.4. Coupled thermo-mechanical modeling 14
    2.4.1. Primary fields with micro-structure changes 14
    2.4.2. The boundary conditions for the coupled problem 15
    2.4.3. Objective free energy function 16
    2.4.4. Dissipation postulate 16
  2.5. Constitutive model in the logarithmic strain space 18
    2.5.1. Strain measure 18
    2.5.2. Definition of transformation tensors 18

3. Computational Gradient Plasticity at Small Strain **19**
  3.1. Rate-type variational principles for gradient plasticity 19
    3.1.1. Primary variables and energetic response function 19
    3.1.2. Secondary variables and dissipative response function 20
    3.1.3. A mixed variational principle for the evolution problem 21
    3.1.4. Euler equations of the mixed variational principle 21
  3.2. Time-discrete incremental variational principle 22
    3.2.1. Euler equations of the mixed incremental variational principle 23
    3.2.2. A reduced three-field global solution strategy 23
  3.3. Analytical solutions and basic ideas of mixed FE design 25
    3.3.1. Deformation-controlled plane shear test for gradient plasticity 25
    3.3.2. Theoretical solution for micro-clamped hardening plasticity 26
    3.3.3. Theoretical solution for perturbed softening plasticity 27
    3.3.4. Study of mixed finite element design and basic difficulties 28
    3.3.5. Elastic-plastic-boundary (EPB) in regular FE discretizations 31

3.4. Q1-P0-type finite element design of gradient plasticity 33
    3.4.1. FE discretization for Quadrilateral or Brick-like elements 33
    3.4.2. Condensation at the element level 35
    3.4.3. Effective element arrays and global solver 35
    3.4.4. Modified setting with elementwise constant driving forces 36
3.5. Mini-type finite element design of gradient plasticity 37
    3.5.1. FE discretization for triangular elements 38
    3.5.2. Partitioned element arrays for newton-type solver 39
    3.5.3. Condensation of bubble degrees at the element level 40
    3.5.4. Modified setting with elementwise constant driving forces 40
3.6. Representative Numerical Examples 42
    3.6.1. Plane Shear Test for Softening Plasticity 42
    3.6.2. Plane shear test for micro-clamped hardening plasticity 46
    3.6.3. 3D shear test of composite RVE for hardening plasticity 49

4. Coupled Thermo-Gradient-Plasticity at Small Strain 53
4.1. Constitutive functions of the coupled problem 53
    4.1.1. Energetic response function 53
    4.1.2. Dissipative response function 54
    4.1.3. Thermodynamic restrictions 54
    4.1.4. Principle of maximum dissipation 55
    4.1.5. Local-global constitutive equations 56
4.2. Algorithmic implementation of thermo-gradient-plasticity 57
    4.2.1. Product formula algorithm 58
    4.2.2. Simultaneous solution scheme 59
4.3. Representative numerical examples 61
    4.3.1. Cross shear localization in tension for softening plasticity 62
    4.3.2. Expansion of a plate with hole for hardening plasticity 64

5. Variational Gradient Plasticity in the Logarithmic Strain Space 67
5.1. Basic kinematics in the Logarithmic Strain Space 67
    5.1.1. Volumetric and isochoric decomposition 67
    5.1.2. Short-range micro-motion fields 68
    5.1.3. Lagrangian logarithmic projection tensors 69
    5.1.4. Long-range micro-motion field 70
5.2. Energetic and dissipative response functions 71
    5.2.1. Energetic response function 71
    5.2.2. Dissipative response function 72
5.3. Mixed variational principle for the evolution problem 72
    5.3.1. Time discrete incremental variational principle 73
    5.3.2. Euler Equations of the Mixed Incremental Variational Principle . . . 74
    5.3.3. Two-steps local-global update schemes 75

5.3.4. Weak form of reduced global equations 76
5.4. Q1-P0–Brick type finite element formulation 79
5.4.1. Finite element discretization 80
5.4.2. Condensation at the element level 81
5.4.3. Effective element arrays and global solver 81
5.5. Mini–Tetrahedral type finite element formulation 82
5.5.1. Finite element discretization 82
5.5.2. Partitioned element arrays for newton-type solver 83
5.5.3. Condensation of bubble degrees at the element level 83
5.6. Representative numerical examples 84
5.6.1. Necking of cylindrical bar 84
5.6.2. Cross shearing of a plate in tension 87
5.6.3. Three dimensional torsion test of a square-section bar 89

6. Phase Field Modeling of Ductile Fracture at Finite Strains 93
6.1. Geometric basis for phase field fracture 93
6.1.1. One dimensional cracked bar 93
6.1.2. Regularized crack surface topology 95
6.1.3. Evolution of the regularized crack surface 97
6.1.4. Irreversible crack evolution without crack healing 97
6.2. Variational gradient-extended phase field modeling of ductile fracture 98
6.2.1. Global primary fields and constitutive state variables 99
6.2.2. Coupling gradient plasticity to gradient damage mechanics 99
6.2.3. Effective elastic-plastic work and degradation functions 100
6.2.4. Driving, resistance and thresholds for plasticity and fracture 101
6.2.5. Rate-dependent evolution equations for the internal variables 102
6.2.6. Minimization principle for the multi-field evolution problem 103
6.3. Micromorphic approach for gradient plasticity-damage models 104
6.3.1. Extended constitutive state and work density function 104
6.3.2. Plastic driving force and resistance 104
6.3.3. Evolution equations of the internal variables 104
6.3.4. Micromorphic regularization of the minimization principle 105
6.4. Numerical implementation of the regularized minimization problem 105
6.4.1. Incremental potential density function 105
6.4.2. Condensation of local variables 106
6.4.3. Reduced global Problem 106
6.4.4. The three governing PDEs of the multi-field problem 107
6.5. Representative numerical examples 109
6.5.1. Local homogeneous response 109
6.5.2. Analysis of a V-Notch Bar in Tension Test 112
6.5.3. Investigation of single-edge notched shear test 116
6.5.4. Three dimensional torsion test of a cylindrical bar 117

7. Summary and Conclusions 121

A. Gurson Model for Ductile Damage in Metals 123
  A.1. Constitutive equations in logarithmic strain space 123
  A.2. Algorithmic implementation of the Gurson model 125
  A.3. Coupling Gurson model to gradient damage mechanics 126
  A.4. One dimensional homogeneous test 128

References 131

1. Introduction

With the recent developments of micro- and nano-technology that have a wide spectrum of engineering applications such as in automotive industry and medical fields, the predictive modeling of the mechanical behavior at small dimensions like on the micro-scale has been a topic of intensive research during the last years. In this context, the term *size effects* is used to describe the influence of the structure-size on the mechanical response during inelastic deformations. The main goal of this work is to develop a theoretical and computational framework for gradient-extended dissipative solids that accounts for micro-structure-based size effects with applications to *phenomenological theories of gradient plasticity* at small and finite strains, *thermo-gradient-plasticity* at small strains and *phase-field modeling of ductile fracture* at finite strains. This incorporates spatial gradients of selected micro-structural fields based on length-scales that describe the evolving dissipative mechanisms.

1.1. Motivation and state of the art

In *conventional theories* of local continuum mechanics, no size effects are predicted. As a result, micro-structure interactions are not involved in the constitutive formulation. One significant limitation of these conventional theories that arises in the computation of localized inelastic deformations in softening materials using finite element techniques is the pathological mesh dependency that leads to loss of ellipticity of the governing equations. To overcome this non-physical behavior, *extended continuum theories* of inelasticity have been proposed in literature, which incorporate length scales. Hereby, additional internal variables and their nonlocal counterparts can be introduced to reflect the micro-structural response. The non-locality is obtained by weighted averaging over a spatial neighborhood of a local quantity. Typical examples are gradient-extended theories of plasticity and damage. With regard to plasticity theories, gradients of the accumulated plastic strain field enter the constitutive formulation and act as localization limiters for softening materials. In the field of damage mechanics, an auxiliary variable denoted as the damage field along with its gradient counterpart enter the constitutive functions to regularize the sharp crack topology. The theoretical basis of such a formulation goes back to the micro-polar theory of COSSERAT brothers [38] and CAPRIZ [34] for order parameter-based models of continua along with micro-structures and gradient extensions of the classical local theory of internal variables by MAUGIN [85] and MAUGIN & MUSCHIK [86, 87]. The book of FRÉMOND [54] outlines a general approach to gradient-type dissipative solids in the thermodynamical context.

In all these treatments, the standard continuum degrees of freedom attached to each material point are extended to include additional global internal variables, which are denoted as order parameters. This leads to additional micro-force balance-type partial differential equations associated with the micro-structure. These PDEs are analogous to the standard balance of linear momentum. FOREST [51] demonstrated that most models of the strain-gradient theories in the literature can be related to a systematic method of construction of higher-order media, denoted as the *micromorphic approach*. The key point here is the introduction of dual internal local-global field variables via a penalty method, where the global fields are defined in the full domain.

Recently, MIEHE [96, 110] proposed a new perspective for embedding of the micro-mechanical models into the macro-mechanical continuum formulation based on a multi-field incremental variational framework for gradient-extended standard dissipative solids. Thereby, an incremental minimization and saddle point principles for a class of gradient-type dissipative materials were developed. This variational principle, formulated in terms of the global displacement and order parameters fields as well as the dissipative driving forces, is based on constitutive energy storage and dissipation functions. In this research work, the following two extensions of the variational formulation are presented: (i) Gradient plasticity at small and finite strains based on von Mises yield criterion function with gradient-extended hardening/softening response as outlined in Miehe et al. [104, 105] and Aldakheel et al. [10]. (ii) Phase-field modeling of ductile fracture that links gradient plasticity and gradient damage at finite strains, see Miehe et al. [108, 109] and Aldakheel et al. [8, 9]. In this context, it is important to account for thermo-mechanical coupling effects due to dissipative heating. To this end, we propose also a coupled thermo-gradient-plasticity model in line with Aldakheel et al. [8].

1.1.1. Phenomenological theories of isotropic gradient plasticity. An example of a rigorous embedding of the micro-mechanical models into the macro-mechanical continuum formulation, which is based on non-standard theories and incorporate length-scales, is the phenomenological theory of strain gradient plasticity. Hereby, the global micro-structural fields are determined by partial differential equations. The physical foundations of such micro-structural interactions are the size effects associated with lattice-curvature-

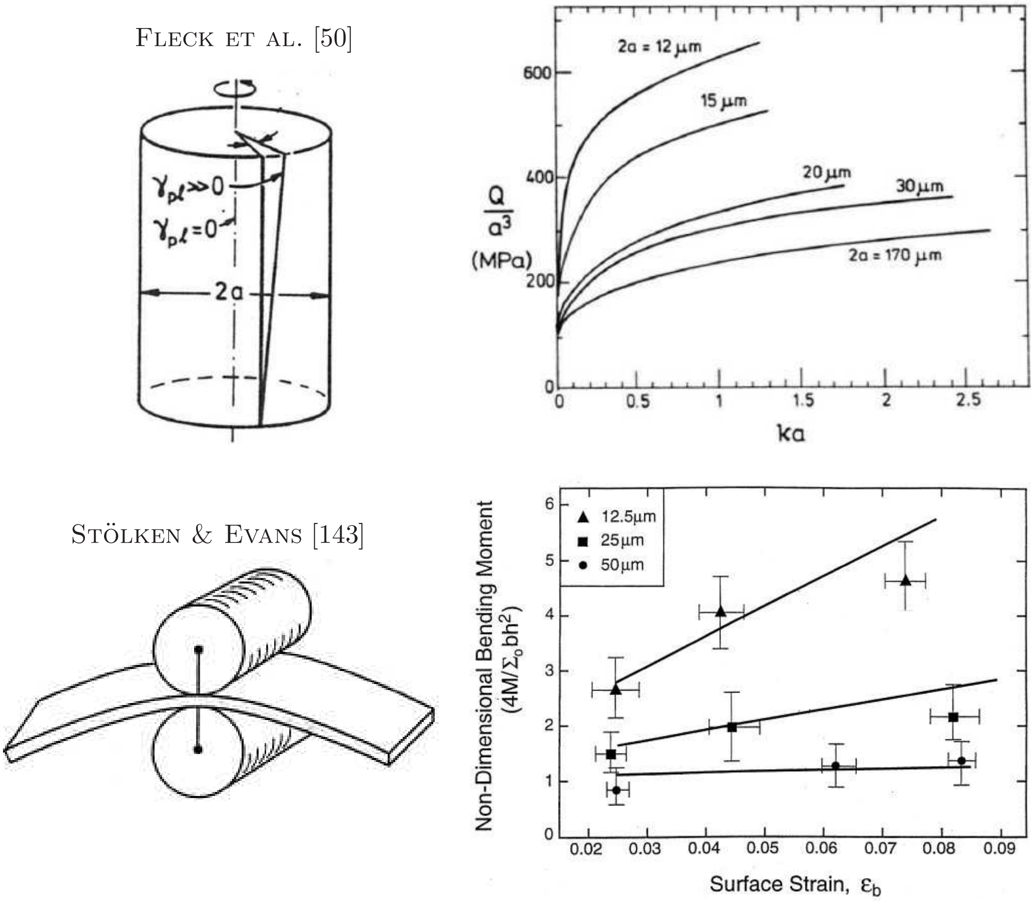

Figure 1.1: The smaller the specimen dimensions are, the stiffer is the material response, as reported in Fleck et al. [50] for torsion of thin copper wires and Stölken & Evans [143] for micro-bending of thin nickel foils.

based dislocation densities as shown in ASHBY [22], FLECK & HUTCHINSON [47], NYE [122], KRÖNER [73], NIX & GAO [121], ARZT [21], and GAO ET AL. [55]. Experimentally, FLECK ET AL. [50] investigated the response of thin copper wires with diameters ranging from 12 μm to 170 μm subjected to torsion as plotted in Figure 1.1. They observed that the thinner wire with 12 μm diameter required higher torsion than the thicker wires to cause equal rotations. This behavior was explained by the greater strain gradient and the higher density of geometrically necessary dislocations of the thinner wires, resulting in an increased amount of work hardening as shown in Figure 1.1. Similar results were found by STÖLKEN & EVANS [143] for micro-bending of thin nickel foils, having thicknesses of $h = 12.5/25/50$ μm. They also observed that the thinner foil with $h = 12.5$ μm required a larger equivalent bending moment than thicker foils for producing the same amount of surface strain as illustrated in Figure 1.1.

Phenomenological theories of gradient plasticity are outlined in the works of AIFANTIS [7], GURTIN [64], FOREST & SIEVERT [52], GUDMUNDSON [61], ANAND ET AL. [16] GURTIN & ANAND [65], REDDY ET AL. [129] and FLECK & WILLIS [48, 49]. In these works, the variational principles are not presented, which recast the formulation of the boundary value problem of gradient plasticity in a canonical format. In this context, MÜHLHAUS & AIFANTIS [114] and DE BORST & MÜHLHAUS [39] proposed a two-field rate-type variational principle. MIEHE [97, 110] and WELSCHINGER [153] suggested a mixed variational principle for gradient-extended plasticity including driving force as a global field. In line with this work, we propose a new theoretical and computational setting of gradient plasticity in terms of a rigorous use of mixed variational principles for the evolution problem. Herein, a saddle point principle based on a rate-type potential determines the evolution of the plastic strain and hardening variables as well as their dual driving forces.

A variety of numerical strategies has been proposed in the literature for finite element design of strain gradient plasticity. In DE BORST & MÜHLHAUS [39], the formulation was based on a rather numerical expensive C^1-continuous two-field formulation that allows the computation of second derivatives for the Laplacian of the incremental plastic parameter in the yield function. The follow-up work of DE BORST & PAMIN [40] suggested a C^0-continuous three-field formulation based on an additional penalty constraint that introduces a new field variable for the gradient of the incremental plastic parameter. In the work of LIEBE & STEINMANN [79], a global active set strategy of gradient plasticity was considered, where Kuhn-Tucker-type loading/unloading conditions were checked in weak form via finite element residuals at the nodes. Such a formulation needs a non-standard global active set search, which is not robust when applied to complex inhomogeneous response. Numerical implementations of gradient plasticity at small strains in terms of discontinuous Galerkin methods are outlined in DJOKO ET AL. [42, 43]. Nevertheless, many problems arise in all of these numerical strategies, such as the observation of spurious oscillations of the plastic variables near the elastic-plastic-boundaries (EPBs), see, e.g. DE BORST & PAMIN [40] and LIEBE & STEINMANN [79]. This has encouraged ENGELEN ET AL. [45], GEERS ET AL. [57] and GEERS [56] to propose a gradient plasticity model based on an accompanying PDE of the modified Helmholtz type, that defines the nonlocal plastic strain in terms of its local counterpart.

In this work, we develop a *mixed finite element design* for the gradient plasticity problem incorporating global hardening/softening parameter and its dual driving force.

This allows a straightforward local definition of plastic loading-unloading driven by the global fields. The proposed procedure includes a rational method for the definition of elastic-plastic-boundaries in gradient plasticity along with a post-processor that defines the plastic variables in the elastic range. Additionally, we develop new families of extended Q1P0-type and MINI-type mixed finite elements for the coupled problem, including a local-global update strategy based on variational principles. Next, we present numerical results that demonstrate the modeling capabilities of our formulation.

Despite the fact that temperature distribution during heat accumulation has a strong influence on the mechanical properties (see SIMO & MIEHE [140]), thermal effects were not included in the constitutive formulation of most of the recently developed strain gradient theories. For a better understanding of this coupling phenomenon, consider some engineering applications, such as the frictional heating of disc brakes in automotive industry, as shown in Figure 1.2a. Hereby, high temperatures and thermal gradients are predicted during the braking operation, which leads to harmful effects of the brake system such as brake fade, premature wear and thermal cracks, see GHADIMI ET AL. [58]. Another example is the hammering of nails, where the mechanical work due to the impact loading is transferred to the nail, which results in high temperature distribution and heat dissipation in the form of sparks as depicted in Figure 1.2b. While the above mentioned examples demonstrate thermal effects arising due to mechanical loading, one can also find a lot of other engineering applications of the reverse phenomenon, where mechanical deformations are caused due to thermal loading. For instance, the expansion joint of a bridge, which is designed in a manner to allow for the expansion and contraction of the bridge as a result of changes in the ambient temperature and prevent bridge-failure due to thermal expansion as illustrated in Figure 1.2c.

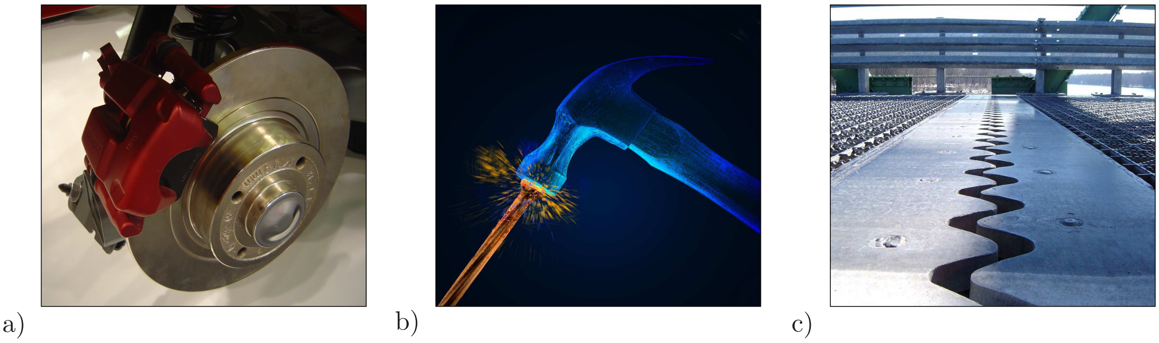
a) b) c)

Figure 1.2: *Thermo-mechanical coupling emerged in some engineering applications.* a) Heat dissipation due to friction in disc-brake (source: `en.wikipedia.org` [6]). b) Thermal dissipation in a nail due to mechanical impact of a hammer (source: `dreamstime.com` [4]). c) Thermal expansion joint of a bridge (source: `durasystemscomputing.com` [5]).

A variational formulation for the thermo-mechanical coupling in finite strain plasticity theory with non-linear kinematic hardening is outlined in CANADIJA & MOSLER [33] based on the works YANG ET AL. [160] and STAINIER & ORTIZ [142]. However no size effects were involved in the constitutive formulation. This has motivated VOYIADJIS & FAGHIHI [150] and FAGHIHI ET AL. [46] to propose a coupled thermo-mechanical framework of higher-order strain gradient plasticity theory that investigates the behavior of small-scale metallic volumes in fast transient times based on energetic and dissipative gradient length scales. In this context, we extended the above mentioned gradient plasticity model introduced in MIEHE ET AL. [104] to account for thermal effects in line with

Aldakheel et al. [8] and Nagaraja [116]. From the numerical implementation aspects, we present the following two solution schemes for the coupled problem: (i) The *global product formula algorithm*, and (ii) an *implicit coupled algorithm* in line with the work of Simo & Miehe [140] and Wriggers et al. [155].

1.1.2. Phase field formulation of ductile fracture. Another example for incorporating the size effects and length scales in the constitutive formulation is the phase-field modeling of *ductile fracture* in gradient-extended elastic-plastic solids. Study of ductile fracture plays a very important role in various engineering applications, e.g., machining, cutting and forming of ductile metals are at the core of automobile, aerospace, bridges or heavy industries as shown in Figure 1.3. These applications can significantly benefit from a precisely predictive computational tool to model ductile fracture in the design phase of products.

a) b) c)

Figure 1.3: *Engineering applications for ductile failure in metals.* a) Damaged airplane due to impact with ground (source: `aviation-safety.net` [1]). b) Car crash scenario (source: `blogs.reuters.com` [2]). c) Failure of Interstate 5 bridge due to overloading (source: `bloomberg.com` [3]).

Two different approaches are introduced in the literature to describe ductile fracture phenomena, which are *discontinuous* and *continuous models*. In the former category, strong-discontinuity strategies are introduced to model the failure response, in which the finite element mesh is adapted to the geometry of the discontinuity. Some key literature can be found in Wells [151], who proposed a failure criterion based on the crack tip opening displacement and Rice [132], who proposed the J-integral method. In both, an extensive plastic deformation ahead of a crack tip was observed. In Song et al. [141], an element deleting method is illustrated, where the elements in which the fracture criterion is met are deleted from the finite element mesh. Alternative solution strategies are based on cohesive zone models, which allow the description of sharp cracks by introducing a strong discontinuity in the kinematical description, see Simo et al. [139], Armero & Garikipati [19], Oliver [123, 124], Armero [18], Mosler & Meschke [113], Mosler [112], Linder & Armero [80] and Linder & Raina [81] for strong discontinuities embedded within the finite element. For strong discontinuities embedded in the interfaces between finite elements, one may refer to Xu & Needleman [157], Ortiz & Pandolfi [126], Zhang & Paulino [161]. Recently Belytschko & Black [26], Moës et al. [111] and Wells & Sluys [152] proposed a promising technique, which is the extended finite element method (XFEM). In this, extra degrees of freedom are added to the nodes of the elements containing the discontinuity, allowing free crack propagation through the mesh.

In the *continuous approaches* to ductile fracture, a great number of purely *phenomenological* and *micro-mechanically* motivated approaches exists, see Kachanov [72], Lemaitre [76, 75] and Lemaitre & Chaboche [77] for a homogenized representation of micro-cracks and voids in a macroscopic format. In the microscopically based models, the macroscopic material response derived from the behavior of the micro-void nucleation and growth mechanism. It is rooted in the pioneering work of Gurson [62] who developed a constitutive model, which assumes the existence of spherical voids embedded into an elasto-plastic material matrix. *Gurson model* was later modified by Tvergaard [148], Tvergaard & Needleman [147], Leblond et al. [74], Reuscha et al. [130, 131], Li et al. [78], Xue [158], Needleman & Tvergaard [120], Nahshon & Hutchinson [118], Xue et al. [159], Besson [27], Boyce et al. [30] and Huespe et al. [71, 70] to account for damage growth, where the yield criterion function has been extended by introducing new material parameters to account for the coalescence effect.

In the aforementioned literature on ductile fracture, local plasticity models are coupled to damage models. This leads to a localized plastic and damage zones in the softening material response. The computation of such a localized ductile fracture behavior with finite element techniques yields pathological mesh dependencies in the post-critical range and non-physical evolution of the fracture zone outside the plastic zone. In this context, gradient-enhanced damage models coupled with the local (J_2-) plasticity models are used as a regularization methods to model ductile failure, see, e.g, Nedjar [119], de Borst et al. [41], Grassl & Jirasek [59], Alessi et al. [11, 12] for small deformations and Aslan et al. [23], Saanouni & Hamed [133] for large deformations. Mesh objective response of these models cannot be established due to the inherent nature of local plastic strains. To overcome this non-physical behavior, we developed a new computational framework for the coupling of gradient plasticity with gradient damage models by introducing two material parameters, namely the *plastic length scale* l_p and the *fracture length scale* l_f, in which $l_f \leq l_p$ to ensure the occurrence of fracture zone inside the plastic zone, see Miehe et al. [106] for additional details and references.

The modeling of macroscopic cracks can be achieved in a convenient way by the continuum phase-field approaches to fracture, which are based on the regularization of sharp crack discontinuities, see Miehe et al. [101, 100], Welschinger [153], Hofacker [68] and Schänzel [135]. This avoids the use of complex discretization methods for crack discontinuities and can account for complex crack patterns. For a recent application of the phase-field modeling of ductile fracture, one may refer to Duda et al. [44], where a small-strain continuum theory for brittle fracture in elastic-plastic solids based on microforce balance is presented. Ambati et al. [13, 14] proposed a mesh sensitive results of ductile fracture by coupling local plasticity to phase-field fracture at the post-critical range. To achieve mesh objectivity in the post-critical range, we introduced a *variational* gradient-extended phase-field modeling of ductile fracture in elastic-plastic solids at finite strains as a key goal of this work. It links a formulation of variational gradient plasticity outlined in Miehe et al. [105], to a specific setting of variational gradient damage, rooted in the phase field approach of fracture suggested by Miehe et al. [101, 100].

1.2. Outline of the thesis

The objective of this dissertation is the development of new aspects for the formulation and numerical implementation of gradient-extended dissipative solids, that account for micro-structure-based size effects and length scales at *small strains* and in the *logarithmic strain space*. The thesis is organized as follows:

Chapter 2 presents the basic notations of this dissertation and the principle equations of non-linear continuum mechanics, that describe the fundamental geometric mappings, basic stress measures and physical balance equations of a solid body undergoing finite mechanical deformations. Next, a general formulation of finite thermo-inelastic material behaviour that accounts for micro-structural length scales is introduced. This coupling is then simplified in Chapter 4 to account for small strain settings. Finally, the basic steps for constructing a constitutive model in the logarithmic strain space is introduced. These steps will be used in Chapter 5 and Chapter 6 to simplify the model equations at finite strains and results in a formulation similar to that of small strain settings.

In **Chapter 3**, we develop a mixed variational principle for the evolution problem of gradient plasticity. A novel finite element design of the coupled problem incorporating a long-range hardening/softening parameter and its dual driving force is proposed. It includes a method for the definition of elastic-plastic-boundaries (EPBs) in gradient plasticity along with a postprocessor that defines the plastic variables in the elastic range. Next, two families of extended Q1P0-type and MINI-type mixed finite elements for the coupled problem are presented, including a local-global update strategy for short- and long-range fields, which are also outlined in a rigorous format based on variational principles. Numerical examples that underline the excellent performance of the proposed mixed finite element design are demonstrated at the end of this chapter. It provides a very robust and easy-to-implement computational framework of variational gradient plasticity.

The aim of **Chapter 4** is to outline a coupled gradient thermo-plasticity model at small strains. To this end, we extend the constitutive formulation of the gradient plasticity model introduced in Chapter 3 to account for thermal effects. Two global solution procedures are developed for the coupled problem, namely the product formula algorithm and the implicit coupled algorithm. In the product formula algorithm, the mechanical and thermal problems are solved separately, resulting in a symmetric problem. However, in the implicit coupled algorithm, a simultaneous solution of the coupled system of equations for thermo-gradient-plasticity is employed. A noteworthy drawback of this solution scheme arises from the high computational efforts in comparison with the product formula algorithm. At the end of this chapter, two numerical examples are introduced to demonstrate the performance of the coupled thermo-gradient-plasticity problem.

Chapter 5 presents an extension of Chapter 3 to a finite deformation setting in the logarithmic strain space. We develop a mixed saddle point principle for metric–type additive plasticity, which is specified for the important model problem of isochoric von Mises plasticity with gradient-extended hardening/softening response. This variational principle is based on the energetic and the dissipative response functions in the logarithmic strain space, that is framed by purely geometric pre- and post-processing steps. The numerical implementation exploits the underlying variational structure, yielding a canonical symmetric structure of the monolithic problem. Various numerical examples, which highlight characteristic features of gradient plasticity, are presented at the end of this chapter.

Finally, in **Chapter 6**, we outline a variational-based framework for the phase-field modeling of ductile fracture in elastic-plastic solids, which accounts for intrinsic material length scales to obtain mesh objectivity. The phase-field method is considered as a *geometric approach* to the diffusive crack modeling. This is based on the introduction of a global balance equation for a regularized crack surface and its modular linkage to the elastic-plastic bulk response. The phase-field evolution is governed by the constitutive crack driving forces, which is based on the elastic and plastic work densities and barrier functions related to the threshold values of these inelastic state variables. To simplify the finite element design, we extend the introduced gradient plasticity-damage towards the *micromorphic regularization approach* to gradient-extended models. For numerical implementation, we construct a stable one-pass operator split scheme that successively updates the crack driving force, the phase-field variable, and the micromorphic gradient-extended elastic-plastic fields together with the deformation fields in a typical time step. The performance of the formulation is demonstrated by means of some representative examples.

2. Fundamentals of Continuum Mechanics

The aim of this chapter is to give a short introduction to the fundamentals of continuum mechanics at finite and small strains based on MIEHE [88, 89, 90], TRUESDELL & NOLL [146], MARSDEN & HUGHES [84], CHADWICK [35] and HOLZAPFEL [69].

2.1. Basic kinematics of finite deformation

2.1.1. Motion of a material body. A *material body* B is a physical object characterized by certain properties such as density, texture or micro-structure. Mathematically, a body B is described by a set of continuously-distributed material points $P \in B$. The configuration $\mathcal{S}$ of a material body B at time t is determined by the placement map as

$$\boldsymbol{\chi}_t := \begin{cases} B \to \mathcal{S} \in \mathbb{R}^3 \ , \\ P \mapsto \boldsymbol{x} = \boldsymbol{\chi}_t(P) \in \mathcal{S} \ . \end{cases} \tag{2.1}$$

where $\mathbb{R}^3$ is the Euclidean space, see Figure 2.1. One defines the *reference* or *Lagrangian configuration* as the placement of the body at time t_0, i.e. $\mathcal{B}{:=}\boldsymbol{\chi}_{t_0}(B)$, with the *reference coordinates* $\boldsymbol{X}:=\boldsymbol{\chi}_0(P) \in \mathcal{B}$ and covariant $\{\boldsymbol{E}_i\}_{i=1,3}$ and contravariant $\{\boldsymbol{E}^i\}_{i=1,3}$ material base vectors. The *current* or *Eulerian configuration* at time t is defined as $\mathcal{S}:=\boldsymbol{\chi}_t(B)$, with the *spatial coordinates* $\boldsymbol{x} := \boldsymbol{\chi}_t(P) \in \mathcal{S}$ and spatial base vectors $\{\boldsymbol{e}_i\}_{i=1,3}$ and $\{\boldsymbol{e}^i\}_{i=1,3}$, which are related through the orthogonality relation

$$\delta^i_{\ j} = \boldsymbol{E}^i \cdot \boldsymbol{E}_j \qquad \text{and} \qquad \delta^i_{\ j} = \boldsymbol{e}^i \cdot \boldsymbol{e}_j \qquad \text{with} \qquad \delta^i_{\ j} = \begin{cases} 1 \text{ if } i = j \\ 0 \text{ if } i \neq j \end{cases} \tag{2.2}$$

with $\delta^i_{\ j}$ being the Kronecker-Delta. Covariant components are denoted with subscript indices and contravariant components with superscript indices. The relative motion is then described by a nonlinear *deformation map* by considering the composition of the mappings $\boldsymbol{\chi}_t$ and $\boldsymbol{\chi}_0$ as

$$\boldsymbol{\varphi} := \boldsymbol{\chi}_t \circ \boldsymbol{\chi}_0^{-1} : \begin{cases} \mathcal{B} \times \mathbb{R}_+ \to \mathcal{S} \in \mathbb{R}^3 \ , \\ (\boldsymbol{X}, t) \mapsto \boldsymbol{x} = \boldsymbol{\varphi}(\boldsymbol{X}, t) = \boldsymbol{\varphi}_t(\boldsymbol{X}) \ , \end{cases} \tag{2.3}$$

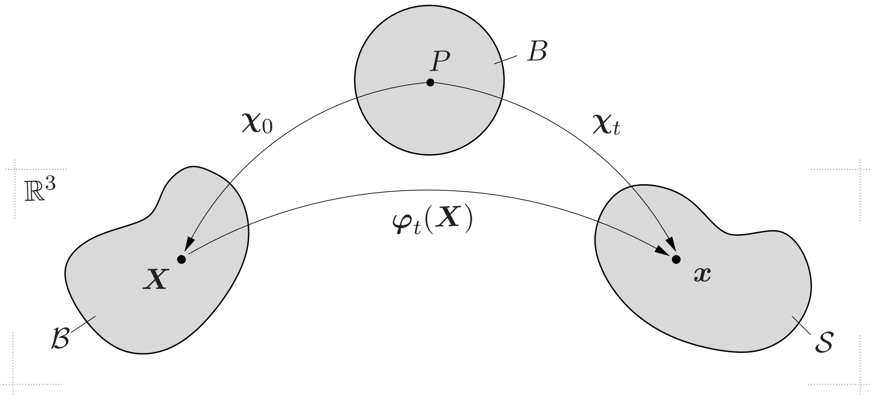

Figure 2.1: Motion of a material body B in the three-dimensional Euclidian space $\mathbb{R}^3$. Reference configuration $\mathcal{B}$ with position $\boldsymbol{X}$ and current configuration $\mathcal{S}$ with position $\boldsymbol{x}$ at time t.

which maps material positions $\boldsymbol{X} \in \mathcal{B}$ of the reference configuration onto points $\boldsymbol{x} \in \mathcal{S}$ of the current configuration as visualized in Figure 2.1.

2.1.2. Material deformation gradient. A key quantity for the description of finite deformations is the deformation gradient, defined by the Fréchet derivative

$$\boldsymbol{F}(\boldsymbol{X}, t) := \nabla_X \boldsymbol{\varphi}_t(\boldsymbol{X}) = \frac{\partial \boldsymbol{\varphi}_t(\boldsymbol{X})}{\partial \boldsymbol{X}} \ . \tag{2.4}$$

It is a linear mapping between tangent vectors $\boldsymbol{T} \in T_X\mathcal{B}$ to material curves and $\boldsymbol{t} \in T_x\mathcal{S}$ to spatial curves

$$\boldsymbol{F} : \begin{cases} T_X\mathcal{B} \to T_x\mathcal{S} \\ \boldsymbol{T} \mapsto \boldsymbol{t} = \boldsymbol{F}\boldsymbol{T} \end{cases} \tag{2.5}$$

where $T_X\mathcal{B}$ and $T_x\mathcal{S}$ are the tangent spaces constructed on the manifolds $\mathcal{B}$ and $\mathcal{S}$ at points $\boldsymbol{X}$ and $\boldsymbol{x}$, respectively, as visualized in Figure 2.2. Next, the relation between the material and spatial area vectors $d\boldsymbol{A}$ and $d\boldsymbol{a}$, also known as *Nanson's formula*, is given as

$$d\boldsymbol{a} = d\boldsymbol{x}_1 \times d\boldsymbol{x}_2 = \boldsymbol{F} d\boldsymbol{X}_1 \times \boldsymbol{F} d\boldsymbol{X}_2 = \det[\boldsymbol{F}]\boldsymbol{F}^{-T}(d\boldsymbol{X}_1 \times d\boldsymbol{X}_2) =: \operatorname{cof}[\boldsymbol{F}] d\boldsymbol{A} \ , \tag{2.6}$$

where $\operatorname{cof}[\boldsymbol{F}]$ represents the cofactor of the deformation gradient. With $d\boldsymbol{A} = \boldsymbol{N} dA$ and $d\boldsymbol{a} = \boldsymbol{n} da$, it is clear, that $\boldsymbol{F}^{-T}$ is a linear mapping between material normal co-vectors $\boldsymbol{N} \in T^*_X\mathcal{B}$ and spatial normal co-vectors $\boldsymbol{n} \in T^*_x\mathcal{S}$

$$\boldsymbol{F}^{-T} : \begin{cases} T^*_X\mathcal{B} \to T^*_x\mathcal{S} \\ \boldsymbol{N} \mapsto \boldsymbol{n} = \boldsymbol{F}^{-T}\boldsymbol{N} \end{cases} \tag{2.7}$$

in the cotangent spaces $T^*_X\mathcal{B}$ and $T^*_x\mathcal{S}$ as visualized in Figure 2.2. Similar to area elements, we investigate the relation between the material volume element dV and the spatial counterpart dv as

$$dv = d\boldsymbol{x}_1 \cdot (d\boldsymbol{x}_2 \times d\boldsymbol{x}_3) = \boldsymbol{F} d\boldsymbol{X}_1 \cdot (\boldsymbol{F} d\boldsymbol{X}_2 \times \boldsymbol{F} d\boldsymbol{X}_3) = \det[\boldsymbol{F}] dV \ . \tag{2.8}$$

The determinant of the deformation gradient can be interpreted as a linear mapping, which relates infinitesimal reference volume elements dV to their deformed spatial counterparts dv via the relation

$$J \ := \ \det[\boldsymbol{F}] : \begin{cases} \mathcal{R} \to \mathcal{R} \\ dV \mapsto dv = J \ dV \ , \end{cases} \tag{2.9}$$

with the constraint $J > 0$ in order to avoid penetration of the material.

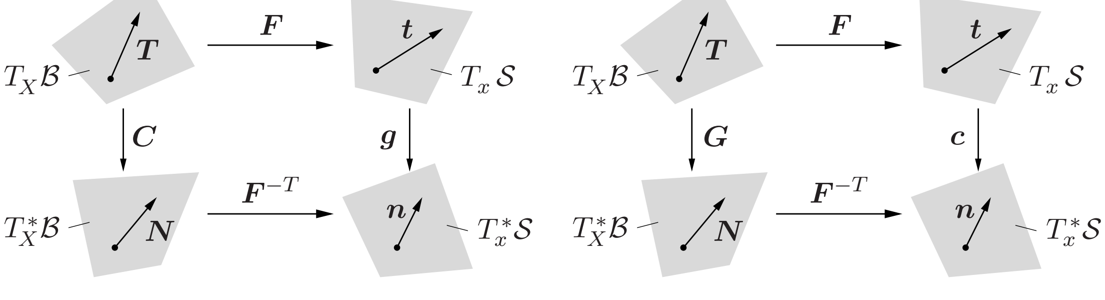
$T_X\mathcal{B}$
$\boldsymbol{T}$
$\boldsymbol{F}$
$\boldsymbol{t}$
$T_x\mathcal{S}$
$\boldsymbol{C}$
$\boldsymbol{g}$
$T^*_X\mathcal{B}$
$\boldsymbol{N}$
$\boldsymbol{F}^{-T}$
$\boldsymbol{n}$
$T^*_x\mathcal{S}$
$T_X\mathcal{B}$
$\boldsymbol{T}$
$\boldsymbol{F}$
$\boldsymbol{t}$
$T_x\mathcal{S}$
$\boldsymbol{G}$
$\boldsymbol{c}$
$T^*_X\mathcal{B}$
$\boldsymbol{N}$
$\boldsymbol{F}^{-T}$
$\boldsymbol{n}$
$T^*_x\mathcal{S}$

Figure 2.2: Fundamental mappings between tangent and cotangent spaces illustrating the *'push-forward'* and *'pull-back'* of the covariant reference metric $\boldsymbol{G}$ and spatial metric $\boldsymbol{g}$.

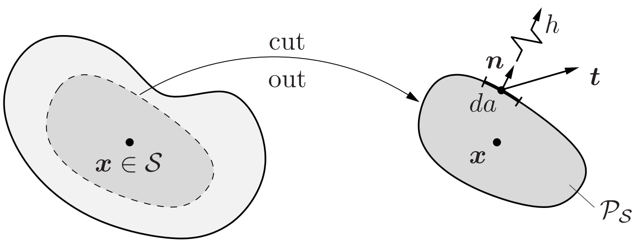

Figure 2.3: *Euler's cut principle.* Eulerian part $\mathcal{P}_{\mathcal{S}}$ cut out of the whole body $\mathcal{S}$. At a point $\boldsymbol{x} \in \partial\mathcal{P}_{\mathcal{S}}$, the mechanical and thermal actions of the remaining part of $\mathcal{S}$ are replaced by the mechanical traction vector $\boldsymbol{t} = \boldsymbol{\sigma n}$ and the heat flux $h = \boldsymbol{q} \cdot \boldsymbol{n}$.

2.1.3. Metric tensors and strain measures. The Lagrangian and Eulerian metric tensors $\boldsymbol{G}$ and $\boldsymbol{g}$ are introduced as

$$\boldsymbol{G} = \delta_{AB}\boldsymbol{E}^A \otimes \boldsymbol{E}^B \quad \text{and} \quad \boldsymbol{g} = \delta_{ab}\boldsymbol{e}^a \otimes \boldsymbol{e}^b \ . \tag{2.10}$$

The metric tensors are mapping between the tangent and cotangent spaces as

$$\boldsymbol{G} := \begin{cases} T_X\mathcal{B} \to T_X^*\mathcal{B} \ , \\ \boldsymbol{T} \mapsto \boldsymbol{N} = \boldsymbol{GT} \ , \end{cases} \qquad \boldsymbol{g} := \begin{cases} T_x\mathcal{S} \to T_x^*\mathcal{S} \ , \\ \boldsymbol{t} \mapsto \boldsymbol{n} = \boldsymbol{gt} \ . \end{cases} \tag{2.11}$$

In index notation, we have $N_A = \delta_{AB}\, T^B$ and $n_a = \delta_{ab}\, t^b$. Capital letter indices are used for Lagrangian objects and small indices for Eulerian ones. The mappings between tangent and cotangent spaces defined on Lagrangian and Eulerian manifolds are depicted in Figure 2.2. We use these geometric quantities to measure the length of vectors with respect to the reference and the current configuration

$$\begin{aligned} |\boldsymbol{T}|_{\boldsymbol{G}} &= \sqrt{\boldsymbol{T} \cdot (\boldsymbol{GT})} &&= \sqrt{\boldsymbol{F}^{-1}\boldsymbol{t} \cdot (\boldsymbol{GF}^{-1}\boldsymbol{t})} &&= \sqrt{\boldsymbol{t} \cdot (\boldsymbol{ct})} &&= |\boldsymbol{t}|_{\boldsymbol{c}} \ , \\ |\boldsymbol{t}|_{\boldsymbol{g}} &= \sqrt{\boldsymbol{t} \cdot (\boldsymbol{gt})} &&= \sqrt{\boldsymbol{FT} \cdot (\boldsymbol{gFT})} &&= \sqrt{\boldsymbol{T} \cdot (\boldsymbol{CT})} &&= |\boldsymbol{T}|_{\boldsymbol{C}} \ . \end{aligned} \tag{2.12}$$

Based on these definitions, we introduce the symmetric and positive definite *right* and *left Cauchy-Green tensors* $\boldsymbol{C}$ and $\boldsymbol{c}$ respectively

$$\boldsymbol{C} = \boldsymbol{\varphi}^*(\boldsymbol{g}) = \boldsymbol{F}^T\boldsymbol{gF} \qquad \text{and} \qquad \boldsymbol{c} = \boldsymbol{\varphi}_*(\boldsymbol{G}) = \boldsymbol{F}^{-T}\boldsymbol{GF}^{-1} \ , \tag{2.13}$$

where $\boldsymbol{\varphi}^*(\boldsymbol{g})$ is a *pull-back* operation of the Eulerian metric $\boldsymbol{g}$ and $\boldsymbol{\varphi}_*(\boldsymbol{G})$ a *push-forward* operation of the Lagrangian metric $\boldsymbol{G}$. A geometrical interpretation is given in Figure 2.2. As a strain measure in the material and spatial configuration, we introduce the Green-Lagrange and the Euler-Almansi strain tensors as

$$\boldsymbol{E} = \tfrac{1}{2}\,(\boldsymbol{C} - \boldsymbol{G}) \qquad \text{and} \qquad \boldsymbol{e} = \tfrac{1}{2}\,(\boldsymbol{g} - \boldsymbol{c}) \ . \tag{2.14}$$

2.2. Definition of stress tensors and heat flux

We consider physical statements in terms of basic phenomenological variables. The introduction of these variables bases on Euler's cut principle. An arbitrary sub domain $\mathcal{P}_{\mathcal{S}}$ is cut out of the body $\mathcal{S}$. The basic idea is to *replace the action of the rest body by contact stresses* $\boldsymbol{t}$ *and heat fluxes* h as illustrated in Figure 2.3.

2.2.1. Stress tensors. The contact force $\boldsymbol{t}$ is assumed to be a function of the normal vector $\boldsymbol{n}$ of the cut surface and its spatial position $\boldsymbol{x}$ at time t. Based on Cauchy's theorem, we have the form

$$\boldsymbol{t}(\boldsymbol{x}, t, \boldsymbol{n}) := \boldsymbol{\sigma}(\boldsymbol{x}, t)\,\boldsymbol{n} \qquad \textit{or} \qquad t^a := \sigma^{ab}\,n_b \ . \tag{2.15}$$

Here $\boldsymbol{\sigma}$ is the *true* or *Cauchy* stress tensor, that maps a normal $\boldsymbol{n} \in T_x^*\mathcal{S}$ on to a vector $\boldsymbol{t} \in T_x\mathcal{S}$

$$\boldsymbol{\sigma} : \begin{cases} T_x^*\mathcal{S} \to T_x\mathcal{S} \\ \boldsymbol{n} \mapsto \boldsymbol{t} = \boldsymbol{\sigma}\boldsymbol{n} \ . \end{cases} \tag{2.16}$$

where $\boldsymbol{t}$ is denoted as the *traction vector*, which is dual to the current metric tensor $\boldsymbol{g}$. A geometrical interpretation is given in Figure 2.4. The Cauchy stress is the canonical stress tensor with basic physical meaning, but not the convenient one for modeling. Besides the Cauchy stress tensor, the so-called *Kirchhoff* stress tensor is defined as $\boldsymbol{\tau} := J\boldsymbol{\sigma}$ which is obtained from $\boldsymbol{\sigma}$ by simply multiplying it with the Jacobian J. In many cases, it is important to relate all quantities to the reference configuration. To this end, we will introduce further stress tensors. Based on *Nanson's formula* (2.6), the *first Piola-Kirchhoff* stress tensor $\boldsymbol{P}$ is defined as

$$\boldsymbol{P} := \operatorname{cof}[\boldsymbol{F}]\,\boldsymbol{\sigma} = \boldsymbol{\tau}\boldsymbol{F}^{-T} \qquad \textit{or} \qquad P^{aB} = \tau^{ab}(F^{-1})^B_b \ . \tag{2.17}$$

It is a two field tensor with one basis referred to the current configuration and the other one to the reference configuration. Hence $\boldsymbol{P}$ is a non-symmetric, mixed tensor that is dual to the material deformation gradient $\boldsymbol{F}$. It is common to work with a symmetric stress tensor in the Lagrangian setting. For this purpose, we introduce the *second Piola-Kirchhoff* stress tensor $\boldsymbol{S}$ dual to the right Cauchy Green tensor $\boldsymbol{C}$

$$\boldsymbol{S} = \boldsymbol{F}^{-1}\boldsymbol{P} = \boldsymbol{F}^{-1}\boldsymbol{\tau}\boldsymbol{F}^{-T} \qquad \textit{or} \qquad S^{AB} = (F^{-1})^A_a\,P^{aB} = (F^{-1})^A_a\,\tau^{ab}\,(F^{-1})^B_b \tag{2.18}$$

which is a contravariant second order symmetric tensor and has the mapping properties

$$\boldsymbol{S} := \begin{cases} T_X^*\mathcal{B} \to T_X\mathcal{B} \ , \\ \boldsymbol{N} \mapsto \boldsymbol{T} = \boldsymbol{S}\boldsymbol{N} \ . \end{cases} \tag{2.19}$$

Note that $\boldsymbol{S}$ doesn't have a straight forward physical interpretation, hence it is a pure mathematical quantity, however commonly used in constitutive theory. In terms of dual

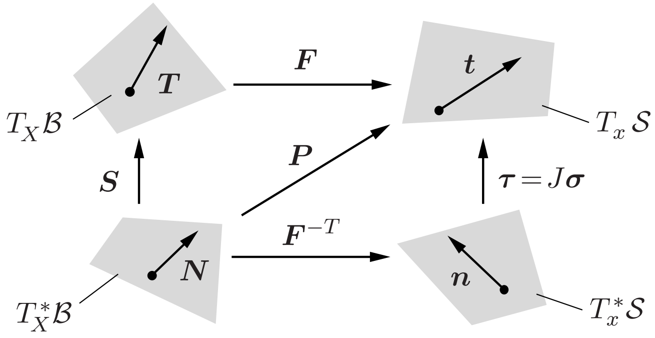

Figure 2.4: Geometrical illustration of the mapping properties of mechanical stress tensors.

objects, we define the stress power per unit volume

$$\mathcal{P} := \underbrace{\boldsymbol{P} : \dot{\boldsymbol{F}}}_{\text{mixed}} = \underbrace{\boldsymbol{S} : \tfrac{1}{2}\dot{\boldsymbol{C}}}_{\text{Lagrangian}} = \underbrace{\boldsymbol{\tau} : \tfrac{1}{2}\,\pounds_{\boldsymbol{v}}\boldsymbol{g}}_{\text{Eulerian}} \tag{2.20}$$

in terms of the time derivative of the material deformation gradient $\boldsymbol{F}$

$$\dot{\boldsymbol{F}} = \frac{d}{dt}\left[\frac{\partial\boldsymbol{\varphi}(\boldsymbol{X},t)}{\partial\boldsymbol{X}}\right] = \boldsymbol{l}\boldsymbol{F} \quad \text{with} \quad \boldsymbol{l} := \frac{\partial}{\partial\boldsymbol{x}}\left[\frac{d\boldsymbol{\varphi}(\boldsymbol{X},t)}{dt}\right] = \nabla_{\boldsymbol{x}}\boldsymbol{v}(\boldsymbol{x},t) \tag{2.21}$$

being the spatial velocity gradient $\boldsymbol{l}$. Furthermore we introduce in the Eulerian setting the so-called *Lie derivative* of the spatial metric $\boldsymbol{g}$ which is defined in three steps

$$\pounds_{\boldsymbol{v}}\boldsymbol{g} = \boldsymbol{\varphi}_*\left[\tfrac{d}{dt}\{\boldsymbol{\varphi}^*(\boldsymbol{g})\}\right] = \boldsymbol{F}^{-T}\dot{\boldsymbol{C}}\boldsymbol{F}^{-1} = \boldsymbol{g}\boldsymbol{l} + \boldsymbol{l}^T\boldsymbol{g} = 2\boldsymbol{d}\,. \tag{2.22}$$

First, a pull-back operation of the tensor $\boldsymbol{g}$ to its material counterpart $\boldsymbol{C}$ is performed. Then, the material time derivative of the Lagrangian object $\boldsymbol{C}$ is performed and finally the resultant quantity $\dot{\boldsymbol{C}}$ is pushed-forward to the spatial configuration. Application of the Lie derivative to the current metric $\boldsymbol{g}$ gives the *spatial rate of deformation tensor* $\boldsymbol{d}$, which is the symmetric part of the spatial velocity gradient $\boldsymbol{l}$.

2.2.2. Heat flux. In thermodynamics, the *Stokes heat flux theorem* is the counterpart of Cauchy's stress theorem (2.15). Figure 2.3 demonstrates the heat flux h on the part $\mathcal{P}_{\mathcal{S}}$, which takes the form

$$h(\boldsymbol{x},t,\boldsymbol{n}) := \boldsymbol{q}(\boldsymbol{x},t)\cdot\boldsymbol{n} \qquad \textit{or} \qquad h = q^a n_a \tag{2.23}$$

where $\boldsymbol{q}$ is the Cauchy heat flux vector. Next we introduce the nominal heat flux vector $\boldsymbol{Q}$ which is the Lagrangian counterpart of $\boldsymbol{q}$ defined as

$$\boldsymbol{Q} = J\boldsymbol{F}^{-1}\boldsymbol{q} \qquad \textit{or} \qquad Q^A = J(F^{-1})^A_{\ a}\, q^a \tag{2.24}$$

2.3. Physical balance principles

The aim of this section is to discuss the global balance principles of continuum thermodynamics and to deduce their local forms. A detailed derivation of these principles can be found in e.g. Holzapfel [69], Truesdell & Noll [146] and Marsden & Hughes [84].

2.3.1. Global equations. The general equations which drive the coupled thermomechanical problem are formulated as balances for a part $\mathcal{P}_{\mathcal{S}} \subset \mathcal{S}$ of the deformed configuration. The *conservation of mass* reads

$$\int_{\mathcal{P}_{\mathcal{S}}} \rho\, dv = \int_{\mathcal{P}_{\mathcal{B}}} \rho_0\, dV \ , \tag{2.25}$$

where $\rho(\boldsymbol{x},t)$ and $\rho_0(\boldsymbol{X})$ are the mass density fields of the current and the reference configuration, respectively. The *balance linear momentum* is

$$\frac{d}{dt}\int_{\mathcal{P}_{\mathcal{S}}} \rho\boldsymbol{v}\, dv = \int_{\partial\mathcal{P}_{\mathcal{S}}} \boldsymbol{t}\, da + \int_{\mathcal{P}_{\mathcal{S}}} \bar{\gamma}\, dv \ , \tag{2.26}$$

and the *balance of angular momentum* states

$$\frac{d}{dt}\int_{\mathcal{P}_\mathcal{S}} \boldsymbol{x} \times \rho \boldsymbol{v}\, dv = \int_{\partial\mathcal{P}_\mathcal{S}} \boldsymbol{x} \times \boldsymbol{t}\, da + \int_{\mathcal{P}_\mathcal{S}} \boldsymbol{x} \times \bar{\gamma}\, dv \ , \tag{2.27}$$

where $\boldsymbol{v}(\boldsymbol{x}, t) := \dot{\boldsymbol{\varphi}} \circ \boldsymbol{\varphi}^{-1}$ is the spatial velocity field. $\bar{\gamma}(\boldsymbol{x}, t)$ is a given body force field per unit volume. Finally, the *balance of total energy* of the part $\mathcal{P}_\mathcal{S} \subset \mathcal{S}$ takes the form

$$\frac{d}{dt}\int_{\mathcal{P}_\mathcal{S}} [\mathcal{E} + \tfrac{1}{2}\rho|\boldsymbol{v}|^2]\, dv = \int_{\partial\mathcal{P}_\mathcal{S}} [\boldsymbol{t}\cdot\boldsymbol{v} - h]\, da + \int_{\mathcal{P}_\mathcal{S}} [\bar{\gamma}\cdot\boldsymbol{v} + r]\, dv \tag{2.28}$$

where $\mathcal{E}$ is the stored internal energy per unit volume of the body and r a given heat source.

2.3.2. Local equations. Pulling back these integrals to the reference configuration by using the volume map $dv = \det[\boldsymbol{F}]dV$, inserting the definitions (2.15)–(2.24) for the traction $\boldsymbol{t}$ and the heat out-flux h, using the Gauss theorem and the standard localization argument, we end up with the *four balance equations*

$$\begin{array}{lll} 1. & \text{conservation of mass} & \rho_0 = \rho J \\ 2. & \text{Balance of linear momentum} & \rho_0 \ddot{\boldsymbol{\varphi}} = \mathrm{Div}[\boldsymbol{P}] + \bar{\gamma} \\ 3. & \text{Balance of angular momentum} & \mathrm{skew}[\boldsymbol{P}\boldsymbol{F}^T] = \boldsymbol{0} \\ 4. & \text{Balance of internal energy} & \dot{\mathcal{E}} = \boldsymbol{P} : \dot{\boldsymbol{F}} - \mathrm{Div}[\boldsymbol{Q}] + r \end{array} \tag{2.29}$$

constructed on the reference configuration $\mathcal{B}$. Recall in this context the Piola transformations $\mathrm{Div}[\boldsymbol{Q}] = J\,\mathrm{div}[\mathbb{h}/J]$ and $\mathrm{Div}[\boldsymbol{P}] = J\,\mathrm{div}[\boldsymbol{\tau}/J]$, which allow to express the above material divergence terms as spatial divergence terms of the Kirchhoff–type heat flux $\mathbb{h} := Jh$ and the Kirchhoff stress tensor $\boldsymbol{\tau} := J\boldsymbol{\sigma}$. Furthermore, note that the third equation simply states the symmetry of the Cauchy stress tensor $\boldsymbol{\sigma}$.

2.4. Coupled thermo-mechanical modeling

Inspired by the recent works Miehe [96, 97] on variational principles of gradient–extended standard dissipative solids, we extend the therein presented nonlocal theory to *thermo-inelastic* material behaviour that accounts for micro-structural length scales. To this end, we focus on a multi-scale viewpoint, which relates the dissipative effects to micro-structural mechanisms. In the phenomenological context, we account for these micro-structural mechanisms by *micro–motion fields* as indicated in Figure 2.5, which generalize the classical notion of internal variables governed by ordinary differential equations to global fields driven by additional micro–force partial differential equations. This induces a multi–field treatment of continua with micro-structure in the spirit of the works Capriz [34], Mariano [82] and Frémond [54].

2.4.1. Primary fields with micro-structure changes. In the large-strain context, we describe the macroscopic motion of the body by the macro–motion field $\boldsymbol{\varphi}$ defined in (2.3) and the *absolute temperature field* $\theta > 0$. Note that the Eulerian heat flux vector $\boldsymbol{q}$ is given by Fourier's law which states that heat exchanges always from hotter to colder regions, i.e.

$$\boldsymbol{q} := -K\nabla_{\boldsymbol{x}}\theta \tag{2.30}$$

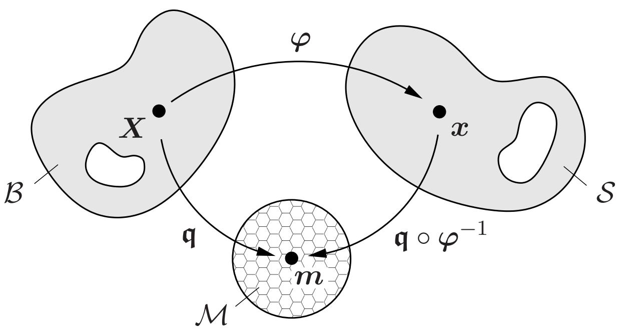

Figure 2.5: Basic fields defined as mappings. a) The dissipative finite deformation process of a solid is governed by the *macro–motion* $\boldsymbol{\varphi} : \mathcal{B} \times \mathcal{T} \mapsto \mathcal{S}$ that determines displaced points $\boldsymbol{x} = \boldsymbol{\varphi}(\boldsymbol{X}.t)$ on the current configuration $\mathcal{S}$ and the *micro–motion* $\mathfrak{q} : \mathcal{B} \times \mathcal{T} \mapsto \mathcal{M}$ that determines local microctructural states $\boldsymbol{m} = \mathfrak{q}(\boldsymbol{X}.t)$ on an abstract manifold $\mathcal{M}$.

where $\nabla_{\boldsymbol{x}}\theta$ is the spatial gradient of the temperature and K is the thermal conductivity which must be positive $(K > 0)$ in order to achieve thermodynamical consistency. For inelastic materials, micro-structural changes of the body are described by additional fields which are not directly observable. These fields are related to the standard concept of internal variables, which describe dissipative mechanisms of the material. However, in contrast to standard treatments, parts of these fields are driven by additional balance equations. We assemble these variables in the *micro-motion field* of the solid

$$\mathfrak{q} : \begin{cases} \mathcal{B} \times \mathcal{T} \to \mathcal{M} \\ (\boldsymbol{X}, t) \mapsto \boldsymbol{m} = \mathfrak{q}(\boldsymbol{X}, t) \end{cases} \tag{2.31}$$

which maps at time $t \in \mathcal{T}$ points $\boldsymbol{X} \in \mathcal{B}$ of the reference configuration $\mathcal{B}$ onto a local micro-structural state $\boldsymbol{m} \in \mathcal{M}$ on the manifold $\mathcal{M} := \mathfrak{q}_t(\mathcal{B}) \subset \mathcal{R}^\delta$ as visualized in Figure 2.5. They constitute in a homogenized sense the micro–motion of the material due to structural changes on lower scales. We associate with $\mathfrak{q}$ order parameters with tonsorial and geometric character, such as damage variables, phase fractions, inelastic strains or hardening-softening variables. The micro–motion fields assembled in $\mathfrak{q}$ are *long–range variables* $\mathfrak{q}^l$ when governed by PDEs with given length scale parameters. However, parts of them may degenerate to *short–range variables* or standard internal variables $\mathfrak{q}^s$, if the gradient terms in the constitutive energy and dissipation functions are dropped for modeling rapid spatial changes at the microscale. As a consequence, these variables evolve by local ODEs. In what follows, we decompose

$$\mathfrak{q} = \{ \, \mathfrak{q}^s, \mathfrak{q}^l \, \} \; . \tag{2.32}$$

2.4.2. The boundary conditions for the coupled problem. The surface $\partial\mathcal{B}$ of the reference configuration is decomposed according to the three primary fields for the deformation, the (long-range) generalized internal variables and the temperature

$$\partial\mathcal{B} = \partial\mathcal{B}^{\varphi} \cup \partial\mathcal{B}^{t} \; , \quad \partial\mathcal{B} = \partial\mathcal{B}^{\mathfrak{q}} \cup \partial\mathcal{B}^{\mathfrak{h}} \; , \quad \partial\mathcal{B} = \partial\mathcal{B}^{\theta} \cup \partial\mathcal{B}^{h} \; , \tag{2.33}$$

respectively, with $\partial\mathcal{B}^{\varphi} \cap \partial\mathcal{B}^{t} = \emptyset$, $\partial\mathcal{B}^{\mathfrak{q}} \cap \partial\mathcal{B}^{\mathfrak{h}} = \emptyset$ and $\partial\mathcal{B}^{\theta} \cap \partial\mathcal{B}^{h} = \emptyset$. We derive Dirichlet– and Neumann–type boundary conditions related to the deformation problem

$$\boldsymbol{\varphi} = \bar{\boldsymbol{\varphi}}(\boldsymbol{X}, t) \text{ on } \partial\mathcal{B}^{\varphi} \quad \text{and} \quad \boldsymbol{P}\boldsymbol{N} = \bar{\boldsymbol{T}}(\boldsymbol{X}, t) \text{ on } \partial\mathcal{B}^{t} \tag{2.34}$$

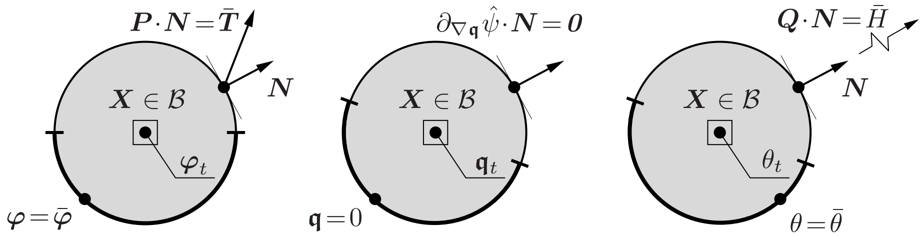
$\boldsymbol{P}\cdot\boldsymbol{N}=\bar{\boldsymbol{T}}$
$\boldsymbol{N}$
$\boldsymbol{X}\in\mathcal{B}$
$\boldsymbol{\varphi}_t$
$\boldsymbol{\varphi}=\bar{\boldsymbol{\varphi}}$
$\partial_{\nabla\mathfrak{q}}\hat{\psi}\cdot\boldsymbol{N}=\boldsymbol{0}$
$\boldsymbol{X}\in\mathcal{B}$
$\mathfrak{q}_t$
$\mathfrak{q}=0$
$\boldsymbol{Q}\cdot\boldsymbol{N}=\bar{H}$
$\boldsymbol{N}$
$\boldsymbol{X}\in\mathcal{B}$
θ_t
$\theta=\bar{\theta}$

deformation field internal variables temperature field

Figure 2.6: Primary fields of the coupled thermo-mechanical model. The deformation field $\boldsymbol{\varphi}$, internal variables $\mathfrak{q}$, temperature field θ are defined on the solid domain $\mathcal{B}$. The boundary $\partial\mathcal{B}$ of the solid is decomposed for Dirichlet- and Neumann-type boundary conditions associated with the mechanical and thermal problem.

and the microstructural changes related to length scales, i.e. for the long-range variables in (2.32)

$$\mathfrak{q} = \boldsymbol{0} \text{ on } \partial\mathcal{B}^{\mathfrak{q}} \quad \text{and} \quad \partial_{\nabla\mathfrak{q}}\hat{\psi}\cdot\boldsymbol{N} = \boldsymbol{0} \text{ on } \partial\mathcal{B}^{\mathbb{h}} \tag{2.35}$$

and for the thermal problem

$$\theta = \bar{\theta} \text{ on } \partial\mathcal{B}^{\theta} \quad \text{and} \quad \boldsymbol{Q}\cdot\boldsymbol{N} = \bar{H} \text{ on } \partial\mathcal{B}^{h}\ , \tag{2.36}$$

with *prescribed* deformation field $\bar{\boldsymbol{\varphi}}$, traction $\bar{\boldsymbol{T}}$, temperature field $\bar{\theta}$ and heat flux $\bar{H}$.

2.4.3. Objective free energy function. The energetic response function is assumed to depend on the primary fields introduced above and their first gradients

$$\psi = \hat{\psi}(\boldsymbol{\varphi}, \nabla\boldsymbol{\varphi}, \mathfrak{q}, \nabla\mathfrak{q}, \theta)\ . \tag{2.37}$$

A graphical interpretation of the generalized primary fields is given in Figure 2.6. Demanding invariance of $\hat{\psi}$ with respect to rigid body motion superimposed on the current configuration $\boldsymbol{\varphi}^{+} = \mathfrak{Q}(t)\boldsymbol{\varphi} + \boldsymbol{c}(t)$ for all translations $\boldsymbol{c}(t)$ and rotations $\mathfrak{Q}(t) \in SO(3)$, where $SO(3) := \{\mathfrak{Q}|\mathfrak{Q}^T\mathfrak{Q} = \boldsymbol{1} \wedge \det[\mathfrak{Q}] = 1\}$, we obtain the reduced form

$$\psi = \hat{\psi}(\boldsymbol{F}, \mathfrak{q}, \nabla\mathfrak{q}, \theta) = \bar{\psi}(\boldsymbol{C}, \mathfrak{q}, \nabla\mathfrak{q}, \theta) \tag{2.38}$$

in terms of the right Cauchy–Green tensor $\boldsymbol{C}$ introduced in (2.13).

2.4.4. Dissipation postulate. The formulation of the constitutive equations must be consistent with the second axiom of thermodynamics. This is expressed by the *global dissipation postulate*

$$\frac{d}{dt}\int_{\mathcal{P}_{\mathcal{S}}} \eta\, dv \geq -\int_{\partial\mathcal{P}_{\mathcal{S}}} \frac{h}{\theta}\, da + \int_{\mathcal{P}_{\mathcal{S}}} \frac{r}{\theta}\, dv \tag{2.39}$$

where $\eta(\boldsymbol{x}, t)$ is the entropy per unit volume of the current configuration and $\theta(\boldsymbol{x}, t)$ the absolute temperature. Pulling back these integrals to the reference configuration by using the volume map $dv = \det[\boldsymbol{F}]dV$, inserting the definitions (2.23)–(2.24) for the heat outflux h, using Gauss theorem, the standard localization argument and inserting the balance equations (2.29) gives the *local dissipation postulate*

$$\mathcal{D} := \boldsymbol{P} : \dot{\boldsymbol{F}} - \eta\dot{\theta} - \dot{\psi} - \frac{1}{\theta}\boldsymbol{Q}\cdot\nabla_{\boldsymbol{X}}\theta \geq 0\ , \tag{2.40}$$

known as the *Clausius–Duhem inequality* (CDI). Here, we eliminated the internal energy based on the Legendre transformation

$$\mathcal{E} = \psi + \theta\eta \ , \tag{2.41}$$

where ψ is the free Helmholtz energy (2.38). CDI can be splitted up into a part due to local actions and a part due to heat conduction

$$\mathcal{D}_{loc} := \boldsymbol{P} : \dot{\boldsymbol{F}} - \eta\dot{\theta} - \dot{\psi} \geq 0 \quad \text{and} \quad \mathcal{D}_{con} := -\frac{1}{\theta}\boldsymbol{Q} \cdot \nabla_{\boldsymbol{X}}\theta \geq 0 \ . \tag{2.42}$$

Inserting (2.38) into $(2.42)_1$ and application of Coleman's exploitation method gives the two constitutive equations for the first Piola-Kirchhoff stress and the entropy per unit volume respectively as

$$\boldsymbol{P} = \partial_{\boldsymbol{F}}\hat{\psi} \quad \text{and} \quad \eta = -\partial_\theta\hat{\psi} \tag{2.43}$$

Next we postulate the reduced *Clausius Planck* inequality

$$\mathcal{D}_{loc}^{int} = -\partial_{\boldsymbol{\mathfrak{q}}}\hat{\psi} \cdot \dot{\boldsymbol{\mathfrak{q}}} - \partial_{\nabla\boldsymbol{\mathfrak{q}}}\hat{\psi} \cdot \nabla\dot{\boldsymbol{\mathfrak{q}}} \geq 0 \ , \tag{2.44}$$

which is assumed to be positive. Integrating the dissipation over the volume of the body

$$\int_{\mathcal{B}} \mathcal{D}_{loc}^{int}\, dV := \int_{\mathcal{B}} \{ -[\ \partial_{\boldsymbol{\mathfrak{q}}}\hat{\psi} - \text{Div}[\partial_{\nabla\boldsymbol{\mathfrak{q}}}\hat{\psi}]\ ] \cdot \dot{\boldsymbol{\mathfrak{q}}}\ \}\, dV - \int_{\partial\mathcal{B}^{\mathbb{h}}} [\partial_{\nabla\boldsymbol{\mathfrak{q}}}\hat{\psi} \cdot \boldsymbol{n}] \cdot \dot{\boldsymbol{\mathfrak{q}}}\, dA \tag{2.45}$$

when inserting the micro–clamped boundary conditions $\dot{\boldsymbol{\mathfrak{q}}} = \boldsymbol{0}$ on $\partial\mathcal{B}_{\boldsymbol{\mathfrak{q}}}$. In order to prescribe the evolution of the internal mechanisms, such as plastic deformation and hardening effects, we define a dissipation potential that depends on the rate $\dot{\boldsymbol{\mathfrak{q}}}$ of the generalized internal variables

$$\phi_{loc} = \hat{\phi}_{loc}(\dot{\boldsymbol{\mathfrak{q}}}; \boldsymbol{\mathfrak{q}}, \theta) \tag{2.46}$$

at a *given* state $\{\boldsymbol{\mathfrak{q}}, \theta\}$ of these variables. Assuming partial differential equations for the evolution of the (long-range) generalized internal variables and Neumann–type boundary conditions of the form

$$-[\ \partial_{\boldsymbol{\mathfrak{q}}}\hat{\psi} - \text{Div}[\partial_{\nabla\boldsymbol{\mathfrak{q}}}\hat{\psi}]\ ] = \partial_{\dot{\boldsymbol{\mathfrak{q}}}}\hat{\phi}_{loc} \text{ in } \mathcal{B} \quad \text{and} \quad \partial_{\nabla\boldsymbol{\mathfrak{q}}}\hat{\psi} \cdot \boldsymbol{N} = \boldsymbol{0} \text{ on } \partial\mathcal{B}^{\mathbb{h}} \ , \tag{2.47}$$

as suggested in Miehe [96], we may recast (2.45) into

$$\int_{\mathcal{B}} \mathcal{D}_{loc}^{int}\, dV := \int_{\mathcal{B}} \{\ \partial_{\dot{\boldsymbol{\mathfrak{q}}}}\hat{\phi}_{loc} \cdot \dot{\boldsymbol{\mathfrak{q}}}\ \}\, dV \ , \tag{2.48}$$

in terms of the constitutive dissipation potential $\hat{\phi}_{loc}$. From (2.48), we conclude for the dissipation due to internal microstructural mechanisms

$$\mathcal{D}_{loc}^{int} = \partial_{\dot{\boldsymbol{\mathfrak{q}}}}\hat{\phi}_{loc} \cdot \dot{\boldsymbol{\mathfrak{q}}} \geq 0 \ . \tag{2.49}$$

This inequality serves as a fundamental physically–based constraint on the constitutive dissipation function $\hat{\phi}_{loc}$. It is a priory satisfied for a *normalized, positive* dissipation function $\hat{\phi}_{loc}$ that is *convex*. Regarding the evolution equation for the temperature field θ, the essential balance equation is the balance of internal energy $(2.29)_4$. After inserting the constitutive equations (2.43) and using the Legendre transformation (2.41), we end up with the evolution equation for the temperature

$$c\,\dot{\theta} = -\mathrm{Div}[\boldsymbol{Q}] + [\ r + \mathcal{L} + \mathcal{D}_{loc}\ ]\ , \tag{2.50}$$

with the *heat capacity* c and the *latent heat* $\mathcal{L}$ defined as

$$c := -\theta\partial^2_{\theta\theta}\hat{\psi} \quad \text{and} \quad \mathcal{L} := \theta\partial^2_{\boldsymbol{F}\theta}\hat{\psi} : \dot{\boldsymbol{F}} + \theta\partial^2_{\mathbf{q}\theta}\hat{\psi}\cdot\dot{\mathbf{q}} + \theta\partial^2_{\nabla\mathbf{q}\theta}\hat{\psi}\cdot\nabla\dot{\mathbf{q}}\ . \tag{2.51}$$

A detailed derivation of thermal balance equations (2.50) will be given in Chapter 4 at small strains.

2.5. Constitutive model in the logarithmic strain space

To simplify the model equations explained above at finite strains, we construct the constitutive model in the logarithmic strain space as outlined in MIEHE, APEL & LAMBRECHT [99]. This results into a formulation similar to the small strain setting.

2.5.1. Strain measure. First, we define the logarithmic strain tensor $\boldsymbol{\varepsilon}$ as a key point in the setting up of a framework for finite inelastic material response. This strain measure is assumed to be a function of the right Cauchy Green tensor (2.13), i.e.

$$\boldsymbol{\varepsilon} = \tfrac{1}{2}\ln[\boldsymbol{C}] \tag{2.52}$$

which enters as a variable the constitutive function that describes the macroscopic energy storage. Note that this strain tensor is the symmetric part of the displacement gradient vector $\boldsymbol{u}$ in the *small strain context* defined as $\boldsymbol{\varepsilon} := \mathrm{sym}[\nabla\boldsymbol{u}] = \tfrac{1}{2}[\nabla\boldsymbol{u} + \nabla^T\boldsymbol{u}]$.

2.5.2. Definition of transformation tensors. The logarithmic strain measure $\boldsymbol{\varepsilon}$ is a function of the right Cauchy Green tensor $\boldsymbol{C} = \boldsymbol{F}^T\boldsymbol{g}\boldsymbol{F}$ which is a function of the deformation gradient $\boldsymbol{F}$ and the Eulerian metric $\boldsymbol{g}$ defined in (2.10). The sensitivity of the strain measure with respect to a change of deformation reads

$$\dot{\boldsymbol{\varepsilon}} = \boldsymbol{\mathcal{P}}_{log} : \dot{\boldsymbol{C}} \quad \text{with} \quad \boldsymbol{\mathcal{P}}_{log} := \partial_{\boldsymbol{C}}\boldsymbol{\varepsilon} \tag{2.53}$$

being the fourth-order nominal transformation tensor $\boldsymbol{\mathcal{P}}_{log}$. The sensitivity of this projection tensor with respect to a change of the deformation reads

$$\dot{\boldsymbol{\mathcal{P}}}_{log} = \boldsymbol{\mathcal{L}}_{log} : \dot{\boldsymbol{C}} \quad \text{with} \quad \boldsymbol{\mathcal{L}}_{log} := \partial^2_{\boldsymbol{CC}}\boldsymbol{\varepsilon}\ , \tag{2.54}$$

where $\boldsymbol{\mathcal{L}}_{log}$ is the sixth-order nominal transformation tensor. Efficient algorithmic representations of these fourth- and sixth-order tensors were given in MIEHE & LAMBRECHT [98] in spectral form. Note that, these *logarithmic projection tensors* are important for the subsequent treatments in Chapter 5 and Chapter 6.

3. Computational Gradient Plasticity at Small Strain

The modeling of size effects in elastic-plastic solids, such as the width of shear bands or the grain size dependence in polycrystals, must be based on non-standard theories which incorporate length-scales. This can be achieved by models of strain gradient plasticity, incorporating spatial gradients of selected micro-structural fields, which describe the evolving dissipative mechanisms. The key aspect of this chapter is to outline a theoretical and computational framework of gradient plasticity based on a rigorous exploitation of mixed variational principles, see MIEHE ET AL. [104]. The numerical implementation exploits the underlying variational structure, yielding a canonical symmetric structure of the monolithic problem. It results in a novel finite element design of the coupled problem including a long-range hardening/softening parameter and its dual driving force. This allows a straightforward local definition of plastic loading-unloading driven by the long-range fields, providing very robust finite element implementations of gradient plasticity. This includes a rational method for the definition of elastic-plastic-boundaries (EPBs) in gradient plasticity along with a postprocessor that defines the plastic variables in the elastic range. We discuss in this chapter also alternative mixed finite element designs of the coupled problem, including a local-global solution strategy of short- and long-range fields. This includes several new aspects, such as extended Q1P0-type and MINI-type finite elements for gradient plasticity. Numerical examples that underline the excellent performance of the proposed mixed finite element design are demonstrated at the end of this chapter.

3.1. Rate-type variational principles for gradient plasticity

3.1.1. Primary variables and energetic response function. Let $\mathcal{B} \in \mathcal{R}^d$ with $d = 2, 3$ be a solid domain with material points $\boldsymbol{x} \in \mathcal{B}$. We study elastic-plastic deformations at time $t \in \mathcal{R}_+$, described by the *displacement field* $\boldsymbol{u}(\boldsymbol{x}, t)$. Its gradient defines the symmetric strain tensor $\nabla_s \boldsymbol{u} := \mathrm{sym}[\nabla \boldsymbol{u}]$. In view of the modeling of decoupled volumetric elastic and isochoric elastic-plastic response, we consider its decomposition

$$\nabla_s \boldsymbol{u} = \tfrac{1}{3}\, e \boldsymbol{1} + \bar{\boldsymbol{\varepsilon}} \tag{3.1}$$

into volumetric and isochoric parts with the definitions

$$e := \mathrm{tr}[\nabla_s \boldsymbol{u}] \quad \text{and} \quad \bar{\boldsymbol{\varepsilon}} := \mathrm{dev}[\nabla_s \boldsymbol{u}] \; . \tag{3.2}$$

In what follows, a superimposed bar $\bar{(\cdot)}$ indicates quantities related to the isochoric part of the deformation. Let furthermore $\boldsymbol{\varepsilon}^p(\boldsymbol{x}, t)$ be the symmetric *plastic strain tensor*. It starts to evolve from the initial condition $\boldsymbol{\varepsilon}^p(\boldsymbol{x}, 0) = \boldsymbol{0}$. We develop a framework of isotropic gradient plasticity at small strains. To this end, a scalar *isotropic hardening variable* $\alpha(\boldsymbol{x}, t)$ is introduced, that defines an accumulated equivalent plastic strain in the small strain space by the evolution equation

$$\dot{\alpha} = \sqrt{\frac{2}{3}}\; ||\dot{\boldsymbol{\varepsilon}}^p|| \quad \text{with} \quad \dot{\alpha} \geq 0 \; . \tag{3.3}$$

It starts to evolve from the initial condition $\alpha(\boldsymbol{x}, t_0) = 0$. In the subsequent treatment, we introduce the *plastic length scale* l_p that accounts for size effects to overcome the non-physical mesh sensitivity of the localized plastic deformation in softening materials.

To this end, we focus on a first order setting of gradient plasticity where the gradient $\nabla\alpha(\boldsymbol{x}, t)$ enters the constitutive functions, see for example De Borst & Mühlhaus [39], Liebe & Steinmann [79], Engelen, Geers & Baaijens [45] and Miehe et al. [104]. Hence, the subsequent model problem of gradient plasticity is described by the three

$$\text{Primary Fields: } \{\, \boldsymbol{u}, \boldsymbol{\varepsilon}^p, \alpha \,\}\ , \tag{3.4}$$

which define the objective

$$\text{Constitutive State: } \mathfrak{c} := \{\, e, \bar{\mathfrak{c}} \,\} \text{ with } \bar{\mathfrak{c}} := \{\, \bar{\boldsymbol{\varepsilon}}, \boldsymbol{\varepsilon}^p, \alpha, \nabla\alpha \,\}\ . \tag{3.5}$$

Its isochoric part contains besides the total strain deviator $\bar{\boldsymbol{\varepsilon}}$ the plastic strain $\boldsymbol{\varepsilon}^p$, the hardening/softening variable α and its gradient $\nabla\alpha$. The *constitutive energy storage function* ψ describes the energy stored in the bulk of the solid per unit volume. A fully isotropic constitutive assumption has the form

$$\psi(\mathfrak{c}) = \frac{\kappa}{2}e^2 + \bar{\psi}(\bar{\mathfrak{c}}) \quad \text{with} \quad \bar{\psi}(\bar{\mathfrak{c}}) = \mu|\bar{\boldsymbol{\varepsilon}} - \boldsymbol{\varepsilon}^p|^2 + \frac{h}{2}\alpha^2 + \frac{\mu l_p^2}{2}|\nabla\alpha|^2\ . \tag{3.6}$$

κ and μ are the elastic bulk and shear moduli, respectively, h is an isotropic hardening modulus and l_p is an energetic length scale. The rate of the stored energy at fixed primary variables $\{\boldsymbol{u}, \boldsymbol{\varepsilon}^p, \alpha\}$ is per definition the time derivative of the energy function (3.6)

$$\frac{d}{dt}\psi(\mathfrak{c}) = p\dot{e} + \bar{\boldsymbol{\sigma}} : (\dot{\bar{\boldsymbol{\varepsilon}}} - \dot{\boldsymbol{\varepsilon}}^p) + f\dot{\alpha} + \boldsymbol{f}\cdot\nabla\dot{\alpha}\ , \tag{3.7}$$

which is considered to be a functional of the rates $\{\dot{\boldsymbol{u}}, \dot{\boldsymbol{\varepsilon}}^p, \dot{\alpha}\}$. Here, we introduced per definition the volumetric and deviatoric stresses

$$p = \kappa e \quad \text{and} \quad \bar{\boldsymbol{\sigma}} := 2\mu(\bar{\boldsymbol{\varepsilon}} - \boldsymbol{\varepsilon}^p)\ , \tag{3.8}$$

as well as the energetic driving forces

$$f := h\,\alpha \quad \text{and} \quad \boldsymbol{f} := \mu l_p^2\,\nabla\alpha\ . \tag{3.9}$$

3.1.2. Secondary variables and dissipative response function. For the subsequent modeling of isochoric plasticity, we introduce dissipative force fields on the solid domain $\mathcal{B}$ dual to the isochoric constitutive state $\bar{\mathfrak{c}}$ introduced in (3.5)

$$\text{Driving Forces: } \bar{\mathfrak{b}} := \{\, \mathbf{0}, \bar{\boldsymbol{\mathfrak{s}}}, -\mathfrak{f}, \mathbf{0} \,\}\ , \tag{3.10}$$

where $\bar{\boldsymbol{\mathfrak{s}}}$ is dual to $\boldsymbol{\varepsilon}^p$ and $\mathfrak{f}$ dual α. For a simple model of von Mises-type gradient plasticity, we focus on the yield function

$$\chi(\bar{\mathfrak{b}}) := |\bar{\boldsymbol{\mathfrak{s}}}| - \sqrt{\tfrac{2}{3}}[\, y_0 + \mathfrak{f}\,]\ , \tag{3.11}$$

where y_0 is the initial yield stress. With this function at hand, we define a dual dissipation function for gradient-type viscoplasticity

$$\phi^*(\bar{\mathfrak{b}}) = \frac{1}{2\eta_p}\langle\, |\bar{\boldsymbol{\mathfrak{s}}}| - \sqrt{\tfrac{2}{3}}[\, y_0 + \mathfrak{f}\,]\,\rangle^2\ , \tag{3.12}$$

where η_p is the viscosity of the plastic over-stress response. Here, $\langle x\rangle := (x + |x|)/2$ is the Macaulay bracket.

3.1.3. A mixed variational principle for the evolution problem. Following conceptually the recent works Miehe et al. [102, 96, 110], a mixed rate-type variational principle that contains the dissipative driving force is based on the potential

$$\Pi^*(\dot{\boldsymbol{u}}, \dot{\alpha}, \dot{\boldsymbol{\varepsilon}}^p, \bar{\boldsymbol{\mathfrak{s}}}, \mathfrak{f}) = \int_{\mathcal{B}} [\, p\dot{e} + \bar{\pi}^*(\dot{\bar{\boldsymbol{\mathfrak{c}}}}, \bar{\boldsymbol{\mathfrak{b}}}; \bar{\boldsymbol{\mathfrak{c}}}) \,]\, dV \; - \; P_{ext}(\dot{\boldsymbol{u}}; t) \tag{3.13}$$

in terms of the *mixed isochoric rate potential* per unit volume

$$\bar{\pi}^*(\dot{\bar{\boldsymbol{\mathfrak{c}}}}, \bar{\boldsymbol{\mathfrak{b}}}) = \frac{d}{dt}\bar{\psi}(\bar{\boldsymbol{\mathfrak{c}}}) + \bar{\boldsymbol{\mathfrak{b}}} \cdot \dot{\bar{\boldsymbol{\mathfrak{c}}}} - \phi^*(\bar{\boldsymbol{\mathfrak{b}}}) \tag{3.14}$$

that contains the evolution of the energy storage function, the dissipation and the dual dissipation function. Note that the potential π^* is *linear* with respect to the rate $\dot{\bar{\boldsymbol{\mathfrak{c}}}}$ of the constitutive state and *concave* with respect to the dissipative driving forces $\bar{\boldsymbol{\mathfrak{b}}}$. The latter property is fully determined by the dual dissipation potential function ϕ^*, whose convexity is implied by the second axiom of thermodynamics. The only nonlinear entry in the potential Π^* occurs through the dual dissipation function ϕ^*. The evolution of the macro- and micro-motion fields as well as the driving forces at a given state is determined by the *mixed variational principle*

$$\{\dot{\boldsymbol{u}}, \dot{\alpha}, \dot{\boldsymbol{\varepsilon}}^p, \bar{\boldsymbol{\mathfrak{s}}}, \mathfrak{f}\} = \text{Arg}\{ \inf_{\dot{\boldsymbol{u}}} \inf_{\dot{\alpha}} \inf_{\dot{\boldsymbol{\varepsilon}}^p} \sup_{\bar{\boldsymbol{\mathfrak{s}}}} \sup_{\mathfrak{f}} \Pi^*(\dot{\boldsymbol{u}}, \dot{\alpha}, \dot{\boldsymbol{\varepsilon}}^p, \bar{\boldsymbol{\mathfrak{s}}}, \mathfrak{f}) \} \ , \tag{3.15}$$

which defines at the given state $\{\boldsymbol{u}, \alpha, \boldsymbol{\varepsilon}^p\}$ at time t the rates of the macro- and micro-motion fields along with the dissipative driving forces. The specification of the continuous rate potential introduced in (3.14) for the mixed plasticity model under consideration reads

$$\bar{\pi}^*(\dot{\bar{\boldsymbol{\mathfrak{c}}}}, \bar{\boldsymbol{\mathfrak{b}}}) = \bar{\boldsymbol{\sigma}} : (\dot{\bar{\boldsymbol{\varepsilon}}} - \dot{\boldsymbol{\varepsilon}}^p) + f\dot{\alpha} + \boldsymbol{f} \cdot \nabla\dot{\alpha} + \bar{\boldsymbol{\mathfrak{s}}} : \dot{\boldsymbol{\varepsilon}}^p - \mathfrak{f}\dot{\alpha} - \phi^*(\bar{\boldsymbol{\mathfrak{s}}}, \mathfrak{f}) \, , \tag{3.16}$$

where $\bar{\boldsymbol{\sigma}}$, f and $\boldsymbol{f}$ are defined in (3.8) and (3.9).

3.1.4. Euler equations of the mixed variational principle. Setting $\pi^* = p\dot{e} + \bar{\pi}^*$ and taking the variation of the potential (3.13), we find as the Euler equations of the mixed variational principle

$$\begin{array}{lll}
1. & \delta_{\dot{\boldsymbol{u}}}\pi^* & \equiv -\text{Div}\,[\, p\boldsymbol{1} + \bar{\boldsymbol{\sigma}} \,] = \overline{\boldsymbol{\gamma}} \ , \\
2. & \delta_{\dot{\alpha}}\pi^* & \equiv f - \text{Div}\,[\, \boldsymbol{f} \,] - \mathfrak{f} = 0 \ , \\
3. & \delta_{\mathfrak{f}}\pi^* & \equiv -\dot{\alpha} + \lambda\sqrt{2/3} = 0 \ , \\
4. & \delta_{\dot{\boldsymbol{\varepsilon}}^p}\pi^* & \equiv -\bar{\boldsymbol{\sigma}} + \bar{\boldsymbol{\mathfrak{s}}} = \boldsymbol{0} \ , \\
5. & \delta_{\bar{\boldsymbol{\mathfrak{s}}}}\pi^* & \equiv \dot{\boldsymbol{\varepsilon}}^p - \lambda\bar{\boldsymbol{\mathfrak{n}}} = \boldsymbol{0} \ ,
\end{array} \tag{3.17}$$

along with the Neumann-type boundary conditions

$$[\, p\boldsymbol{1} + \bar{\boldsymbol{\sigma}} \,] \cdot \boldsymbol{n} = \bar{\boldsymbol{t}} \text{ on } \partial\mathcal{B}_\sigma \quad \text{and} \quad \boldsymbol{f} \cdot \boldsymbol{n} = 0 \text{ on } \partial\mathcal{B}_{\mathbb{h}} \tag{3.18}$$

associated with the macro-motion $\boldsymbol{u}$ and the micro-motion α. In (3.17), we introduced per definition the *amount* and the *direction* of plastic flow

$$\lambda := \frac{1}{\eta_p}\langle\, |\bar{\boldsymbol{\mathfrak{s}}}| - \sqrt{\tfrac{2}{3}}[y_0 + \mathfrak{f}\,] \,\rangle \quad \text{and} \quad \bar{\boldsymbol{\mathfrak{n}}} := \bar{\boldsymbol{\mathfrak{s}}}/|\bar{\boldsymbol{\mathfrak{s}}}| \ . \tag{3.19}$$

This summarizes the formulation of the model of gradient plasticity at small strains.

3.2. Time-discrete incremental variational principle

We consider a finite time increment $[t_n, t_{n+1}]$, where $\tau_{n+1} := t_{n+1} - t_n > 0$ denotes the step length. All fields at time t_n are assumed to be *known.* The goal then is to determine the fields at time t_{n+1} based on variational principles valid for the time increment under consideration. Subsequently, all variables without subscript are evaluated at time t_{n+1}. In particular,

$$\bar{\mathfrak{c}} := \{\bar{\varepsilon}, \boldsymbol{\varepsilon}^p, \alpha, \nabla\alpha\} \quad \text{and} \quad \bar{\mathfrak{c}}_n := \{\bar{\varepsilon}_n, \boldsymbol{\varepsilon}^p_n, \alpha_n, \nabla\alpha_n\} \tag{3.20}$$

denote the isochoric constitutive states (3.5) at time t_{n+1} and time t_n, respectively. Furthermore,

$$\bar{\mathfrak{b}} := \{\, \mathbf{0}, \bar{\mathfrak{s}}, -\mathfrak{f}, \mathbf{0} \,\} \tag{3.21}$$

now denote the array of active dissipative driving forces (3.10) at the current time t_{n+1}. A mixed incremental variational principle of gradient plasticity associated with the finite time increment $[t_n, t_{n+1}]$ is based on the mixed potential

$$\Pi^{*\tau}(\boldsymbol{u}, \alpha, \boldsymbol{\varepsilon}^p, \bar{\mathfrak{s}}, \mathfrak{f}) = \int_{\mathcal{B}} [\, \frac{\kappa}{2} e^2 + \bar{\pi}^{*\tau}(\bar{\varepsilon}, \boldsymbol{\varepsilon}^p, \alpha, \nabla\alpha, \bar{\mathfrak{s}}, \mathfrak{f}) \,]\, dV \; - \; P^\tau_{ext}(\boldsymbol{u}) \tag{3.22}$$

in terms of the isochoric *mixed incremental potential* per unit volume $\bar{\pi}^{*\tau}$, defined by an algorithmic approximation

$$\bar{\pi}^{*\tau}(\bar{\mathfrak{c}}, \bar{\mathfrak{b}}) = Algo\{ \int_{t_n}^{t_{n+1}} \bar{\pi}^*(\dot{\bar{\mathfrak{c}}}, \bar{\mathfrak{b}}) dt \,\} \tag{3.23}$$

in terms of the the continuous rate-type potential π^* introduced in (3.14). We refer to Miehe [96, 110] for a broader theoretical motivation. The algorithm *Algo* approximates the time integration of the continuous rate-potential π^* in the discrete time interval $[t_n, t_{n+1}]$. As a consequence, the incremental potential $\pi^{*\tau}$ is considered to be a function of the current variable $\mathfrak{c}$ and $\bar{\mathfrak{b}}$ at time t_{n+1} at given state $\mathfrak{c}_n$ at time t_n. The macro- and micro-motion fields as well as the driving forces at the discrete time t_{n+1} are then determined by the *mixed incremental variational principle*

$$\{\boldsymbol{u}, \alpha, \boldsymbol{\varepsilon}^p, \bar{\mathfrak{s}}, \mathfrak{f}\} = \operatorname{Arg}\{ \inf_{\boldsymbol{u}} \inf_{\alpha} \inf_{\boldsymbol{\varepsilon}^p} \sup_{\bar{\mathfrak{s}}} \sup_{\mathfrak{f}} \Pi^{*\tau}(\boldsymbol{u}, \alpha, \boldsymbol{\varepsilon}^p, \bar{\mathfrak{s}}, \mathfrak{f}) \,\} \,. \tag{3.24}$$

The algorithm *Algo* is constructed such that the variation of the potential (3.22) for admissible variations $\delta\boldsymbol{u} \in \mathcal{W}^0_{\boldsymbol{u}} = \{\delta\boldsymbol{u} \mid \delta\boldsymbol{u} = \boldsymbol{0} \text{ on } \partial\mathcal{B}_u\}$, $\delta\alpha \in \mathcal{W}^0_\alpha = \{\delta\alpha \mid \delta\alpha = 0 \text{ on } \partial\mathcal{B}_\alpha\}$, $\delta\boldsymbol{\varepsilon}^p \in L^2$, $\delta\bar{\mathfrak{s}} \in L^2$ and $\delta\mathfrak{f} \in L^2$ yields as the Euler equations *consistent algorithmic counterparts* of the Euler equations (3.17) of the continuous rate-type variational principle (3.15). For the model of gradient plasticity considered here, this is achieved by a straightforward application of a backward Euler scheme, yielding the closed form of the incremental potential

$$\bar{\pi}^{*\tau}(\bar{\mathfrak{c}}, \bar{\mathfrak{b}}) = \bar{\psi}(\bar{\varepsilon}, \boldsymbol{\varepsilon}^p, \alpha, \nabla\alpha) + \bar{\mathfrak{s}} : (\boldsymbol{\varepsilon}^p - \boldsymbol{\varepsilon}^p_n) - \mathfrak{f} : (\alpha - \alpha_n) - \tau\phi^*(\bar{\mathfrak{s}}, \mathfrak{f}) \tag{3.25}$$

in terms of the free energy function ψ and the dual dissipation function ϕ^* defined in (3.6) and (3.12), respectively. Here, we dropped constant terms, which do not influence the subsequent formulation.

3.2.1. Euler equations of the mixed incremental variational principle. Setting $\pi^{*\tau} = \kappa e^2/2 + \bar{\pi}^{*\tau}$ and taking the variation of the incremental potential (3.22), we find as the Euler equations of the mixed variational principle

$$\begin{array}{lll} 1. & \delta_{\boldsymbol{u}}\pi^{*\tau} & \equiv -\mathrm{Div}\,[\,p\boldsymbol{1} + \bar{\boldsymbol{\sigma}}\,] = \bar{\boldsymbol{\gamma}}\ , \\ 2. & \delta_{\alpha}\pi^{*\tau} & \equiv f - \mathrm{Div}\,[\,\boldsymbol{f}\,] - \mathfrak{f} = 0\ , \\ 3. & \delta_{\mathfrak{f}}\pi^{*\tau} & \equiv -\alpha + \alpha_n + \gamma\sqrt{2/3} = 0\ , \\ 4. & \delta_{\boldsymbol{\varepsilon}^p}\pi^{*\tau} & \equiv -\bar{\boldsymbol{\sigma}} + \bar{\boldsymbol{\mathfrak{s}}} = \boldsymbol{0}\ , \\ 5. & \delta_{\bar{\boldsymbol{\mathfrak{s}}}}\pi^{*\tau} & \equiv \boldsymbol{\varepsilon}^p - \boldsymbol{\varepsilon}^p_n - \gamma\bar{\boldsymbol{\mathfrak{n}}} = \boldsymbol{0}\ , \end{array} \tag{3.26}$$

along with the Neumann-type boundary conditions

$$[\,p\boldsymbol{1} + \bar{\boldsymbol{\sigma}}\,]\cdot\boldsymbol{n} = \bar{\boldsymbol{t}} \text{ on } \partial\mathcal{B}_{\sigma} \quad \text{and} \quad \boldsymbol{f}\cdot\boldsymbol{n} = 0 \text{ on } \partial\mathcal{B}_{\mathbb{h}} \tag{3.27}$$

at the current time t_{n+1}. In (3.26), we introduced per definition the *amount* and the *direction* of the incremental plastic flow

$$\gamma := \frac{\tau}{\eta_p}\langle\, |\bar{\boldsymbol{\mathfrak{s}}}| - \sqrt{\tfrac{2}{3}}[y_0 + \mathfrak{f}\,]\,\rangle \quad \text{and} \quad \bar{\boldsymbol{\mathfrak{n}}} := \bar{\boldsymbol{\mathfrak{s}}}/|\bar{\boldsymbol{\mathfrak{s}}}|\ . \tag{3.28}$$

Note that these equations are consistent time-discrete algorithmic counterparts of the Euler equations (3.17)-(3.19) of the continuous rate-type variational principle.

3.2.2. A reduced three-field global solution strategy. The solution of this stationary principle is obtained within *two steps*, which correspond to typical algorithmic procedures in computational inelasticity with a *local* constitutive response.

Condensation of local variables. In a *first solution step*, $\Pi^{*\tau}$ in (3.22) is optimized for *given* macro-motion $\boldsymbol{u}$, long-range micro-motion α *and* driving forces $\mathfrak{f}$ with respect to the current short-range micro-motion $\boldsymbol{\varepsilon}^p$ and its dual driving force $\bar{\boldsymbol{\mathfrak{s}}}$. Due to the *local nature* of this optimization problem, we may write

$$(L): \quad \{\boldsymbol{\varepsilon}^p, \bar{\boldsymbol{\mathfrak{s}}}\} = \mathrm{Arg}\{\, \inf_{\boldsymbol{\varepsilon}^p}\sup_{\bar{\boldsymbol{\mathfrak{s}}}} \Pi^{*\tau}(\boldsymbol{u}, \boldsymbol{\varepsilon}^p, \alpha, \bar{\boldsymbol{\mathfrak{s}}}, \mathfrak{f})\,\}\ . \tag{3.29}$$

This variational principle defines locally an isochoric *condensed incremental work potential*

$$\bar{\pi}^{*\tau}_{red}(\bar{\boldsymbol{\mathfrak{r}}}) = \inf_{\boldsymbol{\varepsilon}^p}\sup_{\bar{\boldsymbol{\mathfrak{s}}}} \bar{\pi}^{*\tau}(\bar{\boldsymbol{\varepsilon}}, \boldsymbol{\varepsilon}^p, \alpha, \nabla\alpha, \bar{\boldsymbol{\mathfrak{s}}}, \mathfrak{f}) \tag{3.30}$$

as a function of the *reduced set of constitutive variables*

$$\bar{\boldsymbol{\mathfrak{r}}} := \{\, \bar{\boldsymbol{\varepsilon}}, \alpha, \nabla\alpha, \mathfrak{f}\,\}\ . \tag{3.31}$$

The Euler equations of (3.29) are identical with the equations $(3.26)_{4,5}$ and define the updates of the short-range variable $\boldsymbol{\varepsilon}^p$ including their dual driving forces $\bar{\boldsymbol{\mathfrak{s}}}$. They can be recast into the form

$$\begin{array}{lll} 1. & \delta_{\boldsymbol{\varepsilon}^p}\bar{\pi}^{*\tau} & \equiv -\bar{\boldsymbol{\mathfrak{s}}}^{trial} + 2\mu\gamma\bar{\boldsymbol{\mathfrak{n}}}^{trial} + \bar{\boldsymbol{\mathfrak{s}}} = \boldsymbol{0}\ , \\ 2. & \delta_{\bar{\boldsymbol{\mathfrak{s}}}}\bar{\pi}^{*\tau} & \equiv \boldsymbol{\varepsilon}^p - \boldsymbol{\varepsilon}^p_n - \gamma\bar{\boldsymbol{\mathfrak{n}}}^{trial} = \boldsymbol{0} \end{array} \tag{3.32}$$

in terms of the deviatoric trial stress and flow direction

$$\bar{\boldsymbol{\mathfrak{s}}}^{trial} := 2\mu(\bar{\boldsymbol{\varepsilon}} - \boldsymbol{\varepsilon}^p_n) \quad \text{and} \quad \bar{\boldsymbol{\mathfrak{n}}}^{trial} := \bar{\boldsymbol{\mathfrak{s}}}^{trial}/|\bar{\boldsymbol{\mathfrak{s}}}^{trial}|\ . \tag{3.33}$$

Setting $|\bar{\mathfrak{s}}| = |\bar{\mathfrak{s}}^{trial}| - 2\mu\gamma$, we write the yield function in terms of the incremental plastic slip

$$\chi = |\bar{\mathfrak{s}}^{trial}| - 2\mu\gamma - \sqrt{\tfrac{2}{3}}[y_0 + \mathfrak{f}\,] \ . \tag{3.34}$$

Assuming $\chi > 0$, we compute from (3.28) a trial value of the incremental plastic flow

$$\gamma^{trial} := \frac{1}{2\mu + \eta_p/\tau}(\ |\bar{\mathfrak{s}}^{trial}| - \sqrt{\tfrac{2}{3}}(y_0 + \mathfrak{f})\ ) \tag{3.35}$$

and define the incremental plastic parameter by

$$\gamma = \begin{cases} \gamma^{trial} & \text{for } \chi > 0 \\ 0 & \text{otherwise .} \end{cases} \tag{3.36}$$

Hence, the two equations (3.32) determine $\boldsymbol{\varepsilon}^p$ and $\bar{\mathfrak{s}}$ by a *non-standard radial return step*, driven by the total deviatoric strains $\bar{\boldsymbol{\varepsilon}}$ *and the driving force* $\mathfrak{f}$. Note that this algorithmic treatment allows to include the rate-independent limit $\eta_p = 0$.

Reduced global problem. With the condensed incremental work potential $\pi^{*\tau}_{red}$ defined in (3.30) at hand, we define the reduced potential function

$$\Pi^{*\tau}_{red}(\boldsymbol{u}, \alpha, \mathfrak{f}) = \int_{\mathcal{B}} [\ \frac{\kappa}{2} e^2 + \bar{\pi}^{*\tau}_{red}(\bar{\boldsymbol{\varepsilon}}, \alpha, \nabla\alpha, \mathfrak{f})\ ]\, dV \ - \ P^{\tau}_{ext}(\boldsymbol{u}) \ . \tag{3.37}$$

Then, a *second solution step*, governed by the mixed saddle point principle

$$(G): \quad \{\boldsymbol{u}, \alpha, \mathfrak{f}\} = \text{Arg}\{\ \inf_{\boldsymbol{u}} \inf_{\alpha} \sup_{\mathfrak{f}} \Pi^{*\tau}_{red}(\boldsymbol{u}, \alpha, \mathfrak{f})\ \}\ , \tag{3.38}$$

determines for given state $\{\boldsymbol{\varepsilon}^p_n, \alpha_n\}$ at time t_n and updated short-range variables $\{\boldsymbol{\varepsilon}^p, \bar{\mathfrak{s}}\}$ at time t_{n+1} obtained from step (L) in (3.29) the long-range fields $\{\boldsymbol{u}, \alpha\}$ and the driving forces $\mathfrak{f}$ at time t_{n+1}. The Euler-equations of (3.38) are identical with the equations $(3.26)_{1,2,3}$

$$\begin{array}{lll} 1. & \delta_{\boldsymbol{u}}\pi^{*\tau} & \equiv -\text{Div}\,[\,p\boldsymbol{1} + \bar{\boldsymbol{\sigma}}\,] = \ \overline{\boldsymbol{\gamma}}\ , \\ 2. & \delta_{\alpha}\pi^{*\tau} & \equiv f - \text{Div}\,[\,\boldsymbol{f}\,] - \mathfrak{f} = 0\ , \\ 3. & \delta_{\mathfrak{f}}\pi^{*\tau} & \equiv -\alpha + \alpha_n + \gamma\sqrt{2/3} = 0\ . \end{array} \tag{3.39}$$

Weak form of reduced equations. The variation of the functional (3.37) gives the necessary condition

$$\delta\Pi^{*\tau}_{red} = \int_{\mathcal{B}} [\ \kappa e \delta e + \bar{\boldsymbol{\mathfrak{S}}} \cdot \delta\bar{\mathfrak{e}}\ ]\, dV \ - \ P^{\tau}_{ext}(\delta\boldsymbol{u}) \ = 0\ , \tag{3.40}$$

with the definition of a generalized deviatoric stress array

$$\bar{\boldsymbol{\mathfrak{S}}} := \partial_{\bar{\mathfrak{e}}}\pi^{*\tau}_{red} = \begin{bmatrix} 2\mu(\bar{\boldsymbol{\varepsilon}} - \boldsymbol{\varepsilon}^p_n) \\ h\alpha - \mathfrak{f} \\ \mu l_e^2 \nabla\alpha \\ -\alpha + \alpha_n \end{bmatrix} + s \begin{bmatrix} -2\mu\gamma\bar{\mathfrak{n}}^{trial} \\ 0 \\ \boldsymbol{0} \\ \gamma\sqrt{2/3} \end{bmatrix} \tag{3.41}$$

in terms of the local plastic loading flag

$$s := \begin{cases} 1 & \text{for } \chi > 0 \quad , \\ 0 & \text{otherwise} \quad . \end{cases} \tag{3.42}$$

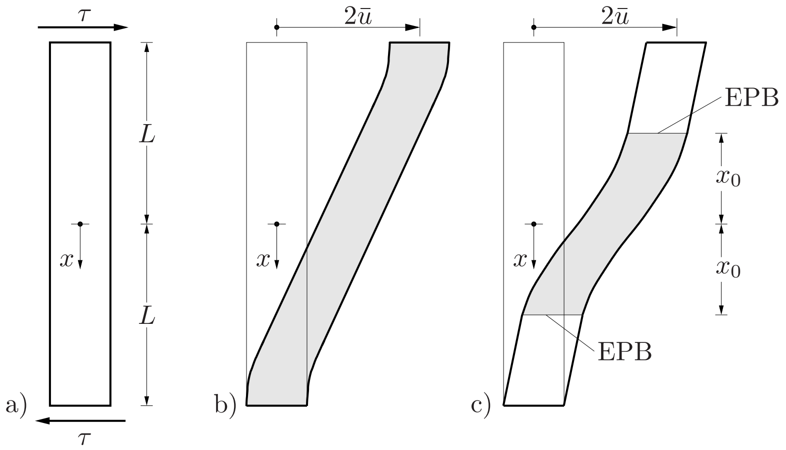

Figure 3.1: Shear Test for Hardening and Softening Plasticity. a) A horizontal infinitely expanded shear field of vertical height $2L$ is deformed by the prescribed displacement $2\bar{u}$, producing the *constant stress* τ. b) Deformed field for *hardening plasticity*, where the full specimen is plastically active. The width of the inhomogeneous boundary deformation layer is governed by the length scale l_p. c) Deformed field for *softening plasticity*, triggered by an initial perturbation at $x = 0$, where only the grey shaded zone is plastically active while the remaining part deforms elastic. The width $2x_0$ of the plastic zone is proportional to the length scale l_p. We denote $x = \pm x_0$ as the *elastic–plastic–boundary* (EPB). The numerical realization of such sharp elastic-plastic boundaries is a key problem in gradient plasticity.

The linearization reads for dead external loads

$$\Delta\delta\Pi^{*\tau}_{red} = \int_{\mathcal{B}} [\, \delta e \kappa \Delta e + \delta\bar{\mathfrak{r}} \cdot \bar{\mathfrak{C}} \cdot \Delta\bar{\mathfrak{r}} \,]\, dV \tag{3.43}$$

in terms of the tangent moduli array

$$\bar{\mathfrak{C}} := \partial^2_{\bar{\mathfrak{r}}\bar{\mathfrak{r}}}\pi^{*\tau}_{red} = \begin{bmatrix} 2\mu\mathbb{P} & \cdot & \cdot & \cdot \\ \cdot & h & \cdot & -\mathit{1} \\ \cdot & \cdot & \mu l_e^2 \boldsymbol{1} & \cdot \\ \cdot & -\mathit{1} & \cdot & \cdot \end{bmatrix} + s \begin{bmatrix} -\mathbb{E}^p & \cdot & \cdot & \boldsymbol{e}^p \\ \cdot & \cdot & \cdot & \cdot \\ \cdot & \cdot & \cdot & \cdot \\ \boldsymbol{e}^{pT} & \cdot & \cdot & -e^p \end{bmatrix} \tag{3.44}$$

with the definitions

$$\begin{aligned} \mathbb{E}^p &:= \frac{4\mu^2}{2\mu + \eta_p/\tau} \bar{\mathfrak{n}}^{trial} \otimes \bar{\mathfrak{n}}^{trial} + \frac{4\mu^2\gamma}{||\mathfrak{s}^{p\,trial}||}[\mathbb{P} - \bar{\mathfrak{n}}^{trial} \otimes \bar{\mathfrak{n}}^{trial}] \ , \\ \boldsymbol{e}^p &:= \frac{2\mu\sqrt{2/3}}{2\mu + \eta_p/\tau} \bar{\mathfrak{n}}^{trial} \quad \text{and} \quad e^p := \frac{2/3}{2\mu + \eta_p/\tau} \ . \end{aligned}$$

3.3. Analytical solutions and basic ideas of mixed FE design

We outline in this Section two characteristic analytical solutions for hardening and softening plasticity. They are used as benchmark problems to demonstrate basic difficulties in the finite element discretization of gradient plasticity and to motivate our ideas to their solution.

3.3.1. Deformation-controlled plane shear test for gradient plasticity. We develop two fundamental benchmarks for hardening and softening plasticity. They are used to demonstrate the basic difficulties in the numerical approximation of the mixed

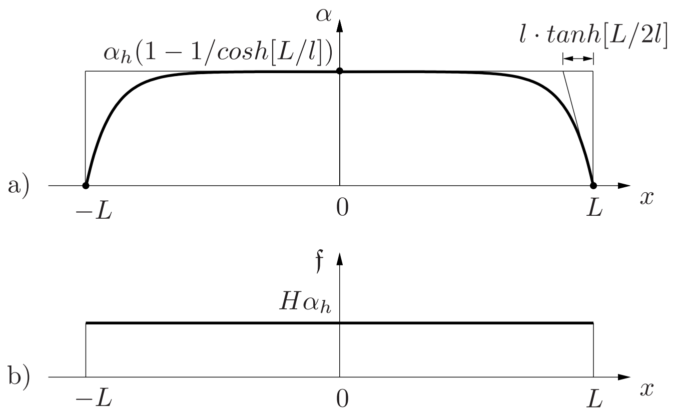

Figure 3.2: Analytical Solutions for Hardening Plasticity. a) Equivalent plastic strain for micro-clamped conditions $\alpha(x=L)=\alpha(x=-L)=0$. The width of the inhomogeneous boundary deformation layer is governed by the length scale $l := l_p\sqrt{\mu/H}$. b) The driving force $\mathfrak{f}=\sqrt{3}\,\tau - y_0 \geq 0$ is *constant* in the full domain.

variational problem of gradient plasticity. Consider a shear test depicted in Figure 3.1a, where an infinitely expanded strip of height $2L$ is sheared by a prescribed horizontal top displacement $2\bar{u}$. The deformation problem is *one-dimensional* and *symmetric* with respect to the chosen origin of the x-coordinate-system. Figures 3.1b and 3.1c show in a qualitative format the deformation modes for hardening and softening plasticity, respectively. For the *hardening case* depicted in Figure 3.1b, the full strip is plastified and an inhomogeneous zone related to the length scale l_p develops at both ends, when *micro-clamped boundary conditions* $\alpha(L)=\alpha(-L)=0$ are applied. For the *softening case* depicted in Figure 3.1c, an inhomogeneous plastic zone of width $2x_0$ related to the length scale l_p develops as a consequence of an *initial imperfection of the yield strength* y_0 in the center $x=0$ of the strip.

The subsequent theoretical solutions for these two problems are achieved by following conceptually ideas outlined in DE BORST & MÜHLHAUS [39]. Focusing on the evolution of plastic flow, the consistency condition based on the yield function (3.11) yields for a shear test of rate-independent plasticity

$$\sqrt{3}\,\tau - [\,y_0 + \mathfrak{f}\,] = 0 \quad \text{with} \quad \mathfrak{f} = h\alpha - \mu l_p^2 \alpha'' \; . \tag{3.45}$$

For given shear stress τ, this is considered as a spatial differential equation for the field $\alpha(x)$ in the domain $x \in [0, L]$ of the bar. Here, we exploit a priori the symmetry property $\alpha(-x)=\alpha(x)$. We consider

$$h = \left\{ \begin{array}{ll} +H > 0: & \text{hardening plasticity} \;, \\ -S < 0: & \text{softening plasticity} \;. \end{array} \right. \tag{3.46}$$

In what follows, we consider closed-form solutions for both parameters in those ranges.

3.3.2. Theoretical solution for micro-clamped hardening plasticity. Defining the effective length scale for hardening $l := l_p\sqrt{\mu/H}$, we get from (3.45) the differential equation for hardening plasticity

$$\alpha - l^2\alpha'' = \alpha_h \quad \text{with} \quad \alpha_h := (\sqrt{3}\,\tau - y_0)/H \geq 0 \; . \tag{3.47}$$

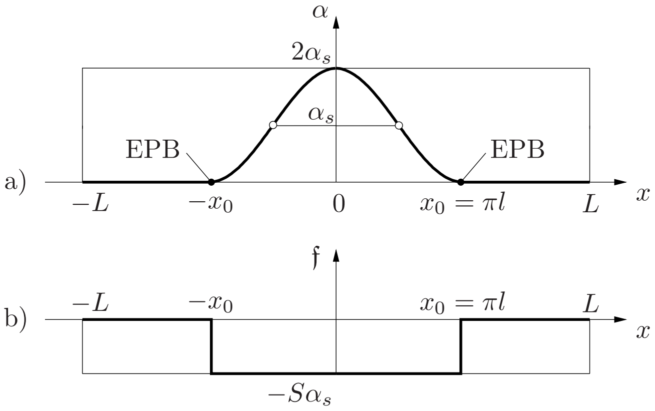

Figure 3.3: Analytical Solutions for Softening Plasticity. a) Equivalent plastic strain triggered by an initial perturbation at $x = 0$. The width x_0 of the plastic zone is proportional to the length scale $l := l_p\sqrt{\mu/S}$. b) The driving force $\mathfrak{f} = \sqrt{3}\,\tau - y_0 \leq 0$ is *constant* in the plastic zone, and *jumps* to zero at the *elastic–plastic–boundary* (EPB).

For an inhomogeneous plastic zone with symmetry property $\alpha(-x) = \alpha(x)$ determined by the two boundary conditions

$$\alpha'(x = 0) = 0 \quad \text{and} \quad \alpha(x = L) = 0 \ , \tag{3.48}$$

representing *micro-clamped conditions* at the two ends of the bar, we get the solution

$$\alpha(x) = \alpha_h(\, 1 - \cosh[x/l]/\cosh[L/l]\,) \tag{3.49}$$

depicted in Figure 3.2a. The driving force computed from (3.45) then takes a constant value in the whole bar

$$\mathfrak{f}(x) = \sqrt{3}\,\tau - y_0 \tag{3.50}$$

as shown in Figure 3.2b. The determination of the constant shear stress τ in the strip for a deformation process *controlled by the displacements* $\bar{u} := u(x = L) = -u(x = -L)$ at the end of the strip is achieved as follows. Integration of the total strain rate, consisting of elastic and plastic contributions $\dot{\gamma}^e := \dot{\tau}/\mu$ and $\dot{\gamma}^p := \sqrt{3}\,\dot{\alpha}$, gives

$$\dot{\bar{u}} = \int_0^L (\frac{\dot{\tau}}{\mu} + \sqrt{3}\,\dot{\alpha})dx = (\frac{L}{\mu} + 3\frac{\bar{L}}{H})\dot{\tau} \ , \tag{3.51}$$

where we set

$$\bar{L} := L - l\tanh[L/l] \ . \tag{3.52}$$

The integration of this equation results in the closed-form

$$\tau = y_0/\sqrt{3} + (\bar{u} - \bar{u}_e)/(\frac{L}{\mu} + 3\frac{\bar{L}}{H}) \quad \text{for} \quad \bar{u} \geq \bar{u}_e := y_0 L/\sqrt{3}\mu \tag{3.53}$$

for the constant shear stress in the strip as a function of the end displacement $\bar{u}$. Insertion of (3.53) into $(3.47)_2$ allows to plot $\alpha(x)$ and $\mathfrak{f}(x)$ in (3.49) and (3.50) for prescribed $\bar{u} \geq \bar{u}_e$.

3.3.3. Theoretical solution for perturbed softening plasticity. Defining the effective length scale for softening $l := l_p\sqrt{\mu/S}$, we get from (3.45) the differential equation for softening plasticity

$$\alpha + l^2\alpha'' = \alpha_s \quad \text{with} \quad \alpha_s := (y_0 - \sqrt{3}\,\tau)/S \geq 0 \ . \tag{3.54}$$

For an inhomogeneous plastic zone with symmetry property $\alpha(-x) = \alpha(x)$ and maximum value $\alpha_0 > 0$ at the center $x = 0$, we get the solution

$$\alpha(x) = \alpha_s + (\alpha_0 - \alpha_s)\cos[x/l] \ . \tag{3.55}$$

Such a solution may be thought to be obtained of an *initial perturbation of the softening modulus* at the center $x = 0$ of the strip. However, as shown in Figure 3.2a, this solution is only valid in the *plastic zone* with $\alpha \geq 0$, i.e.

$$|x| \leq x_0 := \pi l \ . \tag{3.56}$$

Setting the boundary condition at this *elastic-plastic-boundary* (EPB)

$$\alpha(x = x_0) = 0 \ , \tag{3.57}$$

we identify in (3.55) the maximum value $\alpha_0 = 2\alpha_s$. Hence, the solution is

$$\alpha(x) = \begin{cases} \alpha_s(1 + \cos[x/l]) & \text{for } |x| \leq \pi l \ , \\ 0 & \text{otherwise} \end{cases} \tag{3.58}$$

as depicted in Figure 3.2a. The driving force computed with this solution form (3.45) is constant in the plastic zone

$$\mathfrak{f}(x) = \begin{cases} \sqrt{3}\,\tau - y_0 & \text{for } |x| \leq \pi l \ , \\ 0 & \text{otherwise} \end{cases} \tag{3.59}$$

as shown in Figure 3.2b. What remains in order to plot the functions $\alpha(x)$ and $\mathfrak{f}(x)$ in (3.58) and (3.59) is to determine the constant shear stress τ in the strip for a deformation process *controlled by the displacement* $\bar{u} := u(x = L) = -u(x = -L)$ at the ends of the strip. To this end, we integrate the total strain rate in the strip, consisting of elastic and plastic contributions $\dot{\gamma}^e := \dot{\tau}/\mu$ and $\dot{\gamma}^p := \sqrt{3}\,\dot{\alpha}$

$$\dot{\bar{u}} = \int_0^{x_0} (\frac{\dot{\tau}}{\mu} + \sqrt{3}\,\dot{\alpha})dx + \int_{x_0}^{L} \frac{\dot{\tau}}{\mu} dx = (\frac{L}{\mu} - 3\frac{x_0}{S})\dot{\tau} \ . \tag{3.60}$$

The integration of this equation gives the closed-form result

$$\tau = y_0/\sqrt{3} + (\bar{u} - \bar{u}_e)/(\frac{L}{\mu} - 3\frac{x_0}{S}) \quad \text{for} \quad \bar{u} \geq \bar{u}_e := y_0 L/\sqrt{3}\mu \tag{3.61}$$

for the shear stress τ in the elastic-plastic bar as a function of the end displacement $\bar{u}$. Insertion of (3.61) into $(3.54)_2$ allows to plot $\alpha(x)$ and $\mathfrak{f}(x)$ in (3.58) and (3.59) for prescribed $\bar{u} \geq \bar{u}_e$.

3.3.4. Study of mixed finite element design and basic difficulties. We start with a *one-dimensional study*, that addresses basic problems of the spatial discretization of gradient plasticity, referring to the above outlined analytical solutions. Our subsequent construction of the FE discretization is guided by the following concepts:

1. *Regular FE Meshes:* A regular discretization of the full spatial domain is applied, without an (adaptive) alignment of finite elements to the *elastic-plastic-boundary* (EPB), such that this boundary may intersect elements.

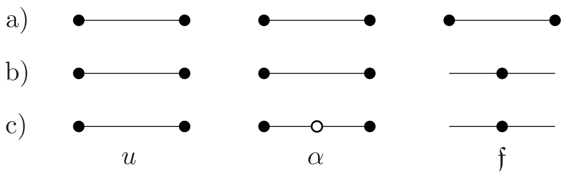

Figure 3.4: 1D Mixed Finite Element Design of Gradient Plasticity. Interpolations investigated for the three fields $\{u, \alpha, \mathfrak{f}\}$ are: a) Q1-Q1Q1 with linear α and $\mathfrak{f}$, b) Q1-Q1Q0 with linear α and constant $\mathfrak{f}$, c) Q1-Q1$_B$Q0 with linear α plus bubble and constant $\mathfrak{f}$. The bubble mode of α_B in c) can be condensed out at the element level. A constant driving force $\mathfrak{f}^e$ in b)–c) cannot be condensed out and enters the global system.

2. *Consistent FE Design:* The mixed finite element solver is designed such that the main characteristics of the dual fields α and $\mathfrak{f}$ are reflected, i.e. *values of the right sign* in plastic zones as well as *zero values* in elastic zones of the spatial domain.
3. *Stable FE Design:* The mixed finite element design must be stable in the sense that *spurious oscillations in space* of the dual fields α and $\mathfrak{f}$ do not appear or have a minor influence on the solution.

In order to achieve these requirements, we consider a family of *two-node finite elements* depicted in Figure 3.4. It uses the shape functions

$$N^I(\xi) = \tfrac{1}{2}\,(1 + \xi\xi^I) \quad \text{and} \quad N^B(\xi) = (1 - \xi^2)\ , \tag{3.62}$$

where $-1 \leq \xi \leq +1$ denotes the natural element parameter and $I = 1, 2$ the element node. N^I are *linear shapes* associated with the nodal degrees and N^B a *quadratic bubble mode.* The first element in Figure 3.4a discretizes the displacement u, the hardening/softening field α and the driving force $\mathfrak{f}$ in a straightforward manner by *linear* interpolations

$$\text{Q1-Q1Q1:} \quad \{u, \alpha, \mathfrak{f}\}^h = \textstyle\sum_{I=1}^{2} N^I(\xi)\,[u_I, \alpha_I, \mathfrak{f}_I] \tag{3.63}$$

in element domain $\mathcal{B}^e \subset \mathcal{B}^h$ with the nodal degrees $[u_I, \alpha_I, \mathfrak{f}_I] \in \mathcal{R}^3$. The second element in Figure 3.4b uses *linear* interpolations for u and α, but an *elementwise constant* driving force $\mathfrak{f}$

$$\text{Q1-Q1Q0:} \quad \{u, \alpha\}^h = \textstyle\sum_{I=1}^{2} N^I(\xi)\,[u_I, \alpha_I] \quad \text{and} \quad \{\mathfrak{f}\}^h = [\mathfrak{f}^e] \tag{3.64}$$

with the nodal degrees $[u_I, \alpha_I] \in \mathcal{R}^2$ and the element degree $\mathfrak{f}^e$. Finally, the element depicted in Figure 3.4c is based on *linear* interpolations for u and α plus a *quadratic bubble* mode for α and an *elementwise constant* driving force $\mathfrak{f}$

$$\text{Q1-Q1}_B\text{Q0:} \quad \{u, \alpha\}^h = \textstyle\sum_{I=1}^{2} N^I(\xi)\,[u_I, \alpha_I] + N^B(\xi)\,[0, a^e] \quad \text{and} \quad \{\mathfrak{f}\}^h = [\mathfrak{f}^e] \tag{3.65}$$

with nodal degrees $[u_I, \alpha_I] \in \mathcal{R}^2$ and the element degrees a^e and $\mathfrak{f}^e$. The variational based finite element implementation for these three 1D elements is a simplification of the multidimensional formulations outline in the two subsections below, and not commented on in detail. Goal at this stage is to show some characteristic numerical results obtained with these 1D elements, which address some fundamental problems and draw some consequences, which are also valid for the multi-dimensional implementation. The problems are related to the difficulty of modeling sharp *elastic-plastic-boundaries* (EPBs) as well as possible *instabilities of the mixed finite element design.* A 1D benchmark that shows a sharp EPB is the problem of softening plasticity in Figure 3.1c with theoretical solution

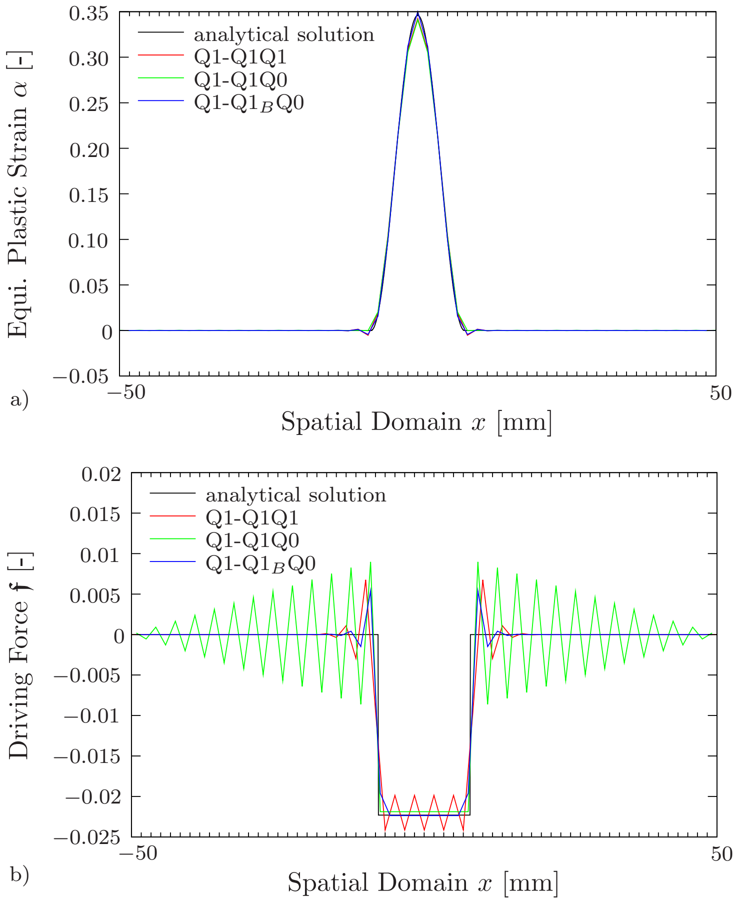

Figure 3.5: Numerical Solutions for Softening Plasticity *without Postprocessing* (3.70). a) Equivalent plastic strain α and b) dual driving force $\mathfrak{f}$, triggered by an initial perturbation at $x = 0$. Oscillations are observed for all elements in the elastic range, with maximum intensity at the EPB. The Q1-Q1Q1 element also shows some oscillations of $\mathfrak{f}$ in the plastic range. The most stable performance has the Q1-Q1$_B$Q0 element, matching the analytical solutions up to some deviations close to the EPB.

depicted in Figure 3.3 above. When discretizing the 1D domain $\mathcal{B} = [-L, L]$ with a *regular mesh of 60 finite elements* of the types outline in Figure 3.4, we observe the following problems:

4. *Negative α:* The C^0 finite element implementation of the field α outlined above cannot model exactly the *elastic-plastic-boundary* (EPB), which might be located inside of an element. As a consequence, non-physical values $\alpha < 0$ may occur at the nodes of the mesh, in particular near the EPB.

5. *Oscillations of $\mathfrak{f}$:* Jumps of the driving force $\mathfrak{f}$ cannot be modeled by C^0 interpolations. As a consequence, for *unstable mixed finite element design*, oscillations and non-physically wrong signs of $\mathfrak{f}$ may be observed, in particular close to the EPB.

6. *Non-Zero α and $\mathfrak{f}$ in Elastic Range:* Due to the two above outlined difficulties of the finite element implementation, non-zero values of α and $\mathfrak{f}$ may occur in the elastic range, where α and $\mathfrak{f}$ is essentially not defined.

The two diagrams in Figure 3.5 visualize these effects for the three element designs, applied to the numerical solution of the strain softening problem depicted in Figure 3.3.

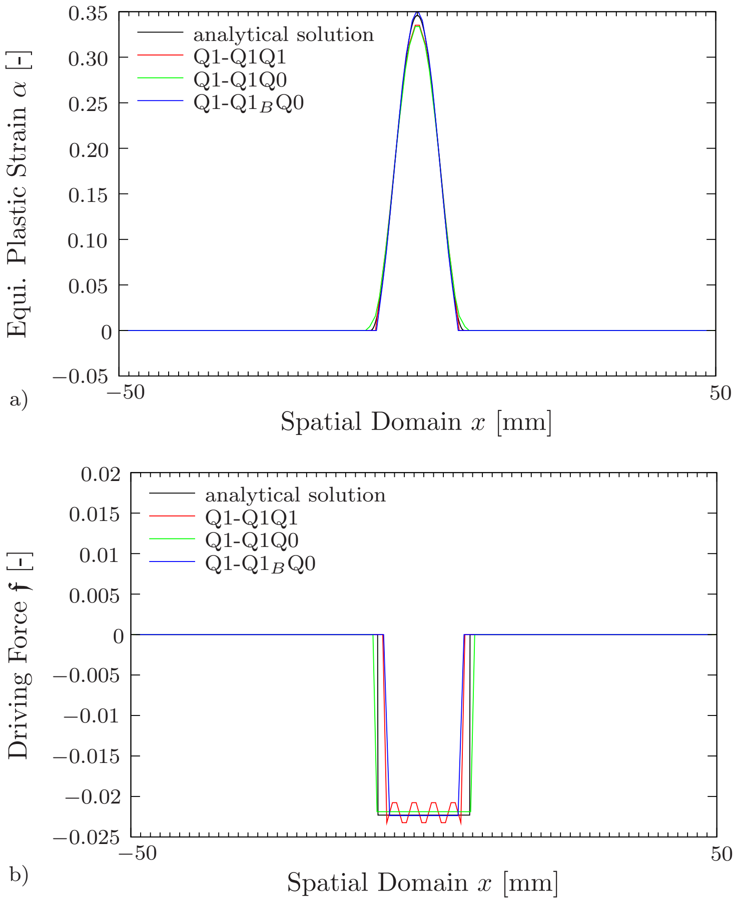

Figure 3.6: Numerical Solutions for Softening Plasticity *with Postprocessing* (3.70). a) Equivalent plastic strain α and b) dual driving force $\mathfrak{f}$, triggered by an initial perturbation at $x = 0$. All elements show reasonable results with *defined values* in the elastic range. The EPB is resolved only at slightly different positions. The Q1-Q1Q1 element shows some oscillations of $\mathfrak{f}$ in the plastic range. However, $\mathfrak{f}$ has the right (negative) sign and these oscillations have a minor effect on the result for α.

3.3.5. Elastic-plastic-boundary (EPB) in regular FE discretizations. We now outline our basic concept to overcome the above mentioned difficulties. A key inconsistency with the theoretical solution is that the finite element discretization is performed in the full spatial domain without resolving the EPB. In particular, the hardening/softening variable α as well as its dual driving force $\mathfrak{f}$ are discretized in a straightforward manner, for the Q1-Q1Q1 design even by C^0 interpolations. However, these variables are essentially only defined in the plastic zone, and *should defined to be zero* in the elastic range. This correlates to the fundamental problem of *defining the EPB in regular FE meshes*, in particular in context with C^0. This becomes even more delicate, if jumps of these variables occur at the EPB. The non-ability of modeling these discontinuities causes non-physical effects in the FE discretization addressed above. The basic constraints in the model of gradient plasticity considered here are

$$\alpha(\boldsymbol{x},t) \geq 0 \quad \text{and} \quad \mathfrak{f}(\boldsymbol{x},t) \begin{cases} \geq 0 & \text{for hardening plasticity,} \\ \leq 0 & \text{for softening plasticity,} \end{cases} \tag{3.66}$$

which must be satisfied in the full domain $\mathcal{B}$ covered by the finite element mesh. This can be *violated at the nodal points* of the finite element mesh as shown above. However, recall that the constitutive response of the finite element formulation is evaluated *point-wise at the integration points* of the finite element mesh. It turns out that the family of mixed finite elements depicted in Figure 3.4 satisfies the condition (3.66) at all *active integration points* with elastic-plastic response. As a consequence, we *define the plastic zone of gradient plasticity by the active set of integration points.* Let $\mathcal{G} := \{1, \ldots, E^h \cdot L\}$ be the total number of integration points of a mesh with E^h elements and L element Gauss points. Then, the set of plastically active integration points is

$$\mathcal{A}(t) := \{ \, g \in \mathcal{G} \mid \chi(\boldsymbol{x}_g, t) > 0 \, \} \ , \tag{3.67}$$

where χ is the yield function defined in (3.11). Our basic observation is that condition (3.66) is satisfied in the plastic zone, i.e. for active integration points $g \in \mathcal{A}$, but might slightly be violated due to the above mentioned reasons in the elastic range, i.e. for non-active integration points $g \in \mathcal{G} \setminus \mathcal{A}$. We then define a *postprocessing corrector to the evolution of the long-range variables at the integration points.* In particular, we set

$$\dot{\alpha}(\boldsymbol{x}_g, t) \Leftarrow \left\{ \begin{array}{ll} \dot{\alpha}(\boldsymbol{x}_g, t) & \text{at } g \in \mathcal{A}(t) \\ 0 & \text{otherwise} \end{array} \right. \tag{3.68}$$

for the long-range hardening variable and

$$\mathfrak{f}(\boldsymbol{x}_g, t) \Leftarrow \left\{ \begin{array}{ll} \mathfrak{f}(\boldsymbol{x}_g, t) & \text{for } g \in \mathcal{A}(t) \\ 0 & \text{otherwise} \end{array} \right. \tag{3.69}$$

for its dual driving force. Hence, the evolution of these variables is exactly *defined* in the elastic range. For the time-discrete algorithmic setting, we define the corrector step associated with the time increment $[t_n, t_{n+1}]$ by

$$\boldsymbol{p}_{n+1} := \{\alpha_{n+1}, \mathfrak{f}_{n+1}\} \Leftarrow \left\{ \begin{array}{ll} \{\alpha_{n+1}, \mathfrak{f}_{n+1}\} & \text{at } g \in \mathcal{A}_{n+1}, \\ \{\alpha_n \quad , 0 \quad \} & \text{otherwise .} \end{array} \right. \tag{3.70}$$

Based on these corrected results at the integration points $g \in \mathcal{G}$, we compute *corrected nodal values by a standard smoothing procedure* based on the weighted residual

$$\int_{\mathcal{B}} \delta \boldsymbol{p}^*_{n+1} \cdot [\, \boldsymbol{p}^*_{n+1} - \boldsymbol{p}_{n+1} \,] \, dV = 0 \ , \tag{3.71}$$

yielding with the ansatz $\boldsymbol{p}^*_{n+1}(\boldsymbol{x}) = \boldsymbol{N}(\boldsymbol{x}) \boldsymbol{P}^*_{n+1}$ based on the matrix $\boldsymbol{N}$ of linear shapes $(3.62)_1$ the corrected nodal values

$$\boldsymbol{P}^*_{n+1} = \left[\mathop{\mathsf{A}}_{e=1}^{E^h} \sum_{l=1}^{L} \boldsymbol{N}_l^T \boldsymbol{N}_l J_l w_l \right]^{-1} \left[\mathop{\mathsf{A}}_{e=1}^{E^h} \sum_{l=1}^{L} \boldsymbol{N}_l^T \boldsymbol{p}_l J_l w_l \right] \ , \tag{3.72}$$

which we approximate by a *lumping procedure* for the coefficient matrix. The corrected nodal variables are only used for the plotting of the fields α and $\mathfrak{f}$. The two diagrams in Figure 3.6 visualize the improvement achieved by the postprocessing steps for the three element designs, applied to the numerical solution of the strain softening problem depicted in Figure 3.3. Finally, we draw the following conclusions:

7. *Stability:* When the postprocessing (3.70) *is not applied*, the Q1-Q1$_B$Q0 element provides the most stable formulation, yielding *minimal oscillations* in the elastic range. The Q1-Q1Q0 element give in this respect the worst response.

8. *Applicability:* If the postprocessing (3.70) *is applied*, all three elements investigated, i.e. Q1-Q1Q1, Q1-Q1Q0 and Q1-Q1$_B$Q0, yield reasonable results with *defined values* in the elastic range. The EPB is resolved for all elements almost at the same position.
9. *Convenience:* In combination with the postprocessing (3.70), the Q1-Q1Q1 element provides the simplest and most straightforward FE implementation, *exclusively based on nodal degrees*. The Q1-Q1$_B$Q0 element needs non-standard FE solvers with global degrees associated with both the nodes *as well as the elements*, because the elementwise constant driving force $\mathfrak{f}^e$ cannot be condensed out.

Recall that the stability of mixed finite elements is related to the Babuška-Brezzi or LBB stability condition, see Babuška [24, 25], Brezzi [31] and Brezzi & Fortin [32]. The mathematical analysis of the proposed mixed finite elements for gradient plasticity is beyond the scope of this work. However, we applied the simple count condition for mixed elements outlined in Zienkiewicz & Taylor [163, 164], Zienkiewicz et al. [162], that is necessary for stability though not sufficient. All the elements proposed here are designed such that the condition

$$n_\alpha \geq n_\mathfrak{f} \tag{3.73}$$

is fulfilled, if *Neumann-type boundary conditions* are applied on the equivalent plastic strain α. Here, n_α and $n_\mathfrak{f}$ are the number of discrete degrees of α and $\mathfrak{f}$ in a representative patch of finite elements. In the micro-clamped hardening test, where *Dirichlet boundary conditions* are applied on α, only the Q1-Q1$_B$Q0 element is fully stable. However, good numerical results are obtained also with the other elements outlined above. This observation is similar to that made for Q1P0 elements considered below, which are known to be not stable even in local plasticity but yield appropriate results for most practical problems. The subsequent two Sections extend the above outlined concepts to the multi-dimensional design of finite elements.

3.4. Q1-P0-type finite element design of gradient plasticity

The von Mises-type gradient plasticity considered above with *isochoric plastic flow* needs further extensions to avoid locking phenomena in finite element discretizations due to the plastic incompressibility. A well-known concept that overcomes these problems is the Q1P0 mixed element design introduced by Simó, Taylor & Pister [136], which we here outline in a consistent variational setting for gradient plasticity. It is based on the decomposition of the small-strain tensor into volumetric and isochoric parts defined in (3.1). With this kinematic decomposition at hand, we extend the reduced incremental potential (3.37) by

$$\Pi^{*\tau}_{red,ext}(\boldsymbol{u}, \alpha, \mathfrak{f}, \tilde{\theta}, p) = \int_\mathcal{B} [\, \frac{\kappa}{2}\tilde{\theta}^2 + p(e - \tilde{\theta}) + \bar{\pi}^{*\tau}_{red}(\bar{\mathfrak{r}}) \,]\, dV \;-\; P^\tau_{ext}(\boldsymbol{u}) \; . \tag{3.74}$$

It introduces the *volume dilatation* $\tilde{\theta}$ and the *pressure* p as additional fields. This implies the extension of the mixed saddle point principle (3.38) towards the five-field variational principle

$$(G_{ext}) : \quad \{\boldsymbol{u}, \alpha, \mathfrak{f}, \tilde{\theta}, p\} = \text{Arg}\{ \inf_{\boldsymbol{u}} \inf_{\alpha} \sup_{\mathfrak{f}} \inf_{\tilde{\theta}} \sup_{p} \Pi^{*\tau}_{red,ext}(\boldsymbol{u}, \alpha, \mathfrak{f}, \tilde{\theta}, p) \} \; . \tag{3.75}$$

3.4.1. FE discretization for Quadrilateral or Brick-like elements. We start with a straightforward extension of Q1P0-finite elements to gradient plasticity, using C^0

interpolations for both the primary fields $\{\,\boldsymbol{u},\alpha\,\}$ *as well as* for the driving force field $\{\,\mathfrak{f}\,\}$ dual to α, but elementwise *constant* volume dilatation and pressure $\{\,\tilde{\theta},p\,\}$. For a triangulation $\mathfrak{T}^h$ with element domains $\mathcal{B}^e \subset \mathcal{B}$, the node I has standard bi- or tri-linear shape functions $N^I(\boldsymbol{\xi})$, e.g.

$$N^I(\boldsymbol{\xi}) = \tfrac{1}{4}\,(1+\xi_1\xi_1^I)(1+\xi_2\xi_2^I) \tag{3.76}$$

for bi-linear Q1 elements with $n = 4$ nodes. Here, $\boldsymbol{\xi} := \{\ \boldsymbol{\xi}| -1 \le \xi_i \le +1\}$ denotes the natural element parameters. The gradients of the shape functions are obtained by using the chain rule $\nabla N^I = \nabla_{\boldsymbol{\xi}} N^I \boldsymbol{J}^{-1}$, where $\boldsymbol{J} := \nabla_{\boldsymbol{\xi}} \boldsymbol{x}^h(\boldsymbol{\xi})$ with $J := \det \boldsymbol{J} > 0$ denotes the Jacobian of the isoparametric map $\boldsymbol{x}^h = \sum_{I=1}^n N^I \boldsymbol{x}_I$ that defines the coordinates of the element in terms of their nodal positions $\boldsymbol{x}_I$. We discretize the extended variational functional (3.74) by *bi-linear* interpolations of $\boldsymbol{u}$, α, $\mathfrak{f}$ but elementwise *constant* $\tilde{\theta}$, p

$$\{\boldsymbol{u},\alpha,\mathfrak{f}\}^h = \textstyle\sum_{I=1}^n N^I\,\boldsymbol{d}_I \quad \text{and} \quad \{\tilde{\theta},p\}^h = \{\tilde{\theta}^e,p^e\} \tag{3.77}$$

in $\mathcal{B}^e \subset \mathcal{B}^h$ with the nodal degrees $\boldsymbol{d}_I := [\boldsymbol{u},\alpha,\mathfrak{f}]_I^T \in \mathcal{R}^4$. Introducing the interpolations

$$e^h = \textstyle\sum_{I=1}^n \boldsymbol{V}^I\,\boldsymbol{d}_I \quad \text{and} \quad \bar{\mathfrak{r}}^h := \textstyle\sum_{I=1}^n \bar{\boldsymbol{B}}^I\,\boldsymbol{d}_I \tag{3.78}$$

with the volumetric interpolation matrix

$$\boldsymbol{V}^I = \begin{bmatrix} N^I_{,1} \\ N^I_{,2} \\ \cdot \\ \cdot \end{bmatrix}^T \tag{3.79}$$

and the deviatoric interpolation matrix

$$\bar{\boldsymbol{B}}^I = \begin{bmatrix} \frac{2}{3}N^I_{,1} & -\frac{1}{3}N^I_{,1} & N^I_{,2} & \cdot & \cdot & \cdot & \cdot \\ -\frac{1}{3}N^I_{,2} & \frac{2}{3}N^I_{,2} & N^I_{,1} & \cdot & \cdot & \cdot & \cdot \\ \cdot & \cdot & \cdot & N^I & N^I_{,1} & N^I_{,2} & \cdot \\ \cdot & \cdot & \cdot & \cdot & \cdot & \cdot & N^I \end{bmatrix}^T . \tag{3.80}$$

Focusing on pure Dirichlet problems with $P^\tau_{ext} = 0$, the spatial discretization of the potential (3.74) reads

$$\Pi^{*\tau\,h}_{red,ext}(\boldsymbol{d},\tilde{\theta}^e,p^e) = \mathop{\mathsf{A}}_{e=1}^{E^h} \sum_{l=1}^{L} \{\ \frac{\kappa}{2}\tilde{\theta}^{e\,2} + p^e(e^h - \tilde{\theta}^e) + \bar{\pi}^{*\tau}_{red}(\bar{\mathfrak{r}}^h)\ \}\, J w_l \tag{3.81}$$

in terms of the isochoric incremental potential density $\bar{\pi}^{*\tau}_{red}$ defined in (3.30). The discretized mixed variational principle then reads

$$\{\boldsymbol{d},\tilde{\theta}^e,p^e\} = \text{Arg}\{\ \mathop{\text{stat}}_{\boldsymbol{d},\tilde{\theta}^e,p^e}\ \Pi^{*\tau\,h}_{red,ext}(\boldsymbol{d},\tilde{\theta}^e,p^e)\ \}\ . \tag{3.82}$$

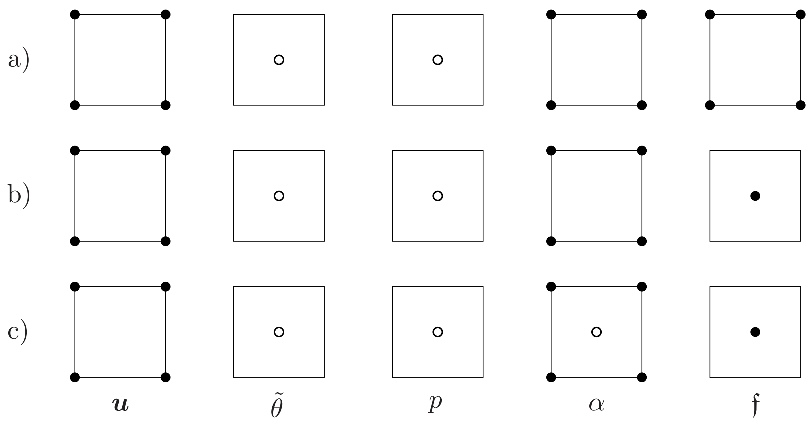

Figure 3.7: Extended Q1P0–Type Mixed Finite Element Design of Gradient Plasticity. Interpolations investigated for the five fields $\{\boldsymbol{u}, \tilde{\theta}, p, \alpha, \mathfrak{f}\}$ are: a) Q1P0-Q1Q1 with bi-linear α and $\mathfrak{f}$, b) Q1P0-Q1Q0 with bi-linear α and constant $\mathfrak{f}$, c) Q1P0-Q1$_B$Q0 with bi-linear α plus bubble and constant $\mathfrak{f}$. The elementwise constant $\tilde{\theta}^e$, p^e in a)-c) and the bubble mode of α_B in c) can be condensed out at the element level. A constant driving force $\mathfrak{f}^e$ in b)–c) cannot be condensed out and enters the global system.

3.4.2. Condensation at the element level. The dilatation and the pressure $\tilde{\theta}^e$ and p^e are discrete values associated with the elements $e = 1...E^h$. Then, we can construct the condensed potential by optimization with respect to these discrete values via

$$\Pi^{*\tau\,h}_{red,ext,cond}(\boldsymbol{d}) = \inf_{\tilde{\theta}^e} \sup_{p^e} \Pi^{*\tau\,h}_{red,ext}(\boldsymbol{d}, \tilde{\theta}^e, p^e)\ . \tag{3.83}$$

The necessary conditions of this variational problem determine the discrete element dilatation

$$\tilde{\theta}^e = \frac{1}{V^e} \sum_{l=1}^{L} \{ \textstyle\sum_{I=1}^{n} \boldsymbol{V}^I \boldsymbol{d}_I \} J w_l \quad \text{with} \quad V^e = \sum_{l=1}^{L} J w_l \tag{3.84}$$

and the mean pressure of the $e = 1...E^h$ elements

$$p^e = \kappa\, \tilde{\theta}^e\ . \tag{3.85}$$

3.4.3. Effective element arrays and global solver. For known dilatation and pressure $\tilde{\theta}^e$ and p^e, the remaining variables are obtained by a monolithic global solver. To this end, the condensed variational problem at the global level

$$\boldsymbol{d} = \text{Arg}\{ \underset{\boldsymbol{d}}{\text{stat}}\ \Pi^{*\tau\,h}_{red,ext,cond}(\boldsymbol{d}) \} \tag{3.86}$$

by the global Newton updates

$$\boldsymbol{d} \Leftarrow \boldsymbol{d} - \boldsymbol{K}^{-1}\boldsymbol{R} \quad \text{until} \quad |\boldsymbol{R}| < tol\ . \tag{3.87}$$

Due to the mixed formulation of the volumetric terms, the global finite element residual takes the effective form

$$\boldsymbol{R} = \mathop{\mathsf{A}}_{e=1}^{E^h} [\, p^e \boldsymbol{L}^{eT} + \sum_{l=1}^{L} \{ \textstyle\sum_{I=1}^{n} \bar{\boldsymbol{B}}^{IT} \bar{\boldsymbol{\mathfrak{S}}} \} J w_l \,]\ . \tag{3.88}$$

The condensed finite element tangent matrix takes the form

$$\boldsymbol{K} = \mathop{\mathsf{A}}_{e=1}^{E^h} [\, \kappa V^e \boldsymbol{L}^{eT} \boldsymbol{L}^e + \sum_{l=1}^{L} \{\, \textstyle\sum_{I=1}^{n} \sum_{J=1}^{n} \bar{\boldsymbol{B}}^{I\,T} \bar{\mathfrak{C}} \bar{\boldsymbol{B}}^J \,\}\, J w_l \,] \,, \tag{3.89}$$

with the definition $\boldsymbol{L}^e := \dfrac{1}{V^e} \sum_{l=1}^{L} \{\, \sum_{I=1}^{n} \boldsymbol{V}^I \,\}\, J w_l$. The isochoric contributions of the finite element residual and tangent are governed by *deviatoric* generalized stress and tangent arrays $\bar{\mathfrak{S}}$ and $\bar{\mathfrak{C}}$ defined in (3.41) and (3.44).

3.4.4. Modified setting with elementwise constant driving forces. Alternatively to (3.77), we investigate a discretization of the extended variational functional (3.74) by the *linear* interpolations of $\boldsymbol{u}$ and α, plus a *bubble mode* for α and elementwise *constant* $\tilde{\theta}$, p and $\mathfrak{f}$

$$\{\boldsymbol{u}, \alpha\}^h = \textstyle\sum_{I=1}^{n} N^I \, \boldsymbol{d}_I + N^B \, \boldsymbol{1}^B a^e \quad \text{and} \quad \{\tilde{\theta}, p, \mathfrak{f}\}^h = \{\tilde{\theta}^e, p^e, \mathfrak{f}^e\} \tag{3.90}$$

in $\mathcal{B}^e \subset \mathcal{B}^h$ with the nodal degrees $\boldsymbol{d}_I := [\boldsymbol{u}, \alpha]_I^T \in \mathcal{R}^3$. Here, $a^e \in \mathcal{R}^3$ is the degree of the bubble mode for α and $\boldsymbol{1}^B$ an array that filters out the associated slot. Introducing the modified interpolations

$$e^h = \textstyle\sum_{I=1}^{n} \boldsymbol{V}^I \, \boldsymbol{d}_I \quad \text{and} \quad \bar{\mathfrak{r}}^h := \sum_{I=1}^{n} \bar{\boldsymbol{B}}^I \, \boldsymbol{d}_I + \bar{\boldsymbol{B}}^B \, a^e + \bar{\boldsymbol{G}} \, \mathfrak{f}^e \tag{3.91}$$

with the constant matrix

$$\bar{\boldsymbol{G}} = \begin{bmatrix} \cdot & \cdot & \cdot & \cdot & \cdot & \cdot & 1 \end{bmatrix}^T \tag{3.92}$$

and the volumetric interpolation matrix

$$\boldsymbol{V}^I = \begin{bmatrix} N^I_{,1} \\ N^I_{,2} \\ \cdot \end{bmatrix}^T \,. \tag{3.93}$$

The deviatoric interpolation matrices are defined by

$$\bar{\boldsymbol{B}}^I = \begin{bmatrix} \frac{2}{3} N^I_{,1} & -\frac{1}{3} N^I_{,1} & N^I_{,2} & \cdot & \cdot & \cdot & \cdot \\ -\frac{1}{3} N^I_{,2} & \frac{2}{3} N^I_{,2} & N^I_{,1} & \cdot & \cdot & \cdot & \cdot \\ \cdot & \cdot & \cdot & N^I & N^I_{,1} & N^I_{,2} & \cdot \end{bmatrix}^T \tag{3.94}$$

and

$$\bar{\boldsymbol{B}}^B = \begin{bmatrix} \cdot & \cdot & \cdot & N^B & N^B_{,1} & N^B_{,2} & \cdot \end{bmatrix}^T \,. \tag{3.95}$$

Focusing on pure Dirichlet problems with $P^{\tau}_{ext} = 0$, the spatial discretization of the potential (3.74) reads

$$\Pi^{*\tau\, h}_{red,ext}(\boldsymbol{d}, \tilde{\theta}^e, p^e, a^e, f^e) = \mathop{\mathsf{A}}_{e=1}^{E^h} \sum_{l=1}^{L} \{\, \frac{\kappa}{2} \tilde{\theta}^{e\,2} + p^e(e^h - \tilde{\theta}^e) + \bar{\pi}^{*\tau}_{red}(\bar{\mathfrak{r}}^h) \,\}\, J w_l \tag{3.96}$$

in terms of the isochoric incremental potential density $\bar{\pi}^{*\tau}_{red}$ defined in (3.30). The condensation of the volumetric variables yields again the results (3.84) and (3.85), yielding a condensed variational problem

$$\{\boldsymbol{d}, \boldsymbol{a}, \mathfrak{f}\} = \text{Arg}\{ \operatorname*{stat}_{\boldsymbol{d}, \boldsymbol{a}, \mathfrak{f}} \Pi^{*\tau\, h}_{red,ext,cond}(\boldsymbol{d}, \boldsymbol{a}, \mathfrak{f}) \,\} \tag{3.97}$$

in analogy to (3.86). The solution of this variational problem by a global Newton-type solver is based on incremental updates of the nodal degrees $\boldsymbol{d}$ and the bubble degrees $\boldsymbol{a}$

$$\begin{bmatrix} \boldsymbol{d} \\ \boldsymbol{a} \\ \mathfrak{f} \end{bmatrix} \Leftarrow \begin{bmatrix} \boldsymbol{d} \\ \boldsymbol{a} \\ \mathfrak{f} \end{bmatrix} - \begin{bmatrix} \boldsymbol{K}_{dd} & \boldsymbol{K}_{da} & \boldsymbol{K}_{d\mathfrak{f}} \\ \boldsymbol{K}_{ad} & \boldsymbol{K}_{aa} & \boldsymbol{K}_{a\mathfrak{f}} \\ \boldsymbol{K}_{\mathfrak{f}d} & \boldsymbol{K}_{\mathfrak{f}a} & \boldsymbol{K}_{\mathfrak{f}\mathfrak{f}} \end{bmatrix}^{-1} \begin{bmatrix} \boldsymbol{R}_d \\ \boldsymbol{R}_a \\ \boldsymbol{R}_{\mathfrak{f}} \end{bmatrix} \tag{3.98}$$

until convergence is achieved. Here, $\boldsymbol{R}_d$ and $\boldsymbol{K}_{dd}$ are identical with (3.88) and (3.89), however, evaluated with the modified matrices defined in (3.93) and (3.94). The additional residuals are defined by

$$\begin{aligned} \boldsymbol{R}_{\boldsymbol{a}} &:= \sum_{l=1}^{L} \{\, \bar{\boldsymbol{B}}^{B\,T} \bar{\mathfrak{S}} \,\}\, J w_l \\ \boldsymbol{R}_{\mathfrak{f}} &:= \sum_{l=1}^{L} \{\, \bar{\boldsymbol{G}}^{T} \bar{\mathfrak{S}} \,\}\, J w_l \end{aligned} \tag{3.99}$$

governed by deviatoric generalized stress array $\bar{\mathfrak{S}}$ defined in (3.41). The second derivatives of the condensed potential gives the additional arrays

$$\begin{aligned} \boldsymbol{K}_{da} &:= \mathop{\mathsf{A}}_{e=1}^{E^h} \sum_{l=1}^{L} \{\, \textstyle\sum_{I=1}^{n} [\, \bar{\boldsymbol{B}}^{I\,T} \bar{\mathfrak{C}} \bar{\boldsymbol{B}}^{B} \,] \,\}\, J w_l \ , \\ \boldsymbol{K}_{d\mathfrak{f}} &:= \mathop{\mathsf{A}}_{e=1}^{E^h} \sum_{l=1}^{L} \{\, \textstyle\sum_{I=1}^{n} [\, \bar{\boldsymbol{B}}^{I\,T} \bar{\mathfrak{C}} \bar{\boldsymbol{G}} \,] \,\}\, J w_l \ , \\ \boldsymbol{K}_{a\mathfrak{f}} &:= \sum_{l=1}^{L} \{\, \bar{\boldsymbol{B}}^{B\,T} \bar{\mathfrak{C}} \bar{\boldsymbol{G}} \,\}\, J w_l \ , \\ \boldsymbol{K}_{\mathfrak{f}\mathfrak{f}} &:= \sum_{l=1}^{L} \{\, \bar{\boldsymbol{G}}^{T} \bar{\mathfrak{C}} \bar{\boldsymbol{G}} \,\}\, J w_l \ , \end{aligned} \tag{3.100}$$

determined by the deviatoric generalized tangent array $\bar{\mathfrak{C}}$ defined in (3.44). The degrees a^e of the bubble mode can also be condensed at the element level, yielding a further condensed system. The condensation of the elementwise constant driving forces $\mathfrak{f}^e$ is *not possible*, because they are not defined by the plastic return mapping.

3.5. Mini-type finite element design of gradient plasticity

In order to avoid locking effects of the standard Galerkin finite element formulation in connection with the overconstrained pressure field in incompressible von Mises-type plastic flow model, we may alternatively use the Mini-type mixed finite element design suggested by Arnold, Brezzi & Fortin [20]. It is also based on the decomposition of the small-strain tensor into volumetric and isochoric parts defined in (3.1). With this kinematic decomposition at hand, we extend the reduced incremental potential (3.37) by

$$\Pi^{*\tau}_{red,ext}(\boldsymbol{u}, \alpha, \mathfrak{f}, p) = \int_{\mathcal{B}} [\, pe - \frac{1}{2\kappa} p^2 + \bar{\pi}^{*\tau}_{red}(\bar{\mathfrak{e}}) \,]\, dV \ - \ P^{\tau}_{ext}(\boldsymbol{u}) \ . \tag{3.101}$$

It introduces the *pressure* p as an additional field. This implies the extension of the mixed saddle point principle (3.38) towards the four-field variational principle

$$(G_{ext}): \quad \{\boldsymbol{u}, \alpha, \mathfrak{f}, p\} = \text{Arg}\{ \inf_{\boldsymbol{u}} \inf_{\alpha} \sup_{\mathfrak{f}} \sup_{p} \Pi^{*\tau}_{red,ext}(\boldsymbol{u}, \alpha, \mathfrak{f}, p) \} \ . \tag{3.102}$$

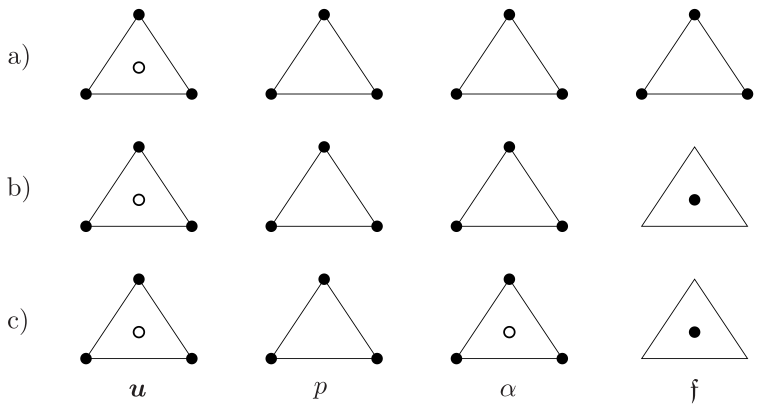

Figure 3.8: Extended Mini-Type Mixed Finite Element Design of Gradient Plasticity. Interpolations investigated for the four fields $\{\boldsymbol{u}, p, \alpha, \mathfrak{f}\}$ are: a) Mini-Q1Q1 with linear α and $\mathfrak{f}$, b) Mini-Q1Q0 with linear α and constant $\mathfrak{f}$, c) Mini-Q1$_B$Q0 with linear α plus bubble and constant $\mathfrak{f}$. The elementwise constant bubble modes in a)–c) can be condensed out at the element level. A constant driving force $\mathfrak{f}^e$ in b)–c) cannot be condensed out and enter the global system.

3.5.1. FE discretization for triangular elements. We start with a straightforward extension of Mini-finite elements to gradient plasticity, using linear C^0 interpolations for all fields $\{\, \boldsymbol{u}, \alpha, \mathfrak{f}, p\}$, including an additional *bubble mode* for $\{\, \boldsymbol{u}\,\}$. For a triangulation $\mathfrak{T}^h$ with element domains $\mathcal{B}^e \subset \mathcal{B}$, we consider the shape functions

$$N^I(\boldsymbol{\xi}) = \xi^I \quad \text{and} \quad N^B(\boldsymbol{\xi}) = \xi^1\xi^2\xi^3 \tag{3.103}$$

associated with the $n = 3$ nodes $I = 1 \dots n$ and the center bubble B. Here, $\boldsymbol{\xi} \in \{\, 0 \le \xi^I \le 1\}$ denotes the natural parameters of the triangle. The gradients of the shape functions are obtained by using the chain rule $\nabla N^I = \nabla_{\boldsymbol{\xi}} N^I \boldsymbol{J}^{-1}$, where $\boldsymbol{J} := \nabla_{\boldsymbol{\xi}} \boldsymbol{x}^h(\boldsymbol{\xi})$ with $J := \det \boldsymbol{J} > 0$ denotes the Jacobian of the isoparametric map $\boldsymbol{x}^h = \sum_{I=1}^n N^I \boldsymbol{x}_I$ that defines the coordinates of the element in terms of their nodal positions $\boldsymbol{x}_I$. We discretize the extended variational functional (3.101) by the *linear* interpolations of $\boldsymbol{u}$, α, $\mathfrak{f}, p$ and an additional bubble mode for $\boldsymbol{u}$

$$\{\boldsymbol{u}, \alpha, \mathfrak{f}, p\}^h = \textstyle\sum_{I=1}^n N^I\, \boldsymbol{d}_I + N^B\, \boldsymbol{1}^B \boldsymbol{a}^e \tag{3.104}$$

in $\mathcal{B}^e \subset \mathcal{B}$ with the nodal degrees $\boldsymbol{d}_I := [\boldsymbol{u}, \alpha, \mathfrak{f}, p]_I^T \in \mathcal{R}^5$. Here, $\boldsymbol{a}^e \in \mathcal{R}^2$ are the degrees of the displacement bubble modes and $\boldsymbol{1}^B$ an array that filters out the displacement slots. Introducing the interpolations

$$p^h = \textstyle\sum_{I=1}^n \boldsymbol{P}^I \boldsymbol{d}_I\,, \quad e^h = \sum_{I=1}^n \boldsymbol{V}^I \boldsymbol{d}_I + \boldsymbol{V}^B \boldsymbol{a}^e\,, \quad \bar{\boldsymbol{\mathfrak{e}}}^h = \sum_{I=1}^n \bar{\boldsymbol{B}}^I\, \boldsymbol{d}_I + \bar{\boldsymbol{B}}^B\, \boldsymbol{a}^e \tag{3.105}$$

with the pressure and dilatation interpolation matrices

$$\boldsymbol{P}^I = \begin{bmatrix} \cdot \\ \cdot \\ \cdot \\ \cdot \\ N^I \end{bmatrix}^T , \quad \boldsymbol{V}^I = \begin{bmatrix} N^I_{,1} \\ N^I_{,2} \\ \cdot \\ \cdot \\ \cdot \end{bmatrix}^T , \quad \boldsymbol{V}^B = \begin{bmatrix} N^B_{,1} \\ N^B_{,2} \\ \cdot \\ \cdot \\ \cdot \end{bmatrix}^T \tag{3.106}$$

and the deviatoric interpolation matrices

$$\bar{\boldsymbol{B}}^I = \begin{bmatrix} \frac{2}{3}N^I_{,1} & -\frac{1}{3}N^I_{,1} & N^I_{,2} & \cdot & \cdot & \cdot & \cdot \\ -\frac{1}{3}N^I_{,2} & \frac{2}{3}N^I_{,2} & N^I_{,1} & \cdot & \cdot & \cdot & \cdot \\ \cdot & \cdot & \cdot & N^I & N^I_{,1} & N^I_{,2} & \cdot \\ \cdot & \cdot & \cdot & \cdot & \cdot & \cdot & N^I \\ \cdot & \cdot & \cdot & \cdot & \cdot & \cdot & \cdot \end{bmatrix}^T \tag{3.107}$$

and

$$\bar{\boldsymbol{B}}^B = \begin{bmatrix} \frac{2}{3}N^B_{,1} & -\frac{1}{3}N^B_{,1} & N^B_{,2} & \cdot & \cdot & \cdot & \cdot \\ -\frac{1}{3}N^B_{,2} & \frac{2}{3}N^B_{,2} & N^B_{,1} & \cdot & \cdot & \cdot & \cdot \\ \cdot & \cdot & \cdot & \cdot & \cdot & \cdot & \cdot \\ \cdot & \cdot & \cdot & \cdot & \cdot & \cdot & \cdot \\ \cdot & \cdot & \cdot & \cdot & \cdot & \cdot & \cdot \end{bmatrix}^T . \tag{3.108}$$

Focusing on pure Dirichlet problems with $P^{\tau}_{ext} = 0$, the spatial discretization of the potential (3.101) reads

$$\Pi^{*\tau\,h}_{red,ext}(\boldsymbol{d},\boldsymbol{a}) = \mathop{\mathsf{A}}\limits_{e=1}^{E^h} \sum_{l=1}^{L} \{\, p^h e^h - \frac{1}{2\kappa} p^{h\,2} + \bar{\pi}^{*\tau}_{red}(\bar{\boldsymbol{\mathfrak{r}}}^h)\,\} J w_l \tag{3.109}$$

in terms of the isochoric incremental potential density $\bar{\pi}^{*\tau}_{red}$ defined in (3.30). The discretized mixed variational principle then reads

$$\{\boldsymbol{d},\boldsymbol{a}\} = \text{Arg}\{\, \underset{\boldsymbol{d},\boldsymbol{a}}{\text{stat}}\ \Pi^{*\tau\,h}_{red,ext}(\boldsymbol{d},\boldsymbol{a})\,\} . \tag{3.110}$$

3.5.2. Partitioned element arrays for newton-type solver. The solution of the variational problem (3.110) by a global Newton-type solver is based on incremental updates of the nodal degrees $\boldsymbol{d}$ and the bubble degrees $\boldsymbol{a}$

$$\begin{bmatrix} \boldsymbol{d} \\ \boldsymbol{a} \end{bmatrix} \Leftarrow \begin{bmatrix} \boldsymbol{d} \\ \boldsymbol{a} \end{bmatrix} - \begin{bmatrix} \boldsymbol{K}_{dd} & \boldsymbol{K}_{da} \\ \boldsymbol{K}_{ad} & \boldsymbol{K}_{aa} \end{bmatrix}^{-1} \begin{bmatrix} \boldsymbol{R}_d \\ \boldsymbol{R}_a \end{bmatrix} \tag{3.111}$$

until convergence is achieved. Here, the residuals follow by taking the first derivative of the potential (3.109)

$$\begin{aligned} \boldsymbol{R}_d &:= \mathop{\mathsf{A}}\limits_{e=1}^{E^h} \sum_{l=1}^{L} \{\, \textstyle\sum_{I=1}^{n} [\, p^e \boldsymbol{V}^{I\,T} + (e^h - \dfrac{p^h}{\kappa}) \boldsymbol{P}^{I\,T} + \bar{\boldsymbol{B}}^{I\,T} \bar{\boldsymbol{\mathfrak{S}}}\,\} J w_l \,] , \\ \boldsymbol{R}_a &:= \sum_{l=1}^{L} \{\, p^h \boldsymbol{V}^{B\,T} + \bar{\boldsymbol{B}}^{B\,T} \bar{\boldsymbol{\mathfrak{S}}}\,\} J w_l , \end{aligned} \tag{3.112}$$

governed by deviatoric generalized stress array $\bar{\boldsymbol{\mathfrak{S}}}$ defined in (3.41). The second derivatives of the potential (3.109) define the partitions of the coupled tangent matrix

$$\begin{aligned} \boldsymbol{K}_{dd} &:= \mathop{\mathsf{A}}\limits_{e=1}^{E^h} \sum_{l=1}^{L} \{\, \textstyle\sum_{I=1}^{n} \sum_{J=1}^{n} [\, \boldsymbol{V}^{I\,T} \boldsymbol{P}^J + \boldsymbol{P}^{I\,T} \boldsymbol{V}^J - \dfrac{1}{\kappa} \boldsymbol{P}^{I\,T} \boldsymbol{P}^J + \bar{\boldsymbol{B}}^{I\,T} \bar{\boldsymbol{\mathfrak{C}}} \bar{\boldsymbol{B}}^J \,\} J w_l , \\ \boldsymbol{K}_{da} &:= \mathop{\mathsf{A}}\limits_{e=1}^{E^h} \sum_{l=1}^{L} \{\, \textstyle\sum_{I=1}^{n} [\, \boldsymbol{P}^{I\,T} \boldsymbol{V}^B + \bar{\boldsymbol{B}}^{I\,T} \bar{\boldsymbol{\mathfrak{C}}} \bar{\boldsymbol{B}}^B \,]\,\} J w_l , \\ \boldsymbol{K}_{aa} &:= \sum_{l=1}^{L} \bar{\boldsymbol{B}}^{B\,T} \bar{\boldsymbol{\mathfrak{C}}} \bar{\boldsymbol{B}}^B \, J w_l , \end{aligned} \tag{3.113}$$

determined by the deviatoric generalized tangent array $\bar{\mathfrak{C}}$ defined in (3.44).

3.5.3. Condensation of bubble degrees at the element level. The degrees $\boldsymbol{a}^e$ of the bubble modes are discrete values associated with the elements $e = 1...E^h$. As a consequence, we can construct the condensed potential by optimization with respect to these discrete values via

$$\Pi^{*\tau\, h}_{red,ext,cond}(\boldsymbol{d}) = \inf_{\boldsymbol{a}} \Pi^{*\tau\, h}_{red,ext}(\boldsymbol{d}, \boldsymbol{a}) \ . \tag{3.114}$$

An appropriate solution strategy is the static condensation of the coupled algebraic system (3.111). To this end, the update of the bubble degrees is performed *locally at the element level* by

$$\boldsymbol{a}_e \Leftarrow \boldsymbol{a}_e + \Delta \boldsymbol{a}_e \quad \text{with} \quad \Delta \boldsymbol{a}_e = -\boldsymbol{K}^{e-1}_{aa} [\, \boldsymbol{R}^e_a + \boldsymbol{K}^e_{ad} \Delta \boldsymbol{d}_e \,] \ . \tag{3.115}$$

Then, assembling the global effective residual and tangent arrays via

$$\tilde{\boldsymbol{R}}_d := \mathop{\mathsf{A}}_{e=1}^{E^h} \{\, \boldsymbol{R}^e_d - \boldsymbol{K}^e_{da} \boldsymbol{K}^{e\,-1}_{aa} \boldsymbol{R}^e_a \,\} \quad \text{and} \quad \tilde{\boldsymbol{K}}_{dd} := \mathop{\mathsf{A}}_{e=1}^{E^h} \{\, \boldsymbol{K}^e_{dd} - \boldsymbol{K}^e_{da} \boldsymbol{K}^{e\,-1}_{aa} \boldsymbol{K}^e_{ad} \,\} \ , \tag{3.116}$$

the *global update of the nodal degrees* is performed by

$$\boldsymbol{d} \Leftarrow \boldsymbol{d} - \tilde{\boldsymbol{K}}^{-1}_{dd} \tilde{\boldsymbol{R}}_d \quad \text{until} \quad |\tilde{\boldsymbol{R}}_d| < tol \ . \tag{3.117}$$

3.5.4. Modified setting with elementwise constant driving forces. Alternatively to (3.104), we investigate a discretization of the extended variational functional (3.101) by the *linear* interpolations of $\boldsymbol{u}$, α, p, additional *bubble modes* for $\boldsymbol{u}$, α and elementwise *constant* driving force $\mathfrak{f}$

$$\{\boldsymbol{u}, \alpha, p\}^h = \textstyle\sum_{I=1}^n N^I \boldsymbol{d}_I + N^B \, \boldsymbol{1}^B \boldsymbol{a}^e \quad \text{and} \quad \{\, \mathfrak{f} \,\}^h = \mathfrak{f}^e \tag{3.118}$$

in $\mathcal{B}^e \subset \mathcal{B}^h$ with the nodal degrees $\boldsymbol{d}_I := [\boldsymbol{u}, \alpha, p]^T_I \in \mathcal{R}^4$. Here, $\boldsymbol{a}^e \in \mathcal{R}^3$ are the degrees of the bubble modes for $\boldsymbol{u}$, α and $\boldsymbol{1}^B$ an array that filters out the associated slots. Introducing the modified interpolations

$$p^h = \textstyle\sum_{I=1}^n \boldsymbol{P}^I \boldsymbol{d}_I \, , \quad e^h = \sum_{I=1}^n \boldsymbol{V}^I \boldsymbol{d}_I + \boldsymbol{V}^B \boldsymbol{a}^e \, , \quad \bar{\mathfrak{e}}^h = \sum_{I=1}^n \bar{\boldsymbol{B}}^I \, \boldsymbol{d}_I + \bar{\boldsymbol{B}}^B \, \boldsymbol{a}^e + \bar{\boldsymbol{G}} \, \mathfrak{f}^e \tag{3.119}$$

with the constant matrix

$$\bar{\boldsymbol{G}} = \begin{bmatrix} \cdot & \cdot & \cdot & \cdot & \cdot & \cdot & 1 \end{bmatrix}^T \tag{3.120}$$

and the pressure and dilatation interpolation matrices

$$\boldsymbol{P}^I = \begin{bmatrix} \cdot \\ \cdot \\ \cdot \\ N^I \end{bmatrix}^T , \quad \boldsymbol{V}^I = \begin{bmatrix} N^I_{,1} \\ N^I_{,2} \\ \cdot \\ \cdot \end{bmatrix}^T , \quad \boldsymbol{V}^B = \begin{bmatrix} N^B_{,1} \\ N^B_{,2} \\ \cdot \\ \cdot \end{bmatrix}^T \tag{3.121}$$

and the deviatoric interpolation matrices

$$\bar{\boldsymbol{B}}^I = \begin{bmatrix} \frac{2}{3} N^I_{,1} & -\frac{1}{3} N^I_{,1} & N^I_{,2} & \cdot & \cdot & \cdot & \cdot \\ -\frac{1}{3} N^I_{,2} & \frac{2}{3} N^I_{,2} & N^I_{,1} & \cdot & \cdot & \cdot & \cdot \\ \cdot & \cdot & \cdot & N^I & N^I_{,1} & N^I_{,2} & \cdot \\ \cdot & \cdot & \cdot & \cdot & \cdot & \cdot & \cdot \end{bmatrix}^T \tag{3.122}$$

and

$$\bar{\boldsymbol{B}}^B = \begin{bmatrix} \frac{2}{3}N^B_{,1} & -\frac{1}{3}N^B_{,1} & N^B_{,2} & \cdot & \cdot & \cdot & \cdot \\ -\frac{1}{3}N^B_{,2} & \frac{2}{3}N^B_{,2} & N^B_{,1} & \cdot & \cdot & \cdot & \cdot \\ \cdot & \cdot & \cdot & N^B & N^B_{,1} & N^B_{,2} & \cdot \\ \cdot & \cdot & \cdot & \cdot & \cdot & \cdot & \cdot \end{bmatrix}^T . \tag{3.123}$$

Focusing on pure Dirichlet problems with $P^\tau_{ext} = 0$, the spatial discretization of the potential (3.101) reads

$$\Pi^{*\tau\,h}_{red,ext}(\boldsymbol{d}, \boldsymbol{a}, \mathfrak{f}) = \mathop{\mathsf{A}}_{e=1}^{E^h} \sum_{l=1}^{L} \{ \, p^h e^h - \frac{1}{2\kappa} p^{h\,2} + \bar{\pi}^{*\tau}_{red}(\bar{\mathfrak{r}}^h) \, \} J w_l \tag{3.124}$$

in terms of the isochoric incremental potential density $\bar{\pi}^{*\tau}_{red}$ defined in (3.30). The discretized mixed variational principle then reads

$$\{\boldsymbol{d}, \boldsymbol{a}, \mathfrak{f}\} = \mathrm{Arg}\{ \operatorname*{stat}_{\boldsymbol{d},\boldsymbol{a}} \Pi^{*\tau\,h}_{red,ext}(\boldsymbol{d}, \boldsymbol{a}, \mathfrak{f}) \} \, . \tag{3.125}$$

The solution of this variational problem by a global Newton-type solver is based on incremental updates of the nodal degrees $\boldsymbol{d}$ and the bubble degrees $\boldsymbol{a}$

$$\begin{bmatrix} \boldsymbol{d} \\ \boldsymbol{a} \\ \mathfrak{f} \end{bmatrix} \Leftarrow \begin{bmatrix} \boldsymbol{d} \\ \boldsymbol{a} \\ \mathfrak{f} \end{bmatrix} - \begin{bmatrix} \boldsymbol{K}_{dd} & \boldsymbol{K}_{da} & \boldsymbol{K}_{d\mathfrak{f}} \\ \boldsymbol{K}_{ad} & \boldsymbol{K}_{aa} & \boldsymbol{K}_{a\mathfrak{f}} \\ \boldsymbol{K}_{\mathfrak{f}d} & \boldsymbol{K}_{\mathfrak{f}a} & \boldsymbol{K}_{\mathfrak{f}\mathfrak{f}} \end{bmatrix}^{-1} \begin{bmatrix} \boldsymbol{R}_d \\ \boldsymbol{R}_a \\ \boldsymbol{R}_\mathfrak{f} \end{bmatrix} \tag{3.126}$$

until convergence is achieved. Here, the residual associated with the elementwise constant driving force is

$$\boldsymbol{R}_\mathfrak{f} := \sum_{l=1}^{L} \{ \, \bar{\boldsymbol{G}}^T \bar{\mathfrak{S}} \, \} J w_l \, , \tag{3.127}$$

governed by deviatoric generalized stress array $\bar{\mathfrak{S}}$ defined in (3.41). The second derivatives of the potential (3.124) related to the elementwise constant driving force are

$$\begin{aligned} \boldsymbol{K}_{d\mathfrak{f}} \; &:= \mathop{\mathsf{A}}_{e=1}^{E^h} \sum_{l=1}^{L} \{ \, \textstyle\sum_{I=1}^{n} [\, \bar{\boldsymbol{B}}^{I\,T} \bar{\mathfrak{C}} \bar{\boldsymbol{G}} \,] \, \} J w_l \, , \\ \boldsymbol{K}_{a\mathfrak{f}} \; &:= \sum_{l=1}^{L} \{ \, \bar{\boldsymbol{B}}^{B\,T} \bar{\mathfrak{C}} \bar{\boldsymbol{G}} \, \} J w_l \, , \\ \boldsymbol{K}_{\mathfrak{f}\mathfrak{f}} \; &:= \sum_{l=1}^{L} \{ \, \bar{\boldsymbol{G}}^T \bar{\mathfrak{C}} \bar{\boldsymbol{G}} \, \} J w_l \, , \end{aligned} \tag{3.128}$$

determined by the deviatoric generalized tangent array $\bar{\mathfrak{C}}$ defined in (3.44). The other arrays in (3.126) are identical in structure with those defined in (3.112) and (3.113), however, evaluated with the modified matrices defined in (3.121), (3.122) and (3.123). Again, the degrees $\boldsymbol{a}^e$ of the bubble modes can be condensed at the element level, by defining the condensed potential by optimization with respect to these discrete values via

$$\Pi^{*\tau\,h}_{red,ext,cond}(\boldsymbol{d}, \mathfrak{f}) = \inf_{\boldsymbol{a}} \Pi^{*\tau\,h}_{red,ext}(\boldsymbol{d}, \boldsymbol{a}, \mathfrak{f}) \, . \tag{3.129}$$

Table 3.1: Material parameters used for the numerical examples.

No.	Parameter	Name	Value	Unit
1.	κ	bulk modulus	164.2	$\mathrm{kN/mm^2}$
2.	μ	shear modulus	80.2	$\mathrm{kN/mm^2}$
3.	h	hardening parameter	$\pm\,0.13$	$\mathrm{kN/mm^2}$
4.	l_p	length-scale parameter	0.1	mm
5.	y_0	yield stress	0.45	$\mathrm{kN/mm^2}$
6.	η_p	viscosity	10^{-7}	$\mathrm{kNs/mm^2}$

The solution step results in the update procedure are in full analogy to (3.115) and the reduced global residual and tangent arrays are in analogy to (3.116), such that we obtain the reduced global system

$$\begin{bmatrix} \boldsymbol{d} \\ \mathfrak{f} \end{bmatrix} \Leftarrow \begin{bmatrix} \boldsymbol{d} \\ \mathfrak{f} \end{bmatrix} - \begin{bmatrix} \tilde{\boldsymbol{K}}_{dd} & \tilde{\boldsymbol{K}}_{d\mathfrak{f}} \\ \tilde{\boldsymbol{K}}_{\mathfrak{f}d} & \tilde{\boldsymbol{K}}_{\mathfrak{f}\mathfrak{f}} \end{bmatrix}^{-1} \begin{bmatrix} \tilde{\boldsymbol{R}}_{d} \\ \tilde{\boldsymbol{R}}_{\mathfrak{f}} \end{bmatrix} \tag{3.130}$$

The condensation of the elementwise constant driving forces $\{\,\mathfrak{f}^e\,\}$ is not possible, because they are not defined by the plastic return mapping.

3.6. Representative Numerical Examples

We now demonstrate the performance of the proposed extended finite element designs of gradient plasticity for the Q1P0-type and Mini-type elements outlined in Section 3.4 and Section 3.5 by means of representative numerical examples. The first part of this section is concerned with the simulation of the benchmark problems in the one-dimensional case as discussed in Section 3.3. Results obtained with the proposed multi-dimensional element families are compared with observations made for the 1D elements. In the second part, we investigate a 3D-dimensional boundary value problem for hardening plasticity. The material parameters used in the examples are given in Table 3.1.

3.6.1. Plane Shear Test for Softening Plasticity. The first example documents the numerical results for a strip under shear deformation for the case of softening plasticity, and compares them with the analytical results outlined in Section 3.3.3. As we are dealing with softening plasticity here, the hardening variable is set to $h = -S = -0.13$ kN/mm^2. The (half) length of the strip is set to $L = 50$ mm and we apply a deformation rate of $2\dot{\bar{u}} = 50$ mm/s at each end of the strip. We report different diagrams of the distributions

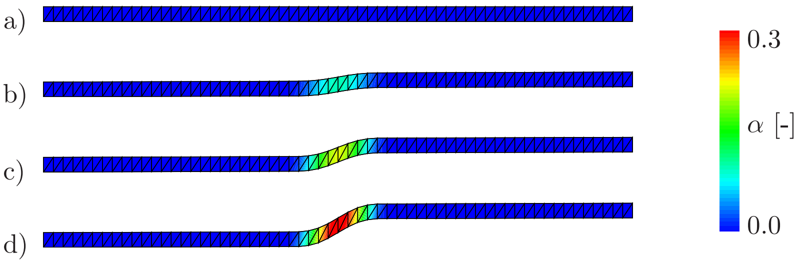

Figure 3.9: Softening Plasticity: Contour plots of the hardening variable α for a length scale of $l_e = 0.1$ mm and for the Mini-Q1Q1 element at different deformation states of shear. a) $2\bar{u} = 0.00$ mm, b) $2\bar{u} = 1.67$ mm, c) $2\bar{u} = 3.33$ mm, d) $2\bar{u} = 5.00$ mm.

of the equivalent plastic strain α and its dual driving force $\mathfrak{f}$, which demonstrate the performance of the different finite element formulations. To this end, we present all the results at time $t = 0.05$ s, i.e. a deformation of $2\bar{u} = 5.0$ mm. The inhomogeneous plastic zone develops as a consequence of an initial imperfection of the yield strength y_0 at the center $x = 0$ of the strip by 3 %. In the numerical simulation the time step is chosen to be $\Delta t = 10^{-4}$ s such that the outlined results are reached in 500 time steps.

Figure 3.9 shows a contour plot for the equivalent plastic strain α obtained with 60 Mini-Q1Q1 elements and for a sequence of different deformation states up to the final value $2\bar{u} = 5.0$ mm. In the Figures 3.10–3.12 the numerical results obtained for the different Mini-type finite element designs are compared with the analytical solution. In the subsequent simulations the length scale parameter is chosen to be $l_p = 0.1$ mm. It is the same length scale parameter as in the one-dimensional study outlined in Section 3.3.3. Figure 3.10 shows results for the equivalent plastic strain α and its dual driving force $\mathfrak{f}$ for the alternative Mini-type elements. Here, the nodal values of α and $\mathfrak{f}$ are plotted without the postprocessing corrector step. We observe the same difficulties which were discussed in the one-dimensional study in Section 3.3.3: Small negative equivalent plastic strain α near the elastic-plastic boundary (EPB) as well as oscillations in the driving force $\mathfrak{f}$ near the jump at the EPB and in the elastic zone. Furthermore, in the Mini-Q1Q1 element minor oscillations in the driving force $\mathfrak{f}$ inside the plastic zone are detected. Note that,

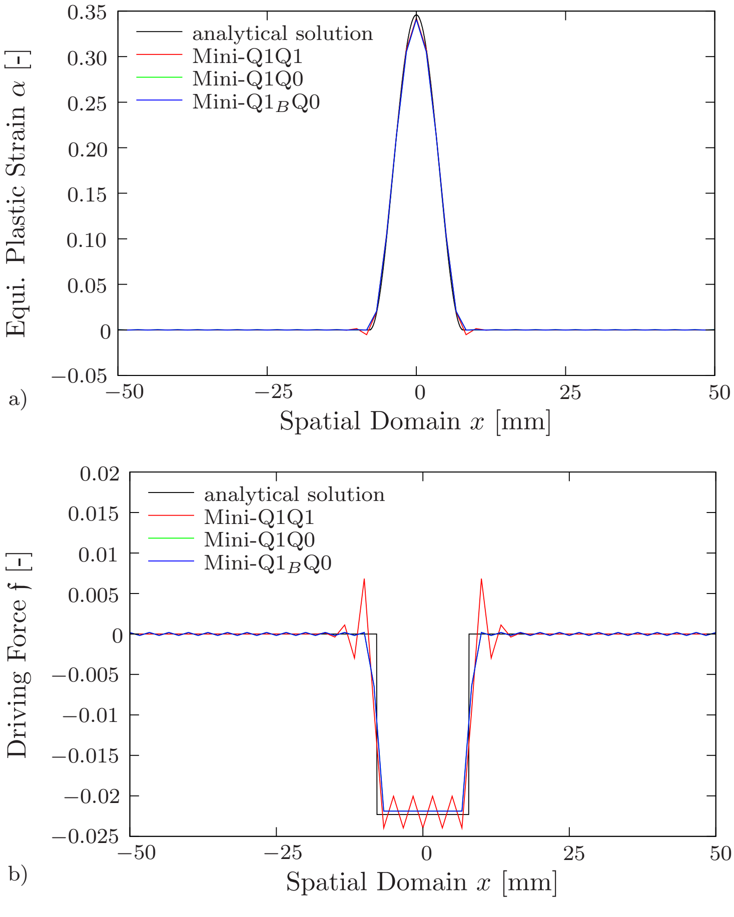

Figure 3.10: Softening Plasticity: Numerical solution with nodal plots for alternative Mini-Type Elements and for a mesh with 60 elements. a) hardening variable α, b) driving force $\mathfrak{f}$.

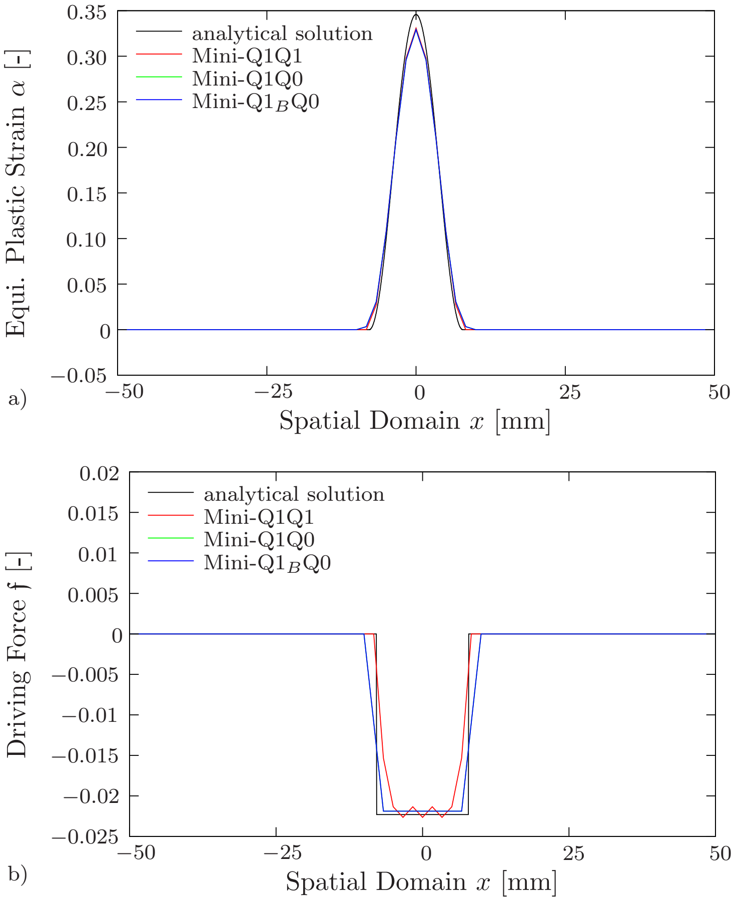

Figure 3.11: Softening Plasticity: Numerical solution with plot at active integration points for alternative Mini-Type Elements and for a mesh with 60 elements. a) hardening variable α, b) driving force $\mathfrak{f}$.

except of the small negative values of the equivalent plastic strain α and the oscillations in the driving force $\mathfrak{f}$, the numerical results fit the analytical solution quite well even for this coarse mesh size. Figure 3.11 depicts the numerical results obtained with the postprocessing corrector step (3.70). Similar to the one-dimensional study, values of α are positive in the whole strip and values of the dual driving force $\mathfrak{f}$ are negative in the whole strip. Hence, we notice that the basic constraints (3.66) are satisfied at all active integration points $g \in \mathcal{A}(t)$ for all three Mini-type finite element formulations. Thus all three proposed Mini-type elements yield consistent and stable solutions. In Figure 3.12 results for the Mini-Q1Q1 element with different mesh sizes are plotted. As mentioned already for the 1D element, this type of elements provides the simplest and most straightforward FE implementation because all the degrees of freedom are related to the nodal points of the element. Again, the responses of α and $\mathfrak{f}$ are plotted with the postprocessing corrector. By decreasing the mesh size we approach to the analytical solution for both the equivalent plastic strain α in Figure 3.12a and the driving force $\mathfrak{f}$ in Figure 3.12b. Furthermore, note that the small oscillations in $\mathfrak{f}$ inside the plastic zone decrease if more elements are used for the simulations. The influence of the size effect governed by the intrinsic material length scale parameter l_p is illustrated in Figures 3.13 and 3.14. Here, we observe in Figure 3.13a and Figure 3.14a that the plastic zone is localized in the weakened element for standard local plasticity with $l_p = 0$. Furthermore, as obtained from the analytical solution in Section 3.3.3, the width of the plastic zone

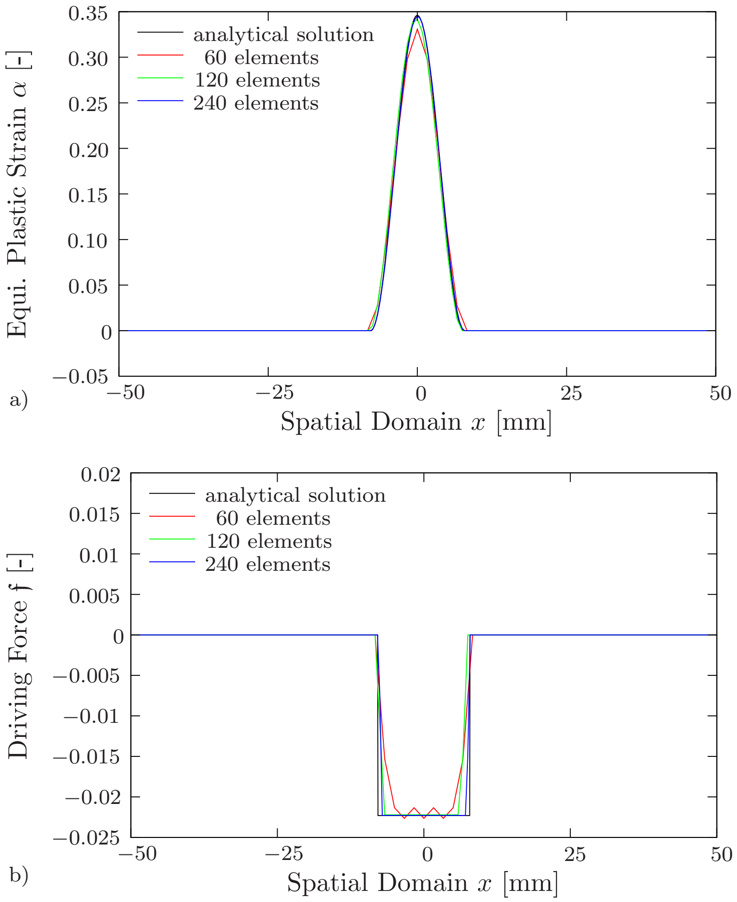

Figure 3.12: Softening Plasticity: Numerical solution with plot at active integration points for the Mini-Q1Q1 element with different mesh sizes. a) hardening variable α, b) driving force $\mathfrak{f}$.

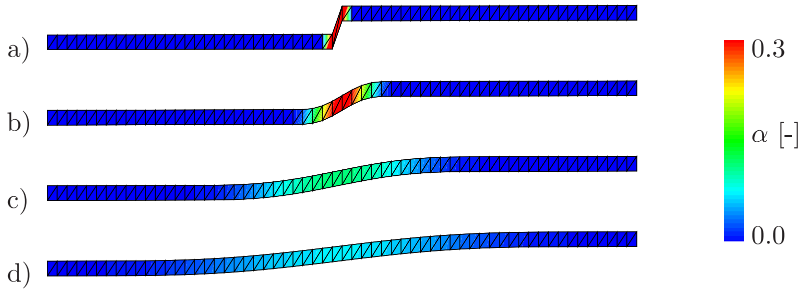

Figure 3.13: Softening Plasticity: Contour plots of the hardening variable α for Mini-Q1Q1 element for different length scales. a) local analysis ($l_p = 0$), b) $l_p = 0.1$ mm, c) $l_p = 0.3$ mm, d) $l_p = 0.5$ mm.

$2x_0$ spreads out for increasing length scale l_p and the maximum value $2\alpha_S$ decreases for increasing the length scale l_p.

Results for the Q1P0-type element family are not presented for this softening plasticity example. However, they are for this 1D example in qualitative agreement with the alternative Mini-type finite element formulations and the family of 1D elements: We detect negative equivalent plastic strain α near the EPB, when the postprocessing corrector is not applied. We also observe oscillations in the driving force $\mathfrak{f}$.

Comparing the performance of the multi-dimensional element families with the one-

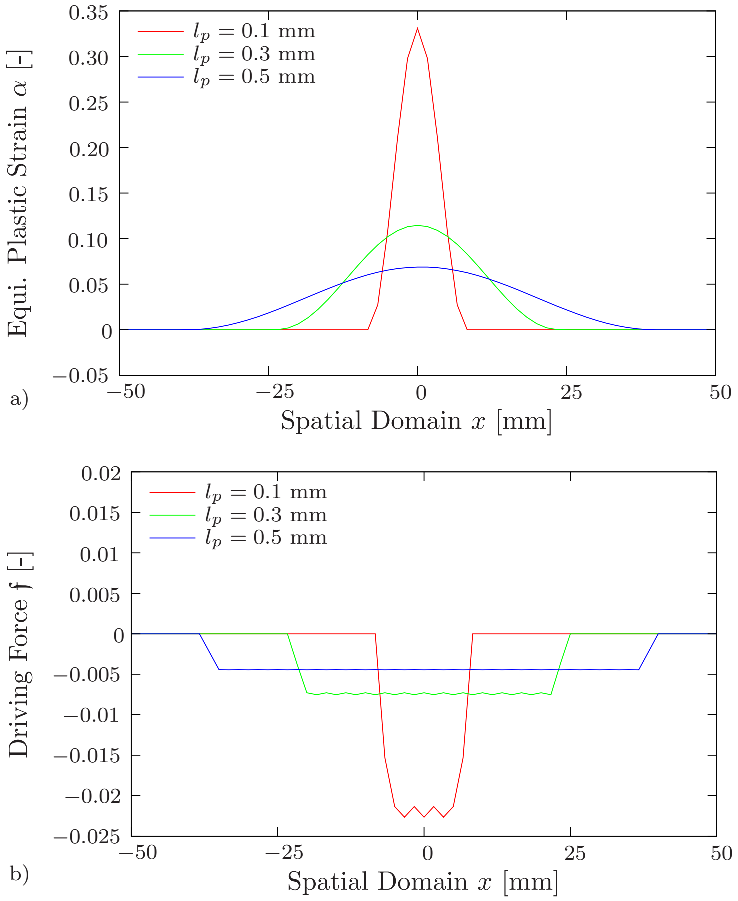

Figure 3.14: Softening Plasticity: Numerical solution with plot at active integration points for the Mini-Q1Q1 element with different length scales l_p. a) hardening variable α, b) driving force $\mathfrak{f}$.

dimensional study, we observe the same properties for the associated FE designs. The best results are obtained for the elements with quadratic bubble mode for the equivalent plastic strain α and elementwise constant driving force $\mathfrak{f}$, i.e. Q1P0-Q1$_B$Q0 and Mini-Q1$_B$Q0. However the elements with linear interpolation for all the global degrees of freedom, Q1P0-Q1Q1 and Mini-Q1Q1, yield reasonable results even for coarse meshes. The basic constraints (3.66) are fulfilled in the whole domain $\mathcal{B}$ for all types of elements. However, with regard to a convenient numerical implementation, we favorite the straightforward use of elements with nodal degrees for all global field variables.

3.6.2. Plane shear test for micro-clamped hardening plasticity. Next, consider the one-dimensional shear test of a strip for micro-clamped hardening plasticity. The analytical solution for this example is given in Section 3.3.2. As in the previous subsection for the softening plasticity example, we focus on the comparison of the spatial distributions of the equivalent plastic strain α and its dual driving force $\mathfrak{f}$ for the alternative FE designs. The hardening variable is set to $h = H = 0.13$ kN/mm^2. The (half) length of the strip is set to $L = 50$ mm and we perform a deformation rate of $2\dot{\bar{u}} = 50$ mm/s at each end of the strip. The strip is micro-clamped at the edges, i.e. $\alpha = 0$ at $x = \pm L$. As before, we present all results at time $t = 0.05$ s, i.e. for a deformation of $2\bar{u} = 5.0$ mm. In the numerical simulation the time step is chosen to be $\Delta t = 10^{-4}$ s such that the solution is reached in 500 time steps.

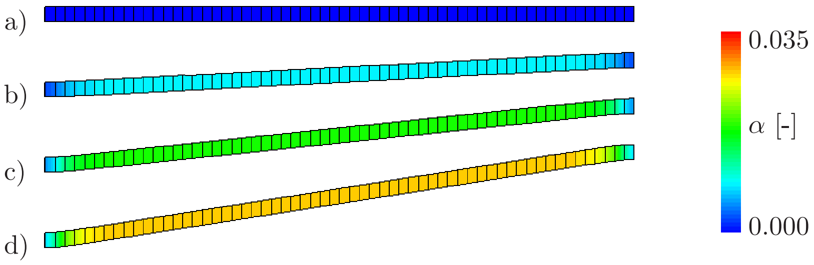

Figure 3.15: Hardening Plasticity: Contour plots of the hardening variable α for a length scale of $l_e = 0.1$ mm and for the Q1P0-Q1Q1 element at different deformation states. a) $2\bar{u} = 0.00$ mm, b) $2\bar{u} = 1.67$ mm, c) $2\bar{u} = 3.33$ mm, d) $2\bar{u} = 5.00$ mm.

Figure 3.15 shows a contour plot for the equivalent plastic strain α obtained with 60 elements by using the Q1P0-Q1Q1 element design and for a series of different deformation states up to the final $2\bar{u} = 5.0$ mm. Figure 3.16 compares the results obtained for the different finite element designs with the analytical solution. The length scale parameter is chosen to be $l_p = 0.1$ mm. The results reported are obtained with the postprocessing corrector. However, as the whole strip is plastified in this hardening example, the set

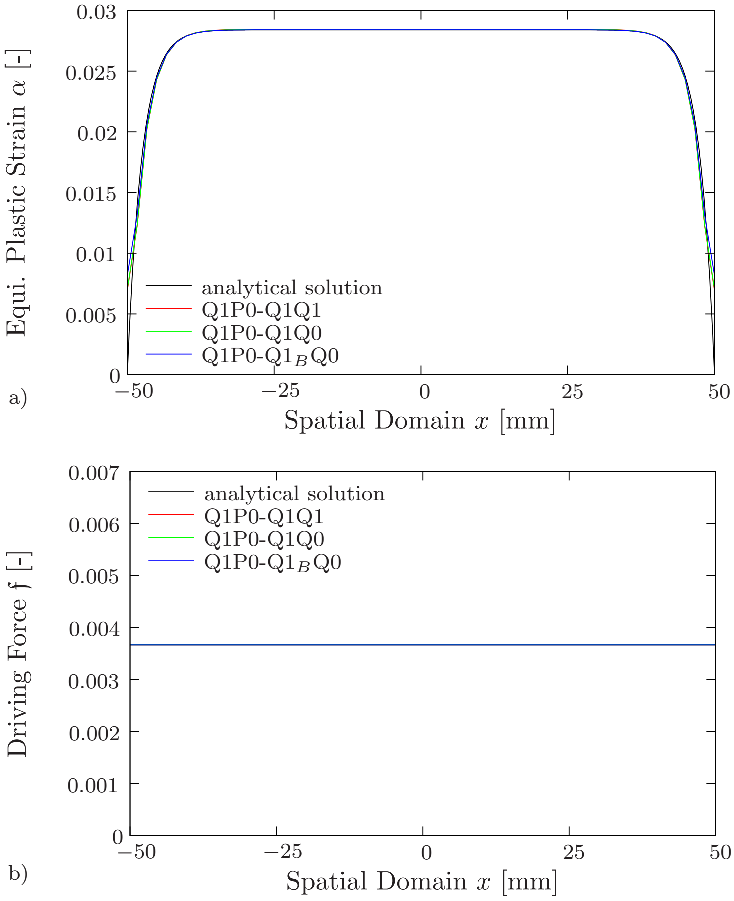

Figure 3.16: Hardening Plasticity: Numerical solution with plot at active integration points for alternative Q1P0-Type Elements and for a mesh with 60 elements. a) hardening variable α, b) driving force $\mathfrak{f}$.

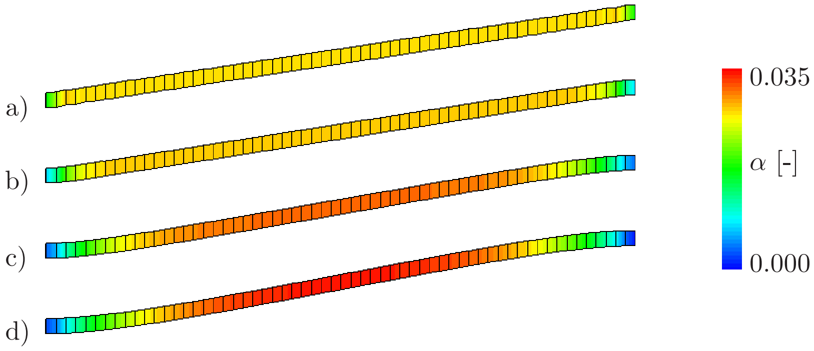

Figure 3.17: Hardening Plasticity: Contour plots of the hardening variable α for Q1P0-Q1Q1 element for different length scales. a) local analysis ($l_p = 0$), b) $l_p = 0.1$ mm, c) $l_p = 0.3$ mm, d) $l_p = 0.5$ mm.

of active integration,points is equal to the whole set of integration points in the mesh. Hence, the plots are the same except of difference due to the smoothing procedure. In Figure 3.16 numerical results are plotted for the three Q1P0-type elements. The (coarse) mesh consists of 60 elements. We observe good agreement with the analytical solution for both the equivalent plastic strain α as well as the driving force $\mathfrak{f}$ for all the FE designs. Small oscillations for $\mathfrak{f}$ can be detected for the Q1P0-Q1Q1 element but they are in the

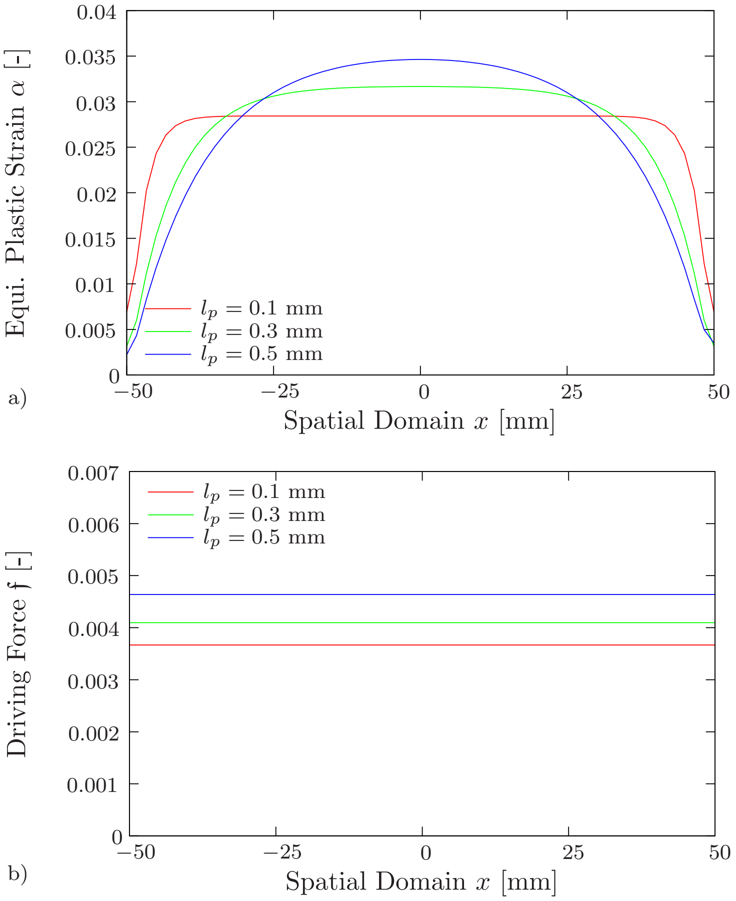

Figure 3.18: Hardening Plasticity: Numerical solution with plot at active integration points for Q1P0-Q1Q1 element and three different length scales l_p. a) hardening variable α, b) driving force $\mathfrak{f}$.

range of $\Delta\mathfrak{f} \approx 10^{-8}$ and are hence of minor influence.

The influence of the size effect governed by the length scale parameter l_p is illustrated in Figures 3.17 and 3.18. Here, Figure 3.17a demonstrate the result for a local analysis with $l_p = 0$. The equivalent plastic strain α decreases from the constant value in the spatial domain to zero within the two elements at the boundaries, where micro-clamped conditions $\alpha = 0$ are applied. In the rest of the strip the equivalent plastic strain α is constant, reflecting the homogeneous plastic deformations of a local theory. Hence, we detect in this area a linear macro-deformation state u, related to the local plasticity analysis. In contrast to the previous subsection, the whole strip is plastified. The length scale l_p has an effect on the width of the inhomogeneous boundary layer zone, i.e. between the micro-clamped boundary with $\alpha = 0$ and the interior of the strip with constant equivalent plastic strain $\alpha = \text{const.}$ Figure 3.17 shows that the macro-deformation u transforms into a s-shape deformation with increasing length scale l_p. The deformation state in Figure 3.17 is scaled by a factor 3.

The numerical results for the three Mini-type element designs are not shown here. But again, the observations are qualitatively similar to those of the Q1P0-type elements. The oscillations in the driving force $\mathfrak{f}$ observed with the Mini-Q1Q1 element are bigger than those obtained with the Q1P0-Q1Q1, and we also observe a deviation from the analytical solution of $\mathfrak{f}$ at the micro-clamped boundaries $x = \pm L$. The reason might be a violation of the stability condition (3.73) for the Dirichlet-type micro-clamped conditions for α considered here. However, the oscillations in the driving force decrease for decreasing mesh size.

3.6.3. 3D shear test of composite RVE for hardening plasticity. As a multi-dimensional BVP, we consider the shear test of a three-dimensional cubic representative volume element (RVE), made up of a composite material. It consists of elastic reinforcements in an elastic-plastic matrix. A similar boundary value problem was introduced by Cleveringa et al. [36] in the context of dislocation-based plasticity, but is widely used in literature also for demonstrating characteristic features of gradient plasticity. The geometric setup and the boundary conditions are illustrated in Figure 3.19. Here, the

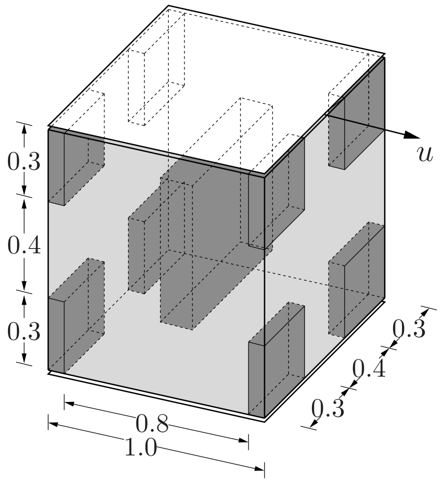

Figure 3.19: Shear test of a composite material. Geometry and boundary conditions. The light shaded areas characterize the matrix material and the dark shaded areas depict the stiff inclusions.

light shaded areas characterize the elastic-plastic matrix material and the dark shaded areas depict the elastic inclusions. The periodicity of the unit cell is taken into account by setting proper boundary and linking conditions: at the lower surface the horizontal and vertical displacements are constrained. At the upper surface the horizontal displacement is prescribed and the vertical displacement is set to zero. The horizontal and vertical displacement of the remaining vertical surfaces are linked. The periodicity of the equivalent plastic strain α and the dual driving forces $\mathfrak{f}$ is realized by linking the discrete variables on all associated parts of the surface. The bulk modulus of the elasto-plastic matrix is chosen to $\kappa = 74.51$ kN/mm^2, the shear modulus is set to $\mu = 28.57$ kN/mm^2, the isotropic hardening modulus to $h = 0.70$ kN/mm^2, the yield strength to $y_0 = 0.208$ kN/mm^2 and the viscosity is chosen to $\eta_p = 10^{-7}$ kN s/mm^2. The bulk modulus of the elastic particles is chosen to be $\kappa = 215.66$ kN/mm^2 and the shear modulus is set to $\mu = 182.48$ kN/mm^2. This set of material parameters is representative for an aluminum matrix with silicon-carbide particles. We perform 2000 time steps using a time step of $\Delta t = 10^{-4}$ s. Hence a maximum deformation of $\bar{u} = 0.2$ mm is applied. The specimen is discretized by $40 \times 40 \times 40$ Q1P0-Q1Q1 finite elements. Figure 3.20 depicts the distribution of the equivalent plastic strain α and the driving force $\mathfrak{f}$ for two different length scales l_p. We observe a concentration of equivalent plastic strain α around the stiff elastic particles. By increasing the length scale, the equivalent plastic strains α spreads over a larger re-

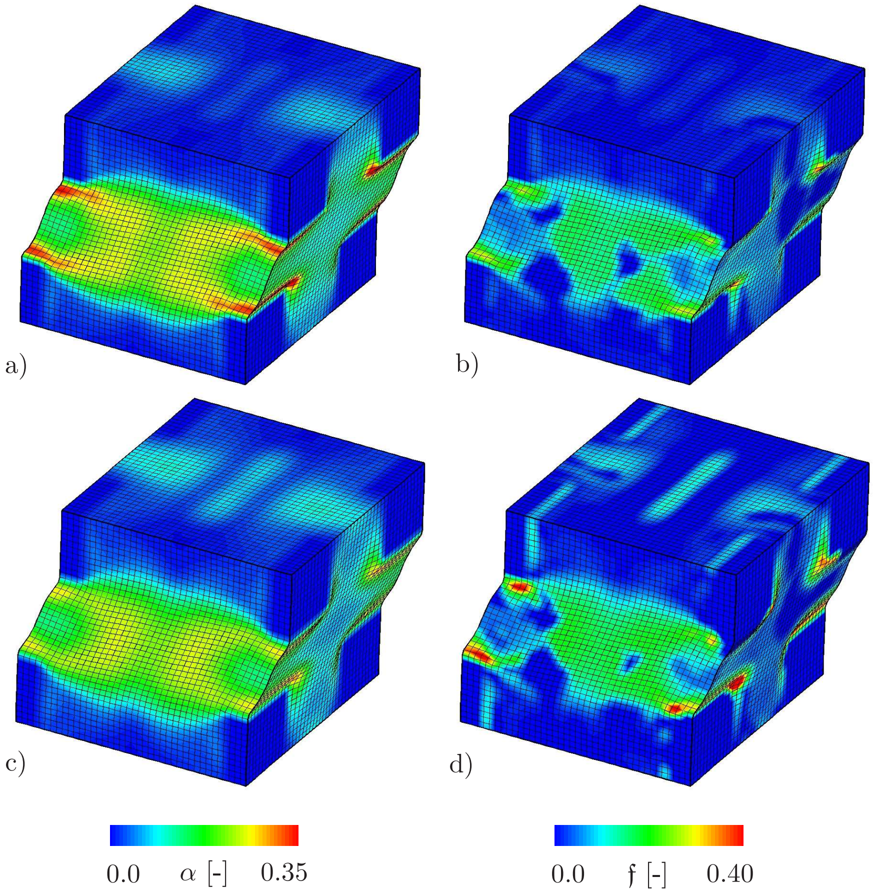

Figure 3.20: Shear test of a composite material. Distribution of equivalent plastic strain α and the dual driving force $\mathfrak{f}$ for a)-b) a length scale parameter $l_p = 0.002$ mm, and for c)-d) a length scale parameter $l_p = 0.006$ mm.

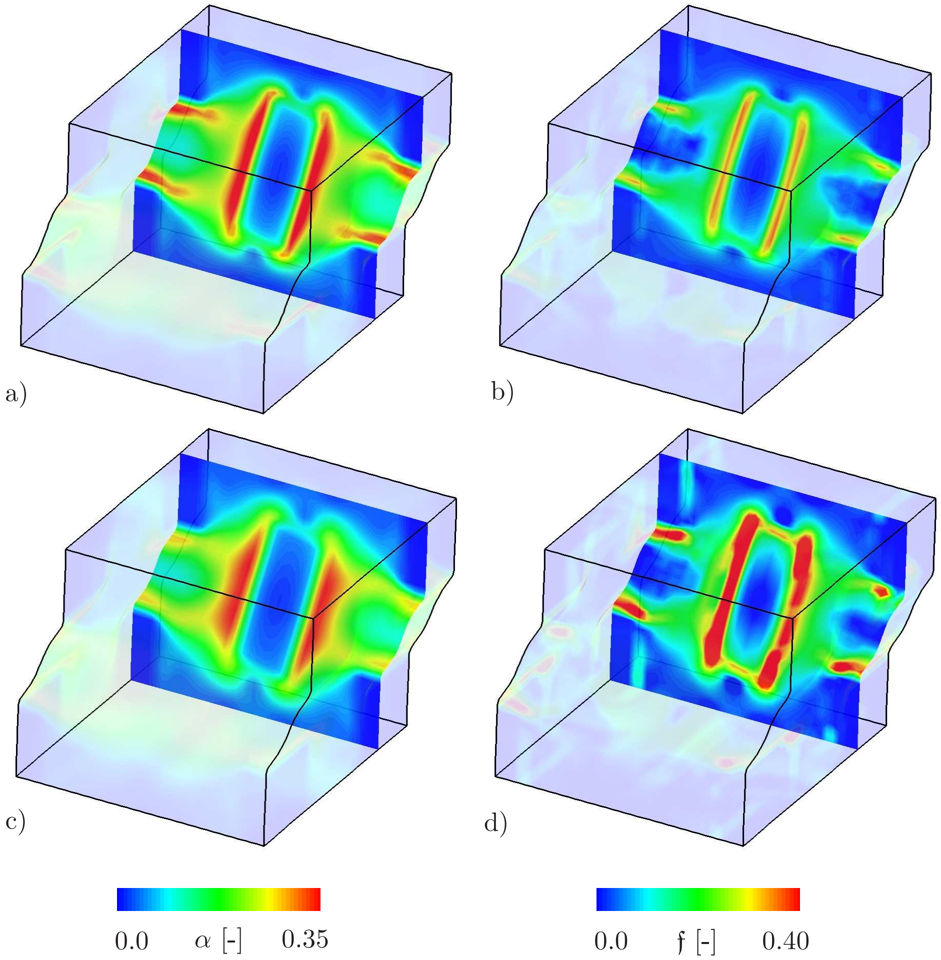

Figure 3.21: Shear test of a composite material. Distribution of equivalent plastic strain α and the dual driving force $\mathfrak{f}$ inside the specimen at position $x = 0.2$ mm for a)-b) a length scale parameter $l_p = 0.002$ mm, and for c)-d) a length scale parameter $l_p = 0.006$ mm.

gion and their maximum values decrease. The maximum values for the driving force $\mathfrak{f}$ are increasing for increasing length scale l_p. Small oscillations as well as slight negative values in the distribution of the driving force $\mathfrak{f}$ still appear, as discussed in the previous examples. For further demonstration of the influence of the size effect, consider the distribution of the equivalent plastic strain α and the driving force $\mathfrak{f}$ in a slice inside the specimen. The results are shown in Figure 3.21. Here we observe that for the smaller length scale parameter $l_p = 0.002$ mm, the equivalent plastic strain α is more localized around the elastic stiff particles with higher maximum value. By increasing the length scale, α is spread out more, however the maximum value is decreasing. The maximum value for the dual driving force $\mathfrak{f}$ gets higher by increasing the length scale l_p.

4. Coupled Thermo-Gradient-Plasticity at Small Strain

The aim of this chapter is to present a thermo-mechanical model for gradient-extended dissipative solids at small strains. In the mechanical part, we consider von-Mises plasticity with gradient-extended hardening/softening material response as discussed in Chapter 3. In the thermal part, we follow the investigations of Simo & Miehe [140] and Wriggers et al. [155] that demonstrate the effect of temperature on the mechanical field resulting in a thermal expansion. To this end, we formulate a free energy storage function based on the coupled problem. From the computational viewpoint, two classes of solution schemes for the coupled problem are considered: (i) *Global product formula algorithm* arising from operator split which leads to a two step solution procedure, and (ii) an *implicit coupled algorithm* which employs simultaneous solution of the coupled system of equations. In the product formula algorithm, the mechanical and thermal problems are solved separately. The idea here is to decompose the coupled field equations of thermo-gradient-plasticity into an elasto-plastic problem with frozen temperature ($\dot{\theta} = 0$), see Chapter 3, followed by a heat conduction problem at fixed updated mechanical configuration. These two sub-problems are then coupled via the plastic structural heating and the mechanical dissipation. Due to the two steps solution procedure, we end up with a *symmetric structure* for each sub-problem. Alternatively, in the implicit coupled algorithm, there is no separation between the mechanical and thermal parts. The temperature field is no longer kept constant in the mechanical step i.e. $\dot{\theta} \neq 0$. All the components of the problem are computed simultaneously using the same time-stepping scheme. The main aspect to be noted here is that the performance of the scheme depends on exact expressions of moduli. This approach has proven to be *computationally more intensive* than the product formula algorithm and leads to a *non-symmetric structure* of the problem as discussed in Simo & Miehe [140] and Wriggers et al. [155]. The performance of the formulation is demonstrated by means of some representative examples.

4.1. Constitutive functions of the coupled problem

4.1.1. Energetic response function. In addition to the primary fields introduced in (3.4), we extend these variables to include the absolute temperature field $\theta > 0$. The constitutive state variables of the coupled thermo-gradient-plasticity model are defined as

$$\text{Constitutive State: } \mathfrak{c} := \{\boldsymbol{\varepsilon}, \boldsymbol{\varepsilon}^p, \alpha, \nabla\alpha, \theta\} \ . \tag{4.1}$$

With this set of variables, we can write the free energy function as $\psi := \hat{\psi}(\mathfrak{c})$ defined per unit volume. This can be split into an *elastic part* $\hat{\psi}^e$ that accounts for the elastic stored energy, a *plastic part* $\hat{\psi}^p$ that considers the plastic contribution of the hardening mechanism along with non local terms accounting for size effects as explained in Chapter 3, a *thermoelastic part* $\hat{\psi}^{th-e}$ that accounts for the thermal expansion and finally a purely *thermal part* $\hat{\psi}^{th}$. This leads to the following form

$$\hat{\psi}(\mathfrak{c}) = \hat{\psi}^e(\boldsymbol{\varepsilon}^e) + \hat{\psi}^p(\alpha, \nabla\alpha, \theta) + \hat{\psi}^{th-e}(\boldsymbol{\varepsilon}^e, \theta) + \hat{\psi}^{th}(\theta) \ . \tag{4.2}$$

Elastic contribution. The isotropic elastic contribution is assumed to be a quadratic function and is decomposed into volumetric and isochoric parts as

$$\hat{\psi}^e(\boldsymbol{\varepsilon}^e) := \hat{\psi}^e_{vol}(e) + \hat{\psi}^e_{iso}(\bar{\boldsymbol{\varepsilon}}^e) \quad \text{with} \quad \hat{\psi}^e_{vol}(e) = \frac{\kappa}{2}e^2 \quad \text{and} \quad \hat{\psi}^e_{iso}(\bar{\boldsymbol{\varepsilon}}^e) = \mu\bar{\boldsymbol{\varepsilon}}^e : \bar{\boldsymbol{\varepsilon}}^e \tag{4.3}$$

with κ, μ being the bulk and shear moduli, respectively. $e = \mathrm{tr}[\boldsymbol{\varepsilon}^e]$ is the volumetric part and $\bar{\boldsymbol{\varepsilon}}^e = \mathrm{dev}[\boldsymbol{\varepsilon}^e] = \boldsymbol{\varepsilon}^e - \frac{1}{3}\, e\boldsymbol{1}$ is the isochoric part of the elastic strain tensor.

Plastic contribution. The plastic part of the energy function is assumed to be quadratic, consisting of the local and gradient parts

$$\hat{\psi}^p(\alpha, \nabla\alpha, \theta) := \frac{h(\theta)}{2}\alpha^2 + \frac{\mu l_p^2}{2}\,|\nabla\alpha|^2 \tag{4.4}$$

where $h(\theta) = h_0\big[1 - w_h(\theta - \theta_0)\big]$ describes temperature-dependent isotropic hardening/softening mechanism with w_h being a hardening/softening parameter and l_p is the plastic length scale parameter.

Thermoelastic contribution. The coupled thermoelastic part of the free energy is linear and has the simple form

$$\hat{\psi}^{th-e}(e, \theta) := -\kappa\alpha_t e(\theta - \theta_0) \ , \tag{4.5}$$

where α_t is the thermal expansion coefficient and θ_0 is the reference temperature.

Thermal contribution. The purely thermal part is defined as

$$\hat{\psi}^{th}(\theta) := c\Big[(\theta - \theta_0) - \theta\ln[\theta/\theta_0]\Big] \ , \tag{4.6}$$

where c is the heat capacity coefficient. From the structure of the free energy function (4.2), it is evident that in an iso-thermal plasticity process in which $\theta = \theta_0$, we arrive at a purely mechanical problem with $\hat{\psi}(\mathfrak{c}) := \hat{\psi}^e(e, \bar{\boldsymbol{\varepsilon}}) + \hat{\psi}^p(\alpha, \nabla\alpha)$.

4.1.2. Dissipative response function. As discussed in Section 3.1.2, the dissipative force fields are: $\bar{\boldsymbol{\mathfrak{s}}}$ and $\mathfrak{f}$ dual to $\boldsymbol{\varepsilon}^p$ and α, respectively. The yield function for our model based on the driving forces and the temperature field θ is

$$\chi(\bar{\boldsymbol{\mathfrak{s}}}, \mathfrak{f}, \theta) := |\bar{\boldsymbol{\mathfrak{s}}}| - \sqrt{\tfrac{2}{3}}\,\big[y(\theta) + \mathfrak{f}\big] \tag{4.7}$$

where $y(\theta) := y_0\big[1 - w_0(\theta - \theta_0)\big]$ is the temperature dependent yield strength with w_0 being a thermal softening parameter. With the yield function at hand, one can define the dual dissipation function for gradient-type thermal viscoplasticity according to Perzyna–type viscoplasticity model as

$$\phi^*(\bar{\boldsymbol{\mathfrak{s}}}, \mathfrak{f}, \theta) := \frac{1}{2\eta_p}\Big\langle |\bar{\boldsymbol{\mathfrak{s}}}| - \sqrt{\tfrac{2}{3}}\,\big[y(\theta) + \mathfrak{f}\big]\Big\rangle^2 \tag{4.8}$$

with η_p being the viscosity parameter that accounts for rate dependency.

4.1.3. Thermodynamic restrictions. For the specific choice of the free energy (4.2), we can evaluate thermodynamic restriction as

$$\mathcal{D}_{loc} := \boldsymbol{\sigma} : \dot{\boldsymbol{\varepsilon}} - \dot{\psi} - \eta\dot{\theta} \geq 0 \ , \tag{4.9}$$

defined per unit volume. Here, $\boldsymbol{\sigma}$ is the stress tensor and η is the entropy per unit volume. The evolution of the free energy function is given by

$$\frac{d}{dt}\hat{\psi}(\mathfrak{c}) = \partial_{\boldsymbol{\varepsilon}}\hat{\psi} : \dot{\boldsymbol{\varepsilon}} + \partial_{\boldsymbol{\varepsilon}^p}\hat{\psi} : \dot{\boldsymbol{\varepsilon}}^p + \partial_\alpha\hat{\psi}\ \dot{\alpha} + \partial_{\nabla\alpha}\hat{\psi}\cdot\nabla\dot{\alpha} + \partial_\theta\hat{\psi}\cdot\dot{\theta} \tag{4.10}$$

Insertion of (4.10) into (4.9), yields

$$\mathcal{D}_{loc} := (\boldsymbol{\sigma} - \partial_{\boldsymbol{\varepsilon}}\hat{\psi}) : \dot{\boldsymbol{\varepsilon}} - (\eta + \partial_\theta \hat{\psi})\,\dot{\theta} - \partial_{\boldsymbol{\varepsilon}^p}\hat{\psi} : \dot{\boldsymbol{\varepsilon}}^p - \partial_\alpha \hat{\psi}\,\dot{\alpha} - \partial_{\nabla\alpha}\hat{\psi}\cdot\nabla\dot{\alpha} \geq 0 \;, \tag{4.11}$$

and applying Coleman's exploitation method gives the two constitutive equations for the stresses $\boldsymbol{\sigma}$ and the entropy η, respectively, as

$$\boldsymbol{\sigma} = \partial_{\boldsymbol{\varepsilon}}\hat{\psi} \quad \text{and} \quad \eta = -\partial_\theta \hat{\psi} \;, \tag{4.12}$$

which gives the constitutive expressions for the stresses as

$$\boldsymbol{\sigma} = p\boldsymbol{1} + \bar{\boldsymbol{\sigma}} \quad \text{with} \quad p := \kappa e - \kappa\alpha_t(\theta - \theta_0) \quad \text{and} \quad \bar{\boldsymbol{\sigma}} := 2\mu(\bar{\boldsymbol{\varepsilon}} - \boldsymbol{\varepsilon}^p) \;. \tag{4.13}$$

The constitutive expression of the entropy is given by

$$\eta := -\partial_\theta \hat{\psi} := \frac{h_0}{2}\, w_h \alpha^2 + \kappa\alpha_t e + c\ln[\theta/\theta_0] \;. \tag{4.14}$$

Note that we do not consider the entropy as a part of our formulation. However, it is used to obtain a temperature evolution via a Legendre transformation. Furthermore, we introduce in (4.11) the energetic driving forces

$$\partial_{\boldsymbol{\varepsilon}^p}\hat{\psi} = -2\mu(\bar{\boldsymbol{\varepsilon}} - \boldsymbol{\varepsilon}^p) = -\bar{\boldsymbol{\sigma}} \;, \quad f := \partial_\alpha\hat{\psi} = h(\theta)\alpha \;, \quad \boldsymbol{f} := \partial_{\nabla\alpha}\hat{\psi} = \mu l_p^2\,\nabla\alpha \tag{4.15}$$

dual to $\boldsymbol{\varepsilon}^p$, α and $\nabla\alpha$, respectively. With the above results at hand, the reduced Clausius Planck inequality reads

$$\mathcal{D}_{loc}^{red} := \bar{\boldsymbol{\sigma}} : \dot{\boldsymbol{\varepsilon}}^p - f\dot{\alpha} - \boldsymbol{f}\cdot\nabla\dot{\alpha} \geq 0 \;. \tag{4.16}$$

The constitutive equations of coupled thermoplasticity are completed by a constitutive assumption with regard to heat flux. In this treatment, the flux in the interior of the body is assumed to be governed by an isotropic Fourier-type law (2.30). This ansatz provides an obviously positive conductive dissipation called the Fourier inequality

$$\mathcal{D}_{con} := \frac{K}{\theta}\,|\nabla\theta|^2 \geq 0 \tag{4.17}$$

for a positive heat conductivity parameter $K > 0$.

4.1.4. Principle of maximum dissipation. The evolution of the internal variables in (4.16) is determined by the regularized *principle of maximum dissipation*, see Perzyna [127, 128]

$$\phi(\dot{\boldsymbol{\varepsilon}}^p, \dot{\alpha}, \theta) = \sup_{\bar{\boldsymbol{\mathfrak{s}}},\mathfrak{f}} \Big[\bar{\boldsymbol{\mathfrak{s}}} : \dot{\boldsymbol{\varepsilon}}^p - \mathfrak{f}\cdot\dot{\alpha} - \frac{1}{2\eta_p}\big\langle\chi(\bar{\boldsymbol{\mathfrak{s}}}, \mathfrak{f}, \theta)\big\rangle^2 \Big] \;. \tag{4.18}$$

The stress $\bar{\boldsymbol{\mathfrak{s}}}$ is *locally* defined by an ODE. In contrast, the stress–like hardening variable $\mathfrak{f}$ is *non–locally* defined by a PDE. This reflects the chosen nature of the short–range internal variable $\boldsymbol{\varepsilon}^p$ and the long–range internal variable α. The unconstrained optimization problem (4.18) is exploited by a penalty-type formulation, with the viscosity η_p playing the role of a penalty parameter

$$\mathcal{P}(\dot{\boldsymbol{\varepsilon}}^p, \dot{\alpha}, \bar{\boldsymbol{\mathfrak{s}}}, \mathfrak{f}, \theta) := -\mathcal{D}_{loc}^{red} + \bar{\boldsymbol{\mathfrak{s}}} : \dot{\boldsymbol{\varepsilon}}^p - \mathfrak{f}\dot{\alpha} - \frac{1}{2\eta_p}\big\langle\chi(\bar{\boldsymbol{\mathfrak{s}}}, \mathfrak{f}, \theta)\big\rangle^2 \quad \rightarrow \quad STAT \tag{4.19}$$

in terms of the constitutive yield function $\chi(\bar{\mathfrak{s}}, \mathfrak{f}, \theta)$ defined in (4.7). The necessary condition of the unconstrained problem (4.19), yields the evolution of hardening and plastic strain along with its dual fields

$$
\begin{aligned}
&1. \quad \partial_{\dot{\boldsymbol{\varepsilon}}^p}\mathcal{P} &&\equiv -\bar{\boldsymbol{\sigma}} + \bar{\mathfrak{s}} = \boldsymbol{0} \ , \\
&2. \quad \partial_{\bar{\mathfrak{s}}}\mathcal{P} &&\equiv \dot{\boldsymbol{\varepsilon}}^p - \lambda \bar{\mathfrak{n}} = \boldsymbol{0} \ , \\
&3. \quad \partial_{\dot{\alpha}}\mathcal{P} &&\equiv f - \mathrm{Div}\,[\boldsymbol{f}] - \mathfrak{f} = 0 \ , \\
&4. \quad \partial_{\mathfrak{f}}\mathcal{P} &&\equiv -\dot{\alpha} + \lambda\sqrt{2/3} = 0 \ ,
\end{aligned}
\tag{4.20}
$$

where we introduced per definition the *amount* and the *direction* of plastic flow

$$
\lambda := \frac{1}{\eta_p}\Big\langle |\bar{\mathfrak{s}}| - \sqrt{\frac{2}{3}}[y(\theta) + \mathfrak{f}]\Big\rangle \quad \text{and} \quad \bar{\mathfrak{n}} := \frac{\bar{\mathfrak{s}}}{|\bar{\mathfrak{s}}|} \ . \tag{4.21}
$$

4.1.5. Local-global constitutive equations. With the specification of ψ in (4.2) and the evolution equations (4.20), we have now fully specified all constitutive functions necessary for the coupled problem. Next, we introduce the governing equations of the initial boundary value problem of coupled thermoplasticity. The first global equation is the balance of linear momentum

$$
\mathrm{Div}[\boldsymbol{\sigma}] = \boldsymbol{0} \ , \tag{4.22}
$$

for vanishing body fores and inertia effects. The second global equation is the evolution law of the equivalent plastic strain $\dot{\alpha}$ governed by $(4.20)_4$, and the third global equation is the definition of the dual driving force $\mathfrak{f}$ governed by equation $(4.20)_3$. Regarding the thermal balance equation, the essential balance equation is the balance of internal energy

$$
\dot{\mathcal{E}} = \boldsymbol{\sigma} : \dot{\boldsymbol{\varepsilon}} + \mathrm{Div}\,[-\boldsymbol{q}] + r \ . \tag{4.23}
$$

Using Legendre transformation $\mathcal{E} = \psi + \theta\eta$, one gets

$$
\dot{\psi} + \dot{\theta}\eta + \theta\dot{\eta} = \boldsymbol{\sigma} : \dot{\boldsymbol{\varepsilon}} - \mathrm{Div}[\boldsymbol{q}] + r \ . \tag{4.24}
$$

Recalling the definition of the reduced local dissipation $\mathcal{D}^{red}_{loc}$ in (4.16), we can express $\dot{\psi}$ in (4.10) as

$$
\dot{\psi} = \boldsymbol{\sigma} : \dot{\boldsymbol{\varepsilon}} - \mathcal{D}^{red}_{loc} - \eta\dot{\theta} \, . \tag{4.25}
$$

With the evolution of the free energy, (4.24) can be written as

$$
\theta\,\dot{\eta} = \mathcal{D}^{red}_{loc} - \mathrm{Div}[\boldsymbol{q}] + r \ . \tag{4.26}
$$

From the definition of the entropy $(4.12)_2$, we obtain the constitutive rate equation

$$
\theta\dot{\eta} = c\,\dot{\theta} - \mathcal{H} \quad \text{with} \quad c := -\theta\,\partial^2_{\theta\theta}\psi \quad \text{and} \quad \mathcal{H} := \theta\,\partial_\theta\Big[\boldsymbol{\sigma} : \dot{\boldsymbol{\varepsilon}} - \mathcal{D}^{red}_{loc}\Big] \ , \tag{4.27}
$$

where c is the heat capacity and $\mathcal{H}$ the latent heat. Insertion of (4.27) into (4.26) finally gives an evolution equation for the global absolute temperature

$$
c\,\dot{\theta} = \big\{\,\mathrm{Div}\,[-\boldsymbol{q}] + r\big\} + \big\{\mathcal{H} + \mathcal{D}^{red}_{loc}\big\} \ . \tag{4.28}
$$

Note that the first bracket vanishes in an adiabatic process, i.e. for $\boldsymbol{q} \equiv \boldsymbol{0}$ and $r \equiv 0$ in the whole body $\mathcal{B}$. The last two terms on the right-hand side characterize the latent (thermoelastic) and dissipative coupling effects. In applications of metal thermoplasticity, it is expected that $|\mathcal{H}| << \mathcal{D}^{red}_{loc}$. Investigations of Miehe [92] for entropic thermoelasticity demonstrated the small amount of latent heating. In our subsequent investigation, we neglect the latent heating effect in the temperature evolution equation by setting $\mathcal{H} \approx 0$. Next we summarize the local–global field equations for the coupled thermo-mechanical problem

$$
\begin{array}{lrl}
1. & \operatorname{Div}[\boldsymbol{\sigma}] & = \boldsymbol{0} \ , \\
2. & f - \operatorname{Div}[\boldsymbol{f}] - \mathfrak{f} & = 0 \ , \\
3. & -\dot{\alpha} + \lambda\sqrt{2/3} & = 0 \ , \\
4. & -\bar{\boldsymbol{\sigma}} + \bar{\boldsymbol{\mathfrak{s}}} & = \boldsymbol{0} \ , \\
5. & \dot{\boldsymbol{\varepsilon}}^p - \lambda\bar{\boldsymbol{\mathfrak{n}}} & = \boldsymbol{0} \ , \\
6. & c\,\dot{\theta} + \operatorname{Div}[\boldsymbol{q}] - \mathcal{D}^{red}_{loc} & = 0 \ .
\end{array}
\tag{4.29}
$$

The global field variables of our coupled gradient thermo-plasticity problem are the *long-range displacement field* $\boldsymbol{u}$, the *long-range micro-motion field* α together with its dual driving force $\mathfrak{f}$, and the *long-range absolute temperature field* θ. The local field variables are the *short-range micro-motion field* $\boldsymbol{\varepsilon}^p$ and its dual driving force $\bar{\boldsymbol{\mathfrak{s}}}$. To solve this system of equations for the coupled problem, we have to set the boundary conditions. To this end, the surface $\partial\mathcal{B}$ is decomposed according to the three primary fields, the displacement $\boldsymbol{u}$, the equivalent plastic strain α and the temperature θ

$$
\partial\mathcal{B} = \partial\mathcal{B}^u \cup \partial\mathcal{B}^t \ , \quad \partial\mathcal{B} = \partial\mathcal{B}^\alpha \cup \partial\mathcal{B}^{\mathbb{h}} \ , \quad \partial\mathcal{B} = \partial\mathcal{B}^\theta \cup \partial\mathcal{B}^h \ , \tag{4.30}
$$

respectively, with $\partial\mathcal{B}^u \cap \partial\mathcal{B}^t = \emptyset$, $\partial\mathcal{B}^\alpha \cap \partial\mathcal{B}^{\mathbb{h}} = \emptyset$ and $\partial\mathcal{B}^\theta \cap \partial\mathcal{B}^h = \emptyset$. We derive Dirichlet– and Neumann–type boundary conditions related to the displacement and traction field

$$
\boldsymbol{u} = \bar{\boldsymbol{u}} \text{ on } \partial\mathcal{B}^u \quad \text{and} \quad \boldsymbol{\sigma}\boldsymbol{n} = \bar{\boldsymbol{t}} \text{ on } \partial\mathcal{B}^t \tag{4.31}
$$

and the *passive* boundary conditions of the equivalent plastic strain variable, defining the *micro-clamped* and *free* constraints for the evolution of the plastic deformation

$$
\alpha = 0 \text{ on } \partial\mathcal{B}^\alpha \quad \text{and} \quad \boldsymbol{f} \cdot \boldsymbol{n} = 0 \text{ on } \partial\mathcal{B}^{\mathbb{h}} \tag{4.32}
$$

and finally for the thermal problem

$$
\theta = \bar{\theta} \text{ on } \partial\mathcal{B}^\theta \quad \text{and} \quad \boldsymbol{q} \cdot \boldsymbol{n} = \bar{h} \text{ on } \partial\mathcal{B}^h \tag{4.33}
$$

with a *prescribed* displacement field $\bar{\boldsymbol{u}}$, traction field $\bar{\boldsymbol{t}}$, temperature field $\bar{\theta}$ and heat flux $\bar{h}$. Note that in the numerical examples in Section 4.3, we set $\bar{h} = 0$ on the boundary $\partial\mathcal{B}^h$.

4.2. Algorithmic implementation of thermo-gradient-plasticity

The next step is to derive the algorithmic treatment of the coupled problem. This involves three major steps. First, we carry out time discretization of the global equations (4.29). Next, the time discrete governing balance equations are recast into their weak form and finally a space discretization is carried out using the finite element method. In this section, we focus on development of two time solution procedures for the coupled problem, namely the *product formula algorithm* and the *simultaneous solution algorithm.*

4.2.1. Product formula algorithm. This solution scheme is constructed based on the methodology of operator splitting of the coupled thermo-mechanical problem in line with the works of Simó & Miehe [140] and Miehe et. al. [103]. The underlying concept here is to exploit a natural operator split of the coupled field equations into a mechanical problem at isothermal state followed by a heat conduction problem at frozen mechanical state. As a result, we obtain partitioned symmetric structures for the mechanical and the thermal sub-problems. It should be also noted that each solution step admits an exact linearisation. To this end, the algorithm obtained by splitting of the system of equations (4.29) into two sub-systems reads

$$
\begin{array}{lr}
 & \underline{\text{Mechanical problem } (M)\text{:}} \\
1. & \mathrm{Div}[p\boldsymbol{1} + \bar{\boldsymbol{\sigma}}] = \boldsymbol{0} \ , \\
2. & f - \mathrm{Div}\,[\boldsymbol{f}] - \mathfrak{f} = 0 \ , \\
3. & -\dot{\alpha} + \lambda\sqrt{2/3} = 0 \ , \\
4. & -\bar{\boldsymbol{\sigma}} + \bar{\boldsymbol{\mathfrak{s}}} = \boldsymbol{0} \ , \\
5. & \dot{\boldsymbol{\varepsilon}}^p - \lambda\bar{\boldsymbol{\mathfrak{n}}} = \boldsymbol{0} \ , \\
 & \underline{\text{Thermal problem } (T)\text{:}} \\
6. & c\dot{\theta} + \mathrm{Div}\,[\boldsymbol{q}] - \mathcal{D}^{red}_{loc} = 0 \ .
\end{array}
\tag{4.34}
$$

(M) represents the mechanical subproblem at frozen temperature θ_n, which can be solved for the new or actual global mechanical state $\{\boldsymbol{u}, \alpha, \mathfrak{f}\}$ and problem (T) is a purely thermal problem at frozen mechanical state, which can be solved for the new or actual temperature θ. In a typical time step $\Delta t = t_{n+1} - t_n$, the thermomechanical coupling algorithm is considered as the composition

$$
ALGO_{TM} = ALGO_T \ \circ \ ALGO_M \tag{4.35}
$$

of two sub-algorithms.

Isothermal deformation predictor. The first sub-algorithm is a *mechanical predictor* at isothermal state ($\dot{\theta} = 0$) governed by a system of equations (M). It gives the update of displacement $\boldsymbol{u}$, equivalent plastic strain α and its dual driving force $\mathfrak{f}$ at time t_{n+1}. To this end, we refer to the study in Chapter 3 for updating the global field at frozen temperature θ_n.

Thermal corrector. With the updated mechanical fields $\{\boldsymbol{u}, \alpha, \mathfrak{f}\}$, we first compute the reduced local dissipation. To this end, the time discrete dissipation functional is given by

$$
\mathcal{D}^{red}_{loc} := \bar{\boldsymbol{\sigma}} : \frac{(\boldsymbol{\varepsilon}^p - \boldsymbol{\varepsilon}^p_n)}{\Delta t} - f\frac{(\alpha - \alpha_n)}{\Delta t} - \boldsymbol{f} \cdot \frac{(\nabla\alpha - \nabla\alpha_n)}{\Delta t} \tag{4.36}
$$

We then insert the reduced dissipation into the second sub-problem which is the *heat conduction corrector*, governed by (T) as specified in (4.34). It determines the temperature θ at a frozen mechanical configuration, which was obtained in the predictor step. The weak form for this sub-algorithm follows from a standard Galerkin procedure of the time discrete counterpart of $(4.34)_6$

$$
\int_{\mathcal{B}} \delta\theta \Big\{ \frac{c}{\tau}(\theta - \theta_n) - \mathcal{D}^{red}_{loc} + \mathrm{Div}[\boldsymbol{q}] \Big\} \, dV = 0 \tag{4.37}
$$

with $\delta\theta$ being a virtual temperature field defined on the reference configuration that satisfies the homogeneous thermal boundary condition $\delta\theta = 0$ on $\partial\mathcal{B}_\theta$. The last term of (4.37) can be recast into

$$\mathrm{Div}(\delta\theta \boldsymbol{q}) := (\delta\theta \boldsymbol{q}_i)_{,i} := \delta\theta_{,i}\boldsymbol{q}_i + \delta\theta \boldsymbol{q}_{i,i} := \nabla\delta\theta \cdot \boldsymbol{q} + \delta\theta \ \mathrm{Div}[\boldsymbol{q}] \ . \tag{4.38}$$

By using of Gauss theorem, one obtains from (4.37) the variational formulation

$$\int_{\mathcal{B}} \delta\theta \Big\{ \frac{c}{\tau}(\theta - \theta_n) - \mathcal{D}^{red}_{loc} \Big\} \, dV - \int_{\mathcal{B}} \nabla\delta\theta \cdot \boldsymbol{q} \, dV + \int_{\partial\mathcal{B}_{\boldsymbol{q}}} \delta\theta \ \bar{h} \, dA = 0 \tag{4.39}$$

for all virtual temperature fields $\delta\theta$ with $\delta\theta = 0$ on $\partial\mathcal{B}_\theta$. (4.39) can be expressed in a generalized formulation as

$$\hat{G}_T(\delta\theta, \nabla\theta, \theta) := \int_{\mathcal{B}} \boldsymbol{\mathfrak{S}}_T \cdot \begin{bmatrix} \nabla\delta\theta \\ \delta\theta \end{bmatrix} \, dV + \int_{\partial\mathcal{B}_{\boldsymbol{q}}} \delta\theta \ \bar{h} \, dA = 0 \ . \tag{4.40}$$

The generalized thermal stress $\boldsymbol{\mathfrak{S}}_T$ can be defined in an array structure as

$$\boldsymbol{\mathfrak{S}}_T = \begin{bmatrix} K\nabla\theta \\ \frac{c}{\tau}(\theta - \theta_n) \end{bmatrix} + s \begin{bmatrix} 0 \\ -\mathcal{D}^{red}_{loc} \end{bmatrix} \tag{4.41}$$

with the loading flag s which defines the elastic/plastic loading case as

$$s := \begin{cases} 1 & \text{for} \quad \chi > 0 \quad \text{plastic step} \\ 0 & \text{otherwise} \quad\ \ \text{elastic step} \ . \end{cases} \tag{4.42}$$

A straightforward linearisation of (4.40)

$$\Delta\hat{G}_T(\delta\theta, \theta) = \int_{\mathcal{B}} \delta\theta \cdot \boldsymbol{\mathfrak{C}}_T \cdot \Delta\theta \, dV \tag{4.43}$$

determines at given temperature θ its linear increment $\Delta\theta$ at a frozen mechanical configuration, which was obtained in the predictor step before. The generalized thermal moduli take the form

$$\boldsymbol{\mathfrak{C}}_T := \begin{bmatrix} K\boldsymbol{1} & \cdot \\ \cdot & c/\tau \end{bmatrix} \tag{4.44}$$

With the stresses and moduli at hand, one can now determine the updated temperature.

4.2.2. Simultaneous solution scheme. This is an alternate solution algorithm for the coupled problem known as the monolithic scheme. The fully coupled thermomechanical problem is solved as a single entity without performing an operator split. Therefore we no longer have a constant temperature during the mechanical step and vice-versa. Algorithms for such a monolithic set of coupled equations have been discussed for example by ARGYRIS & DOLTSINIS [17] and SIMÓ & MIEHE [140] and MARKERT [83]. This approach is significantly more computationally intensive than the scheme based on the product formula algorithm.

Weak form of the equilibrium equations. The weak form of the coupled system of equations is a straightforward addition of all equations in (4.29) after taking the time discretization of the evolution equations, which leads to an *non-symmetric structure* of the problem. Taking into account the condensation of $\boldsymbol{\varepsilon}^p$ and $\bar{\boldsymbol{\mathfrak{s}}}$ as per Chapter 3, the weak form of the reduced set of equations can be written as

$$\begin{aligned} & \int_{\mathcal{B}} \delta \boldsymbol{u} \{ \mathrm{Div}[p \boldsymbol{1} + \bar{\boldsymbol{\sigma}}] \} \, dV + \int_{\mathcal{B}} \nabla \delta \alpha \mu {l_p}^2 \nabla \alpha \, dV + \int_{\mathcal{B}} \delta \alpha \{ h(\theta) \alpha - \mathfrak{f} \} \, dV \\ + & \int_{\mathcal{B}} \delta \mathfrak{f} \{ -\alpha + \alpha_n + \gamma \sqrt{2/3} \} \, dV + \int_{\mathcal{B}} \delta \theta \Big\{ \frac{c}{\tau} (\theta - \theta_n) - \mathcal{D}^{red}_{loc} \Big\} \, dV \\ - & \int_{\mathcal{B}} \nabla \delta \theta \cdot \boldsymbol{q} \, dV + \int_{\partial \mathcal{B}_{\boldsymbol{q}}} \delta \theta \, \bar{h} \, dA = 0 \end{aligned} \tag{4.45}$$

for all admissible virtual fields. Note that *passive* Neumann-type boundary conditions for the equivalent plastic strain $\nabla \alpha \cdot \boldsymbol{n} = 0$ on $\partial \mathcal{B}_{\nabla \alpha}$ has been considered. Equation (4.45) can be reformulated into the form

$$\hat{G}(\delta \boldsymbol{\mathfrak{r}}, \boldsymbol{\mathfrak{r}}) = \int_{\mathcal{B}} \big[(\kappa e - \kappa \alpha_t (\theta - \theta_0)) \delta e + \delta \theta (-\kappa \alpha_t e) + \bar{\boldsymbol{\mathfrak{S}}} \cdot \delta \bar{\boldsymbol{\mathfrak{r}}} \big] \, dV + \int_{\partial \mathcal{B}_{\boldsymbol{q}}} \delta \theta \, \bar{h} \, dA = 0 \tag{4.46}$$

where $\boldsymbol{\mathfrak{r}}$ is the reduced set of variables defined as

$$\boldsymbol{\mathfrak{r}} := \{ e, \theta, \bar{\boldsymbol{\mathfrak{r}}} \} \quad \text{with} \quad \bar{\boldsymbol{\mathfrak{r}}} := \{ \bar{\boldsymbol{\varepsilon}}, \alpha, \nabla \alpha, \mathfrak{f}, \theta, \nabla \theta \}. \tag{4.47}$$

The generalized deviatoric stress array $\bar{\boldsymbol{\mathfrak{S}}}$ is defined as

$$\bar{\boldsymbol{\mathfrak{S}}} := \begin{bmatrix} 2\mu(\bar{\boldsymbol{\varepsilon}} - \boldsymbol{\varepsilon}^p_n) \\ h(\theta)\alpha - \mathfrak{f} \\ \mu l_p^2 \nabla \alpha \\ -\alpha + \alpha_n \\ K \nabla \theta \\ \frac{c}{\Delta t}(\theta - \theta_n) \end{bmatrix} + s \begin{bmatrix} -2\mu \, \gamma \, \bar{\boldsymbol{\mathfrak{n}}}^{tr} \\ 0 \\ 0 \\ \gamma \sqrt{2/3} \\ 0 \\ -\mathcal{D}^{red}_{loc} \end{bmatrix} = \begin{bmatrix} \bar{\boldsymbol{\mathfrak{S}}}_M \\ \\ \ldots . \\ \bar{\boldsymbol{\mathfrak{S}}}_T \end{bmatrix} . \tag{4.48}$$

$\bar{\boldsymbol{\mathfrak{S}}}_M$ and $\bar{\boldsymbol{\mathfrak{S}}}_T$ represent the mechanical and thermal stress arrays respectively. The linearization of (4.46) reads

$$\Delta \hat{G}(\delta \boldsymbol{\mathfrak{r}}, \boldsymbol{\mathfrak{r}}) = \int_{\mathcal{B}} [\delta e \kappa \Delta e + \delta \theta (-\kappa \alpha_t) \Delta e + \delta e (-\kappa \alpha_t) \Delta \theta + \Delta \bar{\boldsymbol{\mathfrak{r}}} \cdot \bar{\boldsymbol{\mathfrak{C}}} \cdot \delta \bar{\boldsymbol{\mathfrak{r}}}] \, dV \tag{4.49}$$

where $\bar{\boldsymbol{\mathfrak{C}}}$ is a non-symmetric array of coupled moduli defined by

$$\bar{\boldsymbol{\mathfrak{C}}} := \begin{bmatrix} 2\mu\mathbb{P} & \cdot & \cdot & \cdot & \cdot & \cdot \\ \cdot & h(\theta) & \cdot & -1 & \cdot & \cdot \\ \cdot & \cdot & \mu l_p^2 & \cdot & \cdot & \cdot \\ \cdot & -1 & \cdot & \cdot & \cdot & \cdot \\ \cdot & \cdot & \cdot & \cdot & K\boldsymbol{1} & \cdot \\ \cdot & \cdot & \cdot & \cdot & \cdot & c/\Delta t \end{bmatrix} + \; s \begin{bmatrix} -\,\mathbb{E}^p & \cdot & \cdot & \boldsymbol{e}^p & \cdot & \cdot \\ \cdot & \cdot & \cdot & \cdot & \cdot & \cdot \\ \cdot & \cdot & \cdot & \cdot & \cdot & \cdot \\ \boldsymbol{e}^{pT} & \cdot & \cdot & -e^p & \cdot & \cdot \\ \cdot & \cdot & \cdot & \cdot & \cdot & \cdot \\ \mathbb{F}^p & \mathbb{G}^p & \mathbb{H}^p & \mathbb{I}^p & \cdot & \cdot \end{bmatrix} \tag{4.50}$$

with the following derivatives

$$
\begin{aligned}
\mathbb{F}^p &= \frac{-1}{\Delta t}\bigg\{ 2\mu(\boldsymbol{\varepsilon}^p - \boldsymbol{\varepsilon}^p_n) - \frac{4\mu^2\tau}{2\mu\tau + \eta_p}\bar{\mathfrak{n}}^{tr} \otimes \bar{\mathfrak{n}}^{tr} : (\boldsymbol{\varepsilon}^p - \boldsymbol{\varepsilon}^p_n) - \frac{4\mu^2\gamma}{\|\bar{\mathfrak{s}}^{tr}\|}[\mathbb{P} - \bar{\mathfrak{n}}^{tr} \otimes \bar{\mathfrak{n}}^{tr}] \\
&\qquad + \ \bar{\mathfrak{S}} : \{ \frac{2\mu\tau}{2\mu\tau + \eta_p}\bar{\mathfrak{n}}^{tr} \otimes \bar{\mathfrak{n}}^{tr} + \frac{2\mu\gamma}{\|\bar{\mathfrak{s}}^{tr}\|}[\mathbb{P} - \bar{\mathfrak{n}}^{tr} \otimes \bar{\mathfrak{n}}^{tr}]\} \bigg\} \ , \\
\mathbb{G}^p &= \frac{h}{\Delta t}(2\alpha - \alpha_n) \ , \\
\mathbb{H}^p &= \frac{\mu {l_p}^2}{\Delta t}(2\nabla\alpha - \nabla\alpha_n) \ , \\
\mathbb{I}^p &= \frac{-1}{\Delta t}\bigg\{ \frac{2\mu\tau\sqrt{2/3}}{2\mu\tau + \eta_p}\bar{\mathfrak{n}}^{tr} : (\boldsymbol{\varepsilon}^p - \boldsymbol{\varepsilon}^p_n) - \frac{\sqrt{2/3}\tau}{2\mu\tau + \eta_p}\bar{\mathfrak{n}} : \bar{\mathfrak{S}} \bigg\} \ .
\end{aligned}
\tag{4.51}
$$

where $\mathbb{E}^p$, $\boldsymbol{e}^p$, and e^p are defined in (3.44).

Regarding the space discretization of the coupled thermo-mechanical problem, the mixed finite element design for gradient plasticity explained in Chapter 3 is extended to account for thermal effects by adding the temperature field to the Galerkin formulation. We end up with two sets of finite element designs:

- ***Q1P0-Q1Q1Q1 element:*** We extend the Q1P0-type finite element design of gradient plasticity outlined in Section 3.4 by introducing the temperature field θ, using bi-linear Q1 elements with $n = 4$ nodes and shape function $N^I(\boldsymbol{\xi})$ defined in (3.76).
- ***MINI-Q1Q1Q1 element:*** We extend the MINI-type finite elements design of gradient plasticity illustrated in Section 3.5 by introducing the temperature field θ, using linear C^0 interpolations with $n = 3$ nodes.

4.3. Representative numerical examples

We demonstrate the performance of the proposed framework of thermo-gradient-plasticity by means of two representative numerical examples for softening and hardening plasticity computed via the product formula algorithm, Which yields, however, similar

Table 4.1: Material parameters used for the numerical examples.

No.	Parameter	Name	Value	Unit
1.	κ	bulk modulus	164.2	kN/mm^2
2.	μ	shear modulus	80.2	kN/mm^2
3.	h	hardening/softening parameter	± 0.13	kN/mm^2
4.	l_p	plastic length-scale parameter	0.1	mm
5.	y_0	yield stress	0.45	kN/mm^2
6.	η_p	viscosity	10^{-7}	kNs/mm^2
7.	α_t	expansion coefficient	10^{-5}	K^{-1}
8.	K	conductivity	0.045	KN/sK
9.	c	capacity	$3.588 \cdot 10^{-3}$	KN/mm^{2}K
10.	w_h	thermal softening parameter	0.002	k^{-1}
11.	w_0	flow stress softening	0.002	k^{-1}

results as the simultaneous solution scheme. The material parameters used are given in Table 4.1.

4.3.1. Cross shear localization in tension for softening plasticity. The first benchmark test is concerned with the development of a symmetric crossed shear band localization of a strip subjected to tensile loading for softening plasticity, i.e. $h = -0.13$ KN/mm^2. The geometric set up and the loading conditions are illustrated in Figure 4.1. Here the size of the specimen is chosen to be $L = 50$ mm and $H = 100$ mm. Due to the underlying symmetry, only a quarter of the specimen is discretized using 400 Mini-Q1Q1Q1 elements. To trigger localization in the center of the specimen, the yield strength y_0 of the first element (lower left, shaded area) is reduced by 3 %. The material parameters of the specimen are listed in Table 4.1.

Figure 4.2 shows the contour plots at the final deformation state for the equivalent plastic strain α, its dual driving force $\mathfrak{f}$ and the incremental temperature θ for different plastic length scales l_p. Figure 4.2 (a),(e) and (i) show the results for local analysis with $l_p = 0$ mm. We observe a plastic shear band with a width of one element size. When increasing the length scale, we detect the equivalent plastic strain α, its dual driving force $\mathfrak{f}$ and the temperature field θ to spread over several elements, see Figure 4.2(b)–(d) for α and Figure 4.2(f)–(h) for $\mathfrak{f}$ and Figure 4.2(j)–(l) for θ, whereas their absolute maximum values decrease as outlined in ALDAKHEEL ET AL. [8] and NAGARAJA [116]. Furthermore, it can also be seen that the temperature distribution inside the specimen is similar to the hardening variable α. We observe that increasing l_p leads to a decrease of the temperature. As the length scale parameter $l_p \propto 1/L$ with L being the macroscopic characteristic size, increasing the plastic length scale is equivalent to a decrease in specimen size and, thus, temperature dissipates faster from a small size medium as illustrated in the work of FAGHIHI ET AL. [46], VOYIADJIS & FAGHIHI [150] and VOYIADJIS & ABU AL-RUB [149]. Next, Figure 4.3 shows the evolution of the equivalent plastic strain α in time at the specimen center for the isothermal and non-isothermal setting in combination with different length scales. We detect a higher amount of plastic strain for the non-isothermal setting because as the temperature increases, thermal softening also increases leading to an increase in plastic strain as shown in VOYIADJIS & FAGHIHI [150] and FAGHIHI ET AL. [46]. The load-displacement curves of the overall structural response are illustrated in Figure 4.4 and Figure 4.5. As observed in Figure 4.2(a), the shear band for a local

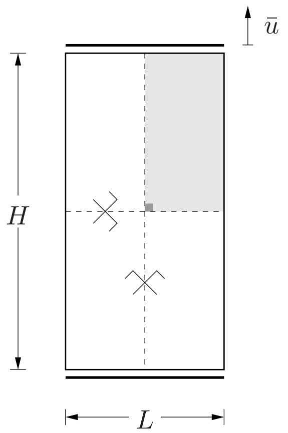

Figure 4.1: Cross shearing of specimen in tension. Geometry and boundary conditions.

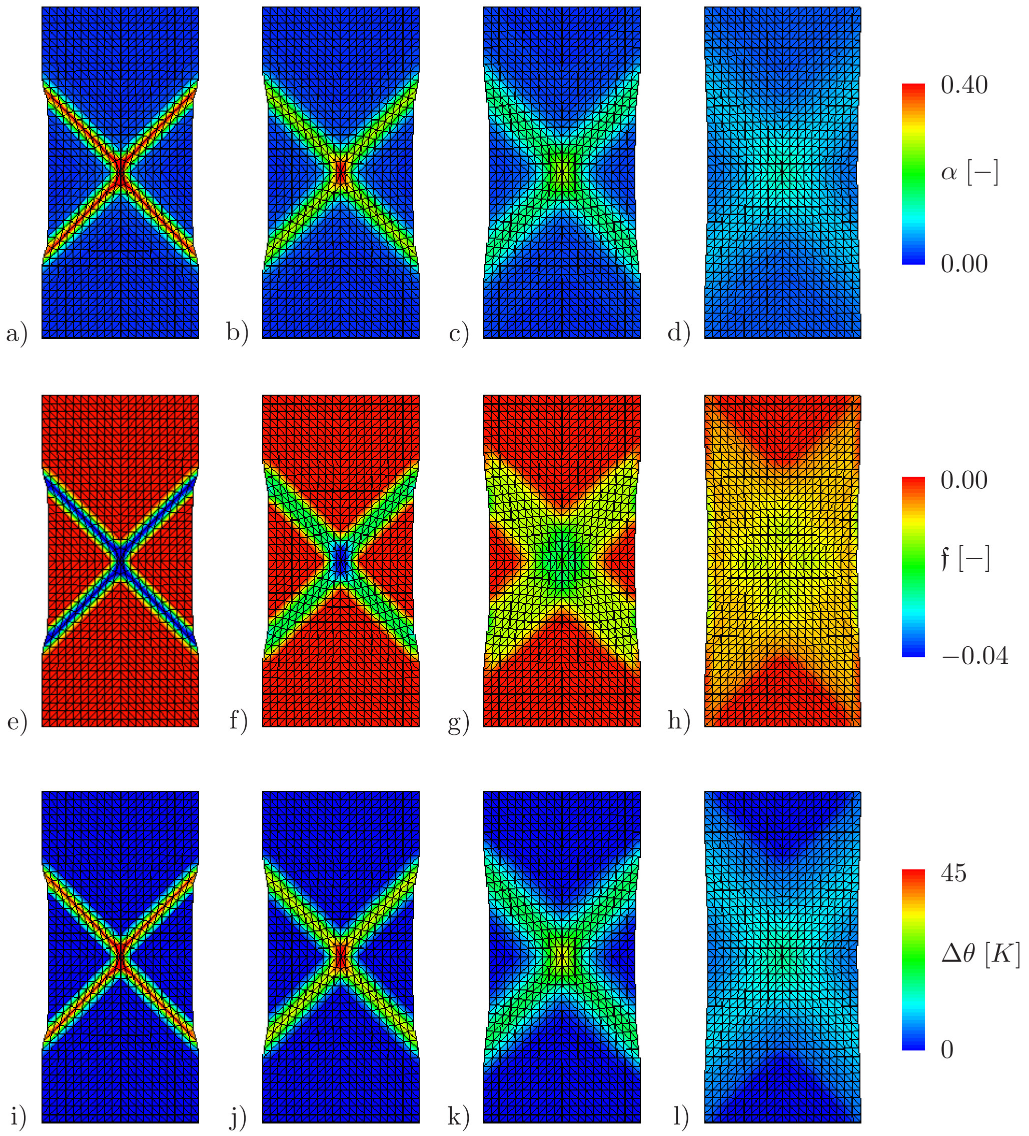

Figure 4.2: Tension test. Contour plots of the hardening variable α (a)-(d); its dual driving force $\mathfrak{f}$ (e)-(h) and incremental temperature θ (i)-(l) for a mesh with 400 elements for different length scales. a), e) and i) Local plasticity $l_p = 0$ mm; b), f) and j) $l_p = 0.05$ mm; c), g) and k) $l_p = 0.10$ mm and $l_p = 0.20$ mm in (d), (h) and (l).

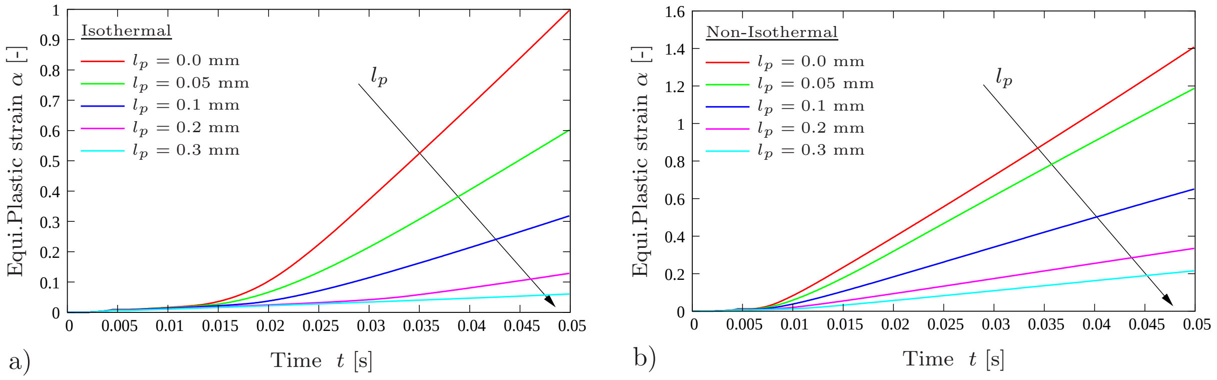

Figure 4.3: Tension Test. Variation of equivalent plastic strain for different length scales l_p a) isothermal setting (see Chapter 3) and b) non-isothermal setting.

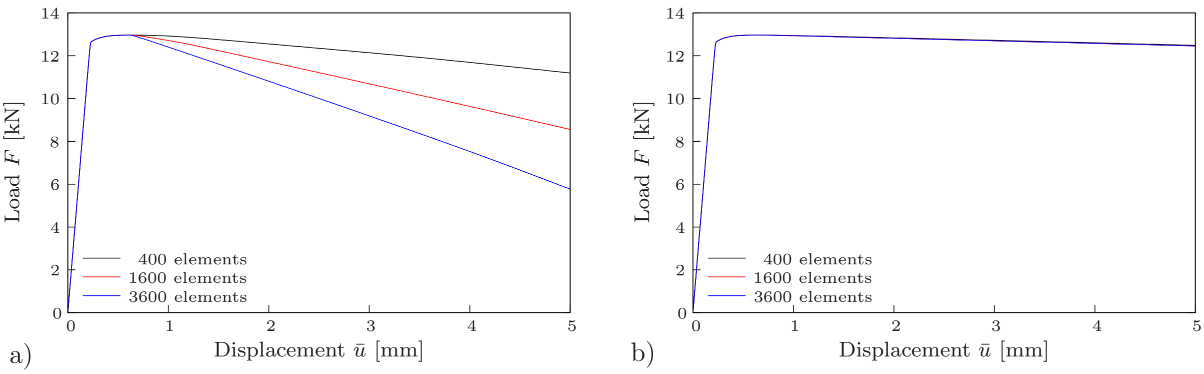

Figure 4.4: Tension test. Load-displacement curves for different mesh sizes a) for local plasticity $l_p = 0$ mm and b) gradient plasticity with $l_p = 0.1$ mm.

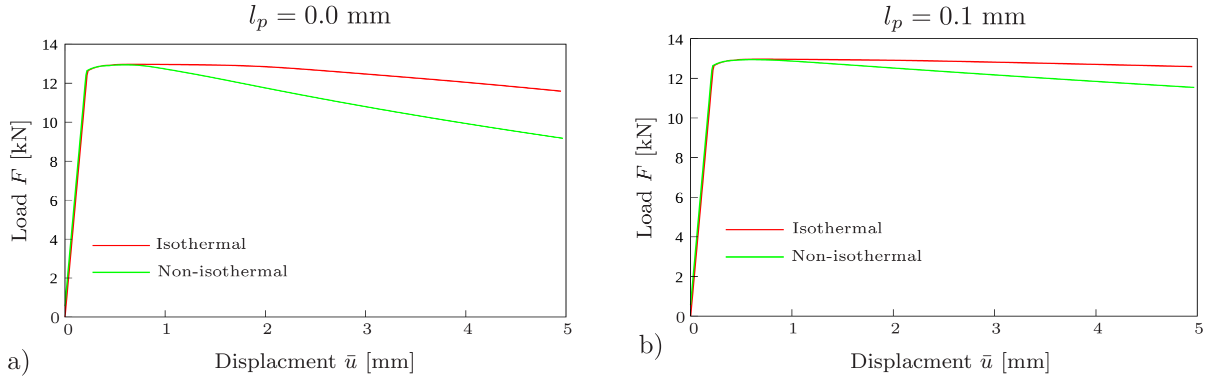

Figure 4.5: Tension Test. Load-displacement curves for Isothermal and Non-isothermal thermo-gradient plasticity with two length scales. a) $l_p = 0.0$ mm, b) $l_p = 0.1$ mm.

analysis ($l_p = 0$) has the width of one element.

The load-displacement curves in Figure 4.4(a) demonstrate the pathological mesh dependence of the local theory. In contrast, Figure 4.4(b) shows results for gradient plasticity with $l_p = 0.1$ mm and different mesh sizes, where mesh objectivity is observed. Next, we investigate in Figure 4.5 the effect of the temperature field on the overall global response for various length scales. The curves indicate an identical initial yield strength in all the cases because we have neglected the thermoelastic heating $\mathcal{H}$ and we also observe that the strain hardening is reduced for the non-isothermal setting, which is obviously true as the temperature increase results in further softening of the specimen.

4.3.2. Expansion of a plate with hole for hardening plasticity. The second example focuses on the effect of hardening plasticity in a squared specimen with a circular hole. The size of the plate is set to $L = 1.0$ mm and the hole has a diameter of $d = 0.25$ mm. The material parameters used are given in Table 4.1. In particular, we set $h = 0.13$ kN/mm^2 for hardening plasticity. The process is deformation-controlled by prescribing a bi-axial extension of the specimen at the full boundary. Due to the symmetry of the boundary value problem only a quarter of the specimen is discretized with 800 Q1P0-Q1Q1Q1 elements. The geometric setup and the boundary conditions are illustrated in Figure 4.6.

Figure 4.7 depicts the distribution of the equivalent plastic strain α, the dual driving force $\mathfrak{f}$ and the temperature field θ at the final deformation for different length scales l_p. We observe a concentration of equivalent plastic strain α Figure 4.7a and the temperature

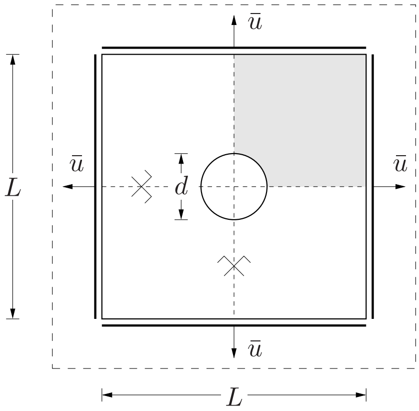

Figure 4.6: Expansion of a plate with hole for hardening plasticity. Geometry and boundary conditions.

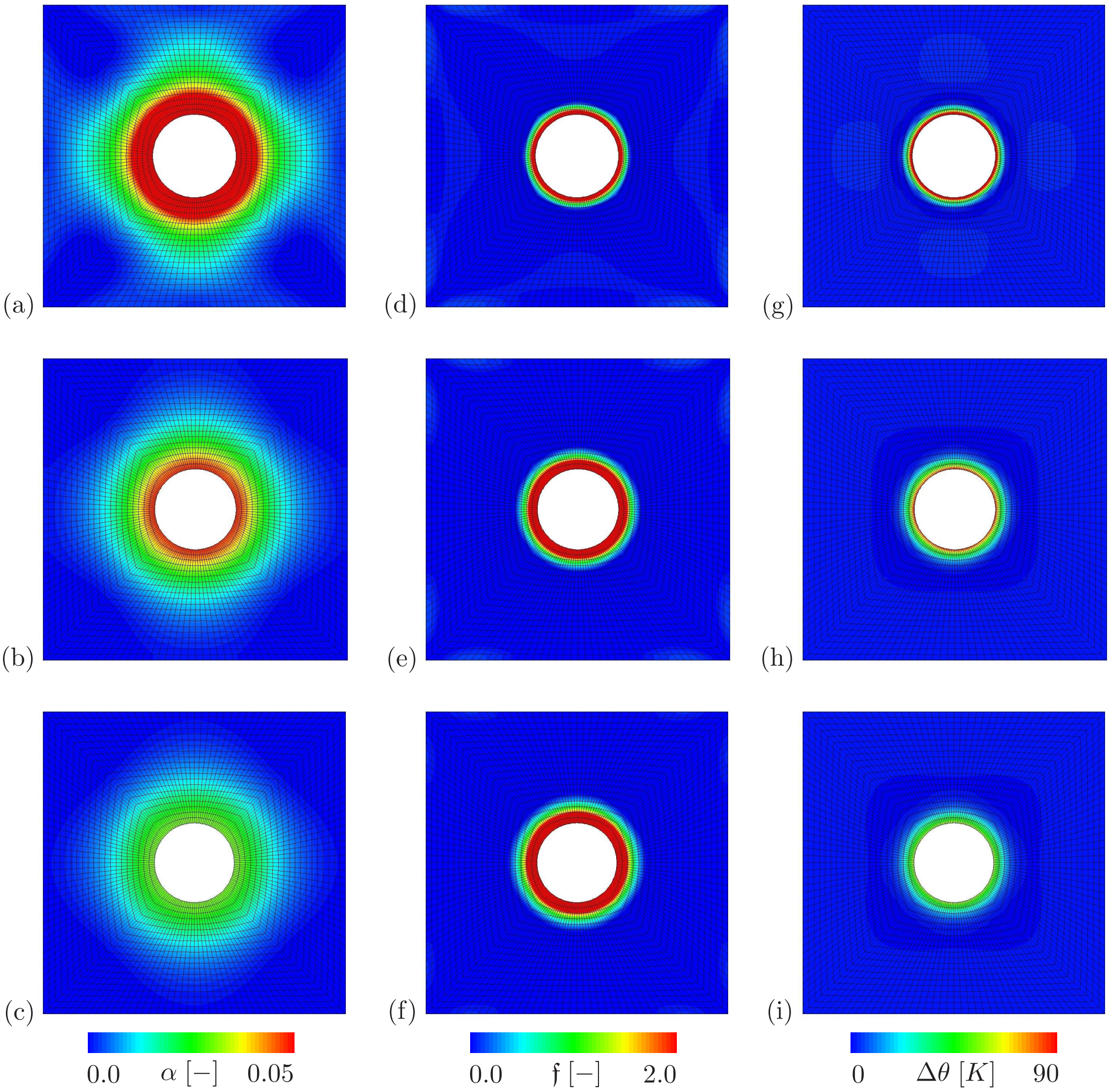

Figure 4.7: Expansion of a plate with hole for hardening plasticity. Distribution of equivalent plastic strain α (a)-(c); its dual driving force $\mathfrak{f}$ (d)-(f) and temperature θ (g)-(i) for a mesh with 400 elements for three different plastic length scales. (a), (d) and (g) $l_p = 0.03$ mm; (b), (e) and (h) $l_p = 0.07$ mm and $l_p = 0.1$ mm in (c), (f) and (i).

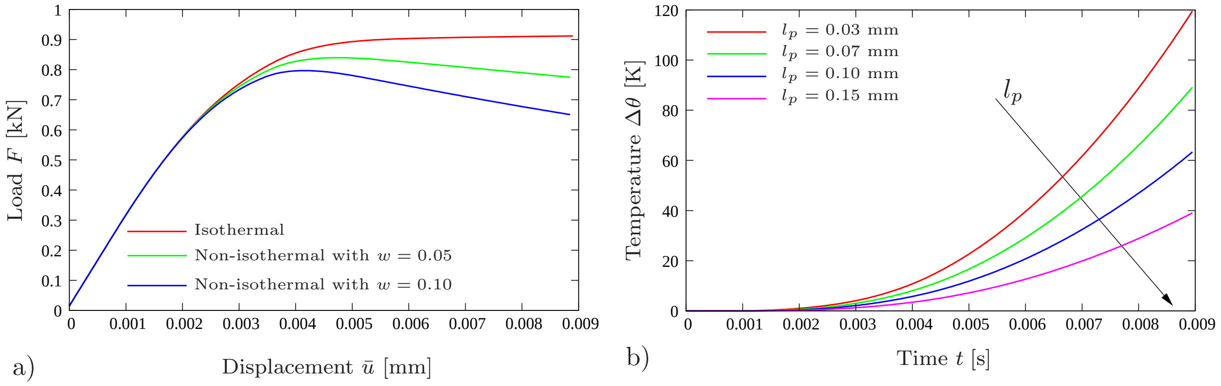

Figure 4.8: Expansion of a plate with hole for hardening plasticity. a) Load-displacement curves for isothermal and non-isothermal analysis and b) evolution of incremental temperature θ at the inner surface and in combination with different length scales .

field θ Figure 4.7g around the hole. By increasing the length scale, α and θ spread out, but the driving force $\mathfrak{f}$ becomes more localized. We observe very small oscillations in the dual driving force $\mathfrak{f}$ near the EPB. However, their amplitudes are extremely small. They do not have a visible influence on the macro-deformation u and the equivalent plastic strain α.

Figure 4.8(a) shows the load displacement curves for isothermal setting (see Chapter 3) compared with non-isothermal setting for two different values of the thermal softening parameter w_h corresponding to a weak and a strong temperature dependence of the flow stress and isotropic hardening modulus. By including the thermal effect, a softer response is observed. For the strong temperature dependence ($w_h = w_0 = 0.1\ K^{-1}$), we detect a softer global response, i.e. strain hardening is reduced further in comparison with weak temperature dependence of the plastic flow ($w_h = w_0 = 0.05\ K^{-1}$) as mentioned in the work of Simo & Miehe [140]. Figure 4.8b shows the evolution of the temperature field at the inner surface of the specimen, computed via the product formula algorithm for different length scales. It can be seen that for a smaller length scale, the absolute temperature field θ has the highest value. As we increase l_p, the maximum value decreases. This is because, increasing the plastic length scale is equivalent to a decrease in the specimen size and temperature dissipates faster from a smaller size medium, which is well documented in Voyiadjis & Faghihi [150], Faghihi et al. [46] and Nagaraja [116].

5. Variational Gradient Plasticity in the Logarithmic Strain Space

In this chapter, we extend the constitutive formulation discussed in Chapter 3 to the finite deformation theory, as outlined in the recent publication of MIEHE ET AL. [105] and ALDAKHEEL ET AL. [10]. A key aspect of this chapter is its core constitutive structure in the Lagrangian logarithmic strain space, that could be chosen to be identical to geometrically linear theories of gradient plasticity. The point of departure is the construction of a variational framework based on mixed saddle point principles for metric-type additive plasticity, which is specified for the important model problem of isochoric von Mises plasticity with gradient-extended hardening/softening response. This variational principle is based on the energetic and the dissipative response functions in the logarithmic strain space, that is framed by a purely geometric pre- and post-processing steps. The numerical implementation exploits the underlying variational structure, yielding a canonical symmetric structure of the monolithic problem. In this context, we develop a robust mixed finite element formulations, including a long-range equivalent plastic strain variable and its dual driving force. To this end, we extend the Q1P0-type and MINI-type finite elements outlined in Chapter 3 to finite gradient plasticity. Various numerical examples, which demonstrate the excellent performance of the proposed mixed variational approach to gradient plasticity in the logarithmic strain space are presented at the end of this chapter.

5.1. Basic kinematics in the Logarithmic Strain Space

5.1.1. Volumetric and isochoric decomposition. We decompose the right Cauchy-Green tensor $\boldsymbol{C}$ defined in (2.13) into volumetric and isochoric parts

$$\boldsymbol{C} = J^{2/3}\bar{\boldsymbol{C}} \tag{5.1}$$

based on the decoupling of the constitutive response into volumetric elastic and isochoric elastic-plastic contributions. The volumetric projection tensors in the Lagrangian geometric setting govern derivatives of *volumetric potentials*

$$\psi_{vol}(\boldsymbol{C}) = U(J) \quad \text{with} \quad J := (\det \boldsymbol{C})^{1/2} \tag{5.2}$$

with respect to the Lagrangian metric tensor $\boldsymbol{C}$. They are defined by

$$\boldsymbol{\mathcal{P}}_{vol} := 2\partial_{\boldsymbol{C}} J \quad \text{and} \quad \boldsymbol{\mathcal{L}}_{vol} := 4\partial^2_{\boldsymbol{CC}} J \tag{5.3}$$

and have the closed-form representations

$$\boldsymbol{\mathcal{P}}_{vol} = J\boldsymbol{C}^{-1} \quad \text{and} \quad \boldsymbol{\mathcal{L}}_{vol} = J[\, \boldsymbol{C}^{-1} \otimes \boldsymbol{C}^{-1} - 2\, \mathbb{I}_{\boldsymbol{C}^{-1}}\,] \tag{5.4}$$

with the fourth-order identity tensor $\mathbb{I}^{ABCD}_{\boldsymbol{C}^{-1}} := \frac{1}{2}\,[C^{-1\,AC}C^{-1\,BD} + C^{-1\,AD}C^{-1\,BC}\,]$ with respect to the metric tensor $\boldsymbol{C}^{-1}$. Given a function $U(J)$, its first derivative by the Lagrangian metric tensor $\boldsymbol{C}$ takes the form

$$\boldsymbol{S}_{vol} := 2\partial_{\boldsymbol{C}} U = U'\boldsymbol{\mathcal{P}}_{vol} \tag{5.5}$$

and the second derivative appears in the format

$$\boldsymbol{\mathcal{C}}_{vol} := 4\partial^2_{\boldsymbol{CC}} U = U''\boldsymbol{\mathcal{P}}_{vol} \otimes \boldsymbol{\mathcal{P}}_{vol} + U'\boldsymbol{\mathcal{L}}_{vol}\ . \tag{5.6}$$

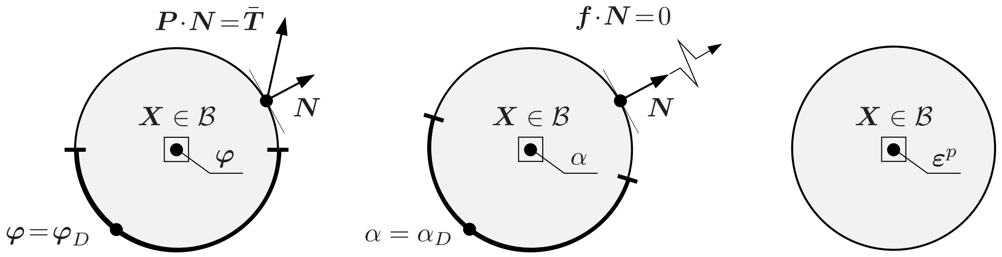
$\boldsymbol{P}\cdot\boldsymbol{N}=\bar{\boldsymbol{T}}$
$\boldsymbol{f}\cdot\boldsymbol{N}=0$
$\boldsymbol{X}\in\mathcal{B}$
$\boldsymbol{N}$
$\boldsymbol{\varphi}$
$\boldsymbol{X}\in\mathcal{B}$
$\boldsymbol{N}$
α
$\boldsymbol{X}\in\mathcal{B}$
$\boldsymbol{\varepsilon}^p$
$\boldsymbol{\varphi}=\boldsymbol{\varphi}_D$
$\alpha=\alpha_D$

macro-motion long-range micro-motion short-range micro-motion

Figure 5.1: Primary fields. a) The macro-motion field $\boldsymbol{\varphi}$ is constrained by the Dirichlet- and Neumann-type boundary conditions $\boldsymbol{\varphi} = \boldsymbol{\varphi}_D$ on $\partial\mathcal{B}_{\boldsymbol{\varphi}}$ and $\boldsymbol{P}\cdot\boldsymbol{N} = \bar{\boldsymbol{T}}$ on $\partial\mathcal{B}_{\boldsymbol{P}}$ with $\partial\mathcal{B} = \partial\mathcal{B}_{\boldsymbol{\varphi}} \cup \partial\mathcal{B}_{\boldsymbol{P}}$. b) The long-range micro-motion field α is restricted by the conditions $\alpha = \alpha_D$ on $\partial\mathcal{B}_\alpha$ and $\boldsymbol{f}\cdot\boldsymbol{N} = 0$ on $\partial\mathcal{B}_{\mathbb{H}}$ with $\partial\mathcal{B} = \partial\mathcal{B}_\alpha \cup \partial\mathcal{B}_{\mathbb{H}}$. c) The short-range micro-motion field $\boldsymbol{\varepsilon}^p$ is locally defined and not constrained by boundary conditions.

The isochoric projection tensors in the Lagrangian geometric setting govern the derivatives of *isochoric potentials*

$$\psi_{iso}(\boldsymbol{C}) = \bar{\psi}(\bar{\boldsymbol{C}}) \quad \text{with} \quad \bar{\boldsymbol{C}} := J^{-2/3}\boldsymbol{C} \tag{5.7}$$

with respect to the Lagrangian metric tensor $\boldsymbol{C}$. They are defined by

$$\boldsymbol{\mathcal{P}}_{iso} := \partial_{\boldsymbol{C}}\bar{\boldsymbol{C}} \quad \text{and} \quad \boldsymbol{\mathcal{L}}_{iso} := 2\partial^2_{\boldsymbol{CC}}\bar{\boldsymbol{C}} \tag{5.8}$$

have the closed-form representation

$$\boldsymbol{\mathcal{P}}_{iso} = J^{-2/3}[\mathbb{I} - \tfrac{1}{3}\boldsymbol{C}\otimes\boldsymbol{C}^{-1}] \ , \tag{5.9}$$

with identity tensor $\mathbb{I}^{AB}{}_{CD} := \delta^A{}_C\delta^B{}_D$, and for the contraction with a given tensor $\bar{\boldsymbol{S}}_{iso}$

$$\begin{aligned} \bar{\boldsymbol{S}}_{iso} : \boldsymbol{\mathcal{L}}_{iso} = {} & \frac{2}{3}J^{-2/3}(\bar{\boldsymbol{S}}_{iso} : \boldsymbol{C})[\mathbb{I}_{\boldsymbol{C}^{-1}} - \tfrac{1}{3}\boldsymbol{C}^{-1}\otimes\boldsymbol{C}^{-1}] \\ - {} & \frac{2}{3}[(\bar{\boldsymbol{S}}_{iso} : \boldsymbol{\mathcal{P}}_{iso})\otimes\boldsymbol{C}^{-1} + \boldsymbol{C}^{-1}\otimes(\bar{\boldsymbol{S}}_{iso} : \boldsymbol{\mathcal{P}}_{iso})] \ , \end{aligned} \tag{5.10}$$

see Miehe & Lambrecht [98] for further details. Given a function $\bar{\psi}(\bar{\boldsymbol{C}})$, its first derivative takes the form

$$\boldsymbol{S}_{iso} := 2\partial_{\boldsymbol{C}}\bar{\psi} = \bar{\boldsymbol{S}}_{iso} : \boldsymbol{\mathcal{P}}_{iso} \quad \text{with} \quad \bar{\boldsymbol{S}}_{iso} := 2\partial_{\bar{\boldsymbol{C}}}\bar{\psi} \ , \tag{5.11}$$

and the second derivative is expressed by

$$\boldsymbol{\mathcal{C}}_{iso} := 4\partial^2_{\boldsymbol{CC}}\bar{\psi} = \boldsymbol{\mathcal{P}}^T_{iso} : \bar{\boldsymbol{\mathcal{C}}}_{iso} : \boldsymbol{\mathcal{P}}_{iso} + \bar{\boldsymbol{S}}_{iso} : \boldsymbol{\mathcal{L}}_{iso} \quad \text{with} \quad \bar{\boldsymbol{\mathcal{C}}}_{iso} := 4\partial^2_{\bar{\boldsymbol{C}}\bar{\boldsymbol{C}}}\bar{\psi} \ . \tag{5.12}$$

5.1.2. Short-range micro-motion fields. Following ideas outlined in the recent work of Miehe [95, 94, 93], we introduce the *Lagrangian plastic metric*

$$\boldsymbol{G}^p \in \mathit{Sym}_+(3) \quad \text{with} \quad \boldsymbol{G}^p(\boldsymbol{X}, t = t_0) = \boldsymbol{G} \tag{5.13}$$

as the basic tensor field that describes locally the plastic deformation. The plastic metric G^p_{AB} is considered as a primitive *short-range internal variable field*, in line with the classical framework of finite plasticity outlined in Green & Naghdi [60]. It is governed by a local flow rule, starting at initial time $t = t_0$ from the reference metric $\boldsymbol{G}$. A simple Lagrangian elastic strain measure, obtained in an *additive format* from the isochoric plastic metric $\bar{\boldsymbol{C}}$ defined in (5.7) and the plastic metric $\boldsymbol{G}^p$ introduced in (5.13), is

$$\bar{\boldsymbol{\varepsilon}}^e := \bar{\boldsymbol{\varepsilon}} - \boldsymbol{\varepsilon}^p \tag{5.14}$$

in terms of the logarithmic Hencky-type total and plastic strains

$$\bar{\boldsymbol{\varepsilon}} := \frac{1}{2} \ln \bar{\boldsymbol{C}} \quad \text{and} \quad \boldsymbol{\varepsilon}^p := \frac{1}{2} \ln \boldsymbol{G}^p \ , \tag{5.15}$$

respectively. Note that $\bar{\boldsymbol{\varepsilon}}$ is a traceless tensor ($\operatorname{tr} \bar{\boldsymbol{\varepsilon}} = 0$). Due to the one–to–one relationship between $\boldsymbol{\varepsilon}^p$ and $\boldsymbol{G}^p$, we consider in what follows the symmetric logarithmic plastic strain

$$\boldsymbol{\varepsilon}^p : \begin{cases} \mathcal{B} \times \mathcal{T} \to \mathbb{R}^6 \\ (\boldsymbol{X}, t) \mapsto \boldsymbol{\varepsilon}^p(\boldsymbol{X}, t) \ , \end{cases} \tag{5.16}$$

as the *micro-motion field for the plastic deformation*, which is illustrated in Figure 5.1c. As shown in Miehe et al. [99], the additive logarithmic measure $\boldsymbol{\varepsilon}^e$ defined in (5.14) is close to logarithmic elastic strain measures in plastic-rotation-free multiplicative plasticity. However, due to its a priori additive nature, it allows a straightforward, modular incorporation of complex anisotropic constitutive structures of the geometric linear theory into the large strain framework. Such a kinematic framework is extremely convenient for the modeling of phenomenological plasticity of metal poly-crystals or glassy polymers, where elastic strains usually remain small.

5.1.3. Lagrangian logarithmic projection tensors. The logarithmic projection tensors in the Lagrangian geometric setting govern derivatives of *potentials defined in the Lagrangian logarithmic strain space*

$$\bar{\psi}(\bar{\boldsymbol{C}}) = \bar{\psi}_{log}(\bar{\boldsymbol{\varepsilon}}) \quad \text{with} \quad \bar{\boldsymbol{\varepsilon}} := \frac{1}{2} \ln \bar{\boldsymbol{C}} \tag{5.17}$$

with respect to the isochoric part $\bar{\boldsymbol{C}}$ of the Lagrangian metric tensor $\boldsymbol{C}$ and defined as

$$\boldsymbol{\mathcal{P}}_{log} := 2 \partial_{\bar{\boldsymbol{C}}} \bar{\boldsymbol{\varepsilon}} \quad \text{and} \quad \boldsymbol{\mathcal{L}}_{log} := 4 \partial^2_{\bar{\boldsymbol{C}}\bar{\boldsymbol{C}}} \bar{\boldsymbol{\varepsilon}} \ . \tag{5.18}$$

Their computation is based on a spectral decomposition of the isochoric metric $\bar{\boldsymbol{C}}$, i.e. based on the solution of the eigenvalue problem $\bar{\boldsymbol{C}} \boldsymbol{n}_i = \lambda_i \boldsymbol{n}_i$. Then, the deviatoric logarithmic strains appear in the spectral form

$$\bar{\boldsymbol{\varepsilon}} = \textstyle\sum_{i=1}^{3} \frac{1}{2} \ln[\lambda_i] \boldsymbol{n}_i \otimes \boldsymbol{n}_i \ . \tag{5.19}$$

The computation of the above projection tensors follows in a straightforward manner, e.g.

$$\boldsymbol{\mathcal{P}}_{log} = \textstyle\sum_{i=1}^{3} \bar{\lambda}_i^{-1} [\boldsymbol{n}^i \otimes \boldsymbol{n}^i] \partial_{\bar{\boldsymbol{C}}} \lambda_i + \sum_{i=1}^{3} \ln[\lambda_i] \partial_{\bar{\boldsymbol{C}}} [\boldsymbol{n}_i \otimes \boldsymbol{n}_i] \ . \tag{5.20}$$

Closed forms are summarized in Box 1, taken form Miehe & Lambrecht [98], which account for special cases with equal eigenvalues. Items 1 and 2 in Box 1 govern *geometric pre- and post-processing steps*, the key ingredients of additive metric-type finite elasto-plasticity in the logarithmic strain space proposed by Miehe et al. [99]. Given a function $\bar{\psi}_{log}(\bar{\boldsymbol{\varepsilon}})$, its first derivative is written as

$$\bar{\boldsymbol{S}}_{iso} := 2 \partial_{\bar{\boldsymbol{C}}} \bar{\psi}_{iso} = \bar{\boldsymbol{S}}_{log} : \boldsymbol{\mathcal{P}}_{log} \quad \text{with} \quad \bar{\boldsymbol{S}}_{log} := \partial_{\bar{\boldsymbol{\varepsilon}}} \bar{\psi}_{log} \ , \tag{5.21}$$

and the second derivative reads

$$\bar{\boldsymbol{\mathcal{C}}}_{iso} := 4 \partial^2_{\bar{\boldsymbol{C}}\bar{\boldsymbol{C}}} \bar{\psi}_{iso} = \boldsymbol{\mathcal{P}}^T_{log} : \bar{\boldsymbol{\mathcal{C}}}_{log} : \boldsymbol{\mathcal{P}}_{log} + \bar{\boldsymbol{S}}_{log} : \boldsymbol{\mathcal{L}}_{log} \quad \text{with} \quad \bar{\boldsymbol{\mathcal{C}}}_{log} := \partial^2_{\bar{\boldsymbol{\varepsilon}}\bar{\boldsymbol{\varepsilon}}} \bar{\psi}_{log} \ . \tag{5.22}$$

Box 1: *ALGO*: Processing in/out of Isochoric Logarithmic Strain Space.

1. *Geometric Pre–Processing.* Given is the current isochoric metric tensor $\bar{\boldsymbol{C}}$. Solving eigenvalue problem $\bar{\boldsymbol{C}}\boldsymbol{n}_i = \lambda_i \boldsymbol{n}_i$ and setting $e_i = \frac{1}{2} \ln \lambda_i$ results in the deviatoric logarithmic strains

   $$\bar{\boldsymbol{\varepsilon}} = \textstyle\sum_{i=1}^{3} e_i \boldsymbol{n}_i \otimes \boldsymbol{n}_i \ .$$

2. *Geometric Post–Processing.* Given are the deviatoric stresses $\bar{\boldsymbol{S}}_{log}$ and the moduli $\bar{\boldsymbol{\mathcal{C}}}_{log}$ in the logarithmic stain space. Setting $\zeta_{ij} = \bar{\boldsymbol{S}}_{log} : (\boldsymbol{n}_i \otimes \boldsymbol{n}_j)$ yields the coefficients:

   For three different eigenvalues $\lambda_{\bar{i}} \neq \lambda_{\bar{j}} \neq \lambda_{\bar{k}}$:

   $$\begin{aligned} &\vartheta_{ij} := (e_i - e_j)/(\lambda_i - \lambda_j),\ \xi_{ij} := (\vartheta_{ij} - \tfrac{1}{2}\lambda_j^{-1})/(\lambda_i - \lambda_j) \\ &\bar{\eta} \ \ := \textstyle\sum_i^3 \sum_{j\neq i}^3 \sum_{k\neq i, k\neq j}^3 e_i/[2(\lambda_i - \lambda_j)(\lambda_i - \lambda_k)] \ , \end{aligned}$$

   for two equal eigenvalues $\lambda_{\bar{i}} = \lambda_{\bar{j}} \neq \lambda_{\bar{k}}$:

   $$\begin{aligned} &\vartheta_{\bar{i}\bar{j}} = \vartheta_{\bar{j}\bar{i}} := \tfrac{1}{2}\lambda_{\bar{i}}^{-1},\ \xi_{\bar{i}\bar{j}} = \xi_{\bar{j}\bar{i}} := -\tfrac{1}{4}\lambda_{\bar{i}}^{-2},\ \bar{\eta} := \xi_{\bar{k}\bar{i}} \\ &\vartheta_{ij} := (e_i - e_j)/(\lambda_i - \lambda_j),\ \xi_{ij} := (\vartheta_{ij} - \tfrac{1}{2}\lambda_j^{-1})/(\lambda_i - \lambda_j) \ \forall\ i, j = \bar{k} \ , \end{aligned}$$

   for three equal eigenvalues $\lambda_{\bar{i}} = \lambda_{\bar{j}} = \lambda_{\bar{k}}$:

   $$\vartheta_{ij} := \tfrac{1}{2}\lambda_{\bar{i}}^{-1},\ \xi_{ij} = \bar{\eta} := -\tfrac{1}{4}\lambda_{\bar{i}}^{-2} \ .$$

   Set $\boldsymbol{m}_{ij} = \boldsymbol{n}_i \otimes \boldsymbol{n}_j + \boldsymbol{n}_j \otimes \boldsymbol{n}_i$ and computing the Lagrangian projection tensors

   $$\begin{aligned} \boldsymbol{\mathcal{P}}_{log} \ &= \textstyle\sum_i^3 \lambda_i^{-1} \boldsymbol{n}_i \otimes \boldsymbol{n}_i \otimes \boldsymbol{m}_{ii} + \sum_i^3 \sum_{j\neq i}^3 \vartheta_{ij} \boldsymbol{n}_i \otimes \boldsymbol{n}_j \otimes \boldsymbol{m}_{ij} \\ \bar{\boldsymbol{S}}_{log} : \boldsymbol{\mathcal{L}}_{log} \ &= \textstyle\sum_i^3 -2\lambda_i^{-2}\zeta_{ii} \boldsymbol{m}_{ii} \otimes \boldsymbol{m}_{ii} + \sum_i^3 \sum_{j\neq i}^3 \sum_{k\neq i, k\neq j}^3 2\bar{\eta}\zeta_{ij} \boldsymbol{m}_{ik} \otimes \boldsymbol{m}_{jk} \\ &\quad + \textstyle\sum_i^3 \sum_{j\neq i}^3 2\xi_{ij} [\zeta_{ij}(\boldsymbol{m}_{ij} \otimes \boldsymbol{m}_{jj} + \boldsymbol{m}_{jj} \otimes \boldsymbol{m}_{ij}) + \zeta_{jj} \boldsymbol{m}_{ij} \otimes \boldsymbol{m}_{ij}] \ , \end{aligned}$$

   allows to compute the Lagrangian stresses and moduli in isochoric space

   $$\bar{\boldsymbol{S}}_{iso} = \bar{\boldsymbol{S}}_{log} : \boldsymbol{\mathcal{P}}_{log} \quad \text{and} \quad \bar{\boldsymbol{\mathcal{C}}}_{iso} = \boldsymbol{\mathcal{P}}_{log}^T : \bar{\boldsymbol{\mathcal{C}}}_{log} : \boldsymbol{\mathcal{P}}_{log} + \bar{\boldsymbol{S}}_{log} : \boldsymbol{\mathcal{L}}_{log} \ .$$

5.1.4. Long-range micro-motion field. We develop a framework of isotropic gradient plasticity at finite strains. To this end, we introduce the long-range micro-motion field $\alpha(\boldsymbol{X}, t)$ demonstrated in Figure 5.1b as a phenomenological hardening/softening variable field

$$\alpha : \left\{ \begin{array}{l} \mathcal{B} \times \mathcal{T} \rightarrow \mathbb{R} \\ (\boldsymbol{X}, t) \mapsto \alpha(\boldsymbol{X}, t) \end{array} \right. \tag{5.23}$$

that defines an equivalent plastic strain in the logarithmic strain space by the evolution equation

$$\dot{\alpha} = \sqrt{\frac{2}{3}}\ ||\dot{\boldsymbol{\varepsilon}}^p|| \quad \text{with} \quad \dot{\alpha} \geq 0 \ . \tag{5.24}$$

It starts to evolve from the initial condition $\alpha(\boldsymbol{X}, t_0) = \mathit{0}$. To account for size effect of the non-local theory of metal plasticity, we introduce the *plastic length scale* l_p as discussed in Chapter 3.

5.2. Energetic and dissipative response functions

5.2.1. Energetic response function. With the above kinematic equations at hand, we specify now a particular model of gradient plasticity in the logarithmic strain space. Hence, the subsequent model problem of von Mises gradient plasticity is described by the three primary fields

$$\text{Primary Fields: } \{\, \boldsymbol{\varphi}, \alpha, \boldsymbol{\varepsilon}^p \,\} \tag{5.25}$$

introduced in (2.3), (5.23) and (5.16). In this, $\boldsymbol{\varphi}$ is the *long-range macro-motion field*, α is a *long-range micro-motion field* and $\boldsymbol{\varepsilon}^p$ is a *short-range micro-motion field* as shown in Figure 5.1. They define the following objective constitutive state:

$$\text{Constitutive State: } \mathfrak{c} := \{\, J, \bar{\mathfrak{c}} \,\} \text{ with } \bar{\mathfrak{c}} := \{\, \bar{\boldsymbol{\varepsilon}}, \boldsymbol{\varepsilon}^p, \alpha, \nabla\alpha \,\}\ . \tag{5.26}$$

It includes, as a total isochoric strain measure, the logarithmic strain deviator $\bar{\boldsymbol{\varepsilon}}$ defined in (5.15). The gradient of the logarithmic plastic strain does not enter the constitutive state. Thus, $\boldsymbol{\varepsilon}^p$ is of short-range in the sense of a classical internal variable field. Here we emphasis that the gradient of equivalent plastic strain is a referential quantity $\nabla\alpha \equiv \nabla_{\boldsymbol{X}}\alpha$. Focusing on *isotropic* metal plasticity, we consider the decomposition of the energy storage function into volumetric elastic and isochoric elastic-plastic parts

$$\psi(\mathfrak{c}) = U(J) + \bar{\psi}_{log}(\bar{\boldsymbol{\varepsilon}}, \boldsymbol{\varepsilon}^p, \alpha, \nabla\alpha) \quad \text{with} \quad \bar{\psi}_{log} = \bar{\psi}^e_{log}(\bar{\boldsymbol{\varepsilon}} - \boldsymbol{\varepsilon}^p) + \bar{\psi}^p(\alpha, \nabla\alpha)\ . \tag{5.27}$$

Here, the isotropic elastic contributions are assumed to be quadratic functions

$$U = \frac{\kappa}{2}(J-1)^2 \quad \text{and} \quad \bar{\psi}^e_{log} = \mu\, \bar{\boldsymbol{\varepsilon}}^e : \bar{\boldsymbol{\varepsilon}}^e\ , \tag{5.28}$$

where κ and μ are the elastic bulk and shear moduli, respectively. The plastic contribution is assumed to be of the form

$$\bar{\psi}^p(\alpha, \nabla\alpha) = \bar{\psi}^p_{loc}(\alpha) + \bar{\psi}^p_{grad}(\nabla\alpha)\ . \tag{5.29}$$

The microscopic energetic contribution $\bar{\psi}^p_{loc}(\alpha)$ that describes a possibly nonlinear isotropic *local* hardening/softening is defined as

$$\bar{\psi}^p(\alpha) = \frac{1}{2}h\alpha^2 + (y_\infty - y_0)(\alpha + \exp[-\omega\alpha]/\omega)\,, \tag{5.30}$$

in terms of the isotropic hardening modulus h, the infinite and initial yield stresses y_∞ and y_0 and the saturation parameter ω are introduced. The gradient part of plastic contribution is assumed to be quadratic and has the form

$$\bar{\psi}^p_{grad}(\nabla\alpha) = \frac{\mu l_p^2}{2}|\nabla\alpha|^2\,, \tag{5.31}$$

governed by the *energetic length scale* l_p that accounts for nonlocal hardening effects. The evolution of the free energy takes the form

$$\frac{d}{dt}\psi(\mathfrak{c}) = \boldsymbol{P} : \nabla\dot{\boldsymbol{\varphi}} - \bar{\boldsymbol{\sigma}} : \dot{\boldsymbol{\varepsilon}}^p + f\dot{\alpha} + \boldsymbol{f}\cdot\nabla\dot{\alpha} \tag{5.32}$$

with the *definition* of the energetic first Piola nominal stress

$$\boldsymbol{P} := \boldsymbol{g}\boldsymbol{F}(\boldsymbol{S}_{vol} + \boldsymbol{S}_{iso}) \tag{5.33}$$

in terms of the second Piola-Kirchhoff stress definitions, as illustrated in Figure 2.4, as

$$\boldsymbol{S}_{vol} := 2\partial_{\boldsymbol{C}} U = U' \boldsymbol{\mathcal{P}}_{vol} \quad \text{and} \quad \boldsymbol{S}_{iso} := 2\partial_{\boldsymbol{C}} \psi^e_{iso} = \bar{\boldsymbol{\sigma}} : \boldsymbol{\mathcal{P}}_{log} : \boldsymbol{\mathcal{P}}_{iso} \tag{5.34}$$

Furthermore, we introduced in (5.32) per definition

$$\bar{\boldsymbol{\sigma}} := 2\mu(\bar{\boldsymbol{\varepsilon}} - \boldsymbol{\varepsilon}^p) \ , \quad f := \bar{\psi}^{p\prime}_{loc} \ , \quad \boldsymbol{f} := \mu l_p^2 \nabla\alpha \ . \tag{5.35}$$

Note that (5.34) contains a successive projection of the deviatoric stress tensor $\bar{\boldsymbol{\sigma}} = \partial_{\bar{\boldsymbol{\varepsilon}}} \bar{\psi}^e = -\partial_{\bar{\boldsymbol{\varepsilon}}^p} \bar{\psi}^e$, first from the logarithmic space into the isochoric space, governed by $\boldsymbol{\mathcal{P}}_{log}$, and then from the isochoric space into the Lagrangian space, governed by $\boldsymbol{\mathcal{P}}_{iso}$.

5.2.2. Dissipative response function. For the model problem under consideration, we introduce the dissipative force fields

$$\bar{\boldsymbol{\mathfrak{s}}} : \begin{cases} \mathcal{B} \times \mathcal{T} \rightarrow \mathbb{R}^6 \\ (\boldsymbol{X}, t) \mapsto \bar{\boldsymbol{\mathfrak{s}}}(\boldsymbol{X}, t) \end{cases} \quad \text{and} \quad \mathfrak{f} : \begin{cases} \mathcal{B} \times \mathcal{T} \rightarrow \mathbb{R} \\ (\boldsymbol{X}, t) \mapsto \mathfrak{f}(\boldsymbol{X}, t) \end{cases} \tag{5.36}$$

where $\bar{\boldsymbol{\mathfrak{s}}}$ is dual to $\boldsymbol{\varepsilon}^p$ given in (5.16) and $\mathfrak{f}$ dual to α given in (5.23). Hence, for the subsequent modeling of isochoric plasticity, we focus on the dissipative force array

$$\text{Driving Forces: } \bar{\boldsymbol{\mathfrak{b}}} := \{ \, \boldsymbol{0}, \bar{\boldsymbol{\mathfrak{s}}}, -\mathfrak{f}, \boldsymbol{0} \, \} \tag{5.37}$$

dual to the isochoric constitutive state $\bar{\boldsymbol{\mathfrak{c}}}$ defined in (5.26). For von Mises-type gradient plasticity, we focus on the yield function

$$\chi(\bar{\boldsymbol{\mathfrak{b}}}) := |\bar{\boldsymbol{\mathfrak{s}}}| - \sqrt{\tfrac{2}{3}}[\, y_0 + \mathfrak{f} \,] \ , \tag{5.38}$$

where y_0 is the initial yield stress. With this function at hand, we define a dual dissipation function for gradient-type finite viscoplasticity

$$\phi^*(\bar{\boldsymbol{\mathfrak{b}}}) = \frac{1}{2\eta_p} \langle \, |\bar{\boldsymbol{\mathfrak{s}}}| - \sqrt{\tfrac{2}{3}}[\, y_0 + \mathfrak{f} \,] \, \rangle^2 \ , \tag{5.39}$$

where η_p is the viscosity of the plastic overstress response. Here, $\langle x \rangle := (x + |x|)/2$ is the Macaulay bracket. It is worth mentioning at this stage that the computational setting of gradient viscoplasticity outlined here is also applicable for the *exact rate-independent limit* $\eta_p = 0$.

5.3. Mixed variational principle for the evolution problem

Following conceptually the recent work of Miehe [96], a mixed rate-type variational principle that contains the dissipative driving force is based on the potential

$$\Pi^*(\dot{\boldsymbol{\varphi}}, \dot{\alpha}, \dot{\boldsymbol{\varepsilon}}^p, \bar{\boldsymbol{\mathfrak{b}}}) = \int_{\mathcal{B}} \pi^*(\dot{\boldsymbol{\mathfrak{c}}}, \bar{\boldsymbol{\mathfrak{b}}}; \boldsymbol{\mathfrak{c}}) \, dV \ - \ P_{ext}(\dot{\boldsymbol{\varphi}}; t) \tag{5.40}$$

with external power functional $P_{ext} := \int_{\mathcal{B}} \dot{\boldsymbol{\varphi}} \cdot \bar{\boldsymbol{\gamma}} dV + \int_{\partial\mathcal{B}_t} \dot{\boldsymbol{\varphi}} \cdot \bar{\boldsymbol{t}} dA$ and the *mixed rate potential* per unit volume given by

$$\pi^*(\dot{\boldsymbol{\mathfrak{c}}}, \bar{\boldsymbol{\mathfrak{b}}}) = \frac{d}{dt}\psi(\boldsymbol{\mathfrak{c}}) + \bar{\boldsymbol{\mathfrak{b}}} \cdot \dot{\bar{\boldsymbol{\mathfrak{c}}}} - \phi^*(\bar{\boldsymbol{\mathfrak{b}}}) \tag{5.41}$$

that contains the evolution of the energy storage function, the dissipation and the dual dissipation function. Note that the potential π^* is *linear* with respect to the rate $\dot{\bar{\mathfrak{c}}}$ of the constitutive state and *concave* with respect to the dissipative driving forces $\bar{\mathfrak{b}}$. The latter property is fully determined by the dual dissipation potential function ϕ^*, whose convexity is implied by the second axiom of thermodynamics. The only nonlinear entry in the potential Π^* occurs through the dual dissipation function ϕ^*. The evolution of the macro- and micro-motion fields as well as the driving forces at a given state is determined by the *mixed variational principle*

$$\{\dot{\boldsymbol{\varphi}}, \dot{\alpha}, \dot{\boldsymbol{\varepsilon}}^p, \bar{\boldsymbol{\mathfrak{s}}}, \mathfrak{f}\} = \operatorname{Arg}\{ \inf_{\dot{\boldsymbol{\varphi}}} \inf_{\dot{\alpha}} \inf_{\dot{\boldsymbol{\varepsilon}}^p} \sup_{\bar{\boldsymbol{\mathfrak{s}}}} \sup_{\mathfrak{f}} \Pi^*(\dot{\boldsymbol{\varphi}}, \dot{\alpha}, \dot{\boldsymbol{\varepsilon}}^p, \bar{\boldsymbol{\mathfrak{s}}}, \mathfrak{f}) \} \,, \tag{5.42}$$

which defines at the given state $\{\boldsymbol{\varphi}, \alpha, \boldsymbol{\varepsilon}^p\}$ at time t the rates of the macro- and micro-motion fields along with the dissipative driving forces. The specification of the continuous rate potential introduced in (5.41) for the mixed plasticity model under consideration reads

$$\pi^*(\dot{\bar{\mathfrak{c}}}, \bar{\mathfrak{b}}) = \boldsymbol{P} : \nabla\dot{\boldsymbol{\varphi}} - \bar{\boldsymbol{\sigma}} : \dot{\boldsymbol{\varepsilon}}^p + f\dot{\alpha} + \boldsymbol{f} \cdot \nabla\dot{\alpha} + \bar{\boldsymbol{\mathfrak{s}}} : \dot{\boldsymbol{\varepsilon}}^p - \mathfrak{f}\dot{\alpha} - \phi^*(\bar{\boldsymbol{\mathfrak{s}}}, \mathfrak{f}) \,, \tag{5.43}$$

where $\boldsymbol{P}$, $\bar{\boldsymbol{\sigma}}$, f and $\boldsymbol{f}$ are defined in (5.33) and (5.35). Taking the variation of the potential (5.40), we find as the Euler equations of the mixed variational principle (5.42)

$$\begin{array}{rrl} 1. & \delta_{\dot{\boldsymbol{\varphi}}}\pi^* & \equiv -\mathrm{DIV}\,[\boldsymbol{P}] = \ \bar{\boldsymbol{\gamma}} \ , \\ 2. & \delta_{\dot{\alpha}}\pi^* & \equiv f - \mathrm{DIV}\,[\boldsymbol{f}] - \mathfrak{f} = 0 \ , \\ 3. & \delta_{\mathfrak{f}}\pi^* & \equiv -\dot{\alpha} + \lambda\sqrt{2/3} = 0 \ , \\ 4. & \delta_{\dot{\boldsymbol{\varepsilon}}^p}\pi^* & \equiv -\bar{\boldsymbol{\sigma}} + \bar{\boldsymbol{\mathfrak{s}}} = \boldsymbol{0} \ , \\ 5. & \delta_{\bar{\boldsymbol{\mathfrak{s}}}}\pi^* & \equiv \dot{\boldsymbol{\varepsilon}}^p - \lambda\bar{\boldsymbol{\mathfrak{n}}} = \boldsymbol{0} \ , \end{array} \tag{5.44}$$

along with the Neumann-type boundary conditions

$$\boldsymbol{P} \cdot \boldsymbol{N} = \bar{\boldsymbol{T}} \text{ on } \partial\mathcal{B}_P \quad \text{and} \quad \boldsymbol{f} \cdot \boldsymbol{N} = \boldsymbol{0} \text{ on } \partial\mathcal{B}_{\mathbb{H}} \tag{5.45}$$

associated with the macro-motion $\boldsymbol{\varphi}$ and the long-range micro-motion α. In (5.44), we introduced per definition the *amount* and the *direction* of plastic flow as

$$\lambda := \frac{1}{\eta_p}\langle\, |\bar{\boldsymbol{\mathfrak{s}}}| - \sqrt{\tfrac{2}{3}}[y_0 + \mathfrak{f}\,]\,\rangle \quad \text{and} \quad \bar{\boldsymbol{\mathfrak{n}}} := \bar{\boldsymbol{\mathfrak{s}}}/|\bar{\boldsymbol{\mathfrak{s}}}| \ . \tag{5.46}$$

This summarizes the formulation of the model of finite gradient plasticity in the logarithmic strain space. Note that all coupled field equations (5.44) in the domain $\mathcal{B}$ are governed by variational derivatives of the rate potential π^* defined in (5.43).

5.3.1. Time discrete incremental variational principle. We consider a finite time increment $[t_n, t_{n+1}]$, where $\tau_{n+1} := t_{n+1} - t_n > 0$ denotes the step length. All fields at time t_n are assumed to be *known*. The goal then is to determine the fields at time t_{n+1} based on variational principles valid for the time increment under consideration. Subsequently, all variables without subscript are evaluated at time t_{n+1}. In particular,

$$\bar{\mathfrak{c}} := \{\bar{\varepsilon}, \boldsymbol{\varepsilon}^p, \alpha, \nabla\alpha\} \quad \text{and} \quad \bar{\mathfrak{c}}_n := \{\bar{\varepsilon}_n, \boldsymbol{\varepsilon}^p_n, \alpha_n, \nabla\alpha_n\} \tag{5.47}$$

denote the isochoric constitutive states (5.26) at time t_{n+1} and time t_n, respectively. Furthermore,

$$\bar{\mathfrak{b}} := \{\, \mathbf{0}, \bar{\boldsymbol{\mathfrak{s}}}, -\mathfrak{f}, \mathbf{0} \,\} \tag{5.48}$$

indicate the array of active dissipative driving forces (5.37) at the current discrete time at time t_{n+1}. A mixed incremental variational principle of gradient plasticity associated with the finite time increment $[t_n, t_{n+1}]$ is based on the mixed potential

$$\Pi^{*\tau}(\boldsymbol{\varphi}, \alpha, \boldsymbol{\varepsilon}^p, \bar{\boldsymbol{\mathfrak{b}}}) = \int_{\mathcal{B}} \pi^{*\tau}(\boldsymbol{\mathfrak{c}}, \bar{\boldsymbol{\mathfrak{b}}})\, dV \;-\; P^{\tau}_{ext}(\boldsymbol{\varphi}) \;, \tag{5.49}$$

in terms of the *mixed incremental potential* per unit volume $\pi^{*\tau}$, defined by an algorithmic approximation

$$\pi^{*\tau}(\boldsymbol{\mathfrak{c}}, \bar{\boldsymbol{\mathfrak{b}}}) = Algo\{ \int_{t_n}^{t_{n+1}} \pi^*(\dot{\boldsymbol{\mathfrak{c}}}, \bar{\boldsymbol{\mathfrak{b}}}) dt \} \tag{5.50}$$

in terms of the continuous rate-type potential π^* introduced in (5.41). The algorithm *Algo* approximates the time integration of the continuous rate-potential π^* in the discrete time interval $[t_n, t_{n+1}]$. As a consequence, the incremental potential $\pi^{*\tau}$ is considered to be a function of the current variables $\boldsymbol{\mathfrak{c}}$ and $\bar{\boldsymbol{\mathfrak{b}}}$ at time t_{n+1} *at given state* $\boldsymbol{\mathfrak{c}}_n$ at time t_n. The macro- and micro-motion fields as well as the driving forces at the discrete time t_{n+1} are then determined by the *mixed incremental variational principle*

$$\{\boldsymbol{\varphi}, \alpha, \boldsymbol{\varepsilon}^p, \bar{\boldsymbol{\mathfrak{s}}}, \mathfrak{f}\} = \text{Arg}\{ \inf_{\boldsymbol{\varphi}} \inf_{\alpha} \inf_{\boldsymbol{\varepsilon}^p} \sup_{\bar{\boldsymbol{\mathfrak{s}}}} \sup_{\mathfrak{f}} \Pi^{*\tau}(\boldsymbol{\varphi}, \alpha, \boldsymbol{\varepsilon}^p, \bar{\boldsymbol{\mathfrak{s}}}, \mathfrak{f}) \} \;. \tag{5.51}$$

The algorithm is constructed such that the variation of the potential (5.49) for admissible variations $\delta\boldsymbol{\varphi} \in \mathcal{W}^0_{\boldsymbol{\varphi}}$, $\delta\alpha \in \mathcal{W}^0_{\alpha}$, $\delta\bar{\boldsymbol{\mathfrak{s}}} \in L^2$ and $\delta\mathfrak{f} \in L^2$ yields as the Euler equations *geometrically consistent algorithmic counterparts* of the Euler equations (5.44) of the continuous rate-type variational principle (5.42). For the model of finite gradient plasticity in the logarithmic strain space considered here, this is achieved by a straightforward application of a backward Euler scheme. This yields the closed form of the incremental potential

$$\pi^{*\tau}(\boldsymbol{\mathfrak{c}}, \bar{\boldsymbol{\mathfrak{b}}}) = U(J) + \bar{\psi}_{log}(\bar{\boldsymbol{\varepsilon}}, \boldsymbol{\varepsilon}^p, \alpha, \nabla\alpha) + \;\bar{\boldsymbol{\mathfrak{s}}} : (\boldsymbol{\varepsilon}^p - \boldsymbol{\varepsilon}^p_n) - \mathfrak{f} \cdot (\alpha - \alpha_n) - \tau\phi^*(\bar{\boldsymbol{\mathfrak{s}}}, \mathfrak{f}) \tag{5.52}$$

in terms of the free energy functions U, $\bar{\psi}_{log}$ and the dual dissipation function ϕ^* defined in (5.27) and (5.39), respectively. Here, we dropped constant terms in order to get a compact notation.

5.3.2. Euler Equations of the Mixed Incremental Variational Principle. Taking the variation of the incremental potential (5.49), we find as the Euler equations of the mixed variational principle

$$\begin{array}{lrl}
1. & \delta_{\boldsymbol{\varphi}}\pi^{*\tau} & \equiv -\text{DIV}\,[\boldsymbol{P}] = \;\bar{\boldsymbol{\gamma}} \;, \\
2. & \delta_{\alpha}\pi^{*\tau} & \equiv f - \text{DIV}\,[\,\boldsymbol{f}\,] - \mathfrak{f} = \mathit{0} \;, \\
3. & \delta_{\mathfrak{f}}\pi^{*\tau} & \equiv -\alpha + \alpha_n + \gamma\sqrt{2/3} = \mathit{0} \;, \\
4. & \delta_{\boldsymbol{\varepsilon}^p}\pi^{*\tau} & \equiv -\bar{\boldsymbol{\sigma}} + \bar{\boldsymbol{\mathfrak{s}}} = \boldsymbol{\mathit{0}} \;, \\
5. & \delta_{\bar{\boldsymbol{\mathfrak{s}}}}\pi^{*\tau} & \equiv \boldsymbol{\varepsilon}^p - \boldsymbol{\varepsilon}^p_n - \gamma\bar{\boldsymbol{\mathfrak{n}}} = \boldsymbol{\mathit{0}} \;,
\end{array} \tag{5.53}$$

along with the Neumann-type boundary conditions

$$\boldsymbol{P} \cdot \boldsymbol{N} = \bar{\boldsymbol{T}} \text{ on } \partial\mathcal{B}_P \quad \text{and} \quad \boldsymbol{f} \cdot \boldsymbol{N} = \mathit{0} \text{ on } \partial\mathcal{B}_{\mathbb{H}} \tag{5.54}$$

at the current time t_{n+1}. In (5.53), we introduced per definition the *amount* and the *direction* of the incremental plastic flow

$$\gamma := \frac{\tau}{\eta_p}\langle\, |\bar{\boldsymbol{\mathfrak{s}}}| - \sqrt{\tfrac{2}{3}}[y_0 + \mathfrak{f}\,]\, \rangle \quad \text{and} \quad \bar{\boldsymbol{\mathfrak{n}}} := \bar{\boldsymbol{\mathfrak{s}}}/|\bar{\boldsymbol{\mathfrak{s}}}| \;. \tag{5.55}$$

Box 2: *ALGO*$_{iso}$: Isochoric Gradient Plasticity in Logarithmic Strain Space.

1. *Long–Range State.* Given are the long-range variables $\{\,\boldsymbol{\varphi}, \alpha, \mathfrak{f}\,\}$ at the current time t_{n+1}. Compute the reduced state array in logarithmic strain space

$$\bar{\boldsymbol{\mathfrak{r}}}_{log} := \{\; \bar{\boldsymbol{\varepsilon}}, \alpha, \nabla\alpha, \mathfrak{f}\;\} \quad \text{with} \quad \bar{\boldsymbol{\varepsilon}} := \mathrm{Dev}\{\, \frac{1}{2}\ln[\nabla^T\boldsymbol{\varphi}\nabla\boldsymbol{\varphi}]\,\}$$

2. *Constitutive Box.* Get generalized stresses and moduli in logarithmic strain space and update of short-range history variables form Box 3

$$\boxed{\{\, \bar{\boldsymbol{\mathfrak{S}}}_{log}, \bar{\boldsymbol{\mathfrak{C}}}_{log}\,\} = \mathit{ALGO}_{log}(\bar{\boldsymbol{\mathfrak{r}}}_{log})}$$

3. *Logarithmic Projection.* Compute the generalized stress and moduli arrays by logarithmic projection

$$\bar{\boldsymbol{\mathfrak{S}}}_{iso} := \boldsymbol{\mathfrak{P}}^{*T}_{log}\cdot\bar{\boldsymbol{\mathfrak{S}}}_{log} \quad \text{and} \quad \bar{\boldsymbol{\mathfrak{C}}}_{iso} := \boldsymbol{\mathfrak{P}}^{*T}_{log}\cdot\bar{\boldsymbol{\mathfrak{C}}}_{log}\cdot\boldsymbol{\mathfrak{P}}_{log} + \bar{\boldsymbol{\mathfrak{S}}}_{log}\cdot\boldsymbol{\mathfrak{L}}^{*}_{log}$$

Note that these equations are consistent time-discrete algorithmic counterparts of the Euler equations (5.44)-(5.46) of the continuous rate-type variational principle. Observe in particular the standard backward Euler update structure in $(5.53)_{3,5}$. This summarizes the time-discrete algorithmic formulation of the model of finite gradient plasticity in the logarithmic strain space. Note that all coupled field equations (5.53) at discrete time t_{n+1} are governed by variational derivatives of the incremental potential $\pi^{*\tau}$ defined in (5.52).

5.3.3. Two-steps local-global update schemes. The solution of this incremental variational principle (5.51) is obtained within *two steps*, which correspond to typical algorithmic procedures in computational inelasticity with a *local* constitutive response.

Condensation of local variables. In a *first solution step*, $\Pi^{*\tau}$ in (5.49) is optimized for *given* macro-motion $\boldsymbol{\varphi}$, long-range micro-motion α *and* driving forces $\mathfrak{f}$ with respect to the current short-range micro-motion $\boldsymbol{\varepsilon}^p$ and its dual driving force $\bar{\boldsymbol{\mathfrak{s}}}$. Due to the *local* nature of this optimization problem, we may write

$$(L): \quad \{\boldsymbol{\varepsilon}^p, \bar{\boldsymbol{\mathfrak{s}}}\} = \mathrm{Arg}\{\, \inf_{\boldsymbol{\varepsilon}^p}\sup_{\bar{\boldsymbol{\mathfrak{s}}}} \Pi^{*\tau}(\boldsymbol{\varphi}, \boldsymbol{\varepsilon}^p, \alpha, \bar{\boldsymbol{\mathfrak{s}}}, \mathfrak{f})\,\}\;. \tag{5.56}$$

This variational principle defines locally an isochoric *condensed incremental work potential*

$$\pi^{*\tau}_{red}(\boldsymbol{\mathfrak{r}}) = \inf_{\boldsymbol{\varepsilon}^p}\sup_{\bar{\boldsymbol{\mathfrak{s}}}} \pi^{*\tau}(\boldsymbol{\mathfrak{c}}, \bar{\boldsymbol{\mathfrak{b}}})\;, \tag{5.57}$$

as a function of an *reduced set of variables*

$$\boldsymbol{\mathfrak{r}} := \{\; \tfrac{1}{2}\boldsymbol{C}, \alpha, \nabla\alpha, \mathfrak{f}\;\}\;. \tag{5.58}$$

The Euler equations of (5.56) are identical with the equations $(5.53)_{4,5}$ and define the updates of the short-range variable $\boldsymbol{\varepsilon}^p$ including their dual driving forces $\bar{\boldsymbol{\mathfrak{s}}}$. For von Mises plastic flow, they can be recast into the form

$$\begin{array}{lll} 1. & \delta_{\boldsymbol{\varepsilon}^p}\pi^{*\tau} & \equiv -\bar{\boldsymbol{\mathfrak{s}}}^{trial} + 2\mu\gamma\bar{\boldsymbol{\mathfrak{n}}}^{trial} + \bar{\boldsymbol{\mathfrak{s}}} = \boldsymbol{0}\;, \\ 2. & \delta_{\bar{\boldsymbol{\mathfrak{s}}}}\pi^{*\tau} & \equiv \boldsymbol{\varepsilon}^p - \boldsymbol{\varepsilon}^p_n - \gamma\bar{\boldsymbol{\mathfrak{n}}}^{trial} = \boldsymbol{0}\;, \end{array} \tag{5.59}$$

in terms of the deviatoric trial stress and flow direction

$$\bar{\boldsymbol{\mathfrak{s}}}^{trial} := 2\mu(\bar{\boldsymbol{\varepsilon}} - \boldsymbol{\varepsilon}^p_n) \quad \text{and} \quad \bar{\boldsymbol{\mathfrak{n}}}^{trial} := \bar{\boldsymbol{\mathfrak{s}}}^{trial}/|\bar{\boldsymbol{\mathfrak{s}}}^{trial}| \; . \tag{5.60}$$

Setting $|\bar{\boldsymbol{\mathfrak{s}}}| = |\bar{\boldsymbol{\mathfrak{s}}}^{trial}| - 2\mu\gamma$, we write the yield function in terms of the incremental plastic slip

$$\chi = |\bar{\boldsymbol{\mathfrak{s}}}^{trial}| - 2\mu\gamma - \sqrt{\tfrac{2}{3}}[y_0 + \mathfrak{f}\,] \; . \tag{5.61}$$

Assuming $\chi > 0$, we compute from (5.55) a trial value of the incremental plastic flow

$$\gamma^{trial} := \frac{1}{2\mu + \eta_p/\tau}(\; |\bar{\boldsymbol{\mathfrak{s}}}^{trial}| - \sqrt{\tfrac{2}{3}}(y_0 + \mathfrak{f})\,) \tag{5.62}$$

and define the incremental plastic parameter by

$$\gamma = \begin{cases} \gamma^{trial} & \text{for } \chi > 0 \\ 0 & \text{otherwise} \; . \end{cases} \tag{5.63}$$

Hence, the two equations (5.59) determine $\boldsymbol{\varepsilon}^p$ and $\bar{\boldsymbol{\mathfrak{s}}}$ by a *non-standard radial return step*, driven by the total deviatoric strains $\bar{\boldsymbol{\varepsilon}}$ *and the driving force* $\mathfrak{f}$. Note carefully that the update (5.63) of incremental plastic flow can be performed for the *exact rate-independent limit* $\eta_p = 0$. The algorithmic steps of the local update are summarized in Box 3.

Reduced Global Problem. With the condensed incremental work potential $\pi^{*\tau}_{red}$ defined in (5.57) at hand, we define the reduced potential function

$$\Pi^{*\tau}_{red}(\boldsymbol{\varphi}, \alpha, \mathfrak{f}) = \int_{\mathcal{B}} \pi^{*\tau}_{red}(\boldsymbol{\mathfrak{e}})\, dV \; - \; P^{\tau}_{ext}(\boldsymbol{\varphi}) \; . \tag{5.64}$$

Then, a *second solution step*, governed by the mixed saddle point principle

$$(G): \quad \{\boldsymbol{\varphi}, \alpha, \mathfrak{f}\} = \text{Arg}\{\, \inf_{\boldsymbol{\varphi}} \inf_{\alpha} \sup_{\mathfrak{f}} \Pi^{*\tau}_{red}(\boldsymbol{\varphi}, \alpha, \mathfrak{f}) \;\} \; , \tag{5.65}$$

determines for given state $\{\boldsymbol{\varepsilon}^p_n, \alpha_n\}$ at time t_n and updated short-range variables $\{\boldsymbol{\varepsilon}^p, \bar{\boldsymbol{\mathfrak{s}}}\}$ at time t_{n+1} obtained form step (L) in (5.56) the long-range fields $\{\boldsymbol{\varphi}, \alpha\}$ and the driving forces $\mathfrak{f}$ at time t_{n+1}. The Euler-equations of (5.66) are identical with the equations $(5.53)_{1,2,3}$

$$\begin{array}{lll} 1. & \delta_{\boldsymbol{\varphi}}\pi^{*\tau} & \equiv -\text{DIV}\,[\boldsymbol{P}] = \overline{\boldsymbol{\gamma}} \; , \\ 2. & \delta_{\alpha}\pi^{*\tau} & \equiv f - \text{DIV}\,[\,\boldsymbol{f}\,] - \mathfrak{f} = \mathit{0} \; , \\ 3. & \delta_{\mathfrak{f}}\pi^{*\tau} & \equiv -\alpha + \alpha_n + \gamma\sqrt{2/3} = \mathit{0} \; . \end{array} \tag{5.66}$$

5.3.4. Weak form of reduced global equations. The variation of the functional (5.64) gives the necessary condition

$$\delta\Pi^{*\tau}_{red} = \int_{\mathcal{B}} \boldsymbol{\mathfrak{S}} \cdot \delta\boldsymbol{\mathfrak{e}}\, dV \; - \; P^{\tau}_{ext}(\delta\boldsymbol{\varphi}) \; = 0 \; , \tag{5.67}$$

having for dead external loads the linearization

$$\Delta\delta\Pi^{*\tau}_{red} = \int_{\mathcal{B}} [\; \boldsymbol{\mathfrak{S}} \cdot \Delta(\delta\boldsymbol{\mathfrak{e}}) + \delta\boldsymbol{\mathfrak{e}} \cdot \boldsymbol{\mathfrak{C}} \cdot \Delta\boldsymbol{\mathfrak{e}} \;]\, dV \; , \tag{5.68}$$

in terms of the generalized stress and tangent moduli arrays, i.e. the derivatives of the incremental potential $\pi^{*\tau}_{red}$ defined in (5.57)

$$\mathfrak{S} := \partial_{\mathfrak{r}} \pi^{*\tau}_{red} \quad \text{and} \quad \mathfrak{C} := \partial^2_{\mathfrak{r}\mathfrak{r}} \pi^{*\tau}_{red} \tag{5.69}$$

with respect to the reduced set of variables (5.58). $\delta\mathfrak{r} := \{ \mathrm{sym}[\nabla^T \boldsymbol{\varphi} \boldsymbol{g} \nabla \delta\boldsymbol{\varphi}], \delta\alpha, \nabla\delta\alpha, \delta\mathfrak{f} \}$ is the variation of this reduced state based on the admissible test functions $\delta\boldsymbol{\varphi} \in \mathcal{W}^0_{\boldsymbol{\varphi}}$, $\delta\alpha \in \mathcal{W}^0_{\alpha}$ and $\delta\mathfrak{f} \in L^2$. Note, that the above statement (5.67) can be interpreted as a *virtual work balance* of internal and external actions at the discrete time t_{n+1}. Furthermore, observe the *symmetry of the tangent arrays* as a consequence of the underlined variational principle.

Volumetric and isochoric projections. The arrays defined in (5.69) decompose into *elastic volumetric* and *elastic-plastic isochoric* contributions according to

$$\mathfrak{S} := U' \boldsymbol{\mathcal{P}}^*_{vol} + \boldsymbol{\mathcal{P}}^{*T}_{iso} \cdot \bar{\mathfrak{S}}_{iso} \tag{5.70}$$

for the generalized stress array and the moduli array

$$\mathfrak{C} := U'' \boldsymbol{\mathcal{P}}^*_{vol} \otimes \boldsymbol{\mathcal{P}}^*_{vol} + U' \boldsymbol{\mathcal{L}}^*_{vol} + \boldsymbol{\mathcal{P}}^{*T}_{iso} \cdot \bar{\mathfrak{C}}_{iso} \cdot \boldsymbol{\mathcal{P}}^*_{iso} + \bar{\mathfrak{S}}_{iso} \cdot \boldsymbol{\mathcal{L}}^*_{iso} \tag{5.71}$$

in terms of the isochoric stress arrays

$$\bar{\mathfrak{S}}_{iso} := \partial_{\bar{\mathfrak{r}}} \pi^{*\tau}_{red} \quad \text{and} \quad \bar{\mathfrak{C}}_{iso} := \partial^2_{\bar{\mathfrak{r}}\bar{\mathfrak{r}}} \pi^{*\tau}_{red} \tag{5.72}$$

obtained by the derivative of the incremental potential $\pi^{*\tau}_{red}$ with respect to the *reduced isochoric state array*

$$\bar{\mathfrak{r}} := \{ \, \tfrac{1}{2} \bar{\boldsymbol{C}}, \alpha, \nabla\alpha, \mathfrak{f} \, \} \; . \tag{5.73}$$

The projection arrays $\boldsymbol{\mathcal{P}}^*_{vol}$ and $\boldsymbol{\mathcal{P}}^*_{iso}$ formally extend the projection tensors introduced in (5.3) and (5.8) to the array structure, such as

$$\boldsymbol{\mathcal{P}}^*_{vol} := \begin{bmatrix} \boldsymbol{\mathcal{P}}_{vol} \\ \cdot \\ \cdot \\ \cdot \end{bmatrix} \quad \text{and} \quad \boldsymbol{\mathcal{P}}^*_{iso} := \begin{bmatrix} \boldsymbol{\mathcal{P}}_{iso} & \cdot & \cdot & \cdot \\ \cdot & \mathit{1} & \cdot & \cdot \\ \cdot & \cdot & \boldsymbol{\mathit{1}} & \cdot \\ \cdot & \cdot & \cdot & \mathit{1} \end{bmatrix} , \tag{5.74}$$

allowing the compact representations (5.70) and (5.71) of the generalized stress and moduli arrays.

Logarithmic projection. In turn, these stress and moduli arrays are expressed in the form

$$\bar{\mathfrak{S}}_{iso} := \boldsymbol{\mathcal{P}}^{*T}_{log} \cdot \bar{\mathfrak{S}}_{log} \quad \text{and} \quad \bar{\mathfrak{C}}_{iso} := \boldsymbol{\mathcal{P}}^{*T}_{log} \cdot \bar{\mathfrak{C}}_{log} \cdot \boldsymbol{\mathcal{P}}_{log} + \bar{\mathfrak{S}}_{log} \cdot \boldsymbol{\mathcal{L}}^*_{log} \tag{5.75}$$

in terms of the stress and the moduli arrays

$$\bar{\mathfrak{S}}_{log} := \partial_{\bar{\mathfrak{r}}_{log}} \pi^{*\tau}_{red} \quad \text{and} \quad \bar{\mathfrak{C}}_{log} := \partial^2_{\bar{\mathfrak{r}}_{log}\bar{\mathfrak{r}}_{log}} \pi^{*\tau}_{red} \tag{5.76}$$

obtained by the derivative of the incremental potential $\pi^{*\tau}_{red}$ with respect to the reduced isochoric state array *in the logarithmic strain space*

$$\bar{\mathfrak{r}}_{log} := \{ \, \bar{\boldsymbol{\varepsilon}}, \alpha, \nabla\alpha, \mathfrak{f} \, \} \; . \tag{5.77}$$

Box 3: *ALGO*$_{log}$: Variational Updates for Isotropic Gradient Plasticity.

1. *Initialization.* Given is the generalized strain array $\bar{\mathfrak{e}}_{log} := \{\bar{\varepsilon}, \alpha, \nabla\alpha, \mathfrak{f}\}$ at time t_{n+1} and the local logarithmic plastic strains $\boldsymbol{\varepsilon}^p_n$ at time t_n. Set $\bar{\mathfrak{s}}^{trial} := 2\mu(\bar{\varepsilon} - \boldsymbol{\varepsilon}^p_n)$ and $\bar{\mathfrak{n}}^{trial} := \bar{\mathfrak{s}}^{trial}/|\bar{\mathfrak{s}}^{trial}|$ and initialize $\boldsymbol{\varepsilon}^p = \boldsymbol{\varepsilon}^p_n$ and $\gamma = 0$.
2. *Check Yielding.* If $|\bar{\mathfrak{s}}^{trial}| - \sqrt{\frac{2}{3}}(y_0 + \mathfrak{f}) < 0$, set $s = 0$, go to 4. Else, $s = 1$.
3. *Update Short Range Variables.* Compute

$$\gamma = \frac{1}{2\mu + \eta_p/\tau}(\,|\bar{\mathfrak{s}}^{trial}| - \sqrt{\tfrac{2}{3}}(y_0 + \mathfrak{f})\,) \quad \text{and} \quad \boldsymbol{\varepsilon}^p = \boldsymbol{\varepsilon}^p_n + \gamma\bar{\mathfrak{n}}^{trial}$$

an store short–range variable $\boldsymbol{\varepsilon}^p$ as a local histoty field.

4. *Generalized Stresses and Moduli.* Compute generalized isochoric stress array

$$\bar{\mathfrak{S}}_{log} = \begin{bmatrix} 2\mu(\bar{\varepsilon} - \boldsymbol{\varepsilon}^p) \\ \bar{\psi}^{p\,\prime}_{loc} - \mathfrak{f} \\ \mu l_e^2 \nabla\alpha \\ -\alpha + \alpha_n + \gamma\sqrt{2/3} \end{bmatrix}$$

and the generalized consistent tangent array

$$\bar{\mathfrak{C}}_{log} := \begin{bmatrix} 2\mu\mathbb{P} & \cdot & \cdot & \cdot \\ \cdot & \bar{\psi}^{p\,\prime\prime}_{loc} & \cdot & -1 \\ \cdot & \cdot & \mu l_e^2 \boldsymbol{1} & \cdot \\ \cdot & -1 & \cdot & \cdot \end{bmatrix} + s \begin{bmatrix} -\mathbb{E}^p & \cdot & \cdot & \boldsymbol{e}^p \\ \cdot & \cdot & \cdot & \cdot \\ \cdot & \cdot & \cdot & \cdot \\ \boldsymbol{e}^{pT} & \cdot & \cdot & -e^p \end{bmatrix}$$

with the definitions

$$\begin{aligned} \mathbb{E}^p &:= \frac{4\mu^2}{2\mu + \eta_p/\tau}\bar{\mathfrak{n}}^{trial} \otimes \bar{\mathfrak{n}}^{trial} + \frac{4\mu^2\gamma}{||\bar{\mathfrak{s}}^{trial}||}[\mathbb{P} - \bar{\mathfrak{n}}^{trial} \otimes \bar{\mathfrak{n}}^{trial}]\ , \\ \boldsymbol{e}^p &:= \frac{2\mu\sqrt{2/3}}{2\mu + \eta_p/\tau}\bar{\mathfrak{n}}^{trial} \quad \text{and} \quad e^p := \frac{2/3}{2\mu + \eta_p/\tau}\ . \end{aligned}$$

Here, the projection arrays extend the projection tensors introduced in (5.18) to the array structure, such as

$$\mathfrak{P}^*_{log} := \begin{bmatrix} \mathfrak{P}_{log} & \cdot & \cdot & \cdot \\ \cdot & 1 & \cdot & \cdot \\ \cdot & \cdot & \boldsymbol{1} & \cdot \\ \cdot & \cdot & \cdot & 1 \end{bmatrix}\ , \tag{5.78}$$

Note that the chain rule operations (5.75) can be coded once and for all-times *for all models of isochoric gradient plasticity in the logarithmic strain space.* Hence, the specific constitutive modeling takes place in the logarithmic isochoric strain space, i.e. by specifying the arrays $\bar{\mathfrak{S}}_{log}$ and $\bar{\mathfrak{C}}_{log}$ defined in (5.76). All other arrays follow by the above outlined projections which are fully geometric in nature.

Stresses and moduli for von Mises plasticity. For the model problem of von Mises gradient plasticity in the logarithmic strain space, the generalized stress array in the logarithmic strain space defined in (5.76) takes the form

$$\bar{\mathfrak{S}}_{log} = \begin{bmatrix} 2\mu(\bar{\boldsymbol{\varepsilon}} - \boldsymbol{\varepsilon}^p_n) \\ \bar{\psi}^{p\,\prime}_{loc} - \mathfrak{f} \\ \mu l_e^2 \nabla\alpha \\ -\alpha + \alpha_n \end{bmatrix} + s \begin{bmatrix} -2\mu\gamma\bar{\mathfrak{n}}^{trial} \\ \mathit{0} \\ \boldsymbol{\mathit{0}} \\ \gamma\sqrt{2/3} \end{bmatrix} \tag{5.79}$$

in terms of the local plastic loading flag

$$s := \begin{cases} 1 & \text{for } \chi > 0 \quad , \\ 0 & \text{otherwise} \quad . \end{cases} \tag{5.80}$$

The generalized tangent moduli has the closed-form representation

$$\bar{\mathfrak{C}}_{log} = \begin{bmatrix} 2\mu\mathbb{P} & \cdot & \cdot & \cdot \\ \cdot & \bar{\psi}^{p\,\prime\prime}_{loc} & \cdot & -\mathit{1} \\ \cdot & \cdot & \mu l_e^2 \boldsymbol{\mathit{1}} & \cdot \\ \cdot & -\mathit{1} & \cdot & \cdot \end{bmatrix} + \; s \begin{bmatrix} -\;\mathbb{E}^p & \cdot & \cdot & \boldsymbol{e}^p \\ \cdot & \cdot & \cdot & \cdot \\ \cdot & \cdot & \cdot & \cdot \\ \boldsymbol{e}^{pT} & \cdot & \cdot & -e^p \end{bmatrix} \tag{5.81}$$

with the definitions

$$\begin{aligned} \mathbb{E}^p \; &:= \frac{4\mu^2}{2\mu + \eta_p/\tau}\bar{\mathfrak{n}}^{trial} \otimes \bar{\mathfrak{n}}^{trial} + \frac{4\mu^2\gamma}{||\bar{\mathfrak{s}}^{trial}||}[\mathbb{P} - \bar{\mathfrak{n}}^{trial} \otimes \bar{\mathfrak{n}}^{trial}] \ , \\ \boldsymbol{e}^p \; &:= \frac{2\mu\sqrt{2/3}}{2\mu + \eta_p/\tau}\bar{\mathfrak{n}}^{trial} \quad \text{and} \quad e^p := \frac{2/3}{2\mu + \eta_p/\tau} \ . \end{aligned}$$

Box 3 summarizes the local update procedure of the generalized stresses and moduli. Note that, due to the frozen long-range hardening/softening variable $\mathfrak{f}$, the algorithm represents a *one-pass radial return* with a simple closed-form solution. Observe furthermore the coupling terms, which appear in the generalized tangent array for the case of plastic loading.

5.4. Q1-P0–Brick type finite element formulation

In order to avoid the locking effects associated with the isochoric plastic flow in low-order standard displacement-type finite element discretizations, we apply a *mixed finite element method* for gradient plasticity. It follows the classical approach outline in NAGTEGAAL ET AL. [117], SIMO ET AL. [136], MIEHE [91] and WRIGGERS [154]. The *geometric basis* for such a decoupling is the *multiplicative split* of the convected current metric $\boldsymbol{C}$ into volumetric and isochoric parts defined in (5.1). With this kinematic decomposition at hand, we express the *reduced incremental potential* defined in (5.57) in the decoupled form

$$\pi^{*\tau}_{red}(\mathfrak{r}) = U(J) + \bar{\pi}^{*\tau}_{red}(\bar{\mathfrak{r}}) \tag{5.82}$$

with volumetric elastic and isochoric elastic-plastic contributions. This constitutive decoupling is the basis for the subsequent mixed finite element design of gradient plasticity. We define the *extended* Hu-Washizu–type potential

$$\Pi^{*\tau}_{red,ext}(\boldsymbol{\varphi}, \alpha, \mathfrak{f}, \tilde{\theta}, p) = \int_{\mathcal{B}} \{\, U(\tilde{\theta}) + p(J - \tilde{\theta}) + \bar{\pi}^{*\tau}_{red}(\bar{\mathfrak{r}}) \,\} dV \; - \; P^{\tau}_{ext}(\boldsymbol{\varphi}) \ , \tag{5.83}$$

which introduces the volume dilatation $\tilde{\theta}$ and the pressure p as additional field variables. Then, the extension of the global minimization principle gives the mixed variational principle

$$(G_{Q1P0}): \quad \{\boldsymbol{\varphi}, \alpha, \mathfrak{f}, \tilde{\theta}, p\} = \text{Arg}\{ \inf_{\boldsymbol{\varphi}} \inf_{\alpha} \sup_{\mathfrak{f}} \inf_{\tilde{\theta}} \sup_{p} \Pi^{*\tau}_{red,ext}(\boldsymbol{\varphi}, \alpha, \mathfrak{f}, \tilde{\theta}, p) \} \ . \tag{5.84}$$

Taking into account the relationships

$$\delta J = \boldsymbol{\mathfrak{P}}^*_{vol} \delta \boldsymbol{\mathfrak{r}} \quad \text{and} \quad \delta \bar{\boldsymbol{\mathfrak{r}}} = \boldsymbol{\mathfrak{P}}^*_{iso} \delta \boldsymbol{\mathfrak{r}} \tag{5.85}$$

based on the projection tensors introduced in (5.74) and focusing on pure Dirichlet problems with $P^{\tau}_{ext} = 0$, the necessary condition of the principle (5.84) reads

$$\delta \Pi^{*\tau}_{red,ext} = \int_{\mathcal{B}} \{ \ \delta\tilde{\theta}(U' - p) + \delta p (J - \tilde{\theta}) + \delta \boldsymbol{\mathfrak{r}}^T \boldsymbol{\mathfrak{S}} \ \} \, dV \ = \ 0 \ , \tag{5.86}$$

where we set for the generalized stress array

$$\boldsymbol{\mathfrak{S}} := p \, \boldsymbol{\mathfrak{P}}^*_{vol} + \boldsymbol{\mathfrak{P}}^{*T}_{iso} \cdot \bar{\boldsymbol{\mathfrak{S}}}_{iso} \ , \tag{5.87}$$

in terms of the array $\bar{\boldsymbol{\mathfrak{S}}}_{iso}$ obtained from Box 2. A further linearization of this term then gives the linear increment of the potential

$$\Delta(\delta \Pi^{*\tau}_{red,ext}) = \int_{\mathcal{B}} \{ \delta\tilde{\theta} U'' \Delta\tilde{\theta} - (\delta\tilde{\theta} \Delta p + \delta p \Delta\tilde{\theta}) + \delta p (\boldsymbol{\mathfrak{P}}^*_{vol} \Delta \boldsymbol{\mathfrak{r}}) + (\delta \boldsymbol{\mathfrak{r}}^T \boldsymbol{\mathfrak{P}}^*_{vol}) \Delta p + \delta \boldsymbol{\mathfrak{r}}^T (\widehat{\boldsymbol{\mathfrak{G}}} + \widehat{\boldsymbol{\mathfrak{C}}}) \Delta \boldsymbol{\mathfrak{r}} \} \, dV \tag{5.88}$$

where we introduced the identity

$$\boldsymbol{\mathfrak{S}} \Delta(\delta \boldsymbol{\mathfrak{r}}) = \delta \boldsymbol{\mathfrak{r}}^T \widehat{\boldsymbol{\mathfrak{G}}} \Delta \boldsymbol{\mathfrak{r}} \tag{5.89}$$

in terms of the geometric matrix $\widehat{\boldsymbol{\mathfrak{G}}}$ with stress contributions and the moduli

$$\widehat{\boldsymbol{\mathfrak{C}}} := p \, \boldsymbol{\mathfrak{L}}^*_{vol} + \boldsymbol{\mathfrak{P}}^{*T}_{iso} \cdot \bar{\boldsymbol{\mathfrak{C}}}_{iso} \cdot \boldsymbol{\mathfrak{P}}^*_{iso} + \bar{\boldsymbol{\mathfrak{S}}}_{iso} \cdot \boldsymbol{\mathfrak{L}}^*_{iso} \tag{5.90}$$

in terms of the arrays $\bar{\boldsymbol{\mathfrak{S}}}_{iso}$ and $\bar{\boldsymbol{\mathfrak{C}}}_{iso}$ obtained from Box 2.

5.4.1. Finite element discretization. We start with a straightforward extension of Q1P0-Q1Q1 finite elements to gradient plasticity using C^0 interpolations for both the primary fields $\{ \boldsymbol{\varphi}, \alpha \}$ *as well as* for the driving force field $\{ \mathfrak{f} \}$ dual to α, but elementwise *constant* volume dilatation and pressure $\{ \tilde{\theta}, p \}$. For a triangulation $\mathfrak{T}^h$ with element domains $\mathcal{B}^e \subset \mathcal{B}$, the node I has standard bi- or tri-linear shape functions $N^I(\boldsymbol{\xi})$, e.g.

$$N^I(\boldsymbol{\xi}) = \tfrac{1}{8} \, (1 + \xi_1 \xi_1^I)(1 + \xi_2 \xi_2^I)(1 + \xi_3 \xi_3^I) \tag{5.91}$$

for bi-linear Q1 elements with $n = 8$ nodes. Here, $\boldsymbol{\xi} := \{ \ \boldsymbol{\xi} | -1 \leq \xi_I \leq +1\}$ denotes the natural element parameters. The gradients of the shape functions are obtained by using the chain rule $\nabla N^I = \nabla_{\boldsymbol{\xi}} N^I \boldsymbol{J}^{-1}$, where $\boldsymbol{J} := \nabla_{\boldsymbol{\xi}} \boldsymbol{X}^h(\boldsymbol{\xi})$ with $D := \det \boldsymbol{J} > 0$ denotes the Jacobian of the isoparametric map $\boldsymbol{X}^h = \sum_{I=1}^n N^I \boldsymbol{X}_I$ that defines the Lagrangian coordinates of the element in terms of their nodal positions $\boldsymbol{X}_I$ in the reference configuration. We discretize the extended variational functional (5.83) by *bi-linear* interpolations of $\boldsymbol{\varphi}$, α, $\mathfrak{f}$ but elementwise *constant* $\tilde{\theta}$, p

$$\text{Q1P0-Q1Q1:} \quad \{\boldsymbol{\varphi}, \alpha, \mathfrak{f}\}^h = \textstyle\sum_{I=1}^n N^I \, \boldsymbol{d}_I \quad \text{and} \quad \{\tilde{\theta}, p\}^h = \{\tilde{\theta}^e, p^e\} \tag{5.92}$$

in $\mathcal{B}^e \subset \mathcal{B}^h$ with the nodal degrees $\boldsymbol{d}_I := [\boldsymbol{\varphi}, \alpha, \mathfrak{f}]_I^T \in \mathbb{R}^5$. With these interpolation, we write the finite element interpolations of the variation of Lagrangian state in the form

$$\delta\mathfrak{r} = \boldsymbol{B}\delta\boldsymbol{d} \tag{5.93}$$

in terms of variations of the *global nodal state vector* $\boldsymbol{d}$, which contains the discrete macro- and micro-motions $\boldsymbol{\varphi}_I$, α_I and the driving forces $\mathfrak{f}_I$ at nodes of the finite element mesh. Here, the *global* matrix $\boldsymbol{B}$ is a symbolic representation of interpolations for the coupled problem, which is never formulated explicitly, but only on the *local* element level. The insertion of the finite element shapes (5.93) into (5.83) gives the spatial discretization of the potential $\Pi^{*\tau\, h}_{red,ext}(\boldsymbol{d}, \tilde{\theta}^e, p^e)$, depending on the nodal degrees $\boldsymbol{d}$ and the element parameters $\tilde{\theta}^e$ and p^e. The discrete counterpart of the variational principle (5.84) reads

$$\{\boldsymbol{d}, \tilde{\theta}^e, p^e\} = \text{Arg}\{ \underset{\boldsymbol{d},\tilde{\theta}^e,p^e}{\text{stat}} \Pi^{*\tau\, h}_{red,ext}(\boldsymbol{d}, \tilde{\theta}^e, p^e) \} \ . \tag{5.94}$$

5.4.2. Condensation at the element level. The dilatation $\tilde{\theta}^e$ and the pressure p^e are discrete values associated with the elements $e = 1...E^h$. Following this, we can construct the condensed potential by optimization with respect to these discrete values via

$$\Pi^{*\tau\, h}_{red,ext,cond}(\boldsymbol{d}) = \inf_{\tilde{\theta}^e} \sup_{p^e} \Pi^{*\tau\, h}_{red,ext}(\boldsymbol{d}, \tilde{\theta}^e, p^e) \ . \tag{5.95}$$

The necessary conditions of this variational problem determine the discrete element variables are obtained by insertion of the shapes (5.91) into (5.86), yielding the closed form results

$$p^e = U'(\tilde{\theta}^e) \quad \text{and} \quad \tilde{\theta}^e = \frac{1}{V^e}\int_{\mathcal{B}^e} J\, dV \tag{5.96}$$

for $e = 1...E^h$, where $V^e := \int_{\mathcal{B}^e} dV$ is the element volume of the reference configuration. As a consequence of (5.96), $\tilde{\theta}^e$ and p^e are now *functions of the global nodal state vector* $\boldsymbol{d}$.

5.4.3. Effective element arrays and global solver. For the above known functions of dilatation $\tilde{\theta}^e$ and pressure p^e, the condensed variational problem at the global level

$$\boldsymbol{d} = \text{Arg}\{ \underset{\boldsymbol{d}}{\text{stat}}\ \Pi^{*\tau\, h}_{red,ext,cond}(\boldsymbol{d}) \} \tag{5.97}$$

determines the global nodal state vector $\boldsymbol{d}$ of the finite element mesh at the current time t_{n+1}. The solution of this variational problem by a global Newton-type solver is based on incremental updates of the nodal degrees $\boldsymbol{d}$

$$\boldsymbol{d} \Leftarrow \boldsymbol{d} - \boldsymbol{K}^{-1}\boldsymbol{R} \quad \text{until} \quad |\boldsymbol{R}| < tol \tag{5.98}$$

until convergence is achieved. Here, the residual and tangent arrays are obtained by insertion of the discrete shapes (5.92) and (5.93) into (5.86) and (5.88). The effective residual takes the form

$$\boldsymbol{R} := \mathop{\mathsf{A}}_{e=1}^{E^h} \int_{\mathcal{B}^e} \{ \boldsymbol{B}^T \mathfrak{S} \}\, dV \ , \tag{5.99}$$

governed by generalized stress array $\mathfrak{S}$ defined in (5.87), but evaluated with the element pressure p^e defined in (5.96). The effective tangent matrix is

$$\boldsymbol{K} := \mathop{\mathsf{A}}_{e=1}^{E^h} \left[(U''V^e)\boldsymbol{k}^{eT}_{vol}\boldsymbol{k}^e_{vol} + \int_{\mathcal{B}^e} \{ \boldsymbol{B}^T (\widehat{\mathfrak{G}} + \widehat{\mathfrak{C}})\boldsymbol{B} \}\, dV \right] \tag{5.100}$$

determined by the geometric tensor $\widehat{\mathfrak{G}}$ and the tangent array $\widehat{\mathfrak{C}}$ defined in (5.89) and (5.90), respectively, and the vector

$$\boldsymbol{k}^e_{vol} := \frac{1}{V^e}\int_{\mathcal{B}^e} \boldsymbol{\mathcal{P}}^*_{vol}\boldsymbol{B}\, dV \ . \tag{5.101}$$

5.5. Mini–Tetrahedral type finite element formulation

Alternatively, we use for the modeling of incompressible plastic flow the Mini–type mixed finite element design suggested by Arnold, Brezzi & Fortin [20]. It is also based on the multiplicative decomposition (5.1) of the metric tensor $\boldsymbol{C}$ into volumetric and isochoric parts, and the associated specific structure (5.82) of the reduced potential $\pi^{*\tau}_{red}$. We define also the extended reduced incremental potential

$$\Pi^{*\tau}_{red,ext}(\boldsymbol{\varphi},\alpha,\mathfrak{f},p) = \int_{\mathcal{B}} [\, p(J-1) - \frac{1}{2\kappa}p^2 + \bar{\pi}^{*\tau}_{red}(\bar{\mathfrak{r}})\,]\, dV \ - \ P^\tau_{ext}(\boldsymbol{\varphi}) \ , \tag{5.102}$$

which introduces the *pressure* p as an additional field. This implies the extension of the mixed saddle point principle (5.65) towards the four-field variational principle

$$(G_{MINI}): \quad \{\boldsymbol{\varphi},\alpha,\mathfrak{f},p\} = \mathrm{Arg}\{ \inf_{\boldsymbol{\varphi}}\inf_{\alpha}\sup_{\mathfrak{f}}\sup_{p} \Pi^{*\tau}_{red,ext}(\boldsymbol{\varphi},\alpha,\mathfrak{f},p) \ \} \ . \tag{5.103}$$

Focusing on pure Dirichlet problems with $P^\tau_{ext} = 0$, the necessary condition reads

$$\delta\Pi^{*\tau}_{red,ext} = \int_{\mathcal{B}} \{ \ \delta p(J - 1 - \frac{p}{\kappa}) + \delta\mathfrak{r}^T\mathfrak{S} \ \}\, dV \ = \ 0 \ , \tag{5.104}$$

in terms of the generalized stress array $\mathfrak{S}$ defined in (5.87). A further linearization of this term then gives the linear increment of the potential

$$\Delta(\delta\Pi^{*\tau}_{red,ext}) = \int_{\mathcal{B}} \{ \ \delta p(\boldsymbol{\mathcal{P}}^*_{vol}\Delta\mathfrak{r}) - \delta p\frac{1}{\kappa}\Delta p + (\delta\mathfrak{r}^T\boldsymbol{\mathcal{P}}^*_{vol})\Delta p + \delta\mathfrak{r}^T(\widehat{\mathfrak{G}} + \widehat{\mathfrak{C}})\Delta\mathfrak{r} \ \}\, dV \, , \tag{5.105}$$

with the geometric matrix $\widehat{\mathfrak{G}}$ and the moduli $\widehat{\mathfrak{C}}$ defined in (5.89) and (5.90), respectively.

5.5.1. Finite element discretization. We use linear interpolations C^0 for all fields $\{\boldsymbol{\varphi},\alpha,\mathfrak{f},p\}$, including an additional *bubble mode* for $\boldsymbol{\varphi}$. For a tetrahedron $\mathfrak{T}^h$ with element domains $\mathcal{B}^e \subset \mathcal{B}$, we consider the shape functions

$$N^I(\boldsymbol{\xi}) = \xi^I \quad \text{and} \quad N^B(\boldsymbol{\xi}) = \xi^1\xi^2\xi^3\xi^4 \tag{5.106}$$

associated with the $n = 4$ nodes $I = 1 \ldots n$ and the center bubble B as outlined in Taylor [145]. Here, $\boldsymbol{\xi} \in \{\ 0 \le \xi^I \le 1\}$ denotes the natural parameters of the tetrahedron. We discretize the extended variational functional (5.102) by the *linear* interpolations of $\boldsymbol{\varphi}$, α, $\mathfrak{f}, p$ and an additional bubble mode for $\boldsymbol{\varphi}$

$$\text{MINI-Q1Q1:} \quad \{\boldsymbol{\varphi},\alpha,\mathfrak{f},p\}^h = \textstyle\sum_{I=1}^n N^I\, \boldsymbol{d}_I + N^B\, \boldsymbol{1}^B \boldsymbol{a}^e \tag{5.107}$$

in $\mathcal{B}^e \subset \mathcal{B}$ with the nodal degrees $\boldsymbol{d}_I := [\boldsymbol{\varphi},\alpha,\mathfrak{f},p]^T_I \in \mathbb{R}^6$. Here, $\boldsymbol{a}^e \in \mathbb{R}^3$ are the degrees of the displacement bubble modes and $\boldsymbol{1}^B$ an array that filters out the displacement slots. With these interpolations at hand, we write the finite element interpolations of the variation of the pressure and the Lagrangian state in the form

$$\delta p = \boldsymbol{P}\delta\boldsymbol{d} \quad \text{and} \quad \delta\mathfrak{r} = \boldsymbol{B}_d\delta\boldsymbol{d} + \boldsymbol{B}_a\delta\boldsymbol{a} \tag{5.108}$$

in terms of variations of the *global nodal state vector* $\boldsymbol{d}$ and the *global vector* $\boldsymbol{a}$ *of bubble modes*. The linear increments of Δp and $\Delta\mathfrak{r}$ have an analogous form. Note that $\boldsymbol{P}$, $\boldsymbol{B}_d$ and $\boldsymbol{B}_a$ are symbolic representation of *global* matrices of interpolations for the coupled problem, which are never formulated explicitly, but only on the *local* element level. The insertion of the finite element shapes (5.107) into (5.102) gives the spatial discretization of the potential $\Pi^{*\tau\,h}_{red,ext}(\boldsymbol{d},\boldsymbol{a})$, depending on the nodal degrees $\boldsymbol{d}$ and the bubble modes $\boldsymbol{a}$. The discrete counterpart of the variational principle (5.103) reads

$$\{\boldsymbol{d},\boldsymbol{a}\} = \text{Arg}\{\ \underset{\boldsymbol{d},\boldsymbol{a}}{\text{stat}}\ \Pi^{*\tau\,h}_{red,ext}(\boldsymbol{d},\boldsymbol{a})\ \}\ , \tag{5.109}$$

which determines all current nodal and element degrees.

5.5.2. Partitioned element arrays for newton-type solver. The solution of the variational problem (5.109) by a global Newton-type solver is based on incremental updates of the nodal degrees $\boldsymbol{d}$ and the bubble degrees $\boldsymbol{a}$

$$\begin{bmatrix} \boldsymbol{d} \\ \boldsymbol{a} \end{bmatrix} \Leftarrow \begin{bmatrix} \boldsymbol{d} \\ \boldsymbol{a} \end{bmatrix} - \begin{bmatrix} \boldsymbol{K}_{dd} & \boldsymbol{K}_{da} \\ \boldsymbol{K}_{ad} & \boldsymbol{K}_{aa} \end{bmatrix}^{-1} \begin{bmatrix} \boldsymbol{R}_d \\ \boldsymbol{R}_a \end{bmatrix} \tag{5.110}$$

until convergence is achieved. Here, the residual and tangent arrays are obtained by insertion of the discrete shapes (5.108) into (5.104) and (5.105). The residuals take the form

$$\begin{aligned} \boldsymbol{R}_d &:= \int_{\mathcal{B}} \{\ (J - 1 - \frac{p}{\kappa})\boldsymbol{P}^T + \boldsymbol{B}_d^T\mathfrak{S}\ \}\, dV\ , \\ \boldsymbol{R}_a &:= \int_{\mathcal{B}} \{\ \boldsymbol{B}_a^T\mathfrak{S}\ \}\, dV\ , \end{aligned} \tag{5.111}$$

governed by generalized stress array $\mathfrak{S}$ defined in (5.87). The partitions of the coupled tangent matrix

$$\begin{aligned} \boldsymbol{K}_{dd} &:= \int_{\mathcal{B}} \{\ \boldsymbol{P}^T \otimes \mathfrak{P}^*_{vol}\boldsymbol{B}_d - \frac{1}{\kappa}\boldsymbol{P}^T \otimes \boldsymbol{P} + \boldsymbol{B}_d^T\mathfrak{P}^{*T}_{vol} \otimes \boldsymbol{P} + \boldsymbol{B}_d^T(\widehat{\mathfrak{G}} + \widehat{\mathfrak{C}})\boldsymbol{B}_d\ \}\, dV\ , \\ \boldsymbol{K}_{da} &:= \int_{\mathcal{B}} \{\ \boldsymbol{B}_a^T\mathfrak{P}^{*T}_{vol} \otimes \boldsymbol{P} + \boldsymbol{B}_d^T(\widehat{\mathfrak{G}} + \widehat{\mathfrak{C}})\boldsymbol{B}_a\ \}\, dV\ , \\ \boldsymbol{K}_{aa} &:= \int_{\mathcal{B}} \{\ \boldsymbol{B}_a^T(\widehat{\mathfrak{G}} + \widehat{\mathfrak{C}})\boldsymbol{B}_a\ \}\, dV\ . \end{aligned} \tag{5.112}$$

5.5.3. Condensation of bubble degrees at the element level. Let $\boldsymbol{a}^e$ be the bubble modes associated with the elements $e = 1...E^h$. They can be condensed out at the element level. As a consequence, we can construct the condensed potential by optimization with respect to these discrete values via

$$\Pi^{*\tau\,h}_{red,ext,cond}(\boldsymbol{d}) = \inf_{\boldsymbol{a}}\ \Pi^{*\tau\,h}_{red,ext}(\boldsymbol{d},\boldsymbol{a})\ , \tag{5.113}$$

Table 5.1: Material parameters used for the numerical examples.

No.	Parameter	Name	Value	Unit
1.	κ	bulk modulus	164.2	kN/mm^2
2.	μ	shear modulus	80.2	kN/mm^2
3.	h	hardening parameter	$\pm\, 0.13$	kN/mm^2
4.	l_p	length-scale parameter	0.1	mm
5.	y_0	initial yield stress	0.45	kN/mm^2
6.	η_p	viscosity	10^{-7}	kNs/mm^2
7.	y_∞	infinite yield stress	1.165	kN/mm^2
8.	ω	saturation parameter	16.96	–

which determines for known bubble degrees $\boldsymbol{a}$ at the element level the global nodal state vector by the variational principle

$$\boldsymbol{d} = \text{Arg}\{ \underset{\boldsymbol{d}}{\text{stat}}\ \Pi^{*\tau\, h}_{red,ext,cond}(\boldsymbol{d}) \}\ . \tag{5.114}$$

An appropriate solution strategy of this condensed principle is the static condensation of the coupled algebraic system (5.110). To this end, the update of the bubble degrees is performed *locally at the element level* by

$$\boldsymbol{a}^e \Leftarrow \boldsymbol{a}^e + \Delta\boldsymbol{a}^e \quad \text{with} \quad \Delta\boldsymbol{a}^e = -\, \boldsymbol{K}^{e-1}_{aa}[\, \boldsymbol{R}^e_a + \boldsymbol{K}^e_{ad}\Delta\boldsymbol{d}_e\,]\ . \tag{5.115}$$

Then, assembling the global effective residual and tangent arrays via

$$\widetilde{\boldsymbol{R}}_d := \mathop{\mathsf{A}}_{e=1}^{E^h}\{\, \boldsymbol{R}^e_d - \boldsymbol{K}^e_{da}\boldsymbol{K}^{e\,-1}_{aa}\boldsymbol{R}^e_a\, \} \quad \text{and} \quad \widetilde{\boldsymbol{K}}_{dd} := \mathop{\mathsf{A}}_{e=1}^{E^h}\{\, \boldsymbol{K}^e_{dd} - \boldsymbol{K}^e_{da}\boldsymbol{K}^{e\,-1}_{aa}\boldsymbol{K}^e_{ad}\, \}\ , \tag{5.116}$$

the *effective global update of the nodal degrees* is performed by

$$\boldsymbol{d} \Leftarrow \boldsymbol{d} - \widetilde{\boldsymbol{K}}^{-1}_{dd}\widetilde{\boldsymbol{R}}_d \quad \text{until} \quad |\widetilde{\boldsymbol{R}}_d| < tol\ . \tag{5.117}$$

5.6. Representative numerical examples

In the following, we demonstrate the performance of the proposed variational framework of gradient plasticity by means of representative numerical examples. The first numerical test employs the nonlinear hardening function, which is concerned with *necking of a cylindrical bar*. The other two numerical simulations, that describe *cross shearing of a plate in tension* and *three dimensional torsion test of a square-section bar*, are elaborated using the linear hardening term only. The material parameters used in the examples are given in Table 5.1. Regarding the selection of the material parameters, we refer to the work of SIMO [137], in which a fit of the material parameters reported in Table 17 with the work of HALLQUIST [66] was made. All numerical results are obtained with the post-processing corrector step outlined in Chapter 3.

5.6.1. Necking of cylindrical bar. The first numerical example is concerned with the *necking phenomenon of a cylindrical bar* for the case of hardening plasticity. It is considered as a standard benchmark problem of finite plasticity, and has been analyzed in the absence of an internal length scale by many authors, see e.g. SIMO ET AL. [138]

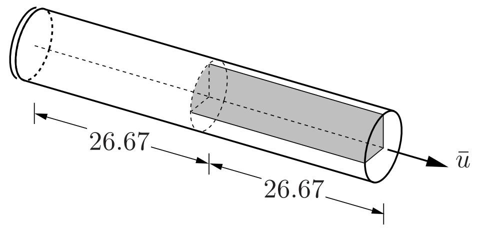

Figure 5.2: Necking of cylindrical bar. Geometry and boundary conditions. Due to the symmetry of the boundary value problem only the shaded area is discretized.

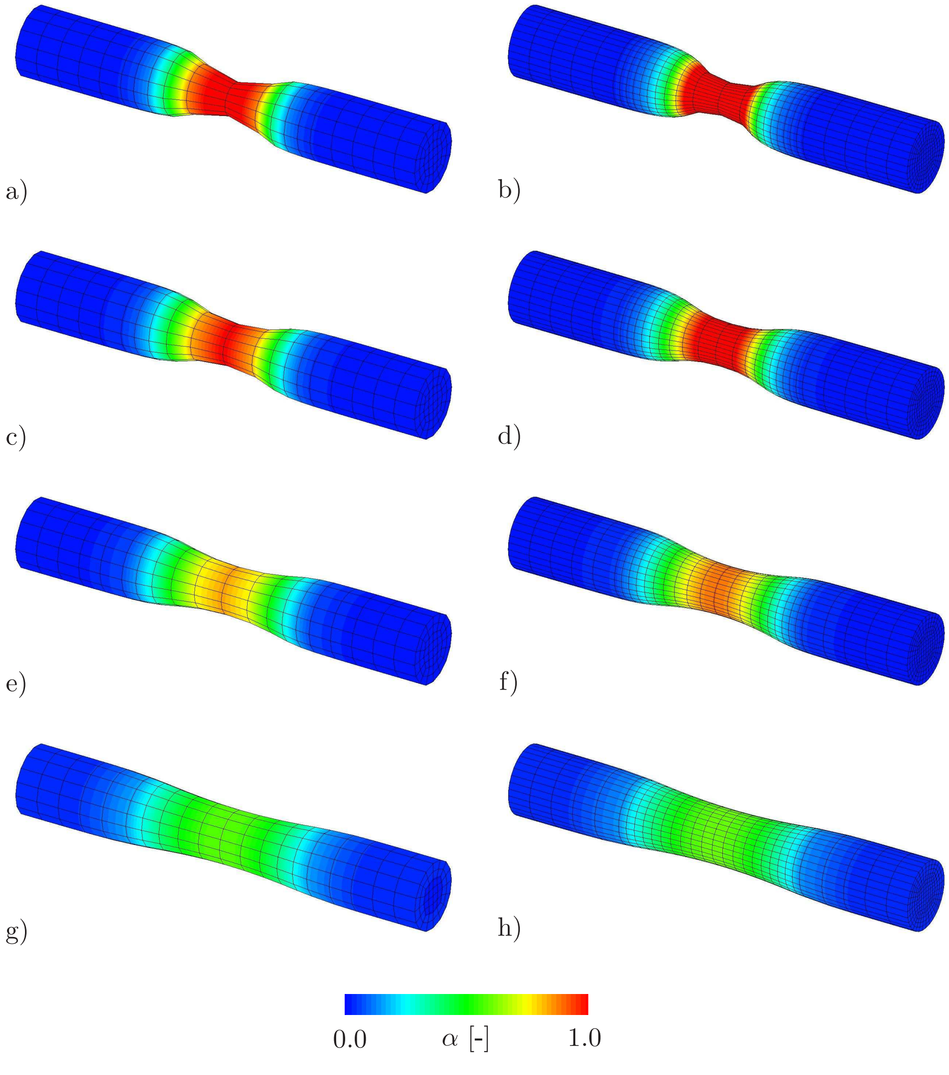

Figure 5.3: Necking of cylindrical bar. Distribution of the equivalent plastic strain α at the final deformation $\bar{u} = 10.0$ mm for two different discretizations with 120×8 and 720×8 elements in combination with several length scales parameter. a)–b) $l_p = 0.1$ mm, c)–d) $l_p = 0.2$ mm, e)–f) $l_p = 0.3$ mm, and g)–h) $l_p = 0.5$ mm.

and Miehe et al. [99]. To study length scale effects, this benchmark test has been discussed in the context of non-local finite strain elasto-plasticity. The geometric setup and the boundary conditions of the cylindrical bar with radius 6.4135 mm are illustrated in Figure 5.2. Due to the symmetry of the boundary value problem only one eighth of the entire geometry is discretized using 120 and 720 mixed Q1P0 finite elements. To trigger

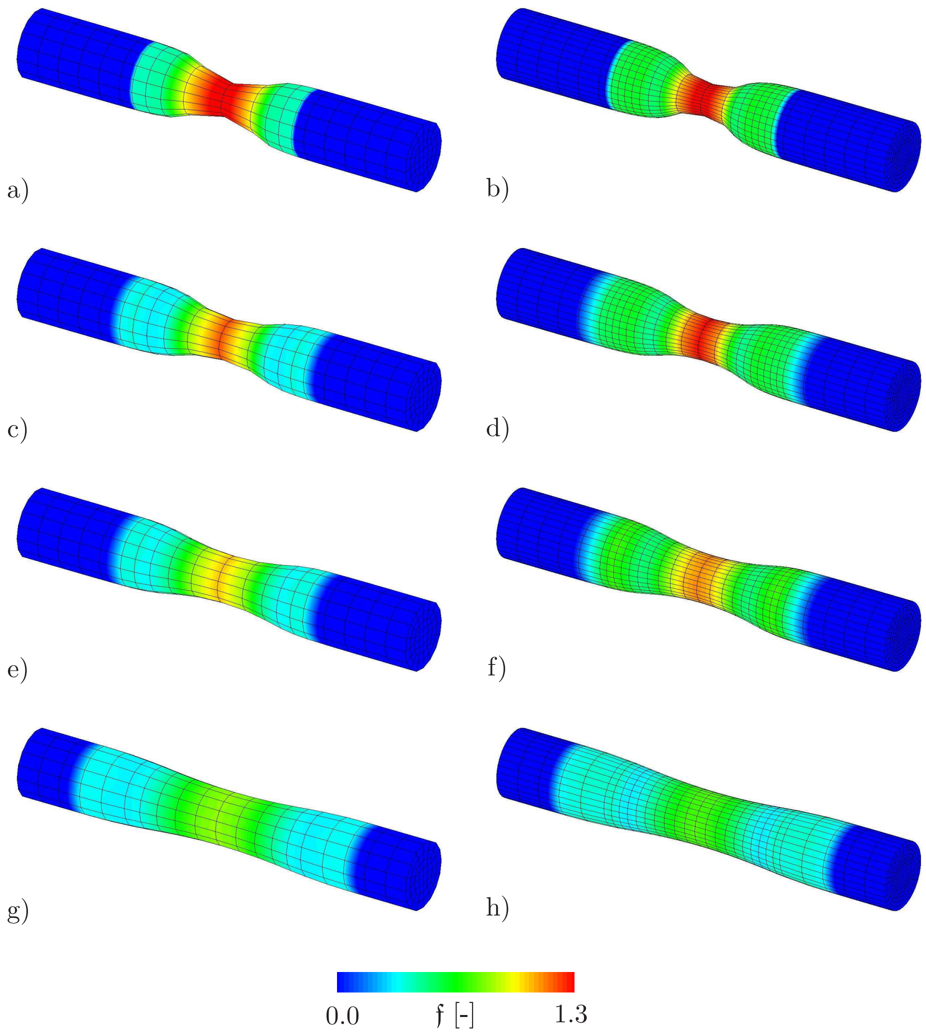

Figure 5.4: Necking of cylindrical bar. Distribution of the dual driving force $\mathfrak{f}$ at the final deformation $\bar{u} = 10.0$ mm for two different discretizations with 120×8 and 720×8 elements in combination with several length scales parameter. a)–b) $l_p = 0.1$ mm, c)–d) $l_p = 0.2$ mm, e)–f) $l_p = 0.3$ mm, and g)–h) $l_p = 0.5$ mm.

localization in the center of the specimen, the yield limit y_0 in the center is reduced by 10%. The material parameters used are given in Table 5.1. The computation is performed in a displacement-driven context. We apply a prescribed deformation rate $\dot{\bar{u}} = 1.0$ mm/s at the right edge of the eighth of the specimen as shown in Figure 5.2. In the numerical simulation the time step is chosen first to be $\Delta t = 0.1$ s with 37 time steps. Then we perform 6300 time steps using a time step of $\Delta t = 0.001$ s to overcome the critical range around the peak load. Hence a maximum deformation of $\bar{u} = 10.0$ mm is reached. Figures 5.3–5.4 depict the distribution of the equivalent plastic strain α and the dual driving force $\mathfrak{f}$ at the final deformation $\bar{u} = 10.0$ mm for several values of the length scale parameter l_p obtained with two different discretizations 120×8 and 720×8 Q1P0 elements. The influence of the length scale parameter on the shape of the necking zone is investigated. For $l_p = 0.1$ mm, a sharp necked zone with concentrated equivalent plastic strain α and driving force $\mathfrak{f}$ is shown in Figure 5.3a-b for α and Figure 5.4a-b for $\mathfrak{f}$ with different mesh discretizations. By increasing the length scale parameter l_p, the necking zone smears out and the equivalent plastic strain α as well as the dual driving force $\mathfrak{f}$

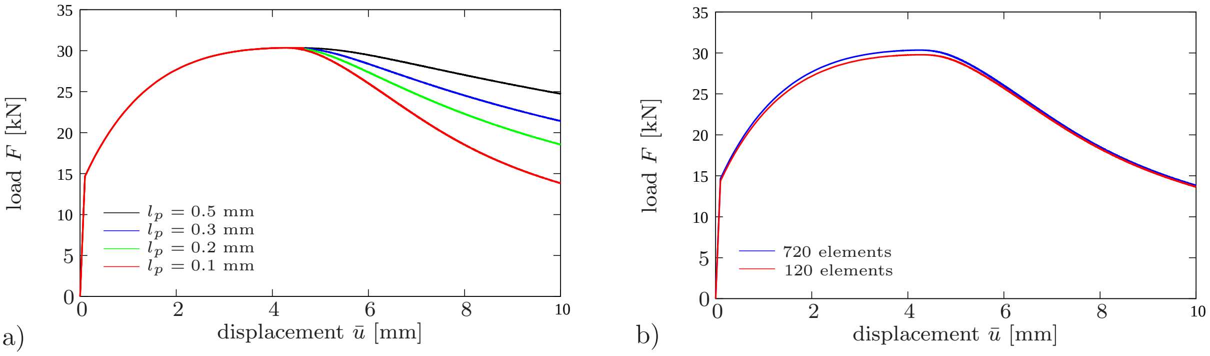

Figure 5.5: Necking of cylindrical bar. Load-displacement curves for a) different length scale parameter l_p for discretization with 720 Q1P0 elements, and b) two different mesh sizes in combination with length scale parameter $l_p = 0.1$ mm.

are spread over several elements. The load–displacement curves of the overall structural response are illustrated in Figure 5.5. Obviously, by increasing the length scale parameter l_p, a stiffer global response, as demonstrated in Figure 5.5a for four different length scales l_p, is obtained. Figure 5.5b shows the results for two different mesh sizes with 120 and 720 finite elements and for gradient plasticity with $l_p = 0.1$ mm, where mesh objectivity is observed. Thus, the incorporation of the length scale parameter l_p enables us not only to predict a size-independent structural response, but also to control the shape of the necking zone.

5.6.2. Cross shearing of a plate in tension. The second benchmark test is concerned with *cross shearing* of a three dimensional plate subjected to tensile loading for softening plasticity, i.e. $h = -0.13$ kN/mm^2. The geometric setup and the loading conditions of the specimen are depicted in Figure 5.6. Due to the underlying symmetry, only one quarter of the specimen is discretized using 3032 , 5413 , 9976 and 33064 mixed Mini-Q1Q1 type finite elements. To trigger localization in the center of the specimen, the yield limit y_0 in the lower left element (the dark shaded area) is reduced by 10%. The material parameters used here are given in Table 5.1. The focus is laid on linear isotropic hardening behaviour. The computation is performed in a displacement-driven context. In this, we

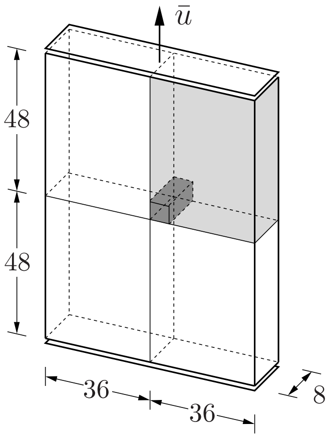

Figure 5.6: Cross shearing of a plate in tension. Geometry and boundary conditions. Due to the symmetry of the boundary value problem, only one quarter is discretized. To trigger localization, the yield limit y_0 in the dark shaded element is reduced by 10%.

apply a prescribed deformation rate $\dot{\bar{u}} = 48$ mm/s at the top of the light shaded part of the specimen as shown in Figure 5.6. In the numerical simulation the time step is chosen to be $\Delta t = 0.0001$ s with 2500 time steps. Hence, a maximum deformation of $\bar{u} = 12.0$ mm is applied. The numerical results are illustrated in Figures 5.7–5.11, obtained with the Mini-Q1Q1 element. Figure 5.7 demonstrates the influence of the size effect governed by the length scale parameter l_p for discretization with 3032×4 Mini-Q1Q1 elements. Here, we observe that by increasing l_p the equivalent plastic strain α and its dual driving force $\mathfrak{f}$ are spread over several elements and the absolute maximum value are decreased by increasing the length scale as shown in Figure 5.7e–f for $l_p = 0.1$ mm. To illustrate the pathological mesh dependence of the local plasticity theory and the mesh objectivity of the gradient plasticity, we plot in Figures 5.8–5.9 the distribution of the equivalent plastic strain α and its dual driving force $\mathfrak{f}$ at the final deformation state $\bar{u} = 12.0$ mm for two length scales parameters obtained with three different discretizations 5413×4 , 9976×4 and 33064×4 Mini-Q1Q1 elements. For the local analysis with zero length scale parameter $l_p = 0$, we observe a plastic shear band with the width of one element size as we refine the mesh, as demonstrated in Figure 5.8a–c for the equivalent plastic strain α and Figure 5.9a–c for the dual driving force $\mathfrak{f}$. By increasing the length scale parameter $l_p = 0.05$ mm, we notice that, the equivalent plastic strain α as well as the dual driving force $\mathfrak{f}$ are spread

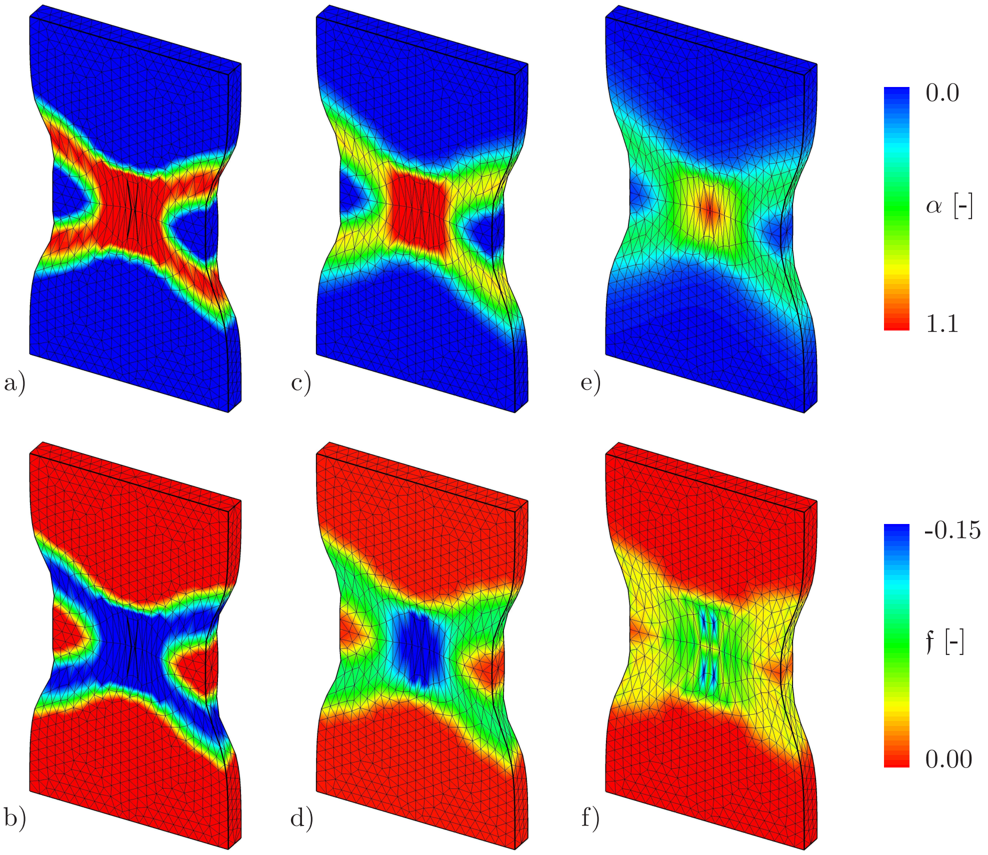

Figure 5.7: Cross shearing of a plate in tension for softening plasticity. Distribution of the equivalent plastic strain α and the dual driving force $\mathfrak{f}$ at the final deformation $\bar{u} = 12.0$ mm for discretizations with 3032×4 Mini-Q1Q1 elements in combination with three different length scales parameter . a)–b) For local plasticity $l_p = 0.0$ mm, c)–d) $l_p = 0.05$ mm, and e)–f) $l_p = 0.1$ mm.

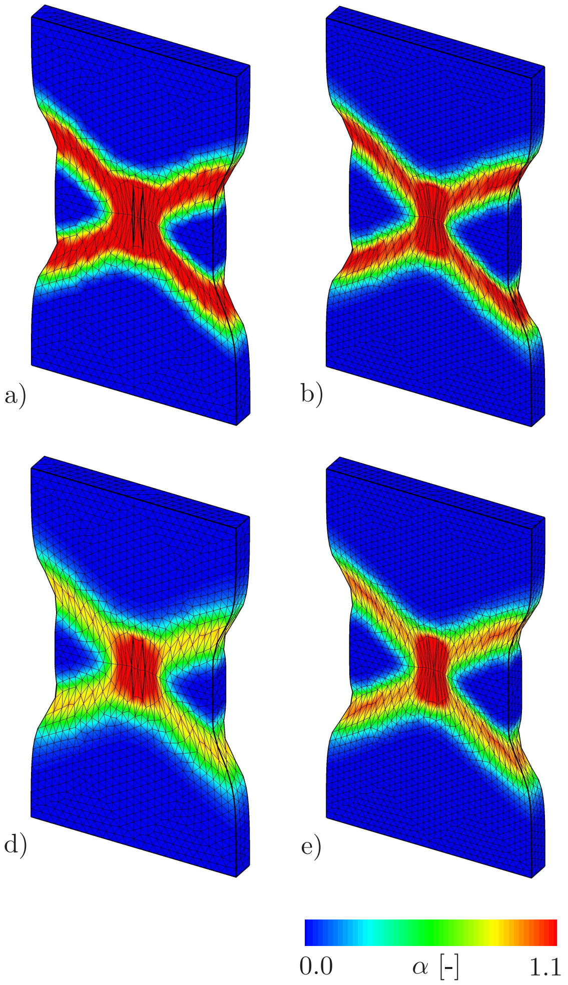

Figure 5.8: Cross shearing of a plate in tension for softening plasticity. Distribution of the equivalent plastic strain α at the final deformation $\bar{u} = 12.0$ mm for three different discretizations with 5413×4 , 9976×4 and 33064×4 Mini-Q1Q1 elements respectively in combination with two different length scales parameter. a)–c) For local plasticity $l_p = 0.0$ mm and d)–f) $l_p = 0.05$ mm.

over several elements, see Figure 5.8d–f for α and Figure 5.9d–f for $\mathfrak{f}$. The condition $\mathfrak{f} < 0$ for softening plasticity is violated around the elastic–plastic boundaries when we increase the length scale parameter. These violations are due to small oscillations in the plastic zone. However, the oscillations of the driving force $\mathfrak{f}$ have no visible influence on the macro-deformation $\boldsymbol{u}$ and the equivalent plastic strain α. The load–displacement curves of the overall structural response are illustrated in Figures 5.10–5.11. As observed in Figure 5.8a–c, the shear band for a local analysis with $l_p = 0$ has the width of one element. The load–displacement curves in Figure 5.10a demonstrate the pathological mesh dependence of the local theory. In contrast, Figure 5.10b shows results for different mesh sizes for gradient plasticity with $l_p = 0.2$ mm, where mesh objectivity is observed. Figure 5.11 demonstrates the influence of the size effect governed by the length scale parameter l_p on the specimen for two different mesh sizes 9976 and 33064 respectively. Obviously, by increasing the length scale parameter l_p, we obtain a stiffer global response.

5.6.3. Three dimensional torsion test of a square-section bar. The last benchmark test consider a square-section bar subjected to torsional loading around z-axis at

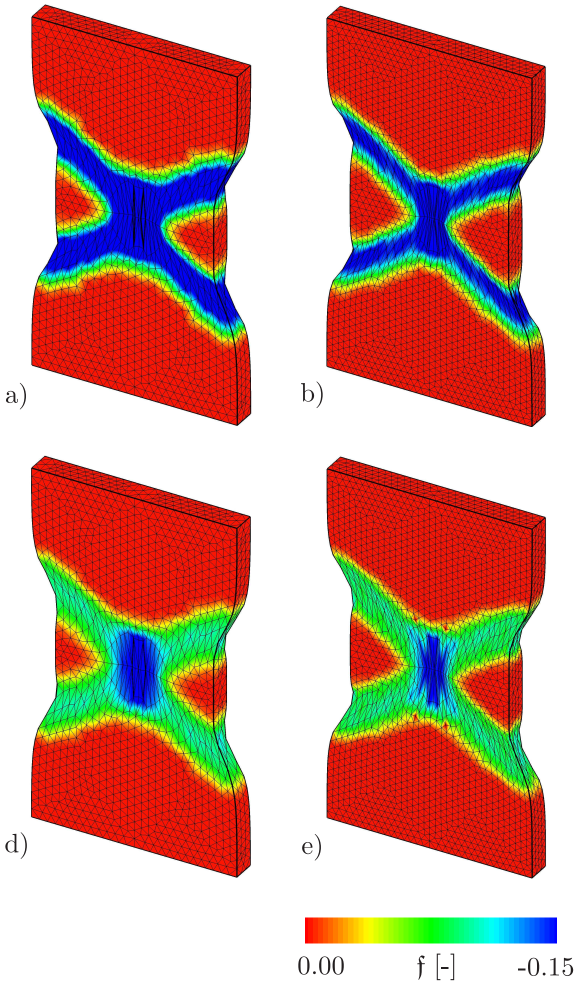

Figure 5.9: Cross shearing of a plate in tension for softening plasticity. Distribution of the dual driving force $\mathfrak{f}$ at the final deformation $\bar{u} = 12.0$ mm for three different discretizations with 5413×4 , 9976×4, and 33064×4 Mini-Q1Q1 elements respectively in combination with two different length scales parameter. a)–c) For local plasticity $l_p = 0.0$ mm and d)–f) $l_p = 0.05$ mm.

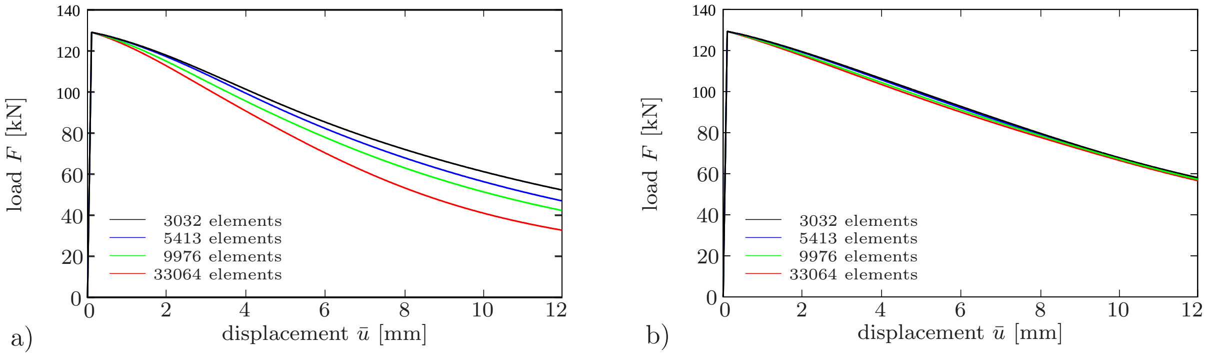

Figure 5.10: Cross shearing of a plate in tension for softening plasticity. Load–displacement curves for four different mesh discretization. a) Local plasticity with $l_p = 0.0$ and b) gradient plasticity with length scale parameter $l_p = 0.2$ mm.

the center. The aim of this test is to illustrate the length changes along the z axis under torsional loading known as *Swift effect*, which are reported in the works Swift [144],

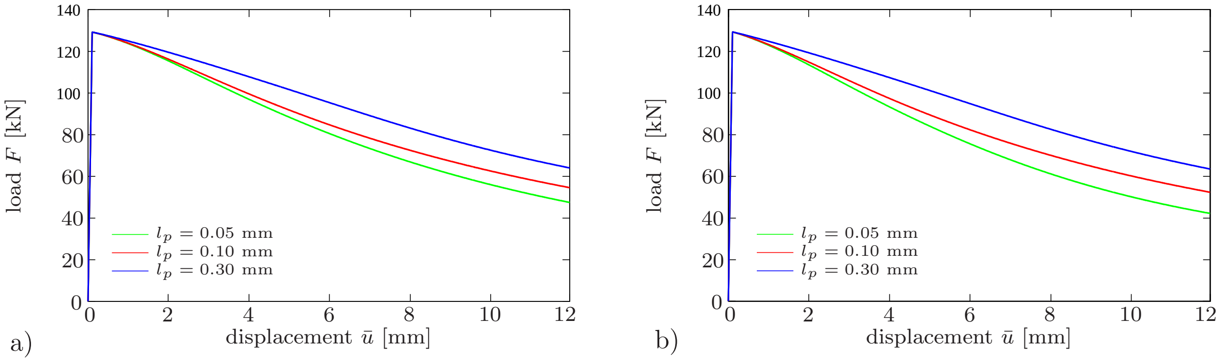

Figure 5.11: Cross shearing of a plate in tension for softening plasticity. Load–displacement curves for two different mesh discretization in combination with three different length scales. For discretization with a) 9976 and b) 33064 Mini-Q1Q1 elements.

Hatada et al. [67] and Wu & Van der Giessen [156]. As a geometric setup, the size of the square-section bar are chosen to be $H = 5L$, where L is the length of the square cross section and H is the height along the third direction z. At the boundaries, we fixed one end of the bar and applied torsion to the other end, as depicted in Figure 5.12. The bar is discretized with $8 \times 8 \times 32$ Q1P0-Q1Q1 finite elements. The material parameters used are given in Table 5.1. We focus on linear isotropic hardening. The computation is performed in a displacement-driven context.

Figure 5.13 demonstrates the distribution of the elongation along the third direction z for length scale parameter $l_p = 0.01$ mm and different rotation angles until one cycle $\Theta = 360°$ is completed. We observe that the axial length of the bar changes by increasing the torsion angel as well documented in Hatada et al. [67] and Swift [144]. To illustrate the influence of the length scale on the overall structure response, we plot in Figure 5.14a the torsion moment T versus the torsion angle Θ in combination with three different length scales l_p. Here, the torsion angle Θ is measured at the free end of the

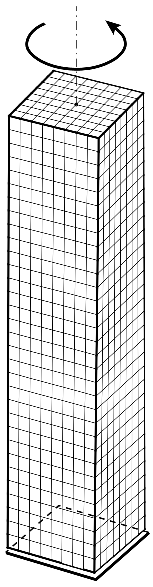

Figure 5.12: Torsion test of a square-section bar. Geometry and boundary conditions. The lower part is fixed and the upper part is loaded by rotating top with $\Theta = 360°$ around z axis at the center.

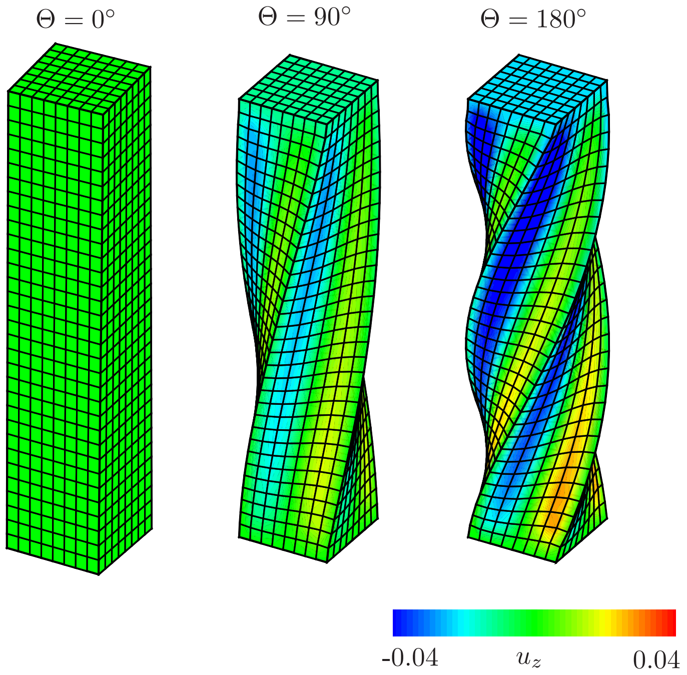

Figure 5.13: Torsion test of a square bar. Distribution of the elongation in the third direction u_z for different rotation angles till it complete one cycle. The bar is discretized with 8×8×32 Q1P0-Q1Q1 elements in combination with length scale parameter $l_p = 0.01$ mm.

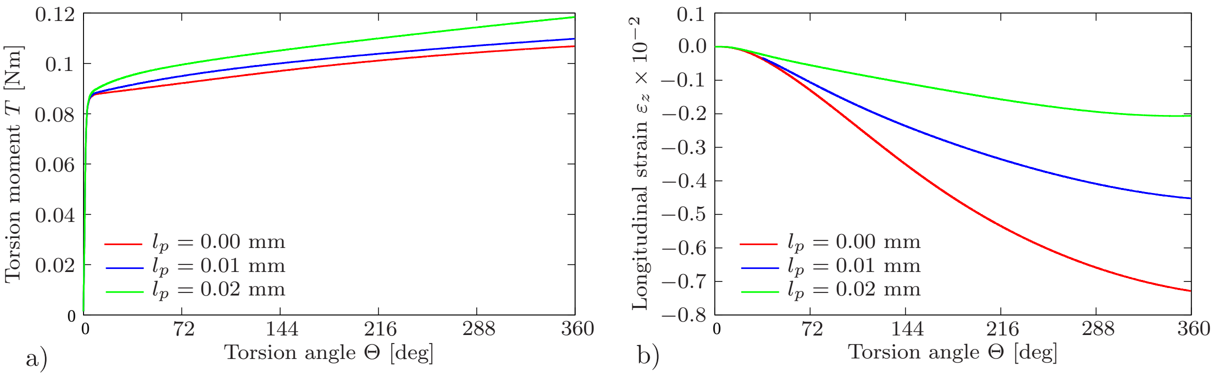

Figure 5.14: Torsion test of a square bar. a) Torsion moment–angle curve and b) longitudinal strain ε_z versus torsion angle for discretization with 8×8×32 Q1P0-Q1Q1 elements in combination with three different length scale parameter l_p.

square-section bar. We observe a stiffer global response by increasing the length scale l_p. Next we plot in Figure 5.14b the longitudinal strain ε_z versus the torsion angle Θ at the free end of the square-section bar. We notice that, by increasing the length scale parameter l_p, the absolute value of the longitudinal strain ε_z will be decreased, i.e. the length changes along the z axis will be decrease compared with the local analysis.

6. Phase Field Modeling of Ductile Fracture at Finite Strains

Most metals fail in a ductile fashion, i.e, fracture is preceded by significant plastic deformation. The modeling of failure in ductile materials must account for complex phenomena at a micro-scale as well as the final rupture at the macro-scale. This chapter outlines a variational based phase field modeling of ductile fracture in elastic-plastic solids which accounts for intrinsic material length scales to obtain mesh objectivity, based on the recent publications of Miehe et al. [108, 109] and Aldakheel et al. [9]. It links a formulation of variational gradient plasticity at finite strains as outlined in Miehe et al. [105] (see Chapter 5), to a specific setting of a variational gradient damage model, rooted in the phase field approach of fracture suggested by Miehe et al. [101, 100]. Such a formulation has recently been outlined in Miehe et al. [106] and is recast in this work into a canonical variational formulation. The finite element design of this formulation is not straightforward and requires additional strategies due to the difficulties near the elastic-plastic boundaries as outlined in the recent works Miehe et al. [105] for finite strains and Miehe et al. [104] for small strain formulation. To simplify the finite element implementation, we extend the introduced gradient plasticity-damage model towards the micromorphic regularization approach in line with the work of Forest [51]. We introduce coupled local-global variables for the gradient plasticity-damage problem linked by a penalty method. This leads to an additional partial differential equation for the micromorphic hardening variable denoted as the *micromorphic momentum balance* equation as shown in Forest [51].

To account for large strains, the constitutive model is constructed in the logarithmic strain space, which simplify the model equations and results in a formulation similar to small strains as outlined in Miehe et al. [99]. We demonstrate the modeling capabilities and algorithmic performance of the proposed formulation by representative simulations of ductile failure mechanisms in metals.

6.1. Geometric basis for phase field fracture

This section summarizes the basic ingredients of a purely geometric approach to the phase field modeling of fracture as outlined in the work of Miehe et al. [101]. It concerns the constitutive evolution of a regularized crack surface and the associated crack surface update module, that is linked in the subsequent section to the gradient extended elasto-plastic bulk response. In a first step, a one-dimensional bar is investigated, which is then generalized to the two and three dimensional settings.

6.1.1. One dimensional cracked bar. Following the works Miehe et al. [101, 100], we motivate the phase field approximation of sharp cracks by considering a simple model problem. To this end, we consider a one dimensional cracked bar occupying the domain $\mathcal{B} = \Gamma \times L$ where Γ is the cross-section and $L = [-\infty, +\infty]$ with the axial position $x \in L$. We assume at $x = 0$, a crack of the bar with the crack surface Γ. This sharp crack topology is indicated by an auxiliary field variable $d(x) \in [0, 1]$ known as the *crack phase field* with

$$d(x) := \begin{cases} 1 & \text{for } x = 0 \\ 0 & \text{otherwise} \end{cases} \tag{6.1}$$

characterizing the unbroken state for $d = 0$ and the fully broken state of the material for $d = 1$, illustrated in Figure 6.1a. The non-smooth phase field (6.1) is approximated by

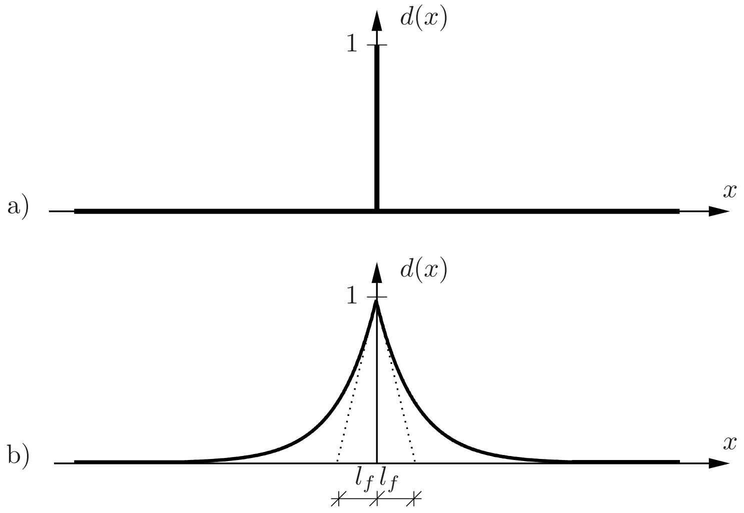

Figure 6.1: Sharp and diffusive crack modeling. a) Sharp crack at $x = 0$. b) Diffusive crack at $x = 0$ modeled with the length scale l_f. Regularized curves obtained from minimization principle of diffusive crack topology $\int_{\mathcal{B}} \widehat{\gamma}_l dV \rightarrow Min!$ with crack surface density function $\widehat{\gamma}_l = d^2/2l_f + l_f|\nabla d|^2/2$ with regularization profile $exp[-|x|/l_f]$ satisfying $d(0) = 1$.

the exponential function

$$d(x) = \mathrm{e}^{-|x|/l_f} \ . \tag{6.2}$$

It smears out the crack over the axial domain L of the bar, representing a regularized or diffusive crack topology governed by the fracture length scale parameter l_f and gives for $l_f \rightarrow 0$ the sharp crack topology as shown in Figure 6.1b. The exponential function (6.2) represents the solution of the homogeneous differential equation

$$d(x) - l_f^2 d''(x) = 0 \quad \text{ in } \mathcal{B} \ . \tag{6.3}$$

This differential equation is the Euler equation of the variational principle

$$d = \mathrm{Arg}\left\{ \inf_{d \in \mathcal{W}} \Pi(d) \right\} \quad \text{ with } \quad \mathcal{W} := \{ d | d(0) = 1, d(\pm\infty) = 0 \} \ , \tag{6.4}$$

expressed in terms of the functional

$$\Pi(d) = \frac{1}{2} \int_{\mathcal{B}} \{ d^2 + l_f^2 d'^2 \} \, dV. \tag{6.5}$$

This functional can easily be constructed by integrating a Galerkin-type weak form of the differential equation (6.3). Insertion of the exponential function (6.2) into (6.5) and evaluation with $dV = \Gamma \, dx$

$$\Pi(d = \mathrm{e}^{-|x|/l_f}) = l_f \Gamma \tag{6.6}$$

gives a relation between the functional Π and the crack surface Γ. Dividing the functional (6.5) by the fracture length scale parameter l_f, yields the functional

$$\Gamma_l(d) := \frac{1}{l_f} \Pi(d) = \frac{1}{2 l_f} \int_{\mathcal{B}} \left\{ d^2 + l_f^2 d'^2 \right\} \, dV \tag{6.7}$$

The minimization of this scaled functional also gives the regularized crack topology (6.2) as shown in Figure 6.1b. Resulting from the scaling by the fracture length scale parameter l_f, the functional $\Gamma_l(d)$ may be considered as the crack surface itself.

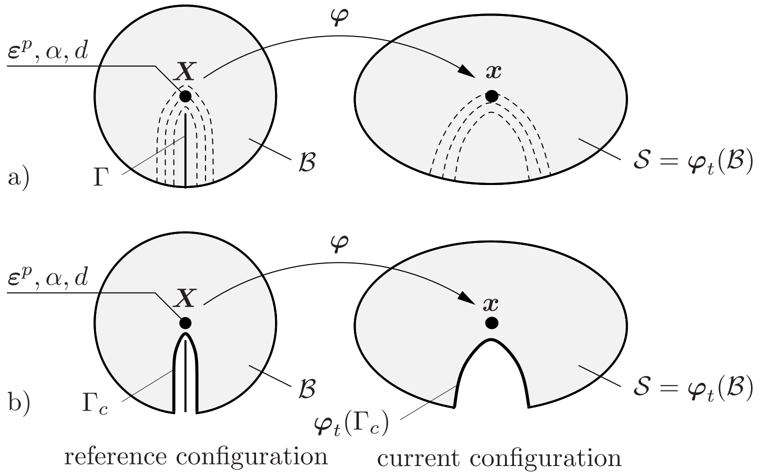
$\boldsymbol{\varepsilon}^p, \alpha, d$
$\boldsymbol{X}$
$\boldsymbol{\varphi}$
$\boldsymbol{x}$
a)
Γ
$\mathcal{B}$
$\mathcal{S} = \boldsymbol{\varphi}_t(\mathcal{B})$
$\boldsymbol{\varepsilon}^p, \alpha, d$
$\boldsymbol{X}$
$\boldsymbol{\varphi}$
$\boldsymbol{x}$
b)
Γ_c
$\mathcal{B}$
$\boldsymbol{\varphi}_t(\Gamma_c)$
$\mathcal{S} = \boldsymbol{\varphi}_t(\mathcal{B})$
reference configuration
current configuration

Figure 6.2: Finite deformation of a body with a regularized crack. The *deformation map* $\boldsymbol{\varphi}$ maps at time $t \in \mathcal{T}$ the reference configuration $\mathcal{B} \in \mathcal{R}^\delta$ onto the current configuration $\mathcal{S}$. a) The *crack phase field* $d \in [0, 1)$ defines a regularized crack surface functional $\Gamma_l(d)$ that converges in the limit $l_f \to 0$ to the sharp crack surface Γ. b) The level set $\Gamma_c = \{\boldsymbol{X} \mid d = c\}$ defines for a constant $c \approx 1$ the crack faces in the regularized setting. Parts of the continuum with $d > c$ are considered to be free space and are not displayed.

6.1.2. Regularized crack surface topology. We extended the one dimensional study introduced above to the multi-dimensional context. Let $\mathcal{B} \subset \mathcal{R}^\delta$ be the reference configuration of a material body with dimension $\delta \in [2, 3]$ in space and $\partial\mathcal{B} \subset \mathcal{R}^{\delta-1}$ its surface as depicted in Figure 6.2. We introduce the time-dependent crack phase field

$$d : \left\{ \begin{array}{l} \mathcal{B} \times \mathcal{T} \to [0, 1] \\ (\boldsymbol{X}, t) \mapsto d(\boldsymbol{X}, t) \end{array} \right. \tag{6.8}$$

defined on the solid $\mathcal{B}$. It governs the *regularized crack surface*

$$\Gamma_l(d) = \int_{\mathcal{B}} \widehat{\gamma}_l(d, \nabla d)\, dV \tag{6.9}$$

that is formulated in terms of the *crack surface density function* per unit volume of $\mathcal{B}$

$$\widehat{\gamma}_l(d, \nabla d) = \frac{1}{2 l_f} d^2 + \frac{l_f}{2} |\nabla d|^2 \ . \tag{6.10}$$

It is governed by the length scale parameter l_f. Assuming a given sharp crack surface topology by prescribing the Dirichlet condition $d = 1$ on $\Gamma \subset \mathcal{B}$, the regularized crack phase field d in the full domain $\mathcal{B}$ is obtained by a *minimization principle of diffusive crack topology*

$$d(\boldsymbol{X}, t) = \text{Arg} \left\{ \inf_{d \,\in\, \mathcal{W}_{\Gamma(t)}} \Gamma_l(d) \right\} \tag{6.11}$$

with the Dirichlet-type boundary constraint $\mathcal{W}_{\Gamma(t)} = \{\, d \,|d(\boldsymbol{X}, t) = 1 \text{ at } \boldsymbol{X} \in \Gamma(t) \,\}$. The Euler equations of this variational principle are

$$d - l_f^2 \Delta d = 0 \ \text{ in } \mathcal{B} \qquad \text{and} \qquad \nabla d \cdot \boldsymbol{N} = 0 \ \text{ on } \partial\mathcal{B} \ , \tag{6.12}$$

where Δd is the Laplacian of the phase field and $\boldsymbol{N}$ is the outward normal on $\partial\mathcal{B}$. For more details, we refer to Miehe et al. [101] and for higher–order regularization of the

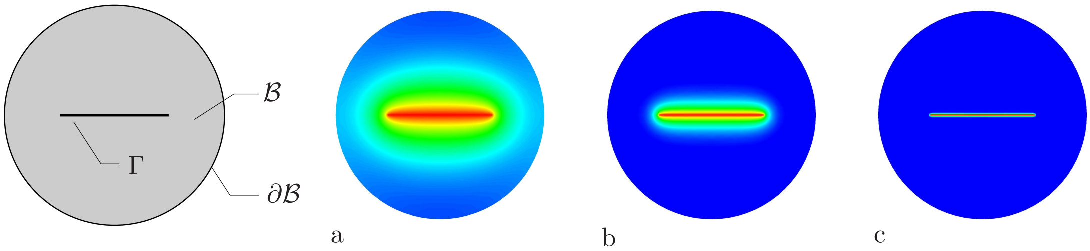

Figure 6.3: Continuum approximation of crack discontinuities. Solutions of the variational principle (6.11) for a circular specimen with a given sharp crack Γ, prescribed by the Dirichlet condition $d = 1$ on $\Gamma \subset \mathcal{B}$. Crack phase field $d \in [0,1]$ for different length scales ${l_f}^a > {l_f}^b > {l_f}^c$. The sequence of plots visualizes the limit $\Gamma_l \to \Gamma$ of the regularized crack surface functional (6.9) when $l_f \to 0$.

Box 6.1: *ALGO*$_1$: Updates of Crack Surface and Bulk Response in $[t_n, t]$.

1. *Initialize Crack Driving Force.* Explicit definition of the crack driving force
$$\mathcal{H}_0 = \mathcal{H}_{0_n}$$
2. *Update of Crack Surface.* Compute current crack phase field by the *linear* algorithm summarized in Box 6.2
$$d = ALGO_2(\mathcal{H}_0)$$
3. *Update of Bulk Response.* For given crack phase field d, update the gradient-extended elastic-plastic fields from an incremental variational principle
$$state := \text{Arg}\left\{ \inf_{state} \Pi^\tau(state) \right\} .$$
4. *Update Crack Driving Force.* For given state variables $state(\boldsymbol{X}, s)$ of bulk response, update crack driving force based on constitutive crack driving state function D_0
$$\mathcal{H}_0(\boldsymbol{X}, t) = \max_{s \in [0,t]} D_0(state(\boldsymbol{X}, s))$$
5. *Multi-Pass Solution.* For a Jacobi-type multi-pass solution of the crack surface and bulk response, go to 2) until convergence is achieved.

fracture phase field to Borden et al. [28]. Figure 6.3 depicts numerical solutions of the variational problem (6.11) for a two dimensional problem, which demonstrate the influence of the fracture length scale parameter l_f. Note that the limit of the principle (6.11)

$$\lim_{l_f \to 0} \left\{ \inf_{d \,\in\, \mathcal{W}_{\Gamma(t)}} \Gamma_l(d) \right\} = \Gamma(t) \tag{6.13}$$

gives the *sharp crack surface* Γ for a vanishing fracture length scale $l_f \to 0$.

6.1.3. Evolution of the regularized crack surface. The evolution of the regularized crack surface functional is driven by constitutive functions, postulating a global *evolution equation of regularized crack surface*

$$\frac{d}{dt}\Gamma_l(d) = \underbrace{\int_{\mathcal{B}} \delta_d \widehat{\gamma}_l(d, \nabla d)\, \dot{d}\; dV}_{evolution\ of\ cracks} = \underbrace{\frac{1}{l_f}\int_{\mathcal{B}} [\,(1-d)\mathcal{H}_0 - \mathcal{R}\,] \cdot \dot{d}\, dV}_{constitutive\ crack\ driving\ power} \geq 0\ . \tag{6.14}$$

The irreversible crack evolution is governed by the two constitutive functions for the effective driving force $\mathcal{H}_0$ and the viscous resistance $\mathcal{R}$. We assume the dependence

$$\mathcal{R}(\boldsymbol{X}, t) = \widetilde{\mathcal{R}}(\dot{d}(\boldsymbol{X}, t)) \quad \text{and} \quad \mathcal{H}_0 = \widetilde{\mathcal{H}}_0(state(\boldsymbol{X}, s), 0 \leq s \leq t))\ . \tag{6.15}$$

where *state* stands for additional variables determined by the model for the gradient-plastic bulk response considered in the next sections below, such as the local *energetic state* and the *plastic deformation state* in the solid. In what follows, we assume the simple constitutive function

$$\widetilde{\mathcal{R}} = \eta^f \dot{d} \tag{6.16}$$

for the viscous crack resistance, where $\eta^f \geq 0$ is a material parameter. Then the evolution statement (6.14) gives the local equation for the evolution of the crack phase field

$$\underbrace{\eta^f \dot{d}}_{evolution} = \underbrace{(1-d)\mathcal{H}_0}_{driving\ force} - \underbrace{[\,d - l_f^2 \Delta d\,]}_{geometric\ resistance} \tag{6.17}$$

in the domain $\mathcal{B}$, along with the homogeneous Neumann condition for the crack phase field $\nabla d \cdot \boldsymbol{N} = 0$ on $\partial\mathcal{B}$. Here, the geometric crack resistance is related to the variational derivative of the crack surface density function, i.e. $d - l_f^2 \Delta d = l_f \delta_d \widehat{\gamma}_l(d, \nabla d)$. The equation makes the evolution of the crack phase field dependent on the difference between the geometric crack driving force and the geometric crack resistance. (6.17) can be seen as a *generalized Ginzburg–Landau* equation, when the right hand side follows by a variational derivative of an energy expression. The framework covers the rate–independent limit for $\eta^f = 0$, where the crack surface is simply defined by an equilibrium for crack driving force and geometric crack resistance.

6.1.4. Irreversible crack evolution without crack healing. Within this work, we focus on an irreversibility of the crack evolution, governed by the constraint

$$\frac{d}{dt}\Gamma_l(d) \geq 0 \tag{6.18}$$

on the evolution of the regularized crack surface. This is realized by expressing the local crack driving force $\mathcal{H}_0$ by the *maximum value* of the associated *effective crack driving state function* D_0

$$\mathcal{H}_0(\boldsymbol{X}, t) = \max_{s \in [0,t]} D_0(state(\boldsymbol{X}, s)) \geq 0 \tag{6.19}$$

obtained in the full process history $s \in [0, t]$. This function must be a monotonous function that depends on state variables *state* of the gradient-extended bulk response, characterizing the unbroken state for $D_0 = 0$ and the fully broken state of the material for $D_0 = \infty$. This is consistent with the local evolution equation

$$\dot{d} = \frac{1}{\eta^f} \Big\langle (1-d) D_0 - l_f \delta_d \widehat{\gamma}_l \Big\rangle \geq 0 \tag{6.20}$$

Box 6.2: *ALGO*$_2$: Evolution and Update of Crack Surface for Given Force $\mathcal{H}_0$.

1. *Incremental Update of Crack Surface.* Semi-implicit time integration in $[t_n, t]$ with crack driving force $\mathcal{H}_0 = const.$ gives update of crack surface

$$\Gamma_l(d) = \Gamma_l(d_n) + \frac{1}{l_f}\int_{\mathcal{B}} \left\{[(d-d_n) - \frac{1}{2}(d^2 - d_n^2)]\mathcal{H}_0 - \frac{\eta^f}{2\tau}(d-d_n)^2\right\} dV$$

and induces the linear equation for the update of the crack phase field

$$\eta^f(d-d_n)/\tau = (1-d)\mathcal{H}_0 - [d - l_f^2\Delta d]$$

2. *Finite Element Update of Crack Surface.* Space discretization of phase field state $\mathfrak{c}_d^h := \{d^h, \nabla d^h\} = \boldsymbol{B}_d\boldsymbol{d}_d$ and optimization of the incremental potential

$$\Pi_d^{\tau\,h}(\boldsymbol{d}_d) = \int_{\mathcal{B}^h} \pi_d^\tau(\boldsymbol{B}_d\boldsymbol{d}_d)\, dV$$

with the potential density function

$$\pi_d^\tau = \frac{\eta^f}{2\tau}(d-d_n)^2 + l_f\widehat{\gamma}_l(d,\nabla d) - l_f\widehat{\gamma}_l(d_n,\nabla d_n) - [(d-d_n) - \frac{1}{2}(d^2-d_n^2)]\mathcal{H}_0$$

results in linear update of nodal degrees of the phase field in $[t_n, t]$

$$\boldsymbol{d}_d = -[\Pi_d^{\tau\,h}]^{-1}_{,\boldsymbol{d}_d\boldsymbol{d}_d}[\Pi_d^{\tau\,h}]_{,\boldsymbol{d}_d}$$

where $\langle x\rangle := (x + |x|)/2$ is the Macaulay bracket. Hence, a non–smooth evolution of the crack phase field takes place when the driving force exceeds the geometric crack resistance $\delta_d\widehat{\gamma}_l$. For the rate–independent limit $\eta^f \to 0$, the local evolution of the phase field is governed by

$$\dot{d} \geq 0, \quad [(1-d)D_0 - l_f\delta_d\widehat{\gamma}_l] \leq 0, \quad \dot{d}\,[(1-d)D_0 - l_f\delta_d\widehat{\gamma}_l] = 0\ . \tag{6.21}$$

Time integration of the evolution equation (6.14) for the regularized crack surface $\Gamma_l(d)$ gives for $\mathcal{H}_0 = const.$ the update equation of the phase field d outlined in Box 6.2, including the linear update of its nodal values in a typical finite element discretization. More details are outlined in the work MIEHE ET AL. [106, 107]. This *modular update tool for the crack surface* is linked in Box 6.1 via a one–pass operator split or a multi–pass Gauss–Seidel–type iteration to the update of the state variables of the gradient-extended bulk response.

6.2. Variational gradient-extended phase field modeling of ductile fracture

This section outlines a theory for the coupling of gradient plasticity with a phase field modeling of fracture that is fully variational in nature. It is based on the definition of constitutive work density and threshold functions, which define a *minimization principle* for the coupled evolution system.

6.2.1. Global primary fields and constitutive state variables. The multi-field setting of gradient plasticity at fracture is based on three *global primary fields*

$$\mathfrak{U} := \{\boldsymbol{\varphi}, \alpha, d\} \ , \tag{6.22}$$

the finite deformation map $\boldsymbol{\varphi}$, the strain-hardening variable α and the crack phase field d. In addition, the plastic strain field $\boldsymbol{\varepsilon}^p$ serves as an additional *local primary field*. The subsequent constitutive approach to the phase field modeling of ductile fracture focuses on the set

$$\mathfrak{C} := \{\nabla\boldsymbol{\varphi}, \boldsymbol{\varepsilon}^p, \alpha, \nabla\alpha, d, \nabla d\} \ , \tag{6.23}$$

reflecting a combination of first-order gradient plasticity with a first-order gradient damage modeling. The state $\mathfrak{C}$ is considered as automatically objective, due to the dependence on the deformation gradient $\nabla\boldsymbol{\varphi}$ through the Lagrangian Hencky strain $\boldsymbol{\varepsilon}$ defined in (2.52). The subsequent theory of gradient plasticity at fracture uses these set of constitutive state variables.

6.2.2. Coupling gradient plasticity to gradient damage mechanics. Consider the stress power acting on a local material element that undergoes elastic-plastic deformation and damage $\mathcal{P} := \boldsymbol{\sigma} : \dot{\boldsymbol{\varepsilon}}$. It is the inner product of stress and rate of strain, the thermodynamic external variables acting on the material element. We use the Lagrangian logarithmic Hencky tensor $\boldsymbol{\varepsilon}$ defined in (2.52) and its dual stress tensor $\boldsymbol{\sigma}$. Let W denote the time-accumulated work per unit volume and $\boldsymbol{\mathcal{W}}$ its accumulation in space

$$W := \int_0^T \mathcal{P}\, dt \quad \text{and} \quad \boldsymbol{\mathcal{W}} := \int_{\mathcal{B}} W\, dV \ , \tag{6.24}$$

i.e. the total work needed to deform and crack the solid $\mathcal{B}$ within the process time $[0, T]$. We base the subsequent development of a phase field approach on a constitutive representation of this work

$$\boldsymbol{\mathcal{W}} = \int_{\mathcal{B}} [\, \widehat{W}(\mathfrak{C}) + D_{vis} \,] dV \ . \tag{6.25}$$

It is governed by a *constitutive work density function* $\widehat{W}$ that describes the *rate-independent part* of the global work $\boldsymbol{\mathcal{W}}$. The a priori dissipative *rate-dependent part* D_{vis} due to viscous resistance forces vanishes in the rate-independent limit. Equation (6.25) holds for particular boundary conditions of the *non-local* generalized internal variable fields α and d. These must be *passive* in the sense that an external driving of these fields is not allowed, which is consistent with (i) *constant Dirichlet data* and (ii) *zero Neumann data* of α and d on the surface $\partial\mathcal{B}$ of the solid. The rate-independent part $\widehat{W}$ is assumed to depend on the array $\mathfrak{C}$ of constitutive state variables introduced in (6.23). We focus on the particular structure

$$\widehat{W}(\mathfrak{C}) = \widehat{g}(d)\widehat{w}_0^{ep}(\boldsymbol{\varepsilon}^e, \alpha, \nabla\alpha) + (1 - \widehat{g}(d))w_c + 2\frac{w_c}{\zeta} l_f \widehat{\gamma}_l(d, \nabla d) \tag{6.26}$$

already suggested in Miehe et al. [106], which provides a particular coupling of gradient plasticity with gradient damage mechanics. The function $\widehat{w}_0^{ep}$ splits up into elastic and plastic contributions according to

$$\widehat{w}_0^{ep}(\boldsymbol{\varepsilon}^e, \alpha, \nabla\alpha) = \widehat{w}_0^e(\boldsymbol{\varepsilon}^e) + \widehat{w}_0^p(\alpha, \nabla\alpha) \ . \tag{6.27}$$

The derivatives of the potential density $\widehat{W}$ determine the rate-independent parts of stresses, the driving forces and the thresholds for the evolution of the plastic strains and the fracture phase field. It models for $d \in [0,1]$ with the first two terms a phase transition of the effective elastic-plastic work density $\widehat{w}_0^{ep}$ towards the *constant threshold value* w_c, and with the third term the accumulated fracture work density. Here, $w_c > 0$ is a specific critical fracture energy per unit volume, that enters the formulation as the key material parameter on the side of fracture mechanics. The second material parameter $\zeta > 0$ controls the post-critical range after crack initialization by scaling the work needed for the generation of the regularized crack surface. The third parameter l_f is the length scale parameter associated with the crack surface regularization introduced above.

6.2.3. Effective elastic-plastic work and degradation functions.

Effective elastic work density. The effective elastic work density function $\widehat{w}_0^e$ in (6.27) models the stored elastic energy of the unbroken material, depending on the logarithmic elastic strain measure

$$\boldsymbol{\varepsilon}^e = \boldsymbol{\varepsilon} - \boldsymbol{\varepsilon}^p = \tfrac{1}{2}\ln \boldsymbol{C} - \tfrac{1}{2}\ln \boldsymbol{G}^p \ . \tag{6.28}$$

For the subsequent model problems, the elastic work density is assumed to have the simple quadratic form

$$\widehat{w}_0^e(\boldsymbol{\varepsilon}^e) = \frac{\kappa}{2}\mathrm{tr}^2[\boldsymbol{\varepsilon}^e] + \mu\,\mathrm{tr}[\mathrm{dev}(\boldsymbol{\varepsilon}^e)^2] \ , \tag{6.29}$$

characterizing an isotropic, linear stress response in the logarithmic strain space. $\kappa > 0$ and $\mu > 0$ are the elastic bulk and the shear modulus, respectively. The function provides a structure identical to the geometrical linear theory of elasticity at small strains.

Effective plastic work density. The effective plastic work density function $\widehat{w}_0^p$ in (6.27) models the dissipated plastic work of the unbroken material per unit volume, in terms of variables which describe the strain gradient hardening effect. For the modeling of length scale effects in isotropic gradient plasticity, we focus on the equivalent plastic strain α and its gradient. It is assumed to have the form

$$\widehat{w}_0^p(\alpha, \nabla\alpha) = \int_0^\alpha \widehat{y}(\widetilde{\alpha})d\widetilde{\alpha} + y_0\frac{l_p^2}{2}|\nabla\alpha|^2 \ , \tag{6.30}$$

where $l_p \geq 0$ is a plastic length scale related to a strain-gradient hardening effect. $\widehat{y}(\alpha)$ is an isotropic local hardening function obtained form homogeneous experiments. We use in what follows the saturation-type function

$$\widehat{y}(\alpha) = (y_\infty - y_0)(\,1 - \exp[-\eta_s\alpha]\,) \,+\, h\alpha \ , \tag{6.31}$$

in terms of the four material parameters $y_0 > 0$, $y_\infty \geq y_0$, $\eta_s > 0$ and $h \geq 0$, where the initial yield stress y_0 determines the threshold of the effective elastic response.

Degradation function. The degradation function $\widehat{g}(d)$ in (6.26) models the degradation of the elastic-plastic work density due to fracture. It interpolates between the unbroken response for $d = 0$ and the fully broken state at $d = 1$ by satisfying the constraints

$$\widehat{g}(0) = 1 \quad , \quad \widehat{g}(1) = 0 \quad , \quad \widehat{g}'(d) \leq 0 \quad , \quad \widehat{g}'(1) = 0 \ . \tag{6.32}$$

In particular, the last constraint ensures that the local driving force dual to d ensures an upper bound of the phase field $d \in [0,1]$. A function that satisfies this constraint is

$$\widehat{g}(d) = (1-d)^2 \; . \tag{6.33}$$

The quadratic nature of this function is an important ingredient for the construction of a *linear equation* for the evolution of the phase field d. It appears in the Γ-convergent regularization by AMBROSIO & TORTORELLI [15] of the Mumford-Shah functional in image segmentation, see MUMFORD & SHAH [115]. Subsequently, it has been used by BOURDIN ET AL. [29] in the incremental approximation of their variational theory of brittle fracture FRANCFORT & MARIGO [53], see also COMI [37] for an early application in gradient damage mechanics. Note that the total work density $\widehat{W}$ introduced in (6.26) applies the same degradation function $\widehat{g}(d)$ on the effective elastic and plastic work densities $\widehat{w}_0^e$ and $\widehat{w}_0^p$, respectively. This is an important assumption with regard to the subsequent construction of a *gradient plasticity model related to the effective quantities* of the undamaged material, where the effective plastic work density $\widehat{w}_0^p$ serves as a ductile contribution to the crack driving force.

6.2.4. Driving, resistance and thresholds for plasticity and fracture. The evolution of the plastic strains and fracture phase field is constructed in a normal-dissipative format related to threshold functions. These functions are formulated in terms of driving and resistance forces related the work density function $\widehat{W}$.

Plasticity. The plastic driving force $\boldsymbol{f}^p$ dual to the plastic strain $\boldsymbol{\varepsilon}^p$ and the resistance force $-r^p$ dual to the hardening variable α are defined by

$$\boldsymbol{f}^p := -\partial_{\boldsymbol{\varepsilon}^p}\widehat{W} \quad \text{and} \quad r^p := \delta_\alpha \widehat{W} \; . \tag{6.34}$$

Here, $\delta_\alpha \widehat{W} := \partial_\alpha \widehat{W} - \mathrm{Div}[\partial_{\nabla\alpha}\widehat{W}]$ denotes the variational derivative of $\widehat{W}$ with respect to α, reflecting characteristics of the gradient-extended plasticity model under consideration. Clearly, for the kinematic assumption (6.28), the plastic driving force $\boldsymbol{f}^p$ is the stress tensor $\boldsymbol{\sigma}$ dual to the Hencky strain $\boldsymbol{\varepsilon}$ in the logarithmic strain space. An *elastic domain* associated with the plastic deformation in the space of the plastic driving force is defined by

$$\mathbb{E}_{plas} := \{\ (\boldsymbol{f}^p, r^p) \,|\, \widehat{\phi}^p(\boldsymbol{f}^p, r^p) \le 0\ \} \tag{6.35}$$

in terms of the *plastic yield function* $\widehat{\phi}^p$. We focus on the function

$$\widehat{\phi}^p(\boldsymbol{f}^p, r^p) = ||\,\mathrm{dev}[\boldsymbol{f}^p]|| - \sqrt{2/3}\, r^p \tag{6.36}$$

of von Mises type in the logarithmic stress space. This yield function can be recast into the form

$$\widehat{\phi}^p(\boldsymbol{f}^p, r^p) = \widehat{g}(d)\, \widehat{\phi}^p_0(\boldsymbol{f}^p_0, r^p_0) \quad \text{with} \quad \widehat{\phi}^p_0 = ||\,\mathrm{dev}[\boldsymbol{f}^p_0]|| - \sqrt{2/3}\, r^p_0 \tag{6.37}$$

in terms of the degradation function $\widehat{g}(d)$ defined in (6.33) and the *effective plastic yield function* formulated in terms of the *effective stress-like variables*

$$\boldsymbol{f}^p_0 := \frac{1}{\widehat{g}(d)}\boldsymbol{f}^p = -\partial_{\boldsymbol{\varepsilon}^p}\widehat{w}^e_0 \quad \text{and} \quad r^p_0 := \frac{1}{\widehat{g}(d)} r^p = \delta_\alpha \widehat{w}^p_0 \; . \tag{6.38}$$

This constitutive structure characterizes a formulation of gradient plasticity related to the effective state variables of the undamaged material. Hence, $\mathbb{E}_{plas}$ in (6.35) can be interpreted to bound the domain

$$\mathbb{E}^0_{plas} := \{ \, (\boldsymbol{f}^p_0, r^p_0) \, | \, \widehat{\phi}^p_0(\boldsymbol{f}^p_0, r^p_0) \leq 0 \, \} \tag{6.39}$$

in the effective stress space.

Fracture. The fracture driving and resistance forces $(f^f - r^f)$ dual to the fracture phase field d are defined by

$$f^f - r^f := -\delta_d \widehat{W} \quad \text{with} \quad \delta_d \widehat{W} := \partial_d \widehat{W} - \text{Div}[\partial_{\nabla d} \widehat{W}] \; . \tag{6.40}$$

A *crack resistance domain* associated with the crack propagation in the space of the crack driving force is defined by

$$\mathbb{E}_{frac} := \{ \, (f^f - r^f) \, | \, \widehat{\phi}^f(f^f - r^f) \leq 0 \, \} \tag{6.41}$$

in terms of the *crack threshold function* $\widehat{\phi}^f$. We focus on the constitutive representation

$$\widehat{\phi}^f(f^f - r^f) = f^f - r^f \; , \tag{6.42}$$

where the *defined* fracture driving force f^f is bounded by the crack resistance r^f.

6.2.5. Rate-dependent evolution equations for the internal variables. With the above introduced threshold and resistance functions at hand, a dissipation potential function can be constructed based on the standard concept of maximum dissipation. A rate-dependent dissipation potential function in a non-constrained manner is defined as

$$\widehat{V}(\dot{\mathfrak{C}}) = \sup_{\boldsymbol{f}^p, r^p, f^f - r^f} [\, \boldsymbol{f}^p : \dot{\boldsymbol{\varepsilon}}^p - r^p \dot{\alpha} + (f^f - r^f) \dot{d} - \widehat{V}^*(\boldsymbol{f}^p, r^p, f^f - r^f) \,] \; , \tag{6.43}$$

in terms of the *dual dissipation potential function*

$$\widehat{V}^*(\boldsymbol{f}^p, r^p, f^f - r^f) = \frac{1}{2\eta_p} \left\langle \widehat{\phi}^p(\boldsymbol{f}^p, r^p) \right\rangle^2 + \frac{1}{2\eta^f} \left\langle \widehat{\phi}^f(f^f - r^f) \right\rangle^2 \tag{6.44}$$

where $\langle x \rangle := (x + |x|)/2$ is the Macaulay bracket. η_p and η^f are additional material parameters which characterize viscosity of the plastic deformation and the crack propagation. Note that the dual dissipation potential $\widehat{V}^*$ can mathematically be interpreted as a quadratic penalty term, that enforces approximately the threshold conditions (6.35) and (6.41). The necessary conditions of the local optimization problem (6.43) yield the *plastic flow rules*

$$\dot{\boldsymbol{\varepsilon}}^p = \lambda^p \partial_{\boldsymbol{f}^p} \widehat{\phi}^p = \lambda^p \frac{\text{dev}[\boldsymbol{f}^p]}{|| \, \text{dev}[\boldsymbol{f}^p] ||} \quad \text{and} \quad \dot{\alpha} = -\lambda^p \partial_{r^p} \widehat{\phi}^p = \lambda^p \sqrt{2/3} \tag{6.45}$$

and the normal-dissipative *evolution equation* for the *crack phase field*

$$\dot{d} = \lambda^f \partial_{f^f - r^f} \widehat{\phi}^f \tag{6.46}$$

in terms of the viscous constitutive functions

$$\lambda^p := \frac{1}{\eta_p} \left\langle \widehat{\phi}^p(\boldsymbol{f}^p, r^p) \right\rangle \geq 0 \quad \text{and} \quad \lambda^f := \frac{1}{\eta^f} \left\langle \widehat{\phi}^f(f^f - r^f) \right\rangle \geq 0 \; . \tag{6.47}$$

Furthermore, note that the positiveness of the parameters λ^p and λ^f imply via (6.45) and (6.46) a *monotonous growth*

$$\dot{\alpha} \geq 0 \quad \text{and} \quad \dot{d} \geq 0 \tag{6.48}$$

of the equivalent plastic strain and the fracture phase field.

6.2.6. Minimization principle for the multi-field evolution problem. With the above introduced functions at hand, the boundary value problem is fully governed by a rate-type minimization principle for the quasi-static case, where inertia effects are neglected. In line with recent treatments on variational principles of gradient-extended materials outlined in MIEHE [96], consider the constitutive rate potential density

$$\pi(\dot{\boldsymbol{\mathfrak{C}}}) = \frac{d}{dt}\widehat{W}(\boldsymbol{\mathfrak{C}}) + \widehat{V}(\dot{\boldsymbol{\mathfrak{C}}}) \tag{6.49}$$

in terms of the basic constitutive functions $\widehat{W}$ and $\widehat{V}$ defined in (6.26) and (6.43), respectively. With this potential density at hand, the evolution of the boundary problem of gradient plasticity coupled with gradient damage mechanics is governed by the *global rate potential*

$$\Pi(\dot{\boldsymbol{\varphi}}, \dot{\alpha}, \dot{d}, \dot{\boldsymbol{\varepsilon}}^p) = \int_{\mathcal{B}} \pi(\dot{\boldsymbol{\mathfrak{C}}})\, dV \; - \; P_{ext}(\dot{\boldsymbol{\varphi}}) \tag{6.50}$$

where $P_{ext}(\dot{\boldsymbol{\varphi}}) := \int_{\mathcal{B}} \overline{\boldsymbol{\gamma}}_0 \cdot \dot{\boldsymbol{\varphi}}\, dV + \int_{\partial\mathcal{B}} \overline{\boldsymbol{t}}_0 \cdot \dot{\boldsymbol{\varphi}}\, dA$ is an external load functional. $\overline{\boldsymbol{\gamma}}_0$ is a given body force per unit volume of the reference configuration, $\overline{\boldsymbol{t}}_0$ a given traction field on the surface of the reference configuration. The evolution of all primary fields is determined by the *minimization principle*

$$\{\dot{\boldsymbol{\varphi}}, \dot{\alpha}, \dot{d}, \dot{\boldsymbol{\varepsilon}}^p\} = \text{Arg}\{ \inf_{\dot{\boldsymbol{\varphi}}, \dot{\alpha}, \dot{d}, \dot{\boldsymbol{\varepsilon}}^p} \Pi(\dot{\boldsymbol{\varphi}}, \dot{\alpha}, \dot{d}, \dot{\boldsymbol{\varepsilon}}^p) \; \} \; . \tag{6.51}$$

Note that the minimization structure of this variational principle is governed by the *convexity of the dissipation potential function* $\widehat{V}$ in (6.43), which ensures the thermodynamical consistency. The combination of the global minimization principle (6.51) with the local maximum problem (6.43) for the definition of the dissipation potential $\widehat{V}$ provides a *mixed variational principle*, that defines all equations of the problem of gradient plasticity at fracture. When introducing the *mixed potential density*

$$\pi^* = \frac{d}{dt}\widehat{W} + \boldsymbol{f}^p : \dot{\boldsymbol{\varepsilon}}^p - r^p \dot{\alpha} + (f^f - r^f)\dot{d} - \frac{1}{2\eta_p}\left\langle \widehat{\phi}^p \right\rangle^2 - \frac{1}{2\eta^f}\left\langle \widehat{\phi}^f \right\rangle^2 \; , \tag{6.52}$$

the Euler equations of the variational principle (6.51) appear in the form

$$\boxed{\begin{array}{llrl}
1. & \textit{Stress equilibrium} & \delta_{\dot{\boldsymbol{\varphi}}}\pi^* \equiv & -\text{Div}\,[\,\partial_{\nabla\boldsymbol{\varphi}}\widehat{W}\,] = \overline{\boldsymbol{\gamma}}_0 \\
2. & \textit{Hardening force} & \delta_{\dot{\alpha}}\pi^* \equiv & \partial_{\alpha}\widehat{W} - \text{Div}\,[\,\partial_{\nabla\alpha}\widehat{W}\,] - r^p = 0 \\
3. & \textit{Fracture force} & \delta_{\dot{d}}\pi^* \equiv & \partial_{d}\widehat{W} - \text{Div}\,[\,\partial_{\nabla d}\widehat{W}\,] + (f^f - r^f) = 0 \\
4. & \textit{Plastic force} & \delta_{\dot{\boldsymbol{\varepsilon}}^p}\pi^* \equiv & \partial_{\boldsymbol{\varepsilon}^p}\widehat{W} + \boldsymbol{f}^p = \boldsymbol{0} \\
5. & \textit{Plastic strains} & \partial_{\boldsymbol{f}^p}\pi^* \equiv & \dot{\boldsymbol{\varepsilon}}^p - \lambda^p \partial_{\boldsymbol{f}^p}\widehat{\phi}^p = \boldsymbol{0} \\
6. & \textit{Equivalent strain} & \partial_{r^p}\pi^* \equiv & -\dot{\alpha} - \lambda^p \partial_{r^p}\widehat{\phi}^p = 0 \\
7. & \textit{Fracture phase field} & \partial_{(f^f - r^f)}\pi^* \equiv & \dot{d} - \lambda^f \partial_{(f^f - r^f)}\widehat{\phi}^f = 0
\end{array}} \tag{6.53}$$

along with Neumann-type boundary conditions of the form defined as

$$\boldsymbol{P}\boldsymbol{N} = \bar{\boldsymbol{t}}_0(\boldsymbol{X}, t) \text{ on } \partial\mathcal{B}^t \quad , \quad \nabla\alpha \cdot \boldsymbol{N} = \boldsymbol{0} \text{ on } \partial\mathcal{B}^{\nabla\alpha} \quad , \quad \nabla d \cdot \boldsymbol{N} = \boldsymbol{0} \text{ on } \partial\mathcal{B}^{\nabla d} \; . \tag{6.54}$$

The loading parameters λ^p and λ^f are defined in (6.47). Note that the above Euler equations are exclusively related to variational derivatives of the potential density π^* defined in (6.52).

6.3. Micromorphic approach for gradient plasticity-damage models

The finite element design of gradient plasticity coupled to gradient damage is not straightforward and requires additional strategies due to the difficulties near the elastic-plastic boundaries EPBs as outlined in the recent works MIEHE ET AL. [105] for finite strains and MIEHE ET AL. [104] for small strains. To simplify the above introduced formulation, we extend it towards the *micromorphic approach* to gradient plasticity-damage model in line with the work of FOREST [51]. Here, coupled local-global variables for the gradient plasticity problem are linked by a penalty method resulting in an additional micromorphic balance equation.

6.3.1. Extended constitutive state and work density function. We extend the constitutive state introduced in (6.23) by an additional variable namely the local equivalent plastic strain $\bar{\alpha}$ in the micromorphic setting, yielding

$$\mathfrak{C}^* := \{\nabla\boldsymbol{\varphi}, \boldsymbol{\varepsilon}^p, \bar{\alpha}, \alpha, \nabla\alpha, d, \nabla d\} \ . \tag{6.55}$$

where α is the global micromorphic variable. With this extended state variables at hand, the extended micromorphic work density function (6.26) reads

$$\widehat{W}(\mathfrak{C}^*) = \widehat{g}(d)\widehat{w}_0^{ep}(\boldsymbol{\varepsilon}^e, \bar{\alpha}, \alpha, \nabla\alpha) + (1 - \widehat{g}(d))w_c + 2\frac{w_c}{\zeta} l_f \widehat{\gamma}_l(d, \nabla d) \ . \tag{6.56}$$

The function $\widehat{w}_0^{ep}$ introduced in (6.27) now reads

$$\widehat{w}_0^{ep}(\boldsymbol{\varepsilon}^e, \bar{\alpha}, \alpha, \nabla\alpha) = \widehat{w}_0^{e}(\boldsymbol{\varepsilon}^e) + \widehat{w}_0^{p}(\bar{\alpha}, \alpha, \nabla\alpha) \ , \tag{6.57}$$

in terms of the extended micromorphic plastic work density function

$$\widehat{w}_0^{p}(\bar{\alpha}, \alpha, \nabla\alpha) = \int_0^{\bar{\alpha}} \widehat{y}(\tilde{\bar{\alpha}})d\tilde{\bar{\alpha}} + y_0\frac{l_p^2}{2}|\nabla\alpha|^2 + \frac{\epsilon_p}{2}(\bar{\alpha} - \alpha)^2 \ . \tag{6.58}$$

Here, ϵ_p is an additional material parameter, in which for $\epsilon_p \to \infty$ it leads to the aforementioned gradient plasticity setting defined in equation (6.30).

6.3.2. Plastic driving force and resistance. The plastic driving and resistance forces defined in (6.34) are now extended to the micromorphic setting as

$$\boldsymbol{f}^p := -\partial_{\boldsymbol{\varepsilon}^p}\widehat{W} \ , \quad r^p := \partial_{\bar{\alpha}}\widehat{W} \ , \quad \delta_\alpha\widehat{W} = 0 \ . \tag{6.59}$$

Here, $\delta_\alpha\widehat{W} := \partial_\alpha\widehat{W} - \mathrm{Div}[\partial_{\nabla\alpha}\widehat{W}]$ denotes again the variational derivative of $\widehat{W}$ with respect to the global micromorphic variable α, reflecting characteristics of the gradient-extended micromorphic plasticity model under consideration. The plastic driving force $\boldsymbol{f}^p$ is the same as in $(6.34)_1$, whereas the non-local plastic resistance force r^p in $(6.34)_2$ is now *locally* defined based on the variables $\bar{\alpha}$ and α. Equation $(6.59)_3$ defines the additional micromorphic balance equation that links the local variable $\bar{\alpha}$ to the global micromorphic variable α.

6.3.3. Evolution equations of the internal variables. With the above introduced driving and resistance forces for the gradient plasticity problem, the dissipation potential is now extended to the micromorphic formulation as

$$\widehat{V}(\dot{\mathfrak{C}}^*) = \sup_{\boldsymbol{f}^p, r^p, f^f - r^f} [\ \boldsymbol{f}^p : \dot{\boldsymbol{\varepsilon}}^p - r^p\dot{\bar{\alpha}} + (f^f - r^f)\dot{d} - \widehat{V}^*(\boldsymbol{f}^p, r^p, f^f - r^f)\ ] \ , \tag{6.60}$$

in terms of the dual dissipation potential function $\widehat{V}^*$. The necessary conditions of the local optimization problem (6.60) yield the evolution equations for the two *local* variables, i.e. the plastic flow rules

$$\dot{\boldsymbol{\varepsilon}}^p = \lambda^p \, \partial_{\boldsymbol{f}^p} \widehat{\phi}^p \quad \text{and} \quad \dot{\bar{\alpha}} = -\lambda^p \, \partial_{r^p} \widehat{\phi}^p \ , \tag{6.61}$$

and the global evolution equation for the crack phase field

$$\dot{d} = \lambda^f \, \partial_{f^f - r^r} \widehat{\phi}^f \ , \tag{6.62}$$

with the viscous constitutive functions λ^p and λ^f defined in (6.47).

6.3.4. Micromorphic regularization of the minimization principle. The evolution of the micromorphic gradient plasticity coupled with gradient damage is governed by the *extended global rate potential*

$$\Pi(\dot{\boldsymbol{\varphi}}, \dot{\alpha}, \dot{d}, \dot{\bar{\alpha}}, \dot{\boldsymbol{\varepsilon}}^p) = \int_{\mathcal{B}} \pi(\dot{\boldsymbol{\mathfrak{C}}}^*) \, dV \ - \ P_{ext}(\dot{\boldsymbol{\varphi}}) \ , \tag{6.63}$$

in terms of the micromorphic regularization of the constitutive potential density function π defined through the modified $\widehat{W}(\boldsymbol{\mathfrak{C}}^*)$ and $\widehat{V}(\dot{\boldsymbol{\mathfrak{C}}}^*)$ in (6.56) and (6.60), respectively. With these two functions at hand, we introduce the *modified mixed potential density function*

$$\pi^* = \frac{d}{dt}\widehat{W} + \boldsymbol{f}^p : \dot{\boldsymbol{\varepsilon}}^p - r^p \dot{\bar{\alpha}} + (f^f - r^f)\dot{d} - \frac{1}{2\eta_p} \left\langle \widehat{\phi}^p \right\rangle^2 - \frac{1}{2\eta^f} \left\langle \widehat{\phi}^f \right\rangle^2 \ . \tag{6.64}$$

The evolution of the extended variables defined in (6.55) is determined by the *micromorphic regularization* of the minimization principle

$$\{\dot{\boldsymbol{\varphi}}, \dot{\alpha}, \dot{d}, \dot{\bar{\alpha}}, \dot{\boldsymbol{\varepsilon}}^p\} = \text{Arg}\{ \inf_{\dot{\boldsymbol{\varphi}}, \dot{\alpha}, \dot{d}, \dot{\bar{\alpha}}, \dot{\boldsymbol{\varepsilon}}^p} \Pi(\dot{\boldsymbol{\varphi}}, \dot{\alpha}, \dot{d}, \dot{\bar{\alpha}}, \dot{\boldsymbol{\varepsilon}}^p) \ \} \ . \tag{6.65}$$

The Euler equations of this variational principle are

$$\boxed{\begin{array}{lllrl}
1. & \textit{Stress equilibrium} & & \delta_{\dot{\boldsymbol{\varphi}}}\pi^* \equiv & -\text{Div}\,[\,\partial_{\nabla\boldsymbol{\varphi}}\widehat{W}\,] = \ \overline{\boldsymbol{\gamma}}_0 \\
2. & \textit{Micromorphic mom. bal.} & & \delta_{\dot{\alpha}}\pi^* \equiv & \partial_{\alpha}\widehat{W} - \text{Div}\,[\,\partial_{\nabla\alpha}\widehat{W}\,] = 0 \\
3. & \textit{Fracture force} & & \delta_{\dot{d}}\pi^* \equiv & \partial_{d}\widehat{W} - \text{Div}\,[\,\partial_{\nabla d}\widehat{W}\,] + (f^f - r^f) = 0 \\
4. & \textit{Hardening force} & & \delta_{\dot{\bar{\alpha}}}\pi^* \equiv & \partial_{\bar{\alpha}}\widehat{W} - r^p = 0 \\
5. & \textit{Plastic force} & & \delta_{\dot{\boldsymbol{\varepsilon}}^p}\pi^* \equiv & \partial_{\boldsymbol{\varepsilon}^p}\widehat{W} + \boldsymbol{f}^p = \boldsymbol{0} \\
6. & \textit{Plastic strains} & & \partial_{\boldsymbol{f}^p}\pi^* \equiv & \dot{\boldsymbol{\varepsilon}}^p - \lambda^p\partial_{\boldsymbol{f}^p}\widehat{\phi}^p = \boldsymbol{0} \\
7. & \textit{Equivalent strain} & & \partial_{r^p}\pi^* \equiv & -\dot{\bar{\alpha}} - \lambda^p\partial_{r^p}\widehat{\phi}^p = 0 \\
8. & \textit{Fracture phase field} & & \partial_{(f^f - r^f)}\pi^* \equiv & \dot{d} - \lambda^f\partial_{(f^f - r^f)}\widehat{\phi}^f = 0
\end{array}} \tag{6.66}$$

along with Neumann-type boundary conditions defined in (6.54).

6.4. Numerical implementation of the regularized minimization problem

6.4.1. Incremental potential density function. We consider a finite time increment $[t_n, t_{n+1}]$, where $\tau_{n+1} := t_{n+1} - t_n > 0$ denotes the step length. All fields at time t_n are assumed to be *known*. The goal then is to determine the fields at time t_{n+1} based on variational principles valid for the time increment under consideration. Subsequently, all variables without subscript are evaluated at time t_{n+1}. Next, we define the *mixed incremental potential density* per unit volume by an algorithmic approximation

$$\pi^{*\tau}(\mathfrak{C}^*) = Algo\Big\{ \int_{t_n}^{t_{n+1}} \pi^* \, dt \Big\} \tag{6.67}$$

in terms of the continuous rate-type potential π^* introduced in (6.64). Using a fully implicit Euler scheme gives

$$\pi^{*\tau} = \widehat{W} + \boldsymbol{f}^p : (\boldsymbol{\varepsilon}^p - \boldsymbol{\varepsilon}^p_n) - r^p(\bar{\alpha} - \bar{\alpha}_n) + (f^f - r^f)(d - d_n) - \frac{\tau}{2\eta_p}\left\langle \widehat{\phi}^p \right\rangle^2 - \frac{\tau}{2\eta^f}\left\langle \widehat{\phi}^f \right\rangle^2 . \tag{6.68}$$

The set $\mathfrak{C}^*$ of the current variables can be decomposed into a *local part* $\mathfrak{C}^*_l$ associated with variables related to local ordinary differential equations ODEs and a *global part* $\mathfrak{C}^*_g$ associated with variables related to global partial differential equations PDEs

$$\mathfrak{C}^* = \mathfrak{C}^*_l + \mathfrak{C}^*_g \quad \text{with} \quad \mathfrak{C}^*_l := \{\bar{\alpha}, \boldsymbol{\varepsilon}^p, \boldsymbol{f}^p, r^p\} \quad \text{and} \quad \mathfrak{C}^*_g := \{\nabla\boldsymbol{\varphi}, \alpha, \nabla\alpha, d, \nabla d, f^f - r^f\} . \tag{6.69}$$

According to this split, the solution procedure for the update of the state variables is decomposed into a local and a global part.

6.4.2. Condensation of local variables. The first part of the incremental solution procedure consists of the condensation of the incremental potential density $\pi^{*\tau}$ by the set of local variables assembled in $\mathfrak{C}^*_l$ defining the *condensed incremental work density*

$$(L): \quad \pi^{*\tau}_{red}(\mathfrak{C}^*_g) = \inf_{\bar{\alpha}, \boldsymbol{\varepsilon}^p} \sup_{\boldsymbol{f}^p, r^p} \pi^{*\tau}(\mathfrak{C}^*) . \tag{6.70}$$

The necessary conditions of this local problem are

$$\begin{aligned}
&1. \quad \delta_{\bar{\alpha}}\pi^{*\tau} && \equiv \partial_{\bar{\alpha}}\widehat{W} - r^p = 0 \ , \\
&2. \quad \delta_{\boldsymbol{\varepsilon}^p}\pi^{*\tau} && \equiv \partial_{\boldsymbol{\varepsilon}^p}\widehat{W} + \boldsymbol{f}^p = \boldsymbol{0} \ , \\
&3. \quad \delta_{\boldsymbol{f}^p}\pi^{*\tau} && \equiv \boldsymbol{\varepsilon}^p - \boldsymbol{\varepsilon}^p_n - \tau\lambda^p \partial_{\boldsymbol{f}^p}\widehat{\phi}^p = \boldsymbol{0} \ , \\
&4. \quad \delta_{r^p}\pi^{*\tau} && \equiv -\bar{\alpha} + \bar{\alpha}_n - \tau\lambda^p \partial_{r^p}\widehat{\phi}^p = 0 \ ,
\end{aligned} \tag{6.71}$$

defining the plastic resistance r^p, plastic driving force $\boldsymbol{f}^p$, the updates of the plastic strain $\boldsymbol{\varepsilon}^p$ and the local equivalent plastic strain $\bar{\alpha}$.

6.4.3. Reduced global Problem. With the condensed incremental work potential $\pi^{*\tau}_{red}$ defined in (6.70) at hand, we define the reduced potential functional

$$\Pi^{*\tau}_{red}(\boldsymbol{\varphi}, \alpha, d, f^f - r^f) = \int_{\mathcal{B}} \pi^{*\tau}_{red}(\mathfrak{C}^*_g) \, dV \ , \tag{6.72}$$

for pure Dirichlet problems with $P_{ext} = 0$ in (6.63). The second part of the incremental solution procedure consist of the solution of the mixed saddle point principle

$$(G): \quad \{\boldsymbol{\varphi}, \alpha, d, f^f - r^f\} = \text{Arg}\{ \inf_{\boldsymbol{\varphi}, \alpha, d} \sup_{f^f - r^f} \Pi^{*\tau}_{red}(\boldsymbol{\varphi}, \alpha, d, f^f - r^f) \} . \tag{6.73}$$

The necessary conditions of this global problem are

$$\begin{array}{llll} 1. & \delta_{\boldsymbol{\varphi}}\pi^{*\tau}_{red} & \equiv \mathrm{Div}\,[\,\partial_{\nabla\boldsymbol{\varphi}}\widehat{W}\,] = \boldsymbol{0} \ , \\ 2. & \delta_{\alpha}\pi^{*\tau}_{red} & \equiv \partial_{\alpha}\widehat{W} - \mathrm{Div}\,[\,\partial_{\nabla\alpha}\widehat{W}\,] = 0 \ , \\ 3. & \delta_{d}\pi^{*\tau}_{red} & \equiv \partial_{d}\widehat{W} - \mathrm{Div}\,[\,\partial_{\nabla d}\widehat{W}\,] + (f^f - r^f) = 0 \ , \\ 4. & \delta_{(f^f-r^f)}\pi^{*\tau}_{red} & \equiv d - d_n - \tau\lambda^f\partial_{(f^f-r^f)}\widehat{\phi}^f = 0 \ , \end{array} \tag{6.74}$$

defining the global fields and the associated driving forces. A straightforward finite element discretization of this problem based on the interpolation

$$\mathfrak{C}^{*h}_g(\boldsymbol{X},t) = \boldsymbol{B}(\boldsymbol{X})\ \boldsymbol{d}^*(t) \quad \text{with} \quad \boldsymbol{d}^*_I := \{\boldsymbol{\varphi}, \alpha, d, f^f - r^f\}^{N_node}_{I=1} \ , \tag{6.75}$$

results in the necessary condition of the FE-discretized mixed variational principle (6.73), yielding the nonlinear algebraic system

$$\partial_{\boldsymbol{d}^*}\Pi^{*\tau h}_{red} = \int_{\mathcal{B}} \boldsymbol{B}^T\mathfrak{S}^*\,dV = \boldsymbol{0} \ . \tag{6.76}$$

Here, $\mathfrak{S}^*$ is a generalized stress array dual to the global part $\mathfrak{C}^*_g$ of the state variables (6.69), defined by

$$\mathfrak{S}^* := \partial_{\mathfrak{C}^*_g}\pi^{*\tau}_{red}(\boldsymbol{B}\boldsymbol{d}^*) = \begin{bmatrix} \partial_{\nabla\boldsymbol{\varphi}}\widehat{W} \\ \partial_{\alpha}\widehat{W} \\ \partial_{\nabla\alpha}\widehat{W} \\ \partial_{d}\widehat{W} + (f^f - r^f) \\ \partial_{\nabla d}\widehat{W} \\ d - d_n - \tau\lambda^f\partial_{(f^f-r^f)}\widehat{\phi}^f \end{bmatrix} \ , \tag{6.77}$$

where λ^p and λ^f are defined in (6.47). The linearization of (6.76) reads

$$\partial_{\boldsymbol{d}^*\boldsymbol{d}^*}\Pi^{*\tau h}_{red} = \int_{\mathcal{B}} \boldsymbol{B}^T\mathfrak{C}^*\boldsymbol{B}\,dV \quad \text{with} \quad \mathfrak{C}^* := \partial_{\mathfrak{C}^*_g\mathfrak{C}^*_g}\pi^{*\tau}_{red}(\boldsymbol{B}\boldsymbol{d}^*) \ , \tag{6.78}$$

in terms of the generalized tangent moduli array $\mathfrak{C}^*$.

6.4.4. The three governing PDEs of the multi-field problem.

The stress equilibrium equation. The first Euler equation $(6.74)_1$ of the variational principle (6.73) is the quasi-static form of the balance of momentum, which follows by taking the variation of the potential $\Pi^{*\tau}_{red}$ in (6.72) with respect to the deformation map $\boldsymbol{\varphi}$, yielding

$$\boxed{\mathrm{Div}\,[\,(1-d)^2\boldsymbol{\sigma}_0 : \mathfrak{P}_{log}\,] = \boldsymbol{0}} \tag{6.79}$$

Here, the first Piola Kirchhoff stress tensor $\boldsymbol{P}$ is obtained from the constitutive work density function $\widehat{W}$ (6.56) by

$$\boldsymbol{P} := \partial_{\boldsymbol{F}}\widehat{W} = \boldsymbol{\sigma} : \mathfrak{P}_{log} \quad \text{with} \quad \mathfrak{P}_{log} := \partial_{\boldsymbol{F}}\boldsymbol{\varepsilon} \ . \tag{6.80}$$

The *projection tensor* $\mathfrak{P}_{log}$ projects the nominal Lagrangian Hencky tensor $\boldsymbol{\sigma}$ from the logarithmic strain space to the first Piola stress. An explicit form of this tensor based on the spectral representation is outlined in MIEHE ET AL. [99, 105], which is also summarized in Chapter 5. The nominal Hencky stress tensor is obtained by

$$\boldsymbol{\sigma} = (1-d)^2 \boldsymbol{\sigma}_0 \quad \text{with} \quad \boldsymbol{\sigma}_0 = \kappa \text{tr}[\boldsymbol{\varepsilon}^e] \boldsymbol{1} + 2\mu \, \text{dev}(\boldsymbol{\varepsilon}^e) \ , \tag{6.81}$$

where $\boldsymbol{\sigma}_0$ is the effective stress tensor dual to the elastic Lagrangian Hencky strain $\boldsymbol{\varepsilon}^e$ defined in (6.28).

The micromorphic global hardening variable. The second Euler equation $(6.74)_2$ of the variational principle (6.73) represents the partial differential equation for the micromorphic hardening variable

$$\partial_\alpha \widehat{W} - \text{Div} \, [\, \partial_{\nabla \alpha} \widehat{W} \,] = \mathit{0} \ . \tag{6.82}$$

Taking the necessary derivatives, we end up with the modified Helmholtz equation determining the link of the local variable $\bar{\alpha}$ to the micromorphic variable α

$$\boxed{\alpha - l_{mp}^2 \Delta \alpha = \bar{\alpha} \quad \text{with} \quad l_{mp} := l_p \, \sqrt{y_0/\epsilon_p}} \tag{6.83}$$

where l_{mp} is the plastic length scale of the micromorphic theory. Note carefully, that the variable α is now defined in the full domain, and not restricted to the plastic zone. Whereas the nonlinear hardening variable $\bar{\alpha}$ is defined *locally* by the ordinary differential equation ODE $(6.71)_4$. This provides a substantial simplification with regard to the finite element implementation.

The fracture phase field equation. The third Euler equation $(6.74)_3$ of the variational principle (6.73) determines the PDE for the fracture phase field update equation. It defines the fracture driving force

$$f^f - r^f = 2(1-d)[\, \widehat{w}_0^{ep}(\boldsymbol{\varepsilon}^e, \bar{\alpha}, \alpha, \nabla \alpha) - w_c \,] - 2\frac{w_c}{\zeta}[\, d - l_f^2 \Delta d \,] \ , \tag{6.84}$$

in terms of the Laplacian Δd of the crack phase field. The last term contains the variational derivative of the crack surface density function $\gamma_l(d, \nabla d)$, and can be considered as the crack resistance. The above partial differential equation PDE is accompanied by the Euler equation $(6.74)_4$ for the update of the crack phase field, which reads

$$(d - d_n)/\tau = \lambda^f \partial_{(f^f - r^f)} \widehat{\phi}^f = \lambda^f \quad \text{with} \quad \lambda^f = \frac{1}{\eta^f} \left\langle f^f - r^f \right\rangle \ . \tag{6.85}$$

Setting for convenience

$$\eta^f = 2 \frac{w_c}{\zeta} \eta_0^f \ , \tag{6.86}$$

the combination of (6.84) and (6.85) characterizes a generalized Ginzburg-Landau- or Allen-Cahn-type equation for the update of the crack phase field d

$$\boxed{(d - d_n)/\tau = \frac{1}{\eta_0^f} \left\langle \, (1-d) \, \zeta \, [\, \frac{\widehat{w}_0^{ep}}{w_c} - 1 \,] - [\, d - l_f^2 \Delta d \,] \, \right\rangle} \tag{6.87}$$

as outlined in Section 6.1.3 and Section 6.1.4, where the Macaulay bracket ensures the irreversibility of the crack evolution. Clearly, the fracture phase field is driven by the effective elastic-plastic work function $\widehat{w}_0^{ep}$ of the undamaged material. Following the recent work Miehe et al. [106], we may recast (6.87) into

$$\underbrace{\eta_0^f (d - d_n)/\tau}_{crack\ update} = \underbrace{(1-d)\mathcal{H}_0}_{crack\ force} - \underbrace{[\, d - l_f^2 \Delta d \,]}_{crack\ resistance} \tag{6.88}$$

with the maximum value

$$\mathcal{H}_0 = \max_{s \in [0,t]} D_0 \geq 0 \tag{6.89}$$

of a dimensionless *crack driving state function*

$$D_0 = \zeta \left\langle \frac{\widehat{w}_0^e(\boldsymbol{\varepsilon}^e)}{w_c} + \frac{\widehat{w}_0^p(\bar{\alpha}, \alpha, \nabla\alpha)}{w_c} - 1 \right\rangle \tag{6.90}$$

obtained in the history of the deformation process. Hence, cracks propagate if the accumulated effective elastic-plastic work density $\widehat{w}_0^{ep}$ exceeds the critical value w_c. This definition has already been proposed by Miehe et al. [106].

A convenient and robust numerical implementation of the above three governing PDEs of the multi-field problem is achieved by a staggered scheme based on incrementally decoupled updates of the fracture phase field d, the micromorphic hardening variable α and the deformation map $\boldsymbol{\varphi}$, in line with the treatments Miehe et al. [100]. Such a scheme uses the variational updates for the gradient-extended elasto-plasticity system with its micromorphic regularization discussed in Section 6.3 at frozen fracture phase field. Note that, we first update the deformation map at frozen micromorphic hardening variable and fracture phase field by using the PDE defined in (6.79). Next we update the micromorphic hardening variable α from (6.83) at frozen local equivalent plastic strain α_n. Finally we update the fracture phase field d by using (6.87) in full analogy to our recent work Miehe et al. [106], which is also summarized in Box 6.1 and Box 6.2.

6.5. Representative numerical examples

We demonstrate the performance of the proposed framework of phase field ductile fracture coupled with gradient plasticity by means of representative boundary-value problems. The first part of this section is concerned with the simulation of the homogeneous problems in the one-dimensional case as outlined in our recent work Miehe et al. [106]. In the second part, we investigate multi-dimensional boundary value problems for gradient extended plasticity coupled to phase field fracture. Section 6.5.2 compares the numerical results of the V-notched bar in tension with experimental data of Li et al. [78]. Section 6.5.3 considers a single-edge notched specimen subjected to shear loading. The key observations of mesh objectivity and physically reasonable interactions of plastic and fracture length scales are highlighted for these two IBVPs. Finally, a three dimensional torsion test of a brittle cast-iron bar and a ductile mild-steel bar is investigated in Section 6.5.4.

6.5.1. Local homogeneous response. In this example the numerical results for a local one dimensional setting of coupled ductile damage under homogeneous test are demonstrated. The aim of this example is to illustrate the performance of the proposed framework for a coupled plastic-damage response. The model problem is based on three

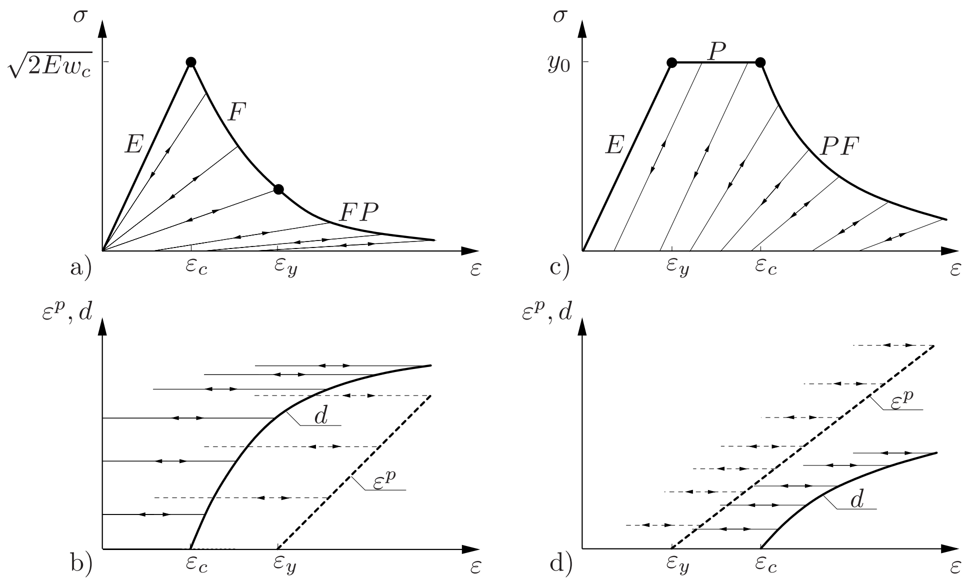

Figure 6.4: Loading-Unloading for Brittle and Ductile Response. Qualitative features for a-b) *brittle E-F-P response* and for c-d) *ductile E-P-F response*. The typical brittle damage and ductile plasticity loading-unloading characteristics for the stress superimpose in the post-critical *FP* and *PF* ranges. Plastic strain ε^p and fracture phase field d remain constant during unloading, reflecting the threshold characteristics of the proposed approach.

material parameters: Young's modulus E, the initial yield stress y_0 and the critical work density w_c. Corresponding to the given material parameters, one obtains the plastic yield strain ε_y and the fracture threshold strain ε_c. Consider a reformulation of the constitutive work density function for the one-dimensional homogeneous response related to ideal plastic conditions without hardening as

$$\widehat{W} = (1-d)^2\frac{E}{2}(\varepsilon-\varepsilon^p)^2 + (1-d)^2[y_0\alpha - w_c] + w_c + \frac{w_c}{\zeta}d^2 \ . \tag{6.91}$$

where the equivalent plastic strain α is defined by the evolution of the plastic strain as $\dot{\alpha} = |\dot{\varepsilon}^p|$. The governing *degrading stress response* is written as

$$\sigma = \partial_\varepsilon \widehat{W} = (1-d)^2 E(\varepsilon - \varepsilon^p) \ , \tag{6.92}$$

and the driving and the resistance forces for plasticity and fracture are

$$\begin{array}{rcrcl} f^p & := & -\partial_{\varepsilon^p}\widehat{W} & = & (1-d)^2E(\varepsilon-\varepsilon^p) \\ r^p & := & \partial_\alpha \widehat{W} & = & (1-d)^2 y_0 \\ f^f - r^f & := & -\partial_d \widehat{W} & = & 2(1-d)[\frac{E}{2}(\varepsilon-\varepsilon^p)^2 + y_0\alpha - w_c] - 2w_c d/\zeta \end{array} \tag{6.93}$$

The evolution of the plastic strains and the fracture phase field is governed by the two threshold functions

$$\widehat{\phi}^p(f^p, r^p) = |f^p| - r^p \quad \text{and} \quad \widehat{\phi}^f(f^f, r^f) = f^f - r^f \ . \tag{6.94}$$

The *fracture phase field evolution* for a homogeneous rate-independent problem is obtained from (6.88) for $\eta = 0$ and $\Delta d = 0$, in closed form as

$$d = \frac{\mathcal{H}_0}{1+\mathcal{H}_0} \quad \text{with} \quad \mathcal{H}_0 = \max_{s\in[0,t]} D_0 \geq 0 \ , \tag{6.95}$$

Box 6.3: Material parameters used for the V-notch bar (Al-6061) [78].

No.	Parameter	Name	Value	Unit
1.	E	Young's modulus	68.9	GPa
2.	ν	Poisson's ratio	0.33	–
3.	h	hardening parameter	0.561	GPa
4.	y_0	initial yield stress	0.475	GPa
5.	w_c	critical work density	0.18	GPa
6.	η_p	plastic viscosity	10^{-7}	GPa.s
7.	η_f	fracture viscosity	10^{-7}	GPa.s
8.	l_p	plastic length scale	0.6/0.8	mm
9.	l_f	fracture length scale	0.2/0.3/0.4	mm
10.	ϵ_p	micromorphic coupling modulus	$30h$	GPa

where the crack driving state function D_0 is defined in (6.90). Cyclic loading is applied to a material point where unloading takes place up to zero stresses. Two cases are introduced which are distinguished by the values of the plastic yield strain ε_y and the fracture threshold strain ε_c as shown in Figure 6.4.

Fracture before Plasticity. In this case, fracture is initiated before plasticity, i.e., $\{\varepsilon_c := (2w_c/E)^{1/2}\} < \{\varepsilon_y := y_0/E\}$. The response of the material point corresponds to the sequence E(elastic) - F(fracture) - FP(fracture plastic) as plotted in Figure 6.4a. Stage E is linear elastic where $\sigma = E\varepsilon$. Stage F is stress degradation where $\sigma = (1-d)^2 E\varepsilon$. Stage FP is fracture coupled to plasticity where $\sigma = (1-d)^2 E(\varepsilon - \varepsilon_p)$. The plastic strain is evolved as $\varepsilon^p = \varepsilon^p_n + \lambda^p \Delta t\, n_p$ with the direction of the plastic flow $n_p = f^p/|f^p|$. The evolution of the plastic strain ε^p and the fracture phase field d are also shown in Figure 6.4b.

Plasticity before Fracture. In this case, plasticity is initiated before fracture, i.e., $\{\varepsilon_c := w_c/y_0 + y_0/2E\} > \{\varepsilon_y := y_0/E\}$. The response of the material point corresponds to the sequence E(elastic) - P(plastic) - PF(plastic-fracture) as plotted in Figure 6.4c. Similar to Case 1, the material response is elastic E until the stress reaches the yield limit y_0. The ideal plasticity starts thereafter up to the fracture threshold strain ε_c. Next, fracture is initiated and coupled with plasticity which is represented by a PF response. The stress-strain loading unloading curves in region PF of Figure 6.4c represent a continuing plastic evolution with the fracture evolution. The evolutions ε^p and d are also shown in Figure 6.4d.

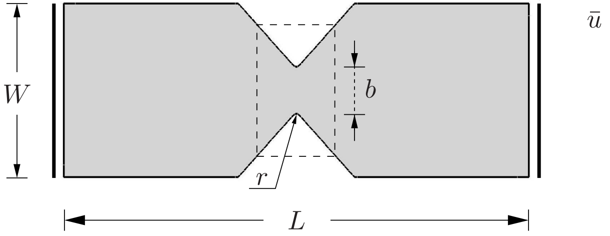

Figure 6.5: Plane strain test of V-notch bar in tension. Geometry and boundary conditions.

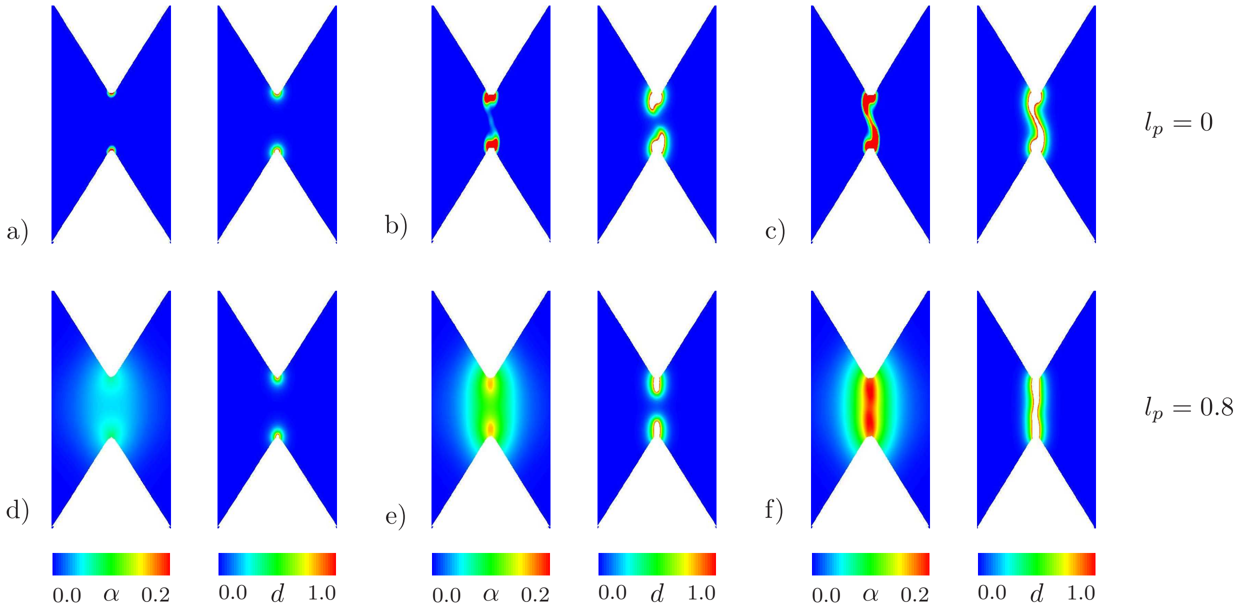

Figure 6.6: V-notch bar in tension. Evolution of equivalent plastic strain α and fracture phase field d with two plastic length scales l_p and fixed fracture length scale $l_f = 0.4$ mm. (a)–(c) Local plasticity $l_p = 0$ and (d)–(f) gradient plasticity $l_p = 0.8$ mm for three different stages during deformation up to final failure with crack surfaces related to $d \approx 1$.

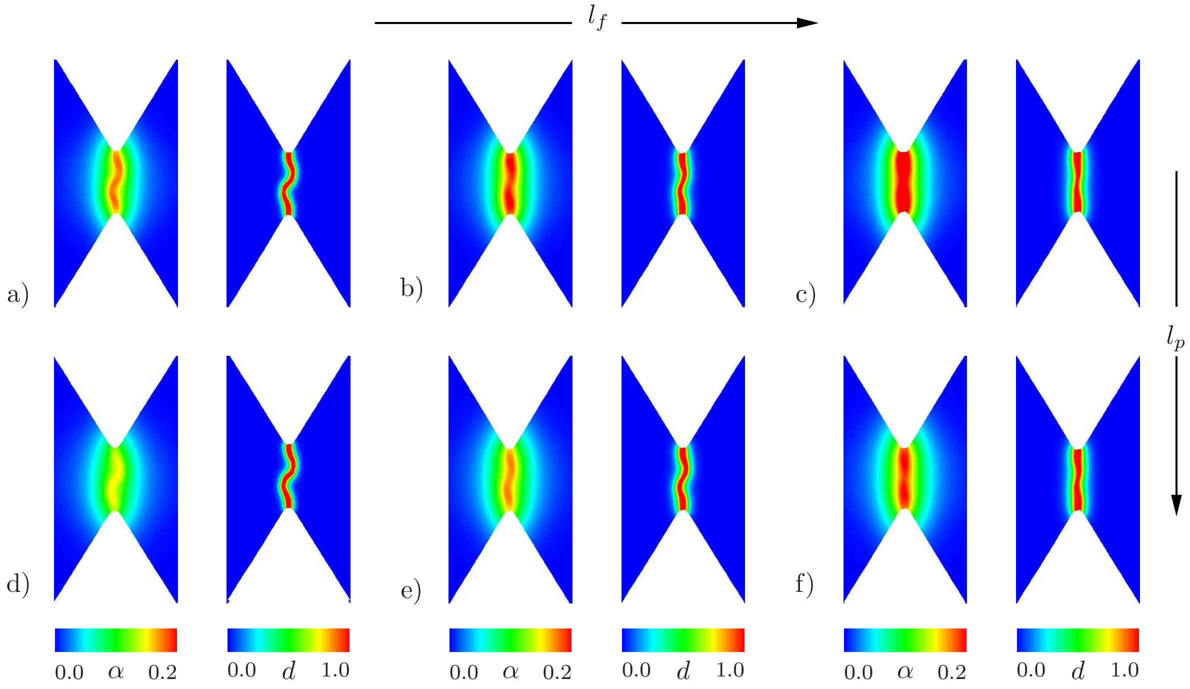

Figure 6.7: V-notch bar in tension. Contours of equivalent plastic strain α and fracture phase field d with different combinations of l_f and l_p. a) $l_f = 0.2$ mm, b) $l_f = 0.3$ mm and c) $l_f = 0.4$ mm with $l_p = 0.6$ mm. d) $l_f = 0.2$ mm, e) $l_f = 0.3$ mm and f) $l_f = 0.4$ mm with $l_p = 0.8$ mm.

6.5.2. Analysis of a V-Notch Bar in Tension Test. We model the fracture phenomena of the Al-alloy (Al-6061) of a V-notch bar under tensile loading as reported in the experiments of Li et al. [78]. The aim here is to demonstrate the need for a *gradient*

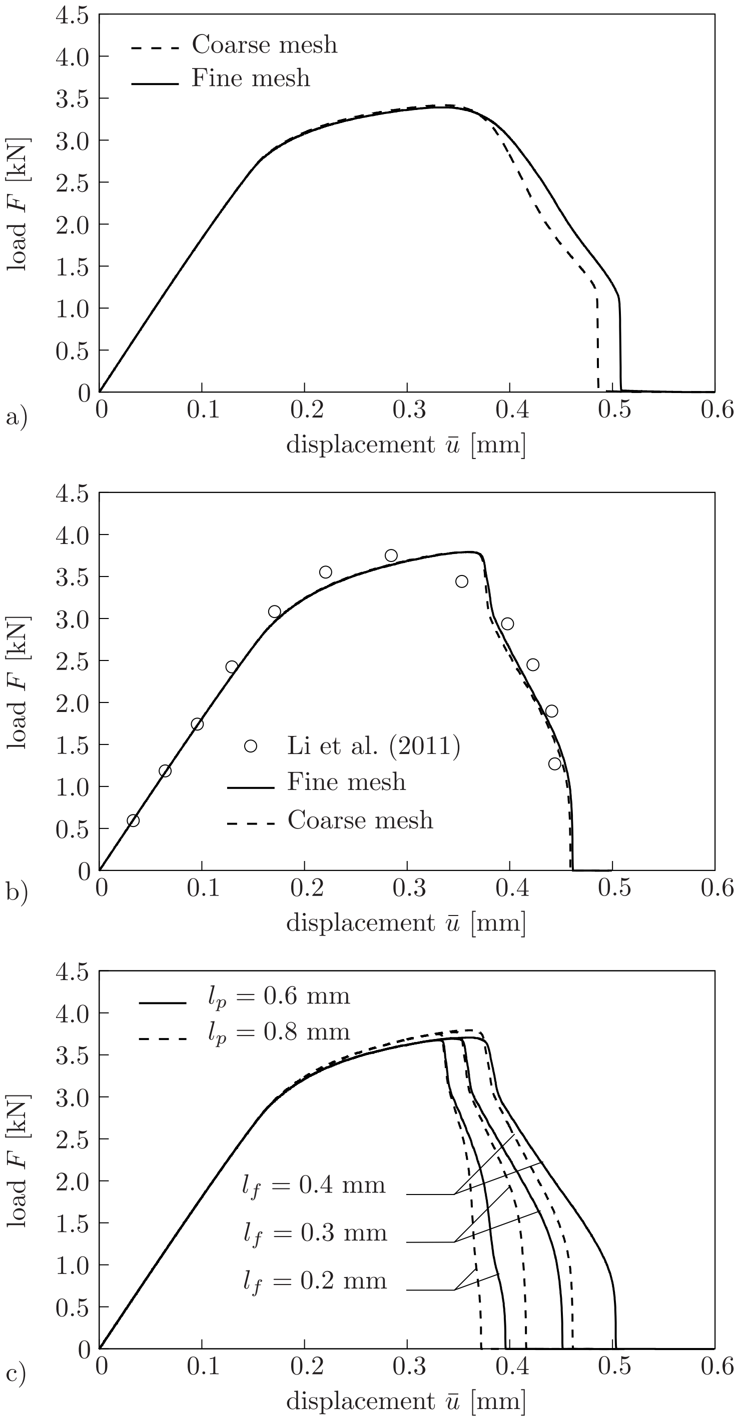

Figure 6.8: Load–displacement responses for V-notched bar in tension. a) Mesh sensitivity of local plasticity in the post-critical range for two different mesh discretizations. b) Mesh objectivity of gradient plasticity compared with the data of Li et al. [78]. b) Effects of plastic length scale l_p and the fracture length scale l_f on the overall structural response.

extended plasticity coupled with the phase field fracture approach to overcome the mesh sensitivity in the post-critical range and capture qualitatively the experimentally observed load-deflection response. The geometric setup and the loading conditions of the specimen are depicted in Figure 6.5. The size of the specimen is chosen to be : $L = 40$ mm, $W = 14$ mm, $b = 4$ mm, $w = 10$ mm, and the radius of the V-notch is $r = 0.25$ mm. The

Box 6.4: Material parameters used for the single-edge notched shear test.

No.	Parameter	Name	Value	Unit
1.	E	Young's modulus	200	GPa
2.	ν	Poisson's ratio	0.3	–
3.	h	hardening parameter	0.130	GPa
4.	y_0	initial yield stress	0.45	GPa
5.	w_c	critical work density	0.013	GPa
6.	η_p	plastic viscosity	10^{-7}	GPa.s
7.	η_f	fracture viscosity	10^{-7}	GPa.s
8.	l_p	plastic length scale	0.016	mm
9.	l_f	fracture length scale	0.008	mm
10.	ϵ_p	micromorphic coupling modulus	$30h$	GPa

same material parameters are used as in [78] and listed in Table 6.3. The mesh size of the specimen is chosen to be $h_e = 0.1$ mm in the expected fracture zone. The computation is performed by applying the displacement $\bar{u}$ on the right vertical boundary.

The evolution of the crack phase field d compared with the evolution of the equivalent plastic strain α is reported in Figure 6.6 for local and gradient plasticity. The contour plots of the local theory with zero plastic length scale parameter $l_p = 0$ and fracture length scale parameter $l_f = 0.4$ mm are shown in Figure 6.6a–c. The crack phase field d initiates at the notch tip where the maximum equivalent plastic strain develops, and successivley propagates unsymmetrically from the notches inwards till final rupture as an S-shape. Comparing these results with the experimental work of LI ET AL. [78], notice first that the *predicted fracture path is not perpendicular to the loading direction* as shown in the experiment. A reason for this effect is the use of the simple von Mises-type isochoric plastic flow. Secondly, we face a *non-physical evolution of the fracture zone outside the plastic zone.*

From the above observations, we conclude the need for a *gradient extended plasticity theory* by introducing the plastic length scale $l_p \geq l_f$ as an additional material parameter in the model. The contour plots of the gradient theory with $l_p = 0.8$ mm and $l_f = 0.4$ mm are shown in Figure 6.6d–f. Observe that the failure zone now occurs inside the plastic zone and appears to be perpendicular to the loading direction. Hence, the

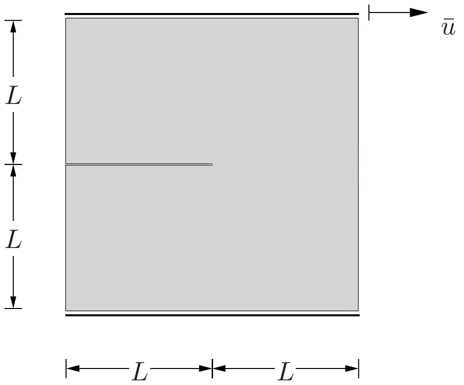

Figure 6.9: Single-edge notched shear test. Geometry and boundary conditions.

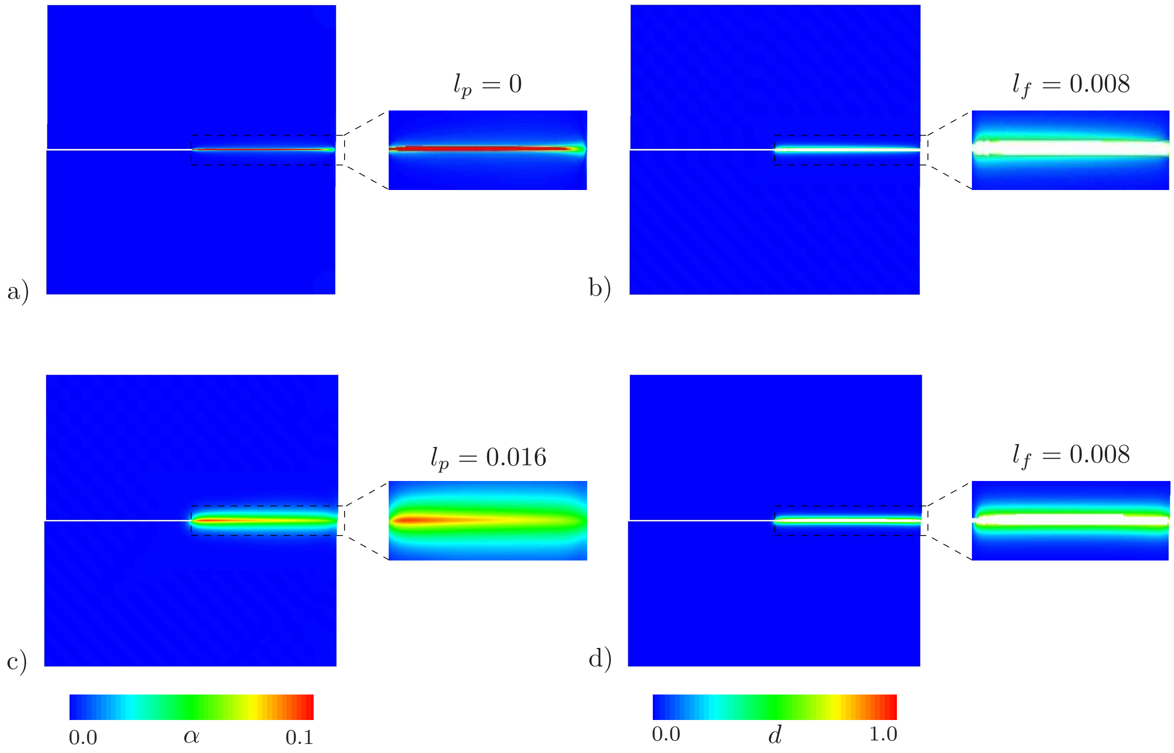

Figure 6.10: Single-edge notched shear test. Contour plots of the equivalent plastic strain α and fracture phase field d for two plastic length scales l_p and fixed fracture length scale $l_f = 0.008$ mm. (a)-(b) Local plasticity $l_p = 0$ and (c)-(d) gradient plasticity $l_p = 0.016$ mm at the final deformation state. The crack surfaces are visualized related to $d \approx 1$.

gradient-plastic regularization provides a spatial smoothing of the plastic, yielding an improved performance of the simple von Mises model in the modeling ductile failure. For visualization of crack surface, deformed regions with a phase field $d \geq c \approx 1$ are not plotted in Figure 6.6.

Figure 6.7 demonstrates the influence of the plastic length scale l_p and the fracture length scale l_f on the final failure response. First, the effect of increasing the fracture length scale is investigated by keeping $l_p = 0.6$ mm fixed as shown in Figure 6.7a–c. We notice a delayed failure response by increasing l_f, resulting in a fracture path that becomes more perpendicular to the loading direction. Furthermore, the maximum equivalent plastic strain α increases, which is clearly the influence of increased l_f. Next, the effect of an increased plastic length scale $l_p = 0.8$ mm is illustrated in Figure 6.7d–f. Observe that the equivalent plastic strain α is smeared out over several elements, thereby reducing the maximum value of α. However, the failure response is similar to Figure 6.7a–c.

In order to further emphasize the need of the gradient extended plasticity theory, we illustrate in Figure 6.8 the load-deflection curves of the overall structural response. The mesh sensitivity in the post-critical range observed in local plasticity is shown in Figure 6.8a for two different discretizations. To overcome this behavior, gradient plasticity with plastic length scale $l_p = 0.8$ mm is used in Figure 6.8b, where mesh objectivity is obtained. Furthermore, observe that the results of the gradient extended plasticity are in qualitative agreement with the experimental results of LI ET AL. [78] for both the coarse as well as the fine mesh. Finally, Figure 6.8c demonstrates the influence of the fracture length scale l_f and the plastic length scale l_p on the load–deflection response,

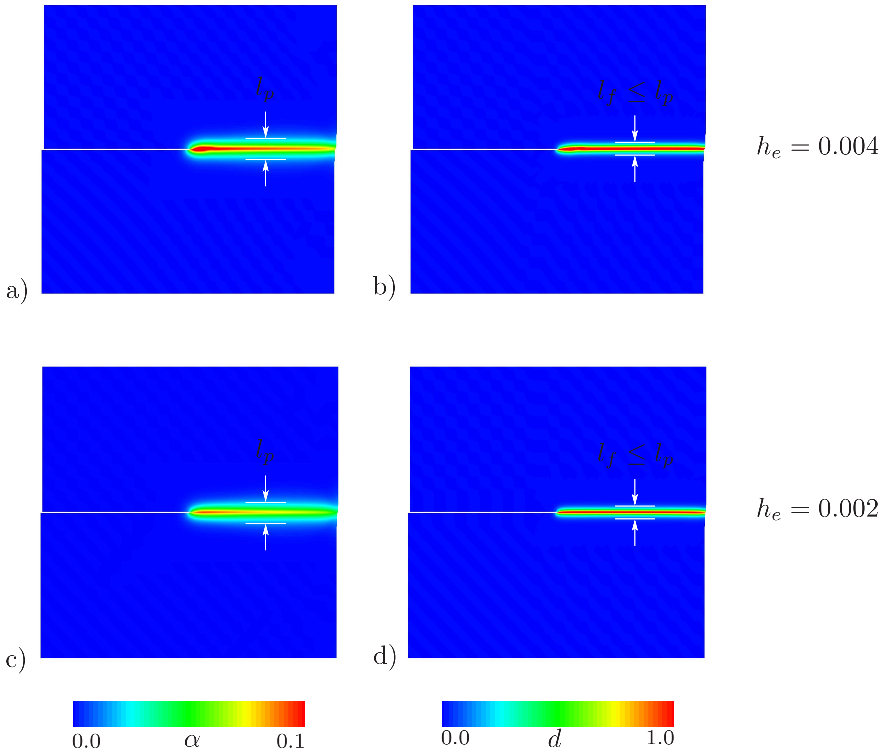

Figure 6.11: Single-edge notched shear test. Contour plots of the equivalent plastic strain α (a)-(c) and the fracture phase field d (b)-(d) for two different mesh discretizations at the final deformation state to demonstrate the mesh objectivity of gradient plasticity.

which corresponds to the analysis in Figure 6.7. We observe a delayed-failure response by increasing the fracture length scale and a slightly more pronounced hardening by increasing the plastic length scale.

6.5.3. Investigation of single-edge notched shear test. The second benchmark test considers a square plate with a horizontal notch placed at the middle height from the left outer surface to the center of the specimen. The geometric setup and the loading conditions of the specimen are depicted in Figure 6.9. The size of the square specimen is chosen to be $L = 0.5$ mm. We fixed the bottom edge of the plate and applied shear loading to the top edge where the vertical displacement is fixed. The material parameters used are given in Table 6.4. The specimen is discretized by using three different meshes with the maximum element size of $h_e = 0.004$ mm in the expected fracture zone.

The contour plots of the equivalent plastic strain α and the fracture phase field d for local and gradient plasticity with fixed fracture length scale $l_f = 0.008$ mm are plotted in Figure 6.10. For local plasticity, observe the non-physical evolution of the fracture zone outside the plastic zone as demonstrated in Figure 6.10a-b. The mesh sensitivity in the post-critical response with local plasticity is shown in Figure 6.12a for three different meshes.

To overcome this behavior, gradient plasticity with plastic length scale $l_p = 0.016$ mm is used, resulting in a fracture zone to be *inside the plastic zone.* Furthermore, the equivalent plastic strain is smeared over several elements as shown in Figure 6.10c-d. Figure 6.11 demonstrate the mesh objectivity of the gradient theory for the coarse and finest mesh discretizations. Observe that α and d are almost the same for all the meshes. The corre-

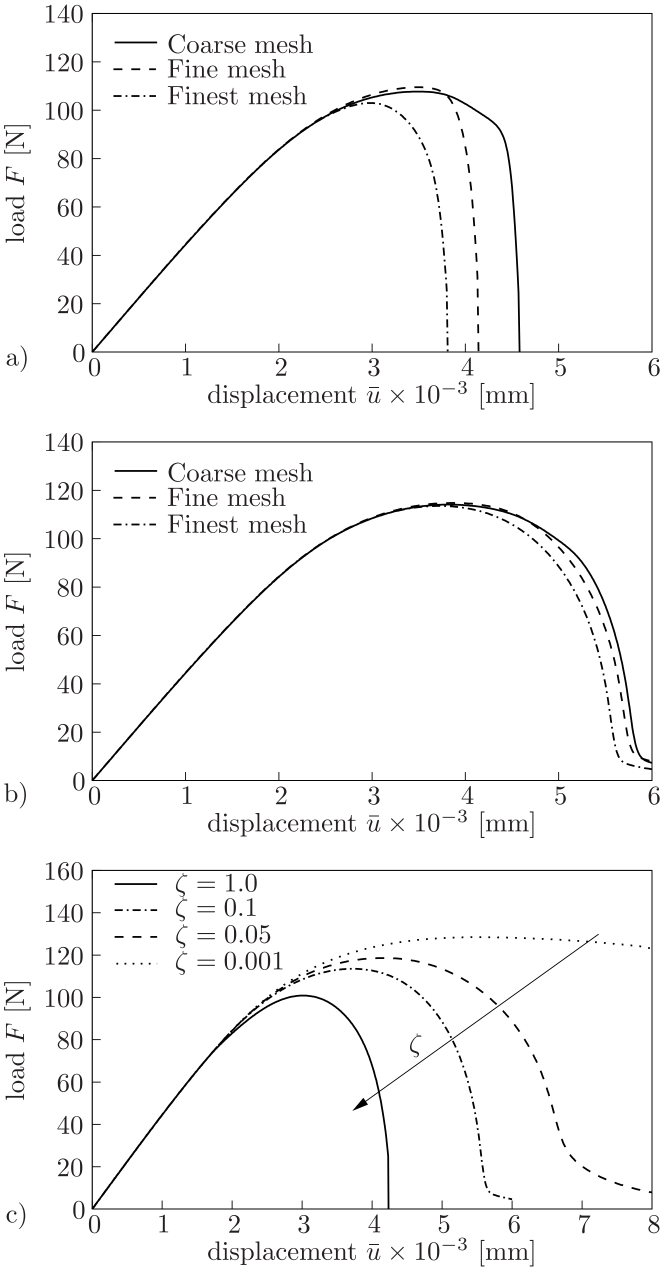

Figure 6.12: Load–displacement responses for single-edge notched shear test. a) Mesh sensitivity of local plasticity model in the post-critical range and b) mesh objectivity of the gradient plasticity model for three different mesh discretizations. c) Effects of four different fracture parameters ζ on the crack initiation and load-displacement response.

sponding load-displacement curves for the three meshes are shown in Figure 6.12b, where the post-critical softening response provides approximately a mesh-objective behavior.

To illustrate the *influence of the fracture parameter* ζ on the crack initiation and propagation, Figure 6.12c plots the load-displacement response for four different values of ζ. One observes the expected delayed failure behavior by decreasing the value of ζ.

6.5.4. Three dimensional torsion test of a cylindrical bar. The last model problem is concerned with analyzing brittle fracture of cast-iron and ductile fracture of mild-steel bars under torsional loading. The purpose of this test is to illustrate the effects of the material response on the crack initiation and propagation. We differentiate between

Box 6.5: Material parameters used for the torsion test of mild-steel bar.

No.	Parameter	Name	Value	Unit
1.	E	Young's modulus	200	GPa
2.	ν	Poisson's ratio	0.3	–
3.	h	hardening parameter	0.2	GPa
4.	y_0	initial yield stress	0.45	GPa
5.	y_∞	infinite yield stress	0.6	GPa
6.	η_s	saturation parameter	16.96	–
7.	w_c	critical work density	0.04	GPa
8.	η_p	plastic viscosity	10^{-7}	GPa.s
9.	η_f	fracture viscosity	10^{-7}	GPa.s
10.	l_p	plastic length scale	1.4	mm
11.	l_f	fracture length scale	1.0	mm
12.	ϵ_p	micromorphic coupling modulus	$30h$	GPa

two cases: *brittle fracture* (elastic-fracture) and *ductile fracture* (elastic-plastic-fracture). As a geometric setup, the length of the cylindrical bar is chosen to be $L = 60$ mm and the radius $R = 10$ mm. The computation is performed by fixing one end of the cylindrical bar and applying torsion to the other end. For *brittle cast-iron*, Young's modulus is

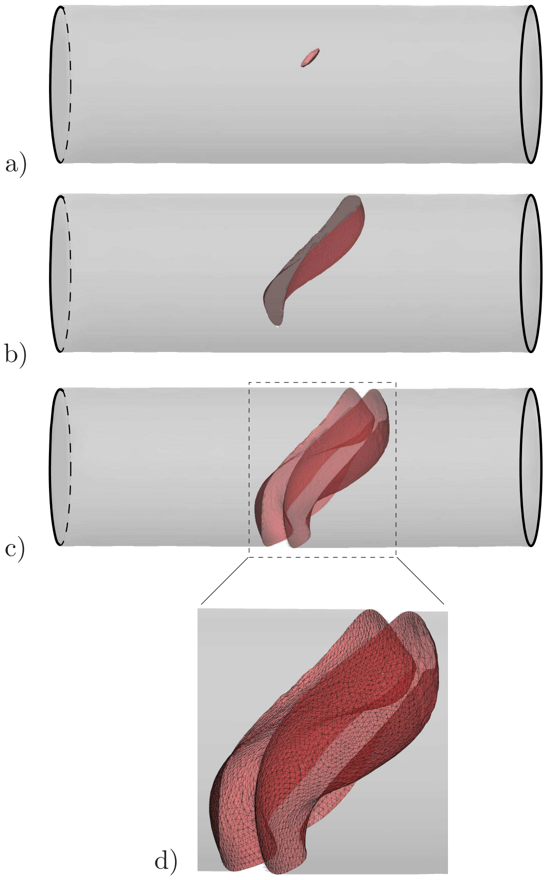

Figure 6.13: Three-dimensional torsion test of a cylindrical bar. a)–c) Fracture phase field d evolution in *brittle cast-iron* test for a twist loading. d) Visualization of the crack faces.

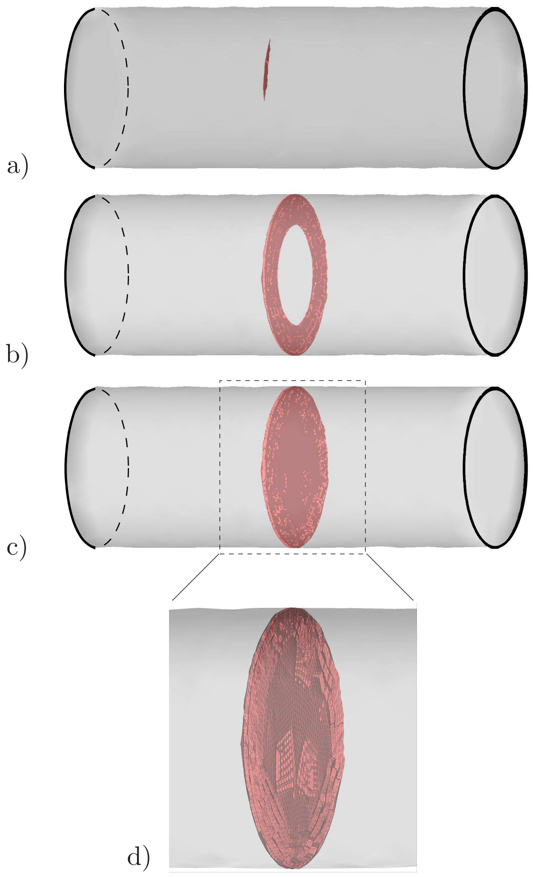

Figure 6.14: Three-dimensional torsion test of a cylindrical bar. a)–c) Fracture phase field d evolution in *ductile mild-steel* test for a twist loading. d) Visualization of the crack faces.

chosen to be $E = 110$ GPa, Poisson's ratio is set to $\nu = 0.3$, the fracture length scale $l_f = 1.0$ mm, and the critical work density to $w_c = 0.1$ MPa. For *ductile mild-steel*, the material parameters used are listed in Table 6.5. The specimens are discretized with a mesh size of $h = l_f/2$ in the expected fracture zone. The evolution of the crack phase field d for the cast-iron and mild-steel bars are depicted in Figures 6.13 and 6.14, respectively.

For the *brittle failure* of cast-iron bar, the crack starts to initiate at a point on the surface near the center of the specimen at an angle of twist of 1.1°, see Figure 6.13a.

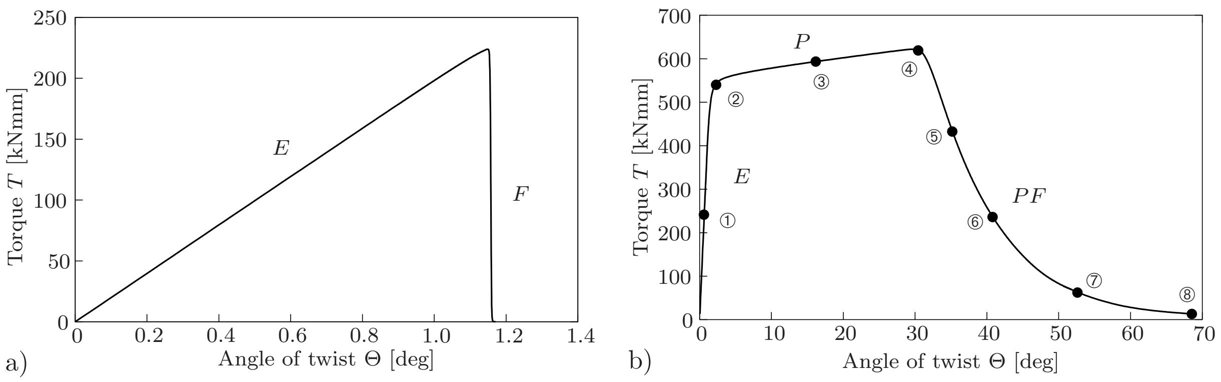

Figure 6.15: Torque versus angle of twist for three dimensional torsion test of a cylindrical bar. a) *Brittle failure* of cast-iron bar and b) *Ductile failure* of mild-steel bar.

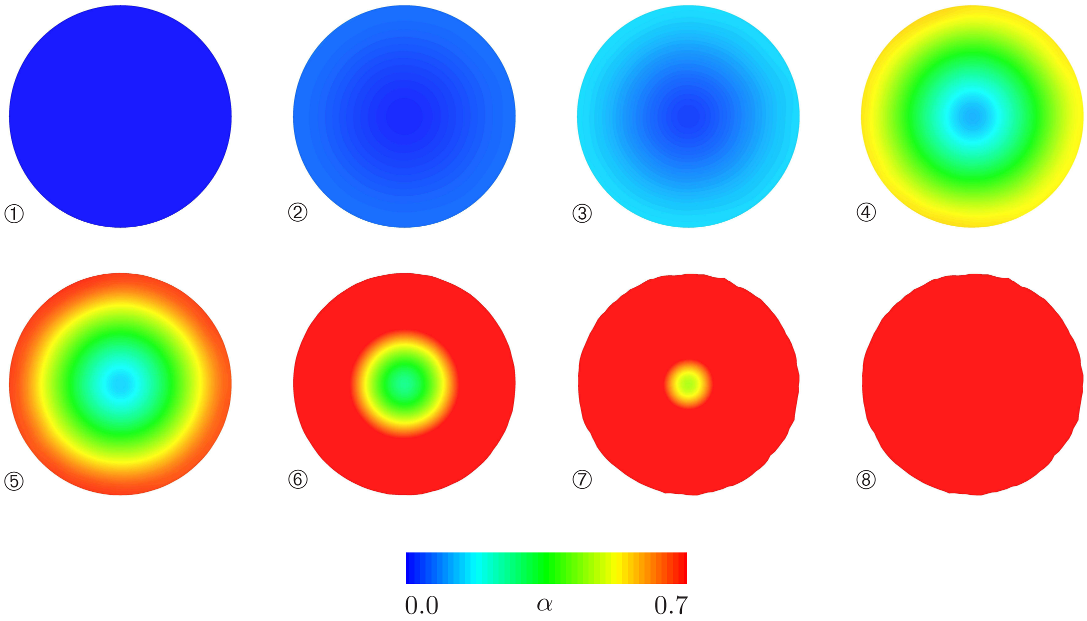

Figure 6.16: Torsion test of a ductile cylindrical bar. ①–⑧ Equivalent plastic strain α evolution of ductile mild-steel in the cross section near the center of the bar for a twist loading corresponding to the torque T versus angle of twist Θ plotted in Figure 6.15b.

The crack then propagates from the surface inwards till final rupture in Figure 6.13c. To illustrate the crack surface, we zoomed out the fractured area as shown in Figure 6.13d. Since the fracture path is about 45° from the longitudinal direction, the fracture surface is complicated and looks like a *helicoid* as plotted in Figure 6.13c, where we used a transparency effect to show the failure surface for $d \geq c \approx 1$.

The torsion test is repeated for the *ductile failure* of mild-steel. An inhomogeneous plastic zone develops as a consequence of an initial imperfection at a point on the central surface. The amplitude of this imperfection is sufficiently small such that it does not effect the overall structural response. Figure 6.14a depicts the crack initiation on the surface near the center of the bar at about 30° angle of twist. The crack then propagates from the surface inwards perpendicular to the longitudinal direction as shown in Figure 6.14c. A zoom of the crack surfaces is shown in Figure 6.14d.

The torque T versus angle of twist Θ for the overall structural response are illustrated in Figure 6.15. The angle of twist Θ is measured at the end of the cylindrical bar. For *brittle fracture*, the material response corresponds to the sequence: E(elastic) - F(fracture) plotted in Figure 6.15a. Here, the local fracture evolution starts when the elastic energy reaches a critical value w_c. Thereafter, a brittle failure response is observed. For *ductile fracture*, the structural response corresponds to the sequence: E(elastic) - P(plastic) - FP(fracture-plastic) as shown in Figure 6.15b, where the crack phase field is driven by the coupled elastic-plastic driving force (6.90). The evolution of the equivalent plastic strain α at the center of the bar, corresponding to Figure 6.15b, is plotted for different stages of deformation up to final failure as in Figure 6.16. α starts to evolve after initial yielding, see Figure 6.16 ②-③, thereafter fracture starts at ④. Observe that the equivalent plastic strain is increasing from the surface to the center of the specimen as illustrated in Figure 6.16 ⑤-⑧, which corresponds with the fracture phase field d depicted in Figure 6.14.

7. Summary and Conclusions

This dissertation focused on the development of a constitutive framework for gradient-extended dissipative solids, that accounts for micro-structure-based length scale effects. It has been shown that the global micro-structure fields, whose gradients enter the energetic and the dissipative response functions, are governed by additional balance equations and boundary conditions. In particular, we proposed a *phenomenological model for gradient thermo-plasticity* and *phase-field modeling of ductile fracture*.

A first application of the proposed framework for gradient-extended dissipative solids was discussed in the context of phenomenological theories of isochoric von Mises plasticity model with gradient-extended hardening/softening response at small strains and in the logarithmic strain space. In contrast to classical local approaches to plasticity based on locally-evolving internal variables, order parameter fields governed by additional balance-type partial differential equations were taken into consideration. The point of departure was the construction of a variational framework based on mixed saddle point principles for the evolution problem of gradient plasticity. This resulted in a novel finite element design of the coupled problem incorporating a long-range hardening/softening parameter and its dual driving force. It allowed a straightforward local definition of plastic loading-unloading driven by the long-range fields, providing a very robust finite element implementation of gradient plasticity. Two important classes of multi-dimensional mixed finite elements for the coupled problem as well as a local-global update strategy for short- and long-range fields were tested. They were all introduced in a rigorous format based on variational principles. In this context, we first discussed a family of extended Q1P0 elements based on a five–field incremental variational principle, where the Jacobian and the pressure field were condensed out at the element level. Thereafter, we developed a family of extended MINI elements based on a four–field incremental variational principle, where bubble–degrees condensed out at the element level. The performance of this approach was examined in several numerical examples, which highlighted characteristic features of gradient plasticity as well as the robust performance of the computational setting, see MIEHE, ALDAKHEEL & MAUTHE[104], MIEHE, WELSCHINGER & ALDAKHEEL[105] and ALDAKHEEL, MAUTHE & MIEHE[10].

A further application of the proposed framework, that covers fully coupled thermo-mechanical problems at small strains was introduced. This was achieved by extending the constitutive formulation of the von Mises gradient-plasticity model to account for thermal effects. In addition to the displacement field, the plastic strains and the scalar hardening variable along with its dual driving force, the absolute temperature field was also introduced describing the coupled thermo-gradient-plasticity at small strains. From the numerical implementation aspects, two global solution procedures were developed for the coupled problem, namely the product formula algorithm and the implicit coupled algorithm. Regarding the space discretization of the coupled problem, the aforementioned Q1P0-type and MINI-type finite elements were extended to account for thermal effects by adding the temperature field to the Galerkin formulation. Two numerical examples demonstrated the performance of the coupled thermo-gradient-plasticity problem, see ALDAKHEEL, MAUTHE & MIEHE[8].

The last application of the proposed framework was concerned with the phase-field modeling of ductile fracture in the logarithmic strain space. Hereby, a variational gradient plasticity was linked to a specific setting of variational gradient damage rooted in the phase-field approach of fracture suggested in the literature. In this regard, we introduced two independent length scales, which regularized both the plastic response as well as the crack discontinuities. This ensured that the failure zone of ductile fracture occurs inside the plastic zone, and guaranteed, from the computational perspective, a mesh objectivity in post-critical range. The finite element design of this formulation was not straightforward and required additional strategies due to the stability-related difficulties near the elastic-plastic boundaries EPBs. To simplify the finite element implementation, we extended the introduced gradient plasticity-damage towards the *micromorphic regularization approach* to gradient-extended models. As a consequence, additional partial differential equation PDE for the micromorphic hardening variable, denoted as the *micromorphic momentum balance equation*, was taken into account. We started our investigation from a homogeneous one-dimensional model problem to illustrate the response of the coupled elastic-plastic phase-field driving force. Later, we presented the heterogeneous multi-dimensional cases where the modeling capabilities and algorithmic performance of the proposed formulation were demonstrated by representative numerical simulations of ductile fracture in elasto-plastic solids and their subsequent comparisons with the data from the literature, see MIEHE, HOFACKER, SCHÄNZEL & ALDAKHEEL[106], MIEHE, ALDAKHEEL & RAINA[108], MIEHE, TEICHTMEISTER & ALDAKHEEL[109] and ALDAKHEEL, RAINA & MIEHE[9].

A. Gurson Model for Ductile Damage in Metals

In Chapter 6, the constitutive formulations were based on the isochoric von Mises yield criterion function for the modeling of plastic material response at the macroscopic level. Thereby, no plastic dilatancy is considered, i.e. volumetric changes are solely due to elastic deformation ($\mathrm{tr}[\boldsymbol{\varepsilon}^p] = 0$). However, the modeling of failure in ductile metals must account for complex phenomena at the micro-scale, such as nucleation, growth and coalescence of micro-voids, as well as the final rupture at the macro-scale. Within a top-down viewpoint, this can be achieved by the combination of a micro-structure-informed elastic-plastic model for a porous medium with a concept for the modeling of macroscopic crack discontinuities. In this appendix, we shortly introduce a computational framework for the phase field modeling of ductile fracture in porous metal plasticity. It combines enhanced structures of *Gurson-Tvergaard-Needelman* GTN-type plasticity model with a new evolution equation for the crack phase field. We construct the constitutive model in the logarithmic strain space, which simplify the model equations and results with a formulation similar to small strains. At the end of this work, a one dimensional homogeneous test is introduced to demonstrate the performance of the coupled problem.

A.1. Constitutive equations in logarithmic strain space

A micro-mechanically based constitutive model for progressively cavitation plastic solids has been developed by GURSON [62, 63] and subsequently modified by TVERGAARD & NEEDLEMAN [147], TVERGAARD [148] and NAHSHON & HUTCHINSON [118]. Herein, the central feature of Gurson model is to account for damage growth, where the yield criterion function depends on the effective void volume fraction and extended by introducing new material parameters to account for the coalescence effect. By vanishing the void volume fraction, we end up with the standard von Mises criterion. The Gurson model for ductile damage is described by the four primary fields

$$\text{Primary Fields: } \{ \boldsymbol{\varphi}, \alpha, \boldsymbol{\varepsilon}^p, f \} \tag{A.1}$$

$\boldsymbol{\varphi}$ is the *long-range macro-motion* field and $\{\boldsymbol{\varepsilon}^p, \alpha, f\}$ are the *short-range micro-motion* fields. The void volume fraction f can be interpreted as a micro-mechanically motivated damage variable and defined as

$$f : \left\{ \begin{array}{l} \mathcal{B} \times \mathcal{T} \to [f_0, f_f] \\ (\boldsymbol{X}, t) \mapsto f(\boldsymbol{X}, t) \end{array} \right. \tag{A.2}$$

where f_0 is the initial porosity and f_f is the final void volume fraction. The objective constitutive state

$$\text{Constitutive State: } \mathfrak{c} := \{ \boldsymbol{\varepsilon}, \boldsymbol{\varepsilon}^p \} \tag{A.3}$$

contains the total logarithmic strain $\boldsymbol{\varepsilon}$ and the plastic strain defined in (6.28). Focusing on *isotropic* metal plasticity, we consider the free energy function

$$\psi(\boldsymbol{\varepsilon}, \boldsymbol{\varepsilon}^p) = \frac{\kappa}{2} \mathrm{tr}^2[\boldsymbol{\varepsilon} - \boldsymbol{\varepsilon}^p] + \mu \, \mathrm{tr}[(\mathrm{dev}[\boldsymbol{\varepsilon} - \boldsymbol{\varepsilon}^p])^2] \; , \tag{A.4}$$

where κ and μ are the elastic bulk and shear moduli, respectively. Following standard argument we obtain the stresses by the first derivative of the energetic response function with respect to the total strain

$$\boldsymbol{\sigma} = \partial_{\boldsymbol{\varepsilon}} \psi(\boldsymbol{\varepsilon}, \boldsymbol{\varepsilon}^p) = p \boldsymbol{1} + \boldsymbol{\mathfrak{s}} \tag{A.5}$$

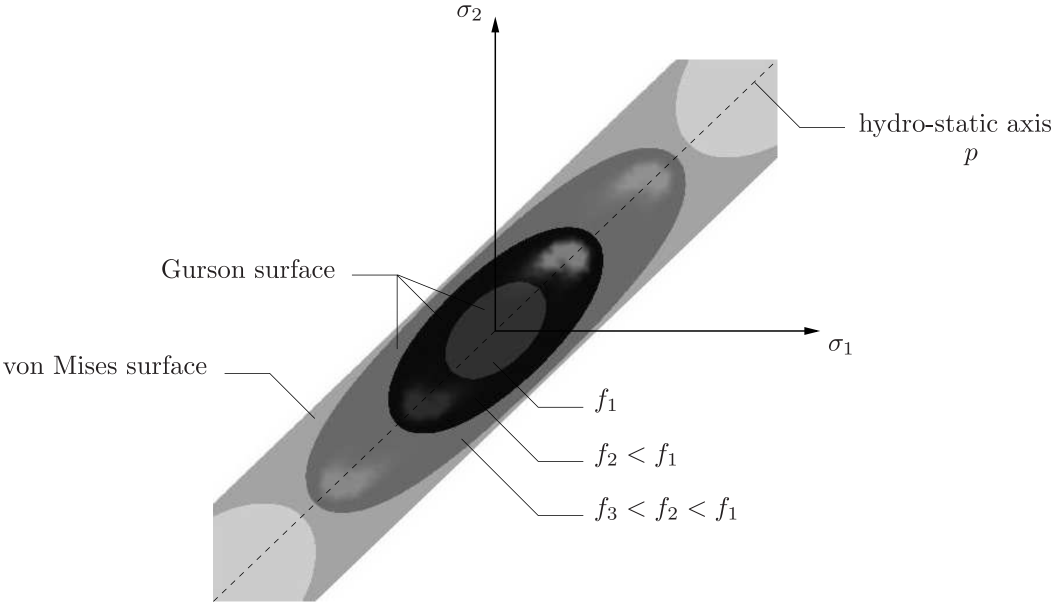

Figure A.1: A representative sketch of the Gurson yield surface with three different void volume fractions $f_1 > f_2 > f_3$ versus the von Mises yield surface with $f = 0$ in the principle stress space.

which split up into a spherical and a deviatoric part, defined by

$$p := \kappa \operatorname{tr}[\boldsymbol{\varepsilon} - \boldsymbol{\varepsilon}^p] \quad \text{and} \quad \boldsymbol{\mathfrak{s}} = 2\mu \operatorname{dev}[\boldsymbol{\varepsilon} - \boldsymbol{\varepsilon}^p] \ . \tag{A.6}$$

The Gurson yield criterion function, which depends on both stresses including the fitting parameters q_1 and q_2 proposed by TVERGAARD [148], is given in the form

$$\phi(\boldsymbol{\sigma}, f, \alpha) = |\boldsymbol{\mathfrak{s}}| - \sqrt{\tfrac{2}{3}}\, \varphi(p, f, \alpha)\, \widehat{y}(\alpha) \tag{A.7}$$

where the pressure-dependent function $\varphi(p, f, \alpha)$ makes the difference to the classical von Mises criterion. It takes the form

$$\varphi(p, f, \alpha) = \sqrt{1 + (q_1 f)^2 - 2 q_1 f \cosh\Big[\, \frac{3 q_2}{2} \frac{p}{\widehat{y}(\alpha)} \,\Big]} \ . \tag{A.8}$$

Note that, by making the void volume fraction $f = 0$, we end up with the standard von Mises yield criterion function. The yield stress of the matrix material $\widehat{y}(\alpha)$ is assumed to have the form

$$\widehat{y}(\alpha) = y_0 \Big[1 + \frac{\alpha}{\alpha_0}\Big]^N \quad \text{with} \quad \alpha_0 = y_0/E \tag{A.9}$$

in terms of the initial yield stress y_0 and the associated strain α_0, where E is the Young's modulus. α is the equivalent plastic strain of the matrix material. A graphical interpretation of the Gurson and von Mises yield surfaces in the principle stresses is given in Figure A.1. We observe that the von Mises yield surface takes a cylindrical shape with a radius of $\sqrt{2/3}\, y_0$ around the hydrostatic axis. With increasing the void volume fraction f, the von Mises cylinder *shrinks*, representing a plastic softening response.

A.2. Algorithmic implementation of the Gurson model

The plastic flow rule takes the associative form

$$\dot{\boldsymbol{\varepsilon}}^p = \lambda \boldsymbol{N} \quad \text{with} \quad \boldsymbol{N} := \partial_{\boldsymbol{\sigma}} \phi(\boldsymbol{\sigma}, f, \alpha) \tag{A.10}$$

along with the loading/unloading conditions

$$\lambda \geq 0 \quad , \quad \phi \leq 0 \quad , \quad \lambda\phi = 0 \tag{A.11}$$

The closed form of the normal is

$$\boldsymbol{N} = \frac{\boldsymbol{\mathfrak{s}}}{|\boldsymbol{\mathfrak{s}}|} - \frac{1}{3}\sqrt{\tfrac{2}{3}}\, \varphi'(p, f, \alpha)\, \widehat{y}(\alpha)\, \boldsymbol{1} \tag{A.12}$$

with

$$\varphi'(p, f, \alpha) := \partial_p \varphi(p, f, \alpha) := -\frac{3}{2}\, \frac{q_1 q_2}{\varphi(p, f, \alpha)\, \widehat{y}(\alpha)}\, f \sinh\Big[\, \frac{3q_2}{2}\, \frac{p}{\widehat{y}(\alpha)} \,\Big] \,. \tag{A.13}$$

Consider the implicit integration of the flow rule

$$\boldsymbol{\varepsilon}^p = \boldsymbol{\varepsilon}^p_n + \gamma \boldsymbol{N} \,, \tag{A.14}$$

with $\gamma = \lambda(t - t_n)$ and the normal evaluated at the current time t. Then, the stresses contribution (A.6) get the algorithmic form

$$p = p^{trial} - \kappa\gamma\, \mathrm{tr}[\boldsymbol{N}] \quad \text{and} \quad \boldsymbol{\mathfrak{s}} = \boldsymbol{\mathfrak{s}}^{trial} - 2\mu\gamma\, \mathrm{dev}[\boldsymbol{N}] \tag{A.15}$$

in terms of the trial values

$$p^{trial} := \kappa\, \mathrm{tr}[\boldsymbol{\varepsilon} - \boldsymbol{\varepsilon}^p_n] \quad \text{and} \quad \boldsymbol{\mathfrak{s}}^{trial} := 2\mu\, \mathrm{dev}[\boldsymbol{\varepsilon} - \boldsymbol{\varepsilon}^p_n] \,. \tag{A.16}$$

Taking into account (A.12), we may write

$$p = p^{trial} + \kappa\gamma\sqrt{\tfrac{2}{3}}\, \varphi'(p, f, \alpha)\, \widehat{y}(\alpha) \quad \text{and} \quad \boldsymbol{\mathfrak{s}} = \boldsymbol{\mathfrak{s}}^{trial} - 2\mu\gamma\frac{\boldsymbol{\mathfrak{s}}}{|\boldsymbol{\mathfrak{s}}|} \tag{A.17}$$

From (A.17), we conclude that $\boldsymbol{\mathfrak{s}}$ and $\boldsymbol{\mathfrak{s}}^{trial}$ are co-axial, i.e. due to

$$|\boldsymbol{\mathfrak{s}}|\frac{\boldsymbol{\mathfrak{s}}}{|\boldsymbol{\mathfrak{s}}|} = |\boldsymbol{\mathfrak{s}}^{trial}|\frac{\boldsymbol{\mathfrak{s}}^{trial}}{|\boldsymbol{\mathfrak{s}}^{trial}|} - 2\mu\gamma\frac{\boldsymbol{\mathfrak{s}}}{|\boldsymbol{\mathfrak{s}}|} \,, \tag{A.18}$$

which it yields with small manipulation, the two important equations

$$\frac{\boldsymbol{\mathfrak{s}}}{|\boldsymbol{\mathfrak{s}}|} = \frac{\boldsymbol{\mathfrak{s}}^{trial}}{|\boldsymbol{\mathfrak{s}}^{trial}|} \quad \text{and} \quad |\boldsymbol{\mathfrak{s}}| = |\boldsymbol{\mathfrak{s}}^{trial}| - 2\mu\gamma \,. \tag{A.19}$$

The evolution of the void volume fraction is divided into a (classical) *growth* part and a part due to *nucleation* of voids

$$\dot{f} = \dot{f}_{Growth} + \dot{f}_{Nucl} \,. \tag{A.20}$$

The growth part takes the classical form

$$\dot{f}_{Growth} = (1 - f)\, \mathrm{tr}\, \dot{\boldsymbol{\varepsilon}}^p \,. \tag{A.21}$$

In this work, we consider the evolution of the void volume fraction to depend only on the growth part i.e $\dot{f} = \dot{f}_{Growth}$. The equivalent plastic strain of the matrix material is related to the macroscopic plastic work by the relationship

$$(1-f)\,\widehat{y}(\alpha)\,\dot{\alpha} = \boldsymbol{\sigma} : \dot{\boldsymbol{\varepsilon}}^p \quad \to \quad \dot{\alpha} = \frac{1}{\widehat{y}(\alpha)}\left[\frac{\boldsymbol{\sigma}}{1-f}\right] : \dot{\boldsymbol{\varepsilon}}^p \tag{A.22}$$

where $\boldsymbol{\sigma}/(1-f)$ can be viewed as an *effective stress*. Next, we update α and f implicitly

$$\begin{aligned} \alpha &= \alpha_n + \gamma\Big[|\mathfrak{s}| - \sqrt{\tfrac{2}{3}}\,\varphi'(p,f,\alpha)\,\widehat{y}(\alpha)\,p\Big] \Big/ \Big[(1-f)\,\widehat{y}(\alpha)\Big] \\ f &= f_n - \gamma(1-f)\sqrt{\tfrac{2}{3}}\,\varphi'(p,f,\alpha)\,\widehat{y}(\alpha) \end{aligned} \tag{A.23}$$

For plastic loading $\phi^{trial} > 0$, the local system of equations are the variables $\{\gamma, p, \alpha, f\}$ to be solved by nonlinear Newton-Raphson iteration scheme by defining the residuum vector in terms of the local solution vector $\boldsymbol{x}$ defined as

$$\boldsymbol{x} := \{\gamma, p, \alpha, f\} \tag{A.24}$$

and the residuum vector for solving the nonlinear set of equations reads

$$\boldsymbol{r} := \widehat{\boldsymbol{r}}(\boldsymbol{x}) = \boldsymbol{0} \tag{A.25}$$

with

$$\widehat{\boldsymbol{r}}(\boldsymbol{x}) = \begin{bmatrix} |\mathfrak{s}^{trial}| - 2\mu\gamma - \sqrt{\tfrac{2}{3}}\,\varphi(p,f,\alpha)\,\widehat{y}(\alpha) \\ p - p^{trial} - \kappa\gamma\sqrt{\tfrac{2}{3}}\,\varphi'(p,f,\alpha)\,\widehat{y}(\alpha) \\ \alpha - \alpha_n - \gamma\Big[|\mathfrak{s}^{trial}| - 2\mu\gamma - \sqrt{\tfrac{2}{3}}\,\varphi'(p,f,\alpha)\,\widehat{y}(\alpha)\,p\Big] \Big/ \Big[(1-f)\widehat{y}(\alpha)\Big] \\ f - f_n + \gamma(1-f)\sqrt{\tfrac{2}{3}}\,\varphi'(p,f,\alpha)\,\widehat{y}(\alpha) \end{bmatrix} .$$

The algorithmic steps of the local update are summarized in Box 4. It results in a highly nonlinear set of equations. In this context, we propose a robust numerical integration scheme for the GTN model, namely the *Explicit-Implicit* integration strategies based on Oliver et al. [125] and Sánchez et al. [134].

A.3. Coupling Gurson model to gradient damage mechanics

A phase-field approach to porous ductile fracture is introduced to describe the coupled problem. The crack phase field d is additionally introduced as a global field, where $d = 0$ characterizes an unbroken material and $d = 1$ a fully broken state of the material. Due to the fracture phase field, the elastic part of the free energy producing a macroscopic stress has to be degraded as follows

$$\psi(\boldsymbol{\varepsilon}, \boldsymbol{\varepsilon}^p; d) = (1-d)^2\Big[\frac{\kappa}{2}\operatorname{tr}^2[\boldsymbol{\varepsilon} - \boldsymbol{\varepsilon}^p] + \mu\operatorname{tr}\big\{(\operatorname{dev}[\boldsymbol{\varepsilon} - \boldsymbol{\varepsilon}^p])^2\big\}\Big] . \tag{A.26}$$

The fracture starts when the void volume fraction reach to a critical value denoted as critical void volume fraction $f = f_{cr}$. In this context, we introduce per definition the

Box 4: *ALGO*: Algorithmic Updates for GTN Plasticity Model.

1. *Initialization.* Given is the logarithmic strain tensor $\boldsymbol{\varepsilon}$ at time t_{n+1} and the local constitutive variables $\{\boldsymbol{\varepsilon}^p_n, \alpha_n, f_n\}$ at time t_n.
2. *Trial State.* Compute the trial stresses

$$\mathfrak{s}^{trial} := 2\mu(\boldsymbol{\varepsilon} - \boldsymbol{\varepsilon}^p_n) \quad , \quad p^{trial} := \kappa\,\mathrm{tr}[\boldsymbol{\varepsilon} - \boldsymbol{\varepsilon}^p_n] \quad , \quad \widehat{y}^{\,trial} := y_0\Big[1 + \frac{\alpha_n}{\alpha_0}\Big]^N$$

3. *Yield criterion.* Compute the trial yield function for zero incremental plastic parameter $\gamma = 0$

$$\phi^{trial} := |\mathfrak{s}^{trial}| - \sqrt{\tfrac{2}{3}}\sqrt{1 + (q_1 f_n)^2 - 2q_1 f_n \cosh\Big[\ \tfrac{3q_2}{2}\,\tfrac{p^{trial}}{\widehat{y}^{\,trial}}\ \Big]}\ \widehat{y}^{\,trial}$$

4. *Check yielding.* If $\phi^{trial} \le 0$, set the incremental plastic parameter $\gamma = 0$, the pressure part of the stress $p = p^{trial}$, the equivalent plastic strain $\alpha = \alpha_n$ and go to 7.
5. *Plastic step.* If $\phi^{trial} > 0$, Compute the residuum vector, where $\boldsymbol{x} := \{\gamma, p, \alpha, f\}$

$$\widehat{\boldsymbol{r}}(\boldsymbol{x}) := \begin{bmatrix} |\mathfrak{s}^{trial}| - 2\mu\gamma - \sqrt{\tfrac{2}{3}}\ \varphi(p, f, \alpha)\ \widehat{y}(\alpha) \\ p - p^{trial} - \kappa\gamma\sqrt{\tfrac{2}{3}}\ \varphi'(p, f, \alpha)\ \widehat{y}(\alpha) \\ \alpha - \alpha_n - \gamma\Big[|\mathfrak{s}^{trial}| - 2\mu\gamma - \sqrt{\tfrac{2}{3}}\ \varphi'(p, f, \alpha)\ \widehat{y}(\alpha)\ p\Big]\Big/\Big[(1-f)\widehat{y}(\alpha)\Big] \\ f - f_n + \gamma(1-f)\sqrt{\tfrac{2}{3}}\ \varphi'(p, f, \alpha)\ \widehat{y}(\alpha) \end{bmatrix}$$

6. *Check tolerance and update short range variables.* If $|\widehat{\boldsymbol{r}}(\boldsymbol{x})| < tol$ go to 7. Perform the updates of the short range variables

$$\boldsymbol{x}_i \Leftarrow \boldsymbol{x}_i - \Big[\frac{\partial \boldsymbol{r}}{\partial \boldsymbol{x}}\Big]^{-1} \cdot \boldsymbol{r}$$

7. *Update plastic strain*

$$\boldsymbol{\varepsilon}^p = \boldsymbol{\varepsilon}^p_n + \gamma\boldsymbol{N} \quad \text{where} \quad \boldsymbol{N} = \frac{\mathfrak{s}^{trial}}{|\mathfrak{s}^{trial}|} - \frac{1}{3}\sqrt{\tfrac{2}{3}}\ \varphi'(p, f, \alpha)\ \widehat{y}(\alpha)\ \boldsymbol{1}$$

8. *Compute logarithmic stresses.*

$$\boldsymbol{\sigma} = p\boldsymbol{1} + \mathfrak{s}^{trial} - 2\mu\gamma\,\mathrm{dev}[\boldsymbol{N}]$$

9. *Stresses and tangent moduli.* Compute the first Piola nominal stress

$$\boldsymbol{P} = \boldsymbol{\sigma} : \mathcal{P}_{log} \quad \text{with} \quad \mathcal{P}_{log} := \partial_{\boldsymbol{F}}\boldsymbol{\varepsilon}$$

and the numerical tangent Moduli $\boldsymbol{\mathcal{C}}$.

crack driving force $\mathcal{H}$ as the maximum of the *crack driving state function* D and takes the form

$$\mathcal{H} := \max_{s\in[0,t]} D(\boldsymbol{\varphi}, \alpha, \boldsymbol{\varepsilon}^p, f; s) \geq 0 \quad \text{with} \quad D := \left\langle (\frac{f}{f_{cr}})^2 - 1 \right\rangle . \tag{A.27}$$

Note that the phase field driving force is zero at the beginning. When the void volume fraction f exceed its critical value, the crack driving force $\mathcal{H}$ will be updated. Next the fracture phase field d is determined conceptually in line with Chapter 6 for rate-independent limit yielding the update equation

$$d - l_f^2 \Delta d = (1-d)\mathcal{H} \tag{A.28}$$

in the domain $\mathcal{B}$, along with the homogeneous Neumann condition for the crack phase field $\nabla d \cdot \boldsymbol{N} = 0$ on $\partial\mathcal{B}$. A convenient and robust numerical implementation of the two governing PDEs of the coupled problem, namely the momentum balance equation and the update equation for the fracture phase field, is achieved by a staggered scheme based on incrementally decoupled updates of the fracture phase field and the deformation map as outlined in Chapter 6.

A.4. One dimensional homogeneous test

We demonstrate the performance of the proposed framework of phase field porous ductile fracture coupled with GTN plasticity model by means of a homogeneous problems in the one-dimensional setting. In Figure A.2a, the stress-strain curves are plotted for three different hardening parameters ($N^1 < N^2 < N^3$). One observes a stiffer overall structure response by increasing the hardening parameter N and a delayed failure behavior

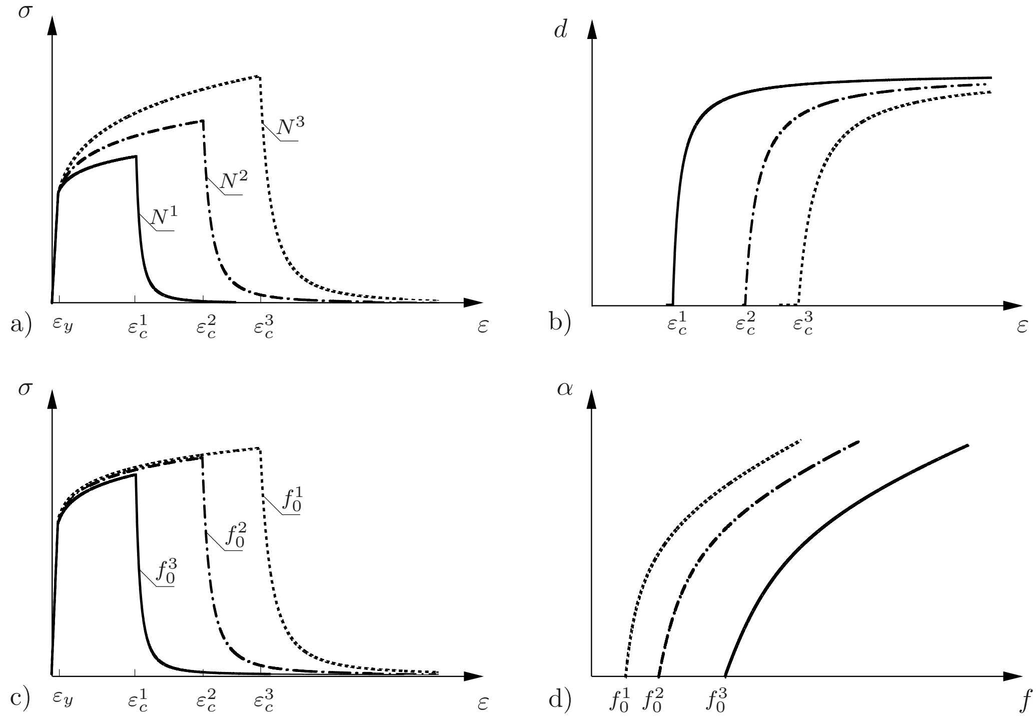

Figure A.2: Performance of porous ductile damage under monotonic loading. Stress-strain response for three different hardening parameters ($N^1 < N^2 < N^3$) in a) and void volume fractions ($f_0^1 < f_0^2 < f_0^3$) in c). Evolution of the phase field fracture in b) corresponding to a) and the equivalent plastic strain in d) corresponding to (c).

as shown in Figure A.2b. On the other hand, by increasing the initial void volume fraction $f_0^1 < f_0^2 < f_0^3$, we notice a softer response and fast failure behavior as demonstrated in Figure A.2c. The corresponding equivalent plastic strain is plotted in Figure A.2d to illustrate the influence of the void volume fraction on the plastic material response.

The presented findings can serve as a base for future studies and applications on porous ductile failure with gradient-extended *Gurson-Tvergaard-Needelman* plasticity model coupled to the phase-field fracture at finite strains.

References

[1] `www.aviation-safety.net/database/record.php?id=20080525-0` [January 20, 2016].

[2] `http://blogs.reuters.com/oddly-enough/files/2011/07/crash-test-490.jpg` [January 20, 2016].

[3] `www.bloomberg.com/news/articles/2013-05-24/bridge-collapse-in-washington-state-sends-cars-into-river` [January 20, 2016].

[4] `www.dreamstime.com/stock-photos-hammer-striking-nail-w-sparks-image443613` [January 20, 2016].

[5] `www.durasystemscomputing.com/Fun/Pictures/DSC00061ExpansionJointoftheFrenchtownbridge.JPG` [January 20, 2016].

[6] `www.en.wikipedia.org/wiki/Disc_brake` [January 20, 2016].

[7] Aifantis, E. C. [1987]: *The physics of plastic deformation.* International Journal of Plasticity, 3: 211–247.

[8] Aldakheel, F.; Mauthe, S.; Miehe, C. [2014]: *Towards phase field modeling of ductile fracture in gradient-extended elastic-plastic solids.* Proceedings in Applied Mathematics and Mechanics, 14: 411–412.

[9] Aldakheel, F.; Raina, A.; Miehe, C. [2015]: *Ductile failure with gradient plasticity coupled to the phase-field fractureat finite strains.* Proceedings in Applied Mathematics and Mechanics, 15: 271–272.

[10] Aldakheel, F.; Mauthe, S.; Miehe, C. [2013]: *Mixed variational principles and robust finite element design of gradient plasticity at finite strains.* Proceedings in Applied Mathematics and Mechanics, 13: 173–174.

[11] Alessi, R.; Marigo, J.-J.; Vidoli, S. [2014]: *Gradient damage models coupled with plasticity and nucleation of cohesive cracks.* Archive for Rational Mechanics and Analysis, 214: 575–615.

[12] Alessi, R.; Marigo, J.-J.; Vidoli, S. [2015]: *Gradient damage models coupled with plasticity: Variational formulation and main properties.* Mechanics of Materials, 80: 351–367.

[13] Ambati, M.; Gerasimov, T.; De Lorenzis, L. [2015]: *Phase-field modeling of ductile fracture.* Computational Mechanics, 55: 1017–1040.

[14] Ambati, M.; Kruse, R.; De Lorenzis, L. [2015]: *A phase-field model for ductile fracture at finite strains and its experimental verification.* Computational Mechanics, in press.

[15] Ambrosio, L.; Tortorelli, V. M. [1990]: *Approximation of functionals depending on jumps by elliptic functionals via Γ-convergence.* Communications on Pure and Applied Mathematics, 43: 999–1036.

[16] Anand, L.; Gurtin, M. E.; Lele, S. P.; Gething, C. [2005]: *A one-dimensional theory of strain-gradient plasticity: formulation, analysis, numerical results.* Journal of the Mechanics and Physics of Solids, 53: 1789–1826.

[17] Argyris, J.; Doltsinis, J. [1981]: *On the natural formulation and analysis of large deformation coupled thermomechanical problems.* Computer Methods in Applied Mechanics and Engineering, 25: 195–253.

[18] Armero, F. [1999]: *Formulation and finite element implementation of a multiplicative model of coupled poro-plasticity at finite strains under fully saturated conditions.* Computer Methods in Applied Mechanics and Engineering, 171(34): 205–241.

[19] Armero, F.; Garikipati, K. [1996]: *An analysis of strong discontinuities in multiplicative finite strain palsticity and their relation with the numerical simulation of strain localization in solids.* International Journal of Solids and Structures, 33: 2863–2885.

[20] Arnold, D. N.; Brezzi, F.; Fortin, M. [1984]: *A stable finite element for the stokes equations.* Calcolo, 21: 337–344.

[21] Arzt, E. [1998]: *Size effects in materials due to microstructural and dimensional constraints: a comparative review.* Acta Materialia, 46: 5611–5626.

[22] Ashby, M. F. [1970]: *The deformation of plastically non-homogeneous materials.* The Philosophical Magazine A, 21: 399–424.

[23] Aslan, O.; Cordero, N.; Gaubert, A.; Forest, S. [2011]: *Micromorphic approach to single crystal plasticity and damage.* International Journal of Engineering Science, 49: 1311–1325.

[24] Babuška, I. [1971]: *Error-bounds for finite element method.* Numer. Math., 16: 322–333.

[25] Babuška, I. [1973]: *The finite element method with lagrangian multipliers.* Numer. Math., 20: 179–192.

[26] Belytschko, T.; Black, T. [1999]: *Elastic crack growth in finite elements with minimal remeshing.* International Journal for Numerical Methods in Engineering, 45: 601–620.

[27] Besson, J. [2010]: *Continuum models of ductile fracture: A review.* International Journal of Damage Mechanics, 19: 3–52.

[28] Borden, M. J.; Hughes, T. J. R.; Landis, C. M.; Verhoosel, C. V. [2014]: *A higher-order phase-field model for brittle fracture: Formulation and analysis within the isogeometric analysis framework.* Computer Methods in Applied Mechanics and Engineering, 273: 100–118.

[29] Bourdin, B.; Francfort, G. A.; Marigo, J. J. [2000]: *Numerical experiments in revisited brittle fracture.* J. Mech. Phys. Solids, 48: 797–826.

[30] Boyce, B. L.; Kramer, S. L. B.; Fang, H. E.; Cordova, T. E.; Neilsen, M. K.; Dion, K.; Kaczmarowski, A. K.; Karasz, E.; Xue, L.; Gross, A. J.; Ghahremaninezhad, A.; Ravi-Chandar, K.; Lin, S.-P.; Chi, S.-W.; Chen, J. S.; Yreux, E.; Rüter, M.; Qian, D.; Zhou, Z.; Bhamare, S.; Connor, D. T.; Tang, S.; Elkhodary, K. I.; Zhao, J.; Hochhalter, J. D.; Cerrone, A. R.; Ingraffea, A. R.; Wawrzynek, P. A.; Carter, B. J.; Emery, J. M.; Veilleux, M. G.; Yang, P.; Gan, Y.; Zhang, X.; Chen, Z.; Madenci, E.; Kilic, B.; Zhang, T.; Fang, E.; Liu, P.; Lua, J.; Nahshon, K.; Miraglia, M.; Cruce, J.; DeFre, R.; Moyer, E. T.; Brinckmann, S.; Quinkert, L.; Pack, K.; Luo, M.; Wierzbicki, T. [2014]: *The sandia fracture challenge: blind round robin predictions of ductile tearing.* International Journal of Fracture, 186: 5–68.

[31] Brezzi, F. [1974]: *On the existence, uniqueness and approximation of saddle-point problems arising from lagrangian multipliers.* Revue française d'automatique, informatique, recherche opérationnelle. Analyse numérique, 8: 129–151.

[32] Brezzi, F.; Fortin, M. [1991]: *Mixed and hybrid finite element methods.* Springer-Verlag.

[33] Canadija, M.; Mosler, J. [2011]: *On the thermomechanical coupling in finite strain plasticity theory with non-linear kinematic hardening by means of incremental*

energy minimization. International Journal of Solids and Structures, 48: 1120–1129.

[34] Capriz, G. [1989]: *Continua with Microstructure.* Springer.

[35] Chadwick, P. [1999]: *Continuum Mechanics.* Dover Publications, Inc., Mineola.

[36] Cleveringa, H. H. M.; Van der Giessen, E.; Needleman, A. [1997]: *Comparison of discrete dislocation and continuum plasticity predictions for a composite material.* Acta Materialia, 45: 3163–3179.

[37] Comi, C. [1999]: *Computational modelling of gradient-enhanced damage in quasi-brittle materials.* Mechanics of Cohesive-Frictional Materials, 4: 17–36.

[38] Cosserat, E.; Cosserat, F. [1909]: *Sur la Théorie des Corps Deformables.* Dunod, Paris.

[39] de Borst, R.; Mühlhaus, H. B. [1992]: *Gradient-dependent plasticity: formulation and algorithmic aspects.* International Journal for Numerical Methods in Engineering, 35: 521–539.

[40] de Borst, R.; Pamin, J. [1996]: *Some novel developments in finite element procedures for gradient-dependent plasticity.* International Journal for Numerical Methods in Engineering, 39: 2477–2505.

[41] de Borst, R.; Pamin, J.; Geers, M. G. D. [1999]: *On coupled gradient-depended plasticity and damage theories with a view to localization analysis.* European Journal of Mechanics A/Solids, 18: 939–962.

[42] Djoko, J. K.; Ebobisse, F.; McBride, A. T.; Reddy, B. D. [2007]: *A discontinuous galerkin formulation for classical and gradient plasticity. part i: Formulation and analysis.* Computer Methods in Applied Mechanics and Engineering, 196: 3881–3897.

[43] Djoko, J. K.; Ebobisse, F.; McBride, A. T.; Reddy, B. D. [2007]: *A discontinuous galerkin formulation for classical and gradient plasticity. part ii: Algorithms and numerical analysis.* Computer Methods in Applied Mechanics and Engineering, 197: 1–21.

[44] Duda, F. P.; Ciarbonetti, A.; sánchez, P. J.; Huespe, A. E. [2014]: *A phase-field/gradient damage model for brittle fracture in elastic-plastic solids.* International Journal of Plasticity, 65: 269–296.

[45] Engelen, R. A. B.; Geers, M. G. D.; Baaijens, F. P. T. [2003]: *Nonlocal implicit gradient-enhanced elasto-plasticity for the modelling of softening behavior.* International Journal of Plasticity, 19: 403–433.

[46] Faghihi, D.; Voyiadjis, Z.; Park, T. [2013]: *Coupled thermomechanical modeling of small volume fcc metals.* Journal of Engineering Materials and Technology, 135: 1–17.

[47] Fleck, N. A.; Hutchinson, J. W. [1997]: *Strain gradient plasticity.* Advances in Applied Mechanics, 33: 295–362.

[48] Fleck, N. A.; Willis, J. R. [2009]: *A mathematical basis for strain-gradient plasticity theory. part i: scalar plastic multiplier.* Journal of the Mechanics and Physics of Solids, 57: 161–177.

[49] Fleck, N. A.; Willis, J. R. [2009]: *A mathematical basis for strain-gradient plasticity theory. part ii: tensorial plastic multiplier.* Journal of the Mechanics and Physics of Solids, 57: 1045–1057.

[50] Fleck, N. A.; Muller, G. M.; Ashby, M. F.; Hutchinson, J. W. [1994]: *Strain gradient plasticity: theory and experiment.* Acta Materialia, 42: 475–487.

[51] Forest, S. [2009]: *Micromorphic approach for gradient elasticity, viscoplasticity,*

and damage. Journal of Engineering Mechanics, 135: 117–131.

[52] Forest, S.; Sievert, R. [2003]: *Elastoviscoplastic constitutive frameworks for generalized continua.* Acta Mechanica, 160: 71–111.

[53] Francfort, G. A.; Marigo, J. J. [1998]: *Revisiting brittle fracture as an energy minimization problem.* J. Mech. Phys. Solids, 46: 1319–1342.

[54] Frémond, H. [2001]: *Non-Smooth Thermomechanics.* Springer, 1st Edition.

[55] Gao, H.; Huang, Y.; Nix, W. D.; Hutchinson, J. W. [1999]: *Mechanism-based strain gradient plasticity i. theory.* Journal of the Mechanics and Physics of Solids, 47: 1239–1263.

[56] Geers, M. G. D. [2004]: *Finite strain logarithmic hyperelasto-plasticity with softening: a strongly non-local imlicit gradient framework.* Computer Methods in Applied Mechanics and Engineering, 193: 3377–3401.

[57] Geers, M. G. D.; Ubachs, R. L. J. M.; Engelen, R. A. B. [2003]: *Strongly nonlocal gradient-enhanced finite strain elastoplasticity.* International Journal for Numerical Methods in Engineering, 56: 2039–2068.

[58] Ghadimi, B.; Kowsary, F.; Khorami, M. [2013]: *Thermal analysis of locomotive wheel-mounted brake disc.* Applied Thermal Engineering, 51: 948–952.

[59] Grassl, P.; Jirasek, M. [2006]: *Damage-plastic model for concrete failure.* International Journal of Solids and Structures, 43: 7166–7196.

[60] Green, A.; Naghdi, P. [1965]: *A general theory of an elastic-plastic continuum.* Archive for Rational Mechanics and Analysis, 18: 251–281.

[61] Gudmundson, P. [2004]: *A unified treatment of strain gradient plasticity.* Journal of the Mechanics and Physics of Solids, 52: 1379–1406.

[62] Gurson, A. L. [1975]: *Plastic flow and fracture behavior of ductile materials incorporating void nucleation, growth and coalescence.* Ph.D. Thesis, Division of Engineering, Brown University.

[63] Gurson, A. L. [1977]: *Continuum theory of ductile rupture by void nucleation and growth, part i - yield criteria and flow rules for porous ductile media.* Journal of Engineering Materials and Technology, 99: 2–15.

[64] Gurtin, M. E. [2003]: *On a framework for small-deformation viscoplasticity: free energy, microforces, strain gradients.* International Journal of Plasticity, 19: 47–90.

[65] Gurtin, M. E.; Anand, L. [2005]: *A theory of strain-gradient plasticity for isotropic, plastically irrotational materials. part i: small deformations.* Journal of the Mechanics and Physics of Solids, 53: 1624–1649.

[66] Hallquist, J. O. [1984]: *Nike 2D: An implicit, finite deformation, finite element code for analyzing the static and dynamic response of two-dimensional solids.* Rept. UCRL-52678, Lawrence Livermore National Laboratory, University of California, Livermore, CA.

[67] Hatada, N.; Ueno, K.; Ueda, M.; Watanabe, S.; Kinoshita, N. [1992]: *Three-dimensional elastic-plastic fem analysis on torsion of square-section bars.* CIRP Annals - Manufacturing Technology, 41(1): 303–306.

[68] Hofacker, M. [2014]: *A Thermodynamically Consistent Phase Field Approach to Fracture.* Ph.D. Thesis, Institute of Applied Mechanics (CE), Chair I, University of Stuttgart.

[69] Holzapfel, G. [2000]: *Nonlinear Solid Mechanics.* John Wiley & Sons.

[70] Huespe, A.; Needleman, A.; Oliver, J.; Sánchez [2009]: *A finite thickness band method for ductile fracture analysis.* International Journal of Plasticity, 25:

2349–2365.

[71] Huespe, A.; Needleman, A.; Oliver, J.; Sánchez [2012]: *A finite strain, finite band method for modeling ductile fracture*. International Journal of Plasticity, 28: 53–69.

[72] Kachanov, L. M. [1986]: *Introduction to Continuum Damage Mechanics*. Maritinus Nijhoff Publishers, 1st Edition.

[73] Kröner, E. [1960]: *Allgemeine kontinuumstheorie der versetzungen und eigenspannungen*. Archive for Rational Mechanics and Analysis, 4: 273–334.

[74] Leblond, J.; Perrin, G.; Devaus, J. [1995]: *An improved gurson-type model for hardenable ductile metals*. European Journal of Mechanics - A/Solids, 14: 499–527.

[75] Lemaitre, J. [1985]: *A continuous damage mechanics model for ductile fracture*. Journal of Engineering Materials and Technology, 107: 83–89.

[76] Lemaitre, J. [1992]: *A course on damage mechanics*. Springer.

[77] Lemaitre, J.; Chaboche, J. [1990]: *Mechanics of Solid Materials*. Cambridge University Press.

[78] Li, H.; Fu, M.; Lu, J.; Yang, H. [2011]: *Ductile fracture: Experiments and computations*. International Journal of Plasticity, 27: 147–180.

[79] Liebe, T.; Steinmann, P. [2001]: *Theory and numerics of a thermodynamically consistent framework for geometrically linear gradient plasticity*. International Journal for Numerical Methods in Engineering, 51: 1437–1467.

[80] Linder, C.; Armero, F. [2007]: *Finite elements with embedded strong discontinuities for the modeling of failure in solids*. International Journal for Numerical Methods in Engineering, 72: 1391–1433.

[81] Linder, C.; Raina, A. [2013]: *A strong discontinuity approach on multiple levels to model solids at failure*. Computer Methods in Applied Mechanics and Engineering, 253: 558–583.

[82] Mariano, P. M. [2001]: *Multifield theories in mechanics of solids*. Advances in Applied Mechanics, 38: 1–93.

[83] Markert, B. [2013]: *A survey of selected coupled multifield problems in computational mechanics*. Journal of Coupled Systems and Multiscale Dynamics, 1: 22–48.

[84] Marsden, J.; Hughes, T. [1994]: *Mathematical Foundations of Elasticity*. Dover Publications, New York.

[85] Maugin, G. A. [1990]: *Internal variables and dissipative structures*. Journal of Non-Equilibrium Thermodynamics, 15: 173–192.

[86] Maugin, G. A.; Muschik, W. [1994]: *Thermodynamics with internal variables part i. general concepts*. Journal of Non-Equilibrium Thermodynamics, 19: 217–249.

[87] Maugin, G. A.; Muschik, W. [1994]: *Thermodynamics with internal variables part ii. applications*. Journal of Non-Equilibrium Thermodynamics, 19: 250–289.

[88] Miehe, C.: *Computational mechanics of materials*. Lecture notes.

[89] Miehe, C.: *Geometrical methods for nonlinear continuum mechanics and continuum thermodynamics*. Lecture notes.

[90] Miehe, C.: *Theoretical and computer-oriented material theory*. Lecture notes.

[91] Miehe, C. [1994]: *Aspects of the formulation and finite element implementation of large strain isotropic elasticity*. International journal of numerical methods in engineering, 37: 1981–2004.

[92] Miehe, C. [1995]: *Entropic thermoelasticity at finite strains. aspects of the formulation and numerical implementation*. Computer Methods in Applied Mechanics

and Engineering, 120: 243–269.

[93] Miehe, C. [1995]: *A theory of large-strain isotropic thermoplasticity based on metric transformation tensors.* Archive of Applied Mechanics, 66: 45–64.

[94] Miehe, C. [1998]: *A constitutive frame of elastoplasticity at large strains based on the notion of a plastic metric.* International Journal of Solids and Structures, 35: 3859–3897.

[95] Miehe, C. [1998]: *A constitutive frame of elastoplasticity at large strains based on the notion of a plastic metric.* International Journal of Solids and Structures, 35: 3859–3897.

[96] Miehe, C. [2011]: *A multi-field incremental variational framework for gradient-extended standard dissipative solids.* Journal of the Mechanics and Physics of Solids, 59: 898–923.

[97] Miehe, C. [2014]: *Variational gradient plasticity at finite strains. Part I: Mixed potentials for the evolution and update problems of gradient-extended dissipative solids.* Computer Methods in Applied Mechanics and Engineering, 268: 677–703.

[98] Miehe, C.; Lambrecht, M. [2001]: *Algorithms for computation of stresses and elasticity moduli in terms of seth-hill's family of generalized strain tensors.* Communications in Numerical Methods in Engineering, 17: 337–353.

[99] Miehe, C.; Apel, N.; Lambrecht, M. [2002]: *Anisotropic additive plasticity in the logarithmic strain space: modular kinematic formulation and implementation based on incremental minimization principles for standard materials.* Computer Methods in Applied Mechanics and Engineering, 191: 5383–5425.

[100] Miehe, C.; Hofacker, M.; Welschinger, F. [2010]: *A phase field model for rate-independent crack propagation: Robust algorithmic implementation based on operator splits.* Computer Methods in Applied Mechanics and Engineering, 199: 2765–2778.

[101] Miehe, C.; Welschinger, F.; Hofacker, M. [2010]: *Thermodynamically consistent phase-field models of fracture: Variational principles and multi-field fe implementations.* International Journal of Numerical Methods in Engineering, 83: 1273–1311.

[102] Miehe, C.; Welschinger, F.; Hofacker, M. [2010]: *Thermodynamically consistent phase-field models of fracture: Variational principles and multi-field fe implementations.* International Journal for Numerical Methods in Engineering, 83: 1273–1311.

[103] Miehe, C.; Méndez Diez, J.; Göktepe, S.; Schänzel, L. [2011]: *Coupled thermoviscoplasticity of glassy polymers in the logarithmic strain space based on the free volume theory.* International Journal of Solids and Structures, 48: 1799–1817.

[104] Miehe, C.; Aldakheel, F.; Mauthe, S. [2013]: *Mixed variational principles and robust finite element implementations of gradient plasticity at small strains.* International Journal for Numerical Methods in Engineering, 94: 1037–1074.

[105] Miehe, C.; Welschinger, F.; Aldakheel, F. [2014]: *Variational gradient plasticity at finite strains. Part II: Local-global updates and mixed finite elements for additive plasticity in the logarithmic strain space.* Computer Methods in Applied Mechanics and Engineering, 268: 704–734.

[106] Miehe, C.; Hofacker, M.; Schänzel, L.; Aldakheel, F. [2015]: *Phase field modeling of fracture in multi-physics problems. part ii. coupled brittle-to-ductile failure criteria and crack propagation in thermo-elastic-plastic solids.* Computer

Methods in Applied Mechanics and Engineering, 294: 486–522.

[107] Miehe, C.; Schänzel, L.; Ulmer, H. [2015]: *Phase field modeling of fracture in multi-physics problems. Part I. balance of crack surface and failure criteria for brittle crack propagation in thermo-elastic solids.* Computer Methods in Applied Mechanics and Engineering, 294: 449–485.

[108] Miehe, C.; Aldakheel, F.; Raina, A. [2016]: *Phase field modeling of ductile fracture at finite strains: A variational gradient-extended plasticity-damage theory.* Submitted to International Journal of Plasticity.

[109] Miehe, C.; Teichtmeister, S.; Aldakheel, F. [2016]: *Phase-field modeling of ductile fracture: A variational gradient-extended plasticity-damage theory and its micromorphic regularization.* Accepted in Philosophical Transactions of the Royal Society A: Mathematical, Physical and Engineering Sciences.

[110] Miehe, C. [2012]: *Mixed variational principles for the evolution problem of gradient-extended dissipative solids.* GAMM-Mitteilungen, 35: 8–25.

[111] Moës, N.; Dolbow, J.; Belytschko, T. [1999]: *A finite element method for crack growth without remeshing.* International Journal for Numerical Methods in Engineering, 46: 131–150.

[112] Mosler, J. [2004]: *On the modeling of highly localized deformations induced by material failure: The strong discontinuity approach.* Archives of Computational Methods in Engineering, 11: 389–446.

[113] Mosler, J.; Meschke, G. [2003]: *3d modelling of strong discontinuities in elastoplastic solids: fixed and rotating localization formulations.* International Journal for Numerical Methods in Engineering, 57: 1553–1576.

[114] Mühlhaus, H.-B.; Aifantis, E. C. [1991]: *A variational principle for gradient plasticity.* International Journal of Solids and Structures, 28: 845–857.

[115] Mumford, D.; Shah, J. [1989]: *Optimal approximations by piecewise smooth functions and associated variational problems.* Communications on Pure and Applied Mathematics, 42: 577–685.

[116] Nagaraja, S. [2014]: *Coupled thermomechanical model for gradient-extended dissipative solids.* Master Thesis, Institute of Applied Mechanics (CE), Chair I, University of Stuttgart.

[117] Nagtegaal, J.; Parks, D.; Rice, J. [1974]: *On numerically accurate finite element solutions in the fully plastic range.* Computer Methods in Applied Mechanics and Engineering, 4: 153–177.

[118] Nahshon, K.; Hutchinson, J. [2008]: *Modification of the gurson model for shear failure.* European Journal of Mechanics A/Solids, 27: 1–17.

[119] Nedjar, B. [2001]: *Elastoplastic-damage modelling including the gradient of damage: formulation and computational aspects.* Inernational Journal of Solids and Structures, 38: 5421–5451.

[120] Needleman, A.; Tvergaard, V. [1984]: *An analysis of ductile rupture in notched bars.* Journal of the Mechanics and Physics of Solids, 32: 461–490.

[121] Nix, W. D.; Gao, H. [1998]: *Indentation size effects in crystalline materials: a law for strain gradient plasticity.* Journal of the Mechanics and Physics of Solids, 46: 411–425.

[122] Nye, J. F. [1953]: *Some geometrical relations in dislocated crystals.* Acta Metallurgica, 1: 153–162.

[123] Oliver, J. [1996]: *Modelling strong discontinuities in solid mechanics via strain*

softening constitutive equations. Part1: Fundamentals. International Journal for Numerical Methods in Engineering, 39: 3575–3600.

[124] Oliver, J. [1996]: *Modelling strong discontinuities in solid mechanics via strain softening constitutive equations. Part2: Numerical simulation.* International Journal for Numerical Methods in Engineering, 39: 3601–3623.

[125] Oliver, J.; Huespe, A.; Blanco, S.; Linero, D. [2005]: *Stability and robustness issues in numerical modeling of material failure with the strong discontinuity approach.* Computer Methods in Applied Mechanics and Engineering, 195: 7093–7114.

[126] Ortiz, M.; Pandolfi, A. [1999]: *Finite-deformation irreversible cohesive elements for three-dimensional crack-propagation analysis.* International Journal for Numerical Methods in Engineering, 44: 1267–1282.

[127] Perzyna, P. [1966]: *Fundamental problems in viscoplasticity.* Advances in Applied Mechanics, 9: 243–377.

[128] Perzyna, P. [1971]: *Thermodynamic theory of viscoplasticity.* Advances in Applied Mechanics.

[129] Reddy, B.; Ebobisse, F.; McBride, A. [2008]: *Well-posedness of a model of strain gradient plasticity for plastically irrotational materials.* International Journal of Plasticity, 24: 55–73.

[130] Reuscha, F.; Svendsenb, B.; Klingbeila, D. [2003]: *A non-local extension of gurson-based ductile damage modeling.* Computational Material Science, 26: 219–229.

[131] Reuscha, F.; Svendsenb, B.; Klingbeila, D. [2003]: *Local and non-local gurson-based ductile damage and failure modelling at large deformation.* European Journal of Mechanics A/Solids, 22: 779–792.

[132] Rice, J. R. [1968]: *A path independent integral and the approximate analysis of strain concentraction by notches and cracks.* Journal of Applied Mechanics, 35: 379–386.

[133] Saanouni, K.; Hamed, M. [2013]: *Micromorphic approach for finite gradient-elastoplasticity fully coupled with ductile damage: Formulation and computational aspects.* International Journal of Solids and Structures, 50: 2289–2309.

[134] Sánchez, P. J.; Huespe, A. E.; Oliver, J. [2008]: *On some topics for the numerical simulation of ductile fracture.* International Journal of Plasticity, 24: 1008–1038.

[135] Schänzel, L. [2014]: *Phase Field Modeling of Fracture in Rubbery and Glassy Polymers at Finite Thermo-Viscoelastic Deformations.* Ph.D. Thesis, Institute of Applied Mechanics (CE), Chair I, University of Stuttgart.

[136] Simo, J.; Taylor, R.; Pister, K. [1985]: *Variational and projection methods for the volume constraint in finite deformation elasto-plasticity.* Computer methods in applied mechanics and engineering, 51: 177–208.

[137] Simo, J. C. [1988]: *A framework for finite strain elastoplasticity based on maximum plastic dissipation and the multiplicative decomposition. part ii: Computational aspects.* Computer Methods in Applied Mechanics and Engineering, 68: 1–31.

[138] Simo, J. C.; Armero, F.; Taylor, R. [1993]: *Improved versions of assumed enhanced strain tri-linear elements for 3d finite deformation problems.* Computer methods in applied mechanics and engineering, 110: 359–386.

[139] Simo, J. C.; Oliver, J.; Armero, F. [1993]: *An analysis of strong discontinu-*

ities induced by strain-softening in rate-independent inelastic solids. Computational Mechanics, 12: 277–296.

[140] Simo, J.; Miehe, C. [1992]: *Associative coupled thermoplasticity at finite strains: Formulation, numerical analysis and implementation.* Computer Methods in Applied Mechanics and Engineering, 98: 41–104.

[141] Song, J.-H.; Wang, H.; Belytschko, T. [2008]: *A comparative study on finite element methods for dynamic fracture.* Computer Methods in Applied Mechanics and Engineering, 42: 239–250.

[142] Stainier, L.; Ortiz, M. [2010]: *Study and validation of thermomechanical coupling in finite strain visco-plasticity.* International Journal of Solids and Structures, 47: 704–715.

[143] Stölken, J.; Evans, A. [1998]: *A microbend test method for measuring the plasticity length scale.* Acta Materialia, 46: 5109–5115.

[144] Swift, H. [1947]: *Length changes in metals under torsional overstrain.* Engineering, 163: 253–257.

[145] Taylor, R. L. [2000]: *A mixed-enhanced formulation for tetrahedral finite elements.* International Journal for Numerical Methods in Engineering, 47: 205–227.

[146] Truesdell, C.; Noll, W. [1965]: *Handbuch der Physik Bd. III/3*, chapter The nonlinear field theories of mechanics. Springer, Berlin.

[147] Tvergaard, V.; Needleman, A. [1984]: *Analysis of the cup-cone fracture in a round tensile bar.* Acta Metallurgica, 32: 157–169.

[148] Tvergaard, V. [1982]: *On localization in ductile materials containing spherical voids.* International Journal of Fracture, 18: 237–252.

[149] Voyiadjis, Z.; Abu Al-Rub, R. K. [2005]: *Gradient plasticity with length scale parameter.* International Journal of solids and structures, 42: 3998–4029.

[150] Voyiadjis, Z.; Faghihi, D. [2012]: *Thermo-mechanical strain gradient plasticity with energetic and dissipative length scales.* International Journal of Plasticity, 30-31: 218–247.

[151] Wells, A. A. [1963]: *Application of fracture mechanics at and beyond general yielding.* British Welding Journal, 10: 563–570.

[152] Wells, G. N.; Sluys, L. J. [2001]: *A new method for modelling cohesive cracks using finite elements.* International Journal for Numerical Methods in Engineering, 50: 2667–2682.

[153] Welschinger, F. [2010]: *A variational framework for gradient-extended dissipative continua: Application to damage mechanics, fracture, and plasticity.* Ph.D. Thesis, Institute of Applied Mechanics (CE), Chair I, University of Stuttgart.

[154] Wriggers, P. [2008]: *Nonlinear Finite Element Methods.* Springer-Verlag.

[155] Wriggers, P.; Miehe, C.; Kleiber, M.; Simo, J. [1992]: *On the coupled thermomechanical treatment of necking problems via finite element methods.* International Journal for Numerical Methods in Engineering, 33: 869–883.

[156] Wu, P.; Giessen, E. Van der [1991]: *Analysis of elastic-plastic torsion of circular bars at large strains.* Archive of Applied Mechanics, 61: 89–103.

[157] Xu, X. P.; Needleman, A. [1994]: *Numerical simulations of fast crack growth in brittle solids.* Journal of the Mechanics and Physics of Solids, 42: 1397–1434.

[158] Xue, L. [2007]: *Ductile Fracture Modeling-Theory, Experimental Investigation and Numerical Verification.* Ph.D. Thesis, Massachusetts Institute of Technology.

[159] Xue, Z.; Pontin, M.; Zok, F.; Hutchinson, J. [2010]: *Calibration procedures*

for a computational model of ductile fracture. Engineering Fracture Mechanics, 77: 492–509.

[160] Yang, Q.; Stainier, L.; Ortiz, M. [2006]: *A variational formulation of the coupled thermo-mechanical boundary-value problem for general dissipative solids.* Journal of th Mechanics and Physics of Solids, 54: 401–424.

[161] Zhang, Z.; Paulino, G. [2005]: *Cohesive zone modeling of dynamic failure in homogeneous and functionally graded materials.* International Journal of Plasticity, 21: 1195–1254.

[162] Zienkiewicz, O. C.; Taylor, R.; Zhu, J. Z. [2005]: *The finite element method: Its basis and fundamentals.* Elsevier.

[163] Zienkiewicz, O.; Taylor, R. [2000]: *The Finite Element Method. Volume 1: The Basis.* Butterworth Heinemann.

[164] Zienkiewicz, O.; Taylor, R. [2000]: *The Finite Element Method. Volume 2: Solid Mechanics.* Butterworth Heinemann.

Curriculum Vitae

Personal Data

Name: Fadi Aldakheel

Date of Birth: January 01, 1984

Place of Birth: Deirazzor, Syria

Parents: Fathia Almtoali and Refat Aldakheel

Siblings: Shadi Aldakheel

Marital Status: Married

School Education

1989 – 1995	Primary School: Abu Dhar alghifari, Alraqqa, Syria
1995 – 1998	Secondary School: Aby Tamam, Alraqqa, Syria
1998 – 2001	High School: Alrashid (scientific branch), Alraqqa, Syria

University Education

2001 – 2006	Bachelor studies of Mechanical Engineering (*2nd Best Student*), Aleppo University, Syria
2009 – 2011	Master studies in Computational Mechanics of Materials and Structures COMMAS (*Honor Roll Student*), University of Stuttgart

Professional Occupation

2006 – 2009	Teaching assistant, Faculty of Petrochemical Engineering, Alfurat University, Syria
Since 09/2011	Research associate and teaching assistant, Institute of Applied Mechanics (Civil Engineering), University of Stuttgart
2012 – 2014	Examination officer master of science study-program COMMAS, University of Stuttgart
Since 07/2014	COMMAS course director, Institute of Applied Mechanics, University of Stuttgart

In dieser Schriftenreihe bisher erschienene Berichte:

I-1 (1996) *Theoretische und algorithmische Konzepte zur phänomenologischen Beschreibung anisotropen Materialverhaltens*, J. Schröder, Dissertation, 1996.

I-2 (1996) *Zur Theorie und Numerik finiter elastoplastischer Deformationen von Schalentragwerken*, B. Seifert, Dissertation, 1996.

I-3 (1996) *Zur Modellierung des künstlichen Infrarot-Dichroismus in Poymerfolien bei großen Verformungen*, J. Buhler, Dissertation, 1996.

I-4 (1998) *Verfahren zur Ermittlung der Erdbebenlasten mit Berücksichtigung des stochastischen Charakters des Bebens*, S. Zhang, Dissertation, 1998.

I-5 (1998) *Zur Beschreibung finiter Deformationen von Polymeren: Experimente, Modellbildung, Parameteridentikation und Finite-Elemente- Formulierung*, J. Keck, Dissertation, 1998.

I-6 (1999) *Berechnungsverfahren instationär erregter Systeme im Frequenzbereich*, A. Jaworek, Dissertation, 1999.

I-7 (2000) *Homogenisierungsmethoden der nichtlinearen Kontinuumsmechanik unter Beachtung von Stabilitätsproblemen*, J. Schröder, Habilitation, 2000.

I-8 (2002) *Theorie und Numerik von Materialinstäbilitaten elastoplastischer Festkörper auf der Grundlage inkrementeller Variationsformulierungen*, M. Lambrecht, Dissertation, 2002.

I-9 (2002) *Mikromechanisch motivierte Modelle zur Beschreibung finiter Deformationen gummiartiger Polymere: physikalische Modellbildung und numerische Simulation*, F. Lulei, Dissertation, 2002.

I-10 (2003) *Adaptive Finite-Elemente-Berechnungen der nichtlinearen Festkörpermechanik bei kleinen und großen Verzerrungen*, A. Koch, Dissertation, 2003.

I-11 (2003) *Theorie und Numerik der Parameteridentikation von Materialmodellen der finiten Elastizität und Inelastizität auf der Grundlage optischer Feldmeßmethoden*, G. Scheday, Dissertation, 2003.

I-12 (2004) *Approaches to the Description of Anisotropic Material Behaviour at Finite Elastic and Plastic Deformations, Theory and Numerics*, N. Apel, Dissertation, 2004.

I-13 (2004) *Temperaturabhängige Beschreibung visko-elasto-plastischer Deformationen kurzglasfaserverstärkter Thermoplaste: Modellbildung, Numerik und Experimente*, S. Rieger, Dissertation, 2004.

I-14 (2005) *Zur Parameteridentikation komplexer Materialmodelle auf der Basis realer und virtueller Testdaten*, A. Rieger, Dissertation, 2005.

I-15 (2005) *Viskoelastisches Verhalten von Elastomeren bei finiten Verzerrungen: Experimente, Modellierung und Simulationen*, H. Zecha, Dissertation, 2005.

I-16 (2005) *Mehrskalenmodelle in der Festkörpermechanik und Kopplung von Mehrgittermethoden mit Homogenisierungsverfahren*, C. G. Bayreuther, Dissertation, 2005.

I-17 (2005) *Static and Dynamic Homogenization Analyses of Discrete Granular and Atomistic Structures on Different Time and Length Scales*, J. Dettmar, Dissertation, 2005.

I-18 (2006) *Incompatibility and Instability Based Size Effects in Crystals and Composites at Finite Elastoplastic Strains*, M. Becker, Dissertation, 2006.

I-19 (2007) *Aspects of Energy Minimization in Solid Mechanics: Evolution of Inelastic Microstructures and Crack Propagation*, E. Gürses, Dissertation, 2007.

I-20 (2007) *Micro-Macro Approaches to Rubbery and Glassy Polymers: Predictive Micromechanically-Based Models and Simulations*, S. Göktepe, Dissertation, 2007.

I-21 (2008) *Material Forces in Finite Inelasticity and Structural Dynamics: Topology Optimization, Mesh Refinement and Fracture*, D. Zimmermann, Dissertation, 2008.

I-22 (2010) *Thermoviscoplasticity of Glassy Polymers: Experimental Characterization, Parameter Identification and Model Validation*, J. Méndez Diez, Dissertation, 2010.

I-23 (2010) *On the Formulation and Numerical Implementation of Dissipative Electro-Mechanics at Large Strains*, D. Rosato, Dissertation, 2010.

I-24 (2010) *A variational framework for gradient-extended dissipative continua: Application to damage mechanics, fracture, and plasticity*, F. Welschinger, Dissertation, 2010.

I-25 (2013) *Variational Multifield Modeling of the Formation and Evolution of Laminate Microstructure*, F. Hildebrand, Dissertation, 2013.

I-26 (2013) *On the Computational Modeling of Micromechanical Phenomena in Solid Materials*, C. Linder, Habilitation, 2013.

I-27 (2013) *Hybrid Micro-Macro Modeling of Texture Evolution in Polycrystal Plasticity Based on Microstructural Reorientation Continua*, I. Zimmermann, Dissertation, 2013.

I-28 (2014) *Finite Element based Electronic Structure Calculations*, V. Schauer, Dissertation, 2014.

I-29 (2014) *A Thermodynamically Consistent Phase Field Approach to Fracture*, M. Hofacker, Dissertation, 2014.

I-30 (2014) *Multi-level descriptions of failure phenomena with the strong discontinuity approach*, A. Raina, Dissertation, 2014.

I-31 (2014) *Phase Field Modeling of Fracture in Rubbery and Glassy Polymers at Finite Thermo-Viscoelastic Deformations*, L. Schänzel, Dissertation, 2014.

I-32 (2014) *Variational Homogenization in Electro-Mechanics: From Micro-Electro-Elasticity to Electroactive Polymers*, D. Zäh, Dissertation, 2014.

I-33 (2014) *Computational Modeling of Ferromagnetics and Magnetorheological Elastomers*, G. Ethiraj, Dissertation, 2014.

I-34 (2016) *Mechanics of Nonlocal Dissipative Solids: Gradient Plasticity and Phase Field Modeling of Ductile Fracture*, F. Aldakheel, Dissertation, 2016.